Conf. Dr. Ing. Fiz. Marius VOLMER

Portofoliu cu 10 lucrări relevante

1. A. Elzwawy, M. Rasly, M. Morsy, H. Piskin, M. Volmer, (2024). Magnetic Sensors: Principles, Methodologies, and Applications, pp 1-38, In: Ali, G.A.M., Chong, K.F., Makhlouf, A.S.H. (eds) Handbook of Nanosensors. Springer, Cham. https://doi.org/10.1007/978-3-031-16338-8_33-1
Capitol carte: https://drive.unitbv.ro/s/pj56mE3ScstC2g3
2. C. Mușuroi, M. Volmer*, M. Oproiu, J. Neamtu, E Helerea, Designing a Spintronic Based Magnetoresistive Bridge Sensor for Current Measurement and Low Field Sensing. *Electronics*. **11**(23), 3888 (2022). https://doi.org/10.3390/electronics11233888
Autor corespondent; articolul: https://drive.unitbv.ro/s/GgC6CcXs22QKQso
3. Amir Elzwawy, Hasan Pişkin, Numan Akdoğan, Marius Volmer, Günter Reiss, Luca Marnitz, Anastasiia Moskaltsova, Ogan Gurel and Jan-Michael Schmalhorst, Current trends in planar Hall effect sensors: evolution, optimization, and applications, J. Phys. D: Appl. Phys. **54,** 353002 (2021), https://doi.org/10.1088/1361-6463/abfbfb
Articolul: https://drive.unitbv.ro/s/yFmCgDe3cM7PRxF
4. C. Mușuroi, M. Oproiu, M. Volmer*, J. Neamtu, M. Avram, E. Helerea, Low Field Optimization of a Non-Contacting High-Sensitivity GMR-Based DC/AC Current Sensor. Sensors, **21**(7), 2564 (2021), https://doi.org/10.3390/s21072564
Autor corespondent; articolul: https://drive.unitbv.ro/s/SEomXdNDQJysxFD
5. M. Volmer, C. Mușuroi, M. Oproiu, A. Avram, M. Avram and E. Helerea, "On Detection of Magnetic Nanoparticles Using a Commercial GMR Sensor," *2021 International Aegean Conference on Electrical Machines and Power Electronics (ACEMP) & 2021 International Conference on Optimization of Electrical and Electronic Equipment (OPTIM)*, 2021, Brasov, Romania, 2-3 Sept. 2021, pp. 1-6, https://doi.org/10.1109/OPTIM-ACEMP50812.2021.9590055
Prim autor; Articolul: https://drive.unitbv.ro/s/zAweTqAQ6bandMW
6. C. Mușuroi, M. Oproiu, M. Volmer*, I. Firastrau, High sensitivity differential GMR based sensor for non-contacting DC/AC current measurement, Sensors, **20**(1), 323 (2020); https://doi.org/10.3390/s20010323
Autor corespondent; articolul: https://drive.unitbv.ro/s/PoZBYde2nSfzTc2
7. M. Volmer, M. Avram, Using Permalloy Based Planar Hall Effect Sensors to Capture and Detect Superparamagnetic Beads for Lab on a Chip Applications, Journal of Magnetism and Magnetic Materials **381**, 481-487 (2015), http://dx.doi.org/10.1016/j.jmmm.2014.10.172
Prim autor; Articolul: https://drive.unitbv.ro/s/f4fHfBzSd8a65SK
8. M. Volmer, M. Avram, Signal Dependence on Magnetic Nanoparticles Position Over a Planar Hall Effect Biosensor, Microelectronic Engineering **108**, 116–120 (2013); https://doi.org/10.1016/j.mee.2013.02.055
Prim autor; Articolul: https://drive.unitbv.ro/s/aFHFiqDkEnDSfig
9. M. Volmer, J. Neamtu, Optimisation of Spin-Valve Planar Hall Effect Sensors for Low Field Measurements, IEEE TRANSACTIONS ON MAGNETICS, **48**(4), 1577-1580 (2012); http://dx.doi.org/10.1109/TMAG.2011.2173671
Prim autor; Articolul: https://drive.unitbv.ro/s/pCCkibGTkgQaSpB
10. M. Volmer, J. Neamtu, Electrical and micromagnetic characterization of rotation sensors made from Permalloy multilayered thin films, Journal of Magnetism and Magnetic Materials, **322**, 1631–1634 (2010), http://dx.doi.org/10.1016/j.jmmm.2009.06.085
Prim autor; Articolul: https://drive.unitbv.ro/s/nMWFb8xgjrR3kJ7

07.05.2025
Conf. Dr. Ing. Fiz. Marius VOLMER

Magnetic Sensors: Principles, Methodologies, and Applications

Amir Elzwawy, Mahmoud Rasly, Mohamed Morsy, Hasan Piskin, and Marius Volmer

Contents

A. Elzwawy (✉)
Ceramics Department, National Research Center (NRC), Cairo, Egypt
e-mail: aa.elzwawy@nrc.sci.eg

M. Rasly (✉)
Electronic and Magnetic Materials Department, Advanced Materials Institute, Central Metallurgical Research and Development Institute (CMRDI), Cairo, Egypt
e-mail: mrasly@cmrdi.sci.eg

M. Morsy
Building Physics and Environment Institute, Housing & Building National Research Center (HBRC), Cairo, Egypt

H. Piskin
Department of Physics, Boğaziçi University, Istanbul, Turkey
e-mail: hasan.piskin@boun.edu.tr

M. Volmer (✉)
Electrical Engineering and Applied Physics Department, Transilvania University of Brasov, Brasov, Romania
e-mail: volmerm@unitbv.ro

G. A. M. Ali et al. (eds.), *Handbook of Nanosensors*,
https://doi.org/10.1007/978-3-031-16338-8_33-1

Abstract

The necessity for magnetic sensors has evolved rapidly in the recent preceding decades for diverse applications. Various sorts of sensors can directly detect physical properties such as temperature, humidity, and pressure and deliver an output signal associated with the intended parameters. Contrary to these sensors, magnetic sensors monitor the fluctuations in magnetic fields pursued by surrounding objects or events. The magnetic sensors provide data on the direction, rotation, and electrical current and convert them to the corresponding output voltage. Due to the feasibility and wireless response, magnetic field sensors are included in robotics, the automobile industry, magnetic recording, target tracking, human body biomagnetic measurements, and much more. This chapter introduces the background behind the magnetic sensing process and its basics. Afterward, the desired materials for the magnetic sensors are surveyed. The coverage of famous magnetic sensors like the magnetic tunnel junction sensors, giant magnetoresistance sensors, and planar Hall effect sensors is covered. The key parameters for evaluating the performance of the sensor such as exchange bias, sensitivity, and detection limit are highlighted in this chapter. Finally, major industrial and medical applications for magnetic sensors are implemented. This chapter overviews the concepts of magnetic sensors from background to applications and can provide a valuable piece of work for upcoming nanotechnological applications on a wide spectrum.

Keywords

Magnetic field · Magnetic sensors · Exchange bias · Sensitivity · Detection limit

Abbreviations

T_{abs}	Absolute temperature
AMR	Anisotropic magnetoresistance
V_{AMR}	Anisotropic magnetoresistance voltage
AFM	Antiferromagnetic

AI	Artificial intelligence
BP	Barber pole
k_B	Boltzmann's constant
q	Charge of electron
H_K	Crystal anisotropy field
i	Current
CIP	Current in plane
R	Electrical resistance
ECG	Electrocardiography
E_{exchange}	Exchange anisotropy energy
H_{exc}	Exchange anisotropy field
H_{ext}	External magnetic field
FCC	Face centered cubic
FM	Ferromagnetic
$S_{1/f}$	Flicker noise
GMR	Giant magnetoresistance
IC	Integrated circuits
S_{Johnson}	Johnson noise
l	Length
D	Magnetic field detectivity
MNPs	Magnetic nanoparticles
Fe_3O_4	Magnetite
M	Magnetization
θ	Magnetization angle
MCG	Magnetocardiography
E_{Crsytal}	Magnetocrystalline energy
MR	Magnetoresistive
NM	Nonmagnetic
$Ni_{80}Fe_{20}$	Permalloy
PHE	Planar Hall effect
V_{PHE}	Planar Hall effect voltage
PHR	Planar Hall resistance
PET	Polyethylene terephthalate
RKKY	Ruderman–Kittel–Kasuya–Yosida
S	Sensitivity
E_{shape}	Shape anisotropy energy
H_{sh}	Shape anisotropy field
S_{Shot}	Shot noise
SNR	Signal-to-noise ratio
t	Thickness
t_{fm}	Thickness of ferromagnetic material
TMR	Tunneling magnetoresistance
V_{bridge}	Voltage of Wheatstone bridge sensor
w	Width
E_{Zeeman}	Zeeman energy

Introduction

The necessity for apparatus and devices with the ability to sense the Earth and surrounding magnetic fields has been progressively spreading in the last few decades. Various sorts of sensors can provide insights into the medium changes upon their corresponding changes in physical or chemical properties. Sensors are basically identified as a device that provides the possibility of transferring physical phenomena to an electrical response, and thus they might work as a bridge connecting the physical world and the electronic devices world [1]. In other words, they are referred to as the basic part of the chain of measurements that transmits the input parameter to a readable signal convenient for the measurement [2]. Magnetic sensors have supported mankind in investigating and monitoring thousands of functions for numerous eras [3]. Supercomputers and ordinary computers possess raised storage capacities via the usage of magnetic sensors in head drives. Airplanes owe increased safety standards according to contactless magnetic sensing switching. Moving vehicles and automobiles employ magnetic sensors for position tracking and more [3]. Sensing weak magnetic fields can be made using magnetoresistive (MR) sensors microfabricated from single or multilayered magnetic thin films. These sensors are categorized into main sorts of magnetic sensors which are anisotropic magnetoresistance (AMR), tunneling magnetoresistance (TMR), giant magnetoresistance (GMR), as well as the planar Hall effect (PHE) ones.

MR sensors can detect magnetic fields ranging from 10^{-9} T to 10^{-1} T with a linear scale up to ~10^{-2} T, depending on sensor structure and measurement setup. In contrast, the silicon-based Hall effect sensors, developed by a prominent technology and integrated in many applications, are less sensitive, being able to detect magnetic fields larger than 10^{-6} T. Using graphene layers can be patterned flexible Hall effect sensors maintaining a sensitivity of 79 V/(AT) and stable characteristics during bending cycles. A boost in sensitivity up to 1600 V/(AT) but with lower stability in time with deviations of up to 9.3% from one day to another was reported for graphene-based Hall sensors used for magnetic scanning probe microscopy. The MR sensors are microfabricated from magnetic thin films or multilayers consisting of magnetic, antiferromagnetic, and nonmagnetic (NM) thin films using well-defined layers stacking, deposition, and patterning methods. They adhere to the principles of Si-based integrated circuits (IC) technology and are convenient for special applications like integration in microfluidic systems [3, 4]. Not at least, because of the demagnetizing field, most of the MR sensors are sensitive only to in-plane applied fields, and this can be beneficial for magnetic nanoparticle (MNP) detection compared with Hall effect sensors. Thus, each type of sensor brings advantages and drawbacks that must be accounted for for specific applications like magnetometer, rotation sensor, detection of MNPs, etc. Moreover, except for the PHE sensors that possess a native linear response about zero field and deliver a bipolar output signal, the response of MR sensors in magnetic field is unipolar, and a biasing field is required for linearization. However, by using spin valves with crossed anisotropies, i.e., mutually perpendicular easy axes of magnetization in two neighboring ferromagnetic layers, or by playing with layers dimensions and thicknesses, the output of GMR and TMR sensors can be linearized around zero field.

Magnetic Sensors

Versatile sorts of sensors are employed in every aspect of daily life activities. This comprises humidity sensors [4–6], gas sensors [7], electrochemical sensors [8–11], pressure sensors [12, 13], temperature sensors [14], optical sensors [15–18], and more. Magnetic sensors are defined as a device that can monitor and detect the existence of the magnetic fields and translate this field into an electrical voltage corresponding to the applied magnetic field delivered to the sensing material. Since the magnetic field can easily spread in the free space, it enables a noncontact sensing in a variety of applications, which encompasses neural signal detection, magnetocardiography, autonomous driving, electrical vehicles sensorization, and even opening doors to novel quantum metrology systems. There are several methods to sense the magnetic field mostly relying on the connection between magnetic and electric phenomena [3]. The principle of working for a magnetic field in general depends on the magnetic moment change for magnetic materials when involved in a magnetic field [19]. Numerous physical impacts are demonstrated in the magnetic sensors [20]. The evolution of significantly sensitive and localized magnetic sensors is a propagating area because of the development in the nano- and microfabrication techniques related technologies [21]. However, there is no ideal candidate which fulfills all the needs and requirements for all application areas. This possibility might arise from the discrepancy in magnetic sensors' sensitivity due to the alteration in the sensing element dimensions or the sophisticated working process. In the following, various classifications of magnetic sensors are introduced.

Anisotropic Magnetoresistive Sensors (AMR)

From a broader point of view, AMR can be defined as a generic magnetotransport property that characterizes ferromagnetic metallic substances (as well as their entailed alloys). The AMR outcome was first introduced to the scientific society in 1856 by Lord Kelvin (Willaim T.). Ferromagnetic materials are composed of Co, Ni, Fe, and alloys such as CoFe and NiFe. At the atomic scale, the manifestation of the AMR effect can be clarified as a result of the ferromagnetic metal particular band structure. Indeed, these types of materials are characterized by the state of occupancy of the 3d and 4 s orbitals. The 3d orbitals seem to be partially filled, while the 4 s orbitals seem to be scattered to the *3d* suborbitals in the presence of magnetic fields [22–24]. The electron orbit asymmetry is used mainly to explain the anisotropic magnetoresistance. Consequently, the scattering cross sections of electrons vary where the electrons move parallel or perpendicular to the applied magnetic field.

Because of the asymmetry in electron orbits, spin-orbit coupling arises. Additional significant parameters including longitudinal (ρ_{xx}) and transverse (ρ_{xy}) resistivity depend on the magnetization M values and the accompanying current density J. For polycrystalline conducting magnetic materials (counting ferromagnetic 3d type alloys), the dependence is expressed by subsequent equations [25]:

$$\rho_{xx} = \rho_{\perp} + \left(\rho_{//} - \rho_{\perp}\right) \cos^2\theta \tag{1}$$

$$\rho_{xy} = \frac{1}{2}\left(\rho_{//} - \rho_{\perp}\right) \sin 2\theta \tag{2}$$

where ρ_{xx} is the parallel magnetoresistance and ρ_{xy} is the perpendicular magnetoresistance while θ is the contained angle between current density (J) and magnetization (M) (Fig. 1). The AMR is defined as the disparity of the longitudinal resistivity, while the transverse resistivity variation is termed as the PHE.

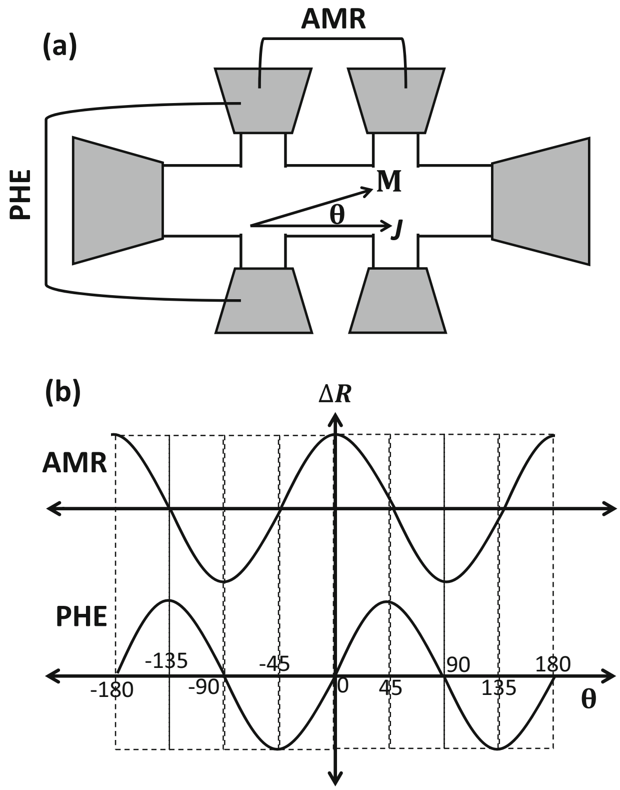

Fig. 1 The AMR and PHE configurations for in-plane and out of plane relativity of magnetization and current density. (Adapted with permission from Ref. [22], (Copyright 2021, IOPSciecne))

Planar Hall Effect Sensors

The signals of the PHE magnetic field sensor depend on the contained angle between magnetic conductor's magnetization and the track of the current flowing through it. The magnetic conductor should be homogeneously magnetized for this application, and in the existence of an applied magnetic field, the magnetization direction should vary predictably, reversibly, and with no-noticeable hysteresis. The magnetic conductor should be uniformly magnetized for this application, and in the company of an externally applied magnetic field, the magnetization direction should vary periodically, reversibly, and with negligible hysteresis.

To achieve this behavior, the layer must be magnetically anisotropic. whenever the above criteria are encountered, the PHE signal designates the magnetization direction that determines the value of the applied perpendicular magnetic field [26–28].

When compared to the AMR, the PHE sensors offer multiple inherent advantages. The largest slope of the AMR sensor as per the θ values (the contained angle among current and magnetization) is achieved at $\frac{\pi}{4} + \frac{n\pi}{2}$, while for the PHE sensor, the largest slope is demonstrated at $\frac{n\pi}{2}$. The PHE offers easy and low-cost fabrication procedures, where the angle θ is equal to the $\frac{n\pi}{2}$ away from the applied magnetic field.

Moreover, the acquired signal from the AMR sensor is usually weak in the range of a few percent and is generally measured over a large DC element connected to a resistance. Hence, temperature variations and aging extremely affect the value of the DC element that is associated with the AMR sensor.

Also, the AMR signal is usually small, at most of the order of a few percent, and it is measured on top of a large DC component associated with the average resistance (see Fig. 1b). Therefore, temperature and aging drifts which affect the DC component are extremely detrimental to AMR sensors. AMR sensors are typically utilized in a Wheatstone bridge configuration of four AMR sensors to generate an output voltage without the DC component. In PHE sensors, such a design is not required as the DC component vanishes at zero.

The AMR signal is also typically small, just a few percent at most, and it is measured on top of a significant DC component related to the average resistance (see Fig. 1b). Thus, AMR sensors are severely harmed by temperature and aging drifts that affect the DC component. To generate an output voltage without the DC component, four AMR sensors are typically used in the Wheatstone bridge configuration. Such a design is not necessary in PHE sensors because the DC component vanishes at zero (see Fig. 1b).

Giant Magnetoresistance Sensors

Magnetoresistance outcome is recognized as an alteration in the electrical resistance of a specific material upon the application of an externally applied magnetic field. Because of the strength and orientation of the magnetic field, the variation in the electrical resistance lies between maximum (R_{max}) and minimum (R_{min}) resistance magnitudes. The difference in resistance (ΔR) can be normalized with respect to the minimum resistance as a reference value, and thus the magnetoresistance effect can be estimated as follows [22, 29]:

$$MR = \frac{R_{\max} - R_{\min}}{R_{\min}} = \frac{\Delta R}{R_{\min}} \tag{3}$$

The so-called GMR and tunnel magnetoresistance (TMR) influences are the chief two effects incorporated in low-magnetic field sensing applications. GMR was discovered in 1988, when two independent research groups unveiled multilayer structures with tremendous MR values, now known as GMR. These multilayer structures are composed of a stack structure of ferromagnetic layers detached by a tiny layer of nonmagnetic metals. The nominal thickness of each individual layer may reach down to the atomistic scale. One research group headed by Peter Grünberg participated in the first experiments that led to the discovery of GMR where they utilized Fe/Cr/Fe trilayer system [30]. The second research group, directed by Albert Fert, employed a [31], multilayers with the general formula of $(Fe/Cr)_n$ where n might approach 60. For a GMR element, the ferromagnetic layers equal to or more than two layers are insulated by a very slender non-ferromagnetic spacer. The RKKY coupling among contiguous ferromagnetic layers is transformed to antiferromagnetic at specific thicknesses. Consequently, it is preferred for the magnetizations of contiguous layers to orient in antiparallel directions. The device's electrical resistance is often larger in the antiparallel scenario, and the variation might be greater than 10% at ambient temperature as depicted schematically in Fig. 2.

The device's electrical resistance is typically higher with the antiparallel state, and the difference can approach more than 10% at ambient temperature, as illustrated schematically in Fig. 2.

Without the incidence of exterior magnetic fields, antiparallel magnetization is achieved in the ferromagnetic layers. Without the application of the external

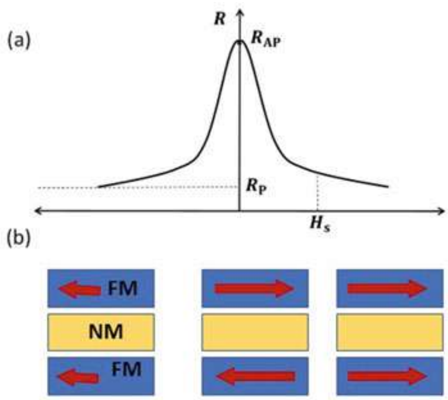

Fig. 2 (**a**, **b**) The configuration of GMR structure, showing the parallel and antiparallel alignments of the magnetization. (Adapted with permission from Ref. [32], Copyright 2016, MDPI)

magnetic field, the ferromagnetic layer magnetizations are aligned antiparallel state. In the presence of an external magnetic field, the magnetic moments are aligned and besides the magnetization is saturated; thereby, the resistance of the multilayers decreases rapidly. The two groups, Grünberg and Fert groups, observed large resistance changes of 6% and 50%, respectively. The amplitude of GMR effect was much smaller for the Grünberg group's system, not because they used a trilayer but mostly because the experiments were carried out at room temperature, whereas the experiments conducted by Fert and co-workers were at very low temperature (4.2 K).

Spin-Valve GMR

This structure consists of two ferromagnetic layers spaced by a small non-ferromagnetic layer but without RKKY interaction. To do this, there must be a huge difference in the coercive fields of each layer to be switched independently. The parallel and antiparallel alignments can be therefore achieved, and the value of resistance would be higher at the antiparallel state [1–3]. The scheme for the spin-valve structure is demonstrated in Fig. 3a.

Pseudo-Spin GMR

The similarities between the pseudo-spin-valve devices and the spin-valve configurations are very close. The major difference is represented in the coercive force of the ferromagnetic layers. The functional magnetic field is varied for the pseudo-spin-valve structure (Fig. 3b) in the first layer, and a weak magnetic field will be applied, while for the other layers, an intensive filed will be used. This, in turn, will flip the magnetization of the first layer before the remaining layers as a result of the applied magnetic field, hence affording the same antiferromagnetic impact that is needed for GMR instruments. The working principle of pseudo-spin-valve devices generally

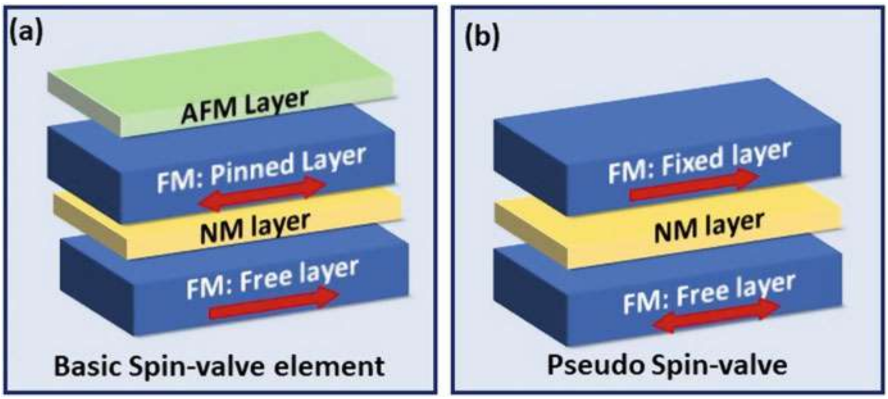

Fig. 3 (**a**) The schematic representation of spin-valve GMR structure (Adapted with permission from Ref. [33], 2013, MDPI) and (**b**) multilayer components of pseudo-spin-valve GMR structure. (Adapted with permission from Ref. [34], Copyright 2008, AIP)

depends on the nominal thickness of the nonmagnetic layer; it must deliver enough thickness to minimize the exchange coupling. The interaction experienced between the two successive ferromagnetic layers must be prevented to grasp complete control over the device.

The GMR discovery achieved a revolution in modern technologies focusing on recent magnetic sensors as well as data storage in hard drives. Currently, the magnetoelectronic phenomena have attracted the attention of many scientists all over the world to investigate their possible applications in many related applications. The discovery of the GMR is a good example for demonstrating the unpredicted scientific findings that may lead to novel technologies with related commercial products.

Tunnel Magnetoresistance

Magnetic tunnel junctions (MTJs) are a famous type of magnetoresistive sensors with numerous layer structures which resemble the spin-valve layer structure. However, a thin insulator layer is introduced here as an insulating barrier, largely aluminum oxide (Al_2O_3) or magnesium oxide (MgO) material. Once the desired voltage has functioned onto the top magnetic electrode, electron spins can tunnel across the insulating barrier to the bottom electrode depending on the magnetization configuration between top and bottom electrodes [54], which might be designated using a spin-dependent tunneling influence [55]. Therefore, the electrons tunneling could be investigated as binary separate spin channels, where Fermi level electrons for the initial ferromagnetic electrode (i.e., FM1) tunnel across the barrier and proceed into free equivalent spin positions at the second ferromagnetic electrode's Fermi level (i.e., FM2). Because of the strong spin imbalance occurring at the Fermi level, ferromagnetic materials behave as spin filters for both cases of up spinning and down spinning electrons of the charge current. Consequently, when there is a parallel magnetization configuration among the upper and lower electrodes, the conduction mechanism arises mainly due to tunneling of the majority electron spin. However, when the magnetization configuration is antiparallel, conduction is due to tunneling of minority electron spin, which restricts the conductance value. Figure 4 is a demonstration of the represented density of states (DOS) and spin-dependent tunneling through a nonconducting barrier.

Since the conductance (G) relies on the entire quantity of the passing electrons through the junction, it can be introduced as the outcome of the Fermi level density of states in both ferromagnetic electrodes as follows:

$$\text{Conductance during parallel configuration} \qquad G_{\mathrm{P}} \propto D_1^{\uparrow} D_2^{\uparrow} + D_1^{\downarrow} D_2^{\downarrow} \tag{4}$$

$$\text{Conductance during antiparallel configuration} \qquad G_{\mathrm{AP}} \propto D_1^{\uparrow} D_2^{\downarrow} + D_1^{\downarrow} D_2^{\uparrow} \tag{5}$$

where $D_{\mathrm{i}}^{\uparrow}$ and $D_{\mathrm{i}}^{\downarrow}$ refers to the density of states volumes in spin up and spin down cases by the Fermi level in the ferromagnetic electrode. Accordingly, when the

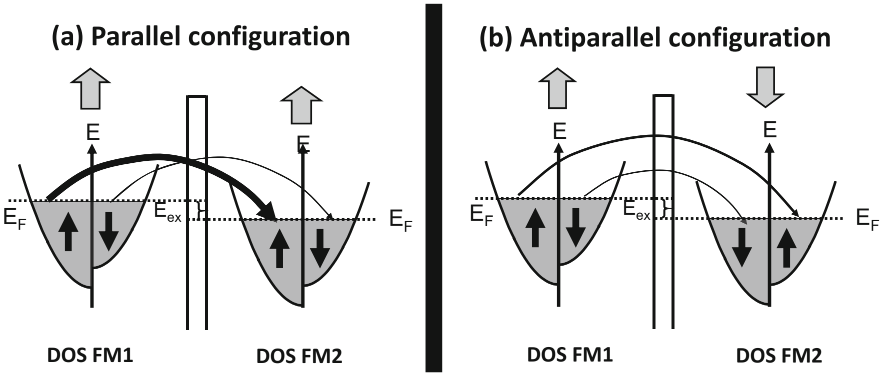

Fig. 4 The represented density of states (DOS) and spin-dependent tunneling through a non-conducting barrier, between ferromagnetic layers having analogous magnetization arrangement (parallel) (**a**) and non-analogous arrangement (antiparallel) (**b**). (Adapted with permission from Ref. [35], Copyright 2020, Elsevier)

magnetization alignments of both ferromagnetic contacts have similar directions, electron-spin tunneling arises among spin bands that have alike density of states, providing a high conductance channel. Conversely, when the magnetization alignments are antiparallel, electron-spin tunneling arises among spin bands that owe changed density of states delivering a reduced conductance channel. Therefore, as the conductance has an inverse proportion to the electrical resistance ($R = 1/G$), the TMR ratio might be stated as the alteration in resistance among the parallel and antiparallel magnetization arrangements as follows [36, 37]:

$$TMR, \% = \frac{R_{AP} - R_P}{R_P} \times 100 = \frac{G_P - G_{AP}}{G_{AP}} \times 100 \tag{6}$$

Because of the oxide insulator, MTJs demonstrate a great resistance difference between parallel and antiparallel states and thereby a higher MR ratio than in the case of spin-valves sensors.

During the foremost age of MTJs with Al_2O_3 layer as an amorphous barrier, TMR ratio was in the range of 70% [56]. Thereafter, presenting MgO as a crystalline barrier led to the enhancement of TMR ratio reaching 200% that exists in Fe/MgO/Fe junctions at ambient temperature [57].

MTJ Layer Structures

Basic Layer Structures

The standard structure of a MTJ layer structure comprises dual ferromagnetic layers detached by a nonconducting nonmetallic thin barrier; herein first ferromagnetic layer possesses a fixed magnetization direction (*known as reference layer*), and the second is free to rotate (referred to as *free or sensing layer*) with the variation in the applied magnetic field. The reference layer magnetization can be pinned through a

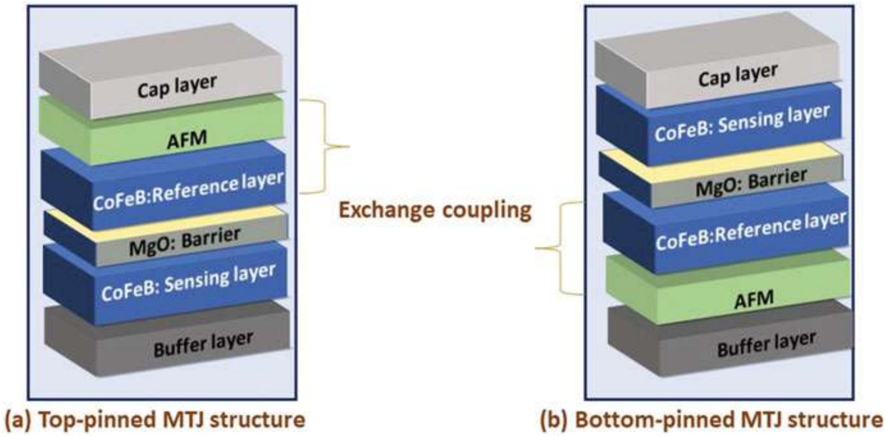

Fig. 5 The representation of MTJ structure. (Adapted with permission from Ref. [37], Copyright 2015, MDPI, and from Ref. [38], Copyright 2016, Springer)

specific direction by the occurring coupling with a thick antiferromagnetic (AF) material layer as IrMn. The AF layer generates an exchange-bias result, which pins the magnetization of the adjacent ferromagnetic layer through a certain direction by annealing under an external magnetic field. As shown in Fig. 5, when an AF layer is coupled with the top (bottom) ferromagnetic layer, the structure is then called a top (bottom) pinned MTJ. Overall, the layer structure can't be deposited directly on top of a substrate because of a roughness issue. Therefore, seed layers or buffer layers must be sputtered first to enhance the surface interface, enhancing the tunneling probabilities across layer structures and principally insulator barriers. Finally, to hinder the corrosion and oxidation of the layer structure from the surrounding medium, a thin capping layer is frequently deposited on the top of the structure.

The Synthetic Ferromagnetic Structure

With SF structure, magnetization alignments can be installed. This structure ensures an antiferromagnetic coupling between the two ferromagnetic contacts (FM1 and FM2) via the interlayer-exchange coupling effect, i.e., across a nonmagnetic barrier (NM). Since the ferromagnetic layers are free to rotate, e.g., no exchange bias, a low effective magnetic thickness t_{eff} can be adapted, and an increased physical free-layer thickness can be preserved according to the following: $t_{\text{real}} = t_{\text{FM1}} + t_{\text{NM}} + t_{\text{FM2}}$.

$$t_{\text{eff}} = \frac{M_1 t_1 - M_2 t_2}{M_{\text{eff}}} \tag{7}$$

where t_{i} and M_{i} are the thickness and magnetization, correspondingly, of both FM layers $i = 1, 2$, and M_{eff} $(= M_1 + M_2)$ is the SF free-layer effective magnetization. The effective magnetic moment and thickness can be therefore specified by minimizing the self-demagnetization field formed using the free layer. Nevertheless, a lesser effective magnetic thickness generates an offset field H_0 due to enhancement in the Neel interlayer coupling field, viewing $1/t_{\mathrm{eff}}$ dependence. Thus, an adaptation of synthetic antiferromagnetic coupling across the nonmagnetic spacer is more appropriate for applications.

The Synthetic Antiferromagnetic (SAF) Structure

Synthetic antiferromagnetic (SAF) coupling structure has announced to enhance the exchange-bias field, i.e., improve magnetic stability, and to decrease the occurring magnetostatic coupling among the free and the reference layer owing to a minor resultant moment for the SAF structure. The SAF includes a layered structure, whereas both ferromagnetic layers are imparted by a low thickness nonmagnetic layer (NM). One ferromagnetic layer (FM1) is in contact with an antiferromagnet layer through the exchange coupling effect, while the remaining ferromagnetic layer (FM2) is coupled antiferromagnetically to the FM1 through (Ruderman–Kittel–Kasuya–Yosida) RKKY interaction [66]. This contacting interaction displays the coupling impact through two ferromagnetic layers parted by a separating nonmagnetic spacer and fluctuates between antiferromagnetic and ferromagnetic layers based on the thickness of the nonmagnetic spacing layer.

Sensor Materials

Polycrystalline Sensing Layers

To ensure low-noise characteristics of MTJ sensors, the origin of the frequency-dependent (1/f) noise and thermal noise should be identified and minimized. For that, the later has admitted to the reduction of junction resistance and the former is by improving the quality of the layer structures. According to the application and the limit of detection, magnetic sensors can be categorized. For extremely low-sensing applications such as magnetocardiography, MTJs are the most promising magnetic sensors. Therefore, the requirements and recent advances on magnetic materials in MTJ structures are discussed.

Figure 6 shows a schematic structure of the MTJ sensor processed with the soft-pinning technique. Soft-pinning technique is applied to obtain a cross-magnetization between reference and sensing layers. Cross-magnetization is mandatory to induce a kind of coherent rotation of sensing layer magnetization with the change in external magnetic field, i.e., linear transfer from parallel state to antiparallel state and vice versa. In the forthcoming section, the linearization techniques will be discussed in more detail. In most cases, soft-magnetic materials such as permalloy (NiFe) are strong candidates as sensing magnetic materials because it has small magnetic anisotropy, which defines the special resolution of magnetic sensors. Therefore, NiFe is introduced as a sensing layer. However, it has fcc 111 texture, and CoFeB (CFB) must acquire bcc 100 texture in order to improve electron-spin tunneling and thereby high TMR ratios. To reduce the propagation of fcc texture from NiFe over

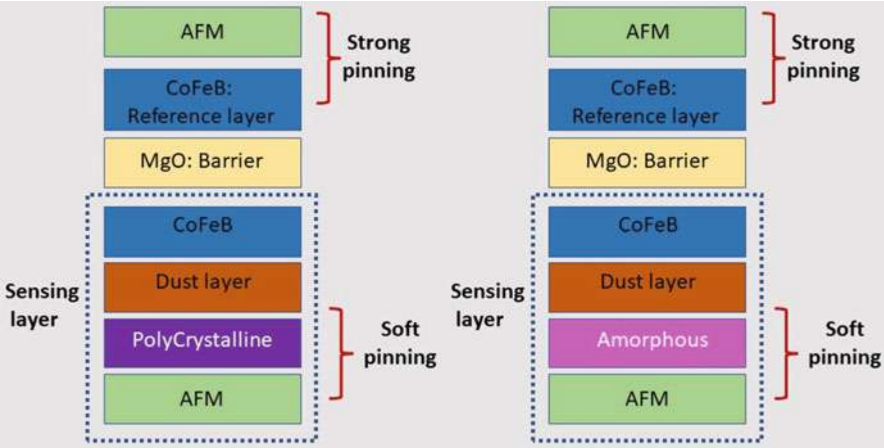

Fig. 6 Magnetic tunnel junction element with polycrystalline sensing layer (left) (Adapted with permission form Ref. [37], Copyright 2015, MDPI) and magnetic tunnel junction element with amorphous sensing layer (right). (Adapted with permission from Ref. [39], Copyright 2023, AIP)

the layer structure, a thin dust layer of Ta, Ru, or W has to be grown on top of NiFe. However, the difference in the crystal orientations has still influenced the texture of CoFeB, enriching the source of noise within the layer structure and thereby reducing TMR ratios. Also, the soft-magnetic properties of NiFe degrade by annealing at high annealing temperature ($\geq$ 350 °C), which is required to achieve a high TMR ratio.

Amorphous Sensing Layers

Alternatively, amorphous soft-magnetic alloys like CoFeBX, where X is Si, Ta, and Hf, are needed owing to their high crystallization temperatures [40] (Fig. 6). Particularly, introducing Ta to CoFeB leads to increasing the crystallization temperature to more than 500 °C. There is no (crystalline) template transferring from the sensing layer to the spacer, which promotes in high tunneling magnetoresistance ratio (TMR).

Linearization Techniques

The transfer curve can be considered as an indicator for the magnetic sensor performance where the resistance depends on the applied field. A typical magnetic tunnel junction with parallel/antiparallel magnetization configuration cannot be used as a magnetic sensor. This is because the transfer curve exhibits an abrupt change in the resistance values while the magnetization configuration changes between parallel/antiparallel states, generating a squared hysteresis loop as shown in (Fig. 7a).

In order to use MTJ as a type of magnetic sensors, the transfer curve must show linearity without a hysteresis curve throughout the active operating range. This happens only if there is an orthogonal-magnetization configuration between the sensing and reference layers (Fig. 7b). Several techniques have been reported through the literature to produce linear transfer curves. Figure 8 summarizes the essence of the most usable techniques.

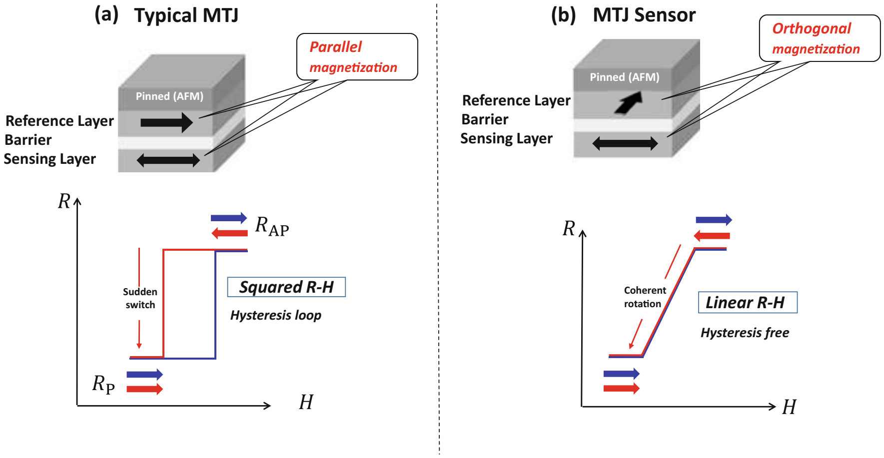

Fig. 7 The change in resistance with magnetic field showing square and linear transfer curves. (Adapted with permission from Ref. [37], Copyright 2015, MDPI)

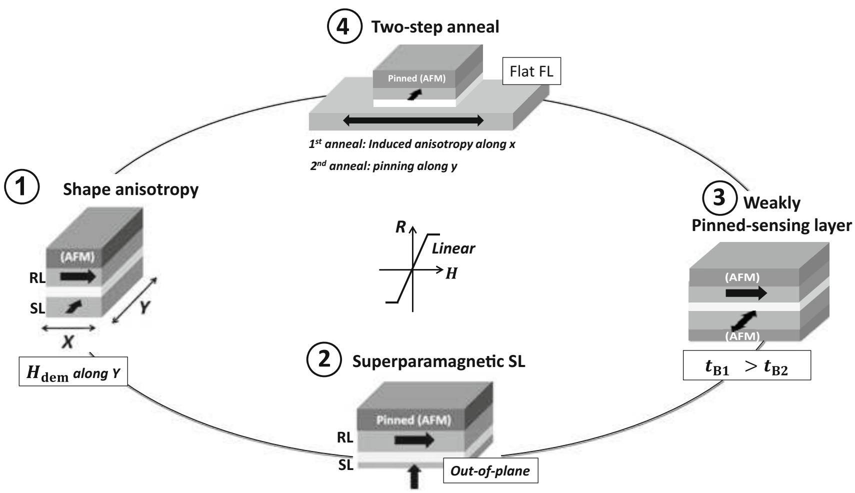

Fig. 8 MTJ sensor linearization techniques. Orthogonal-magnetization configuration between the sensing and reference layers (Fig. 7b)

Shape Anisotropy Technique

In addition to magnetocrystalline anisotropy, the shape anisotropy effect of the ferromagnetic material can control the magnetoresistance effect in magnetic tunnel junctions and the linearity of the transfer curve as well [46]. Lu et al. [46] investigated the shape of the transfer curve in two different MTJ series. In the first series, they have patterned MTJs with the same nominal areas and different shapes; the morphology of the rectangle demonstrated a needlelike rectangle normal to the easy-axis of the film to a squarish profile in the intermediate of the series to a thin needle at the right end. In the second series, they have patterned junctions with the same shape but different sizes, all rectangle junctions having a 5:1 aspect ratio through the easy-axis direction. The study showed that shape anisotropy has more importance than intrinsic magnetocrystalline anisotropy for the linearization process. One can easily generate a linear transfer curve using needlelike rectangular junctions, in which the shape anisotropy dominates the magnetization direction perpendicularly to the thin film easy-axis.

Superparamagnetic Sensing Layer

A different technique uses a thin layer of CoFeB as a superparamagnetic sensing layer. This thin layer can be utilized to attain a response with linearity and non-remarkable hysteresis, along with unpretentious designs and without the necessity of the shape anisotropy effect. Since the magnetization of the CoFeB turns to be an out-of-plane direction at thicknesses less than 1.5 nm, an orthogonal-magnetization configuration will be presented with the already-existing in-plane magnetization of the reference layer. A linear response with change in external in-plane magnetic field can be attained.

Soft-Pinned Sensing Layer

Magnetic tunnel junction (MTJ) stacks that have a softly pinned sensing layer are composed of multilayer structure having a dual antiferromagnetic film, with one layer located close to the pinned layer while the second layer is adjacent to the sensing layer. Thus, together, antiferromagnetic layers manipulate the ferromagnetic layer magnetization in an orthogonal direction to each other by manipulating the exchange-bias directions. To do this, the exchange-bias field (H_{ex}) of the sensing layer (FM2) should be smaller than the exchange field regarding the reference layer (FM1), enabling high sensitivity linear response. This is because the field at saturation is defined typically by the sensing layer's exchange coupling magnitude.

A suitable selection of the antiferromagnet thickness can determine the desired difference in the blocking temperature and thereby the exchange-bias effect. As exemplified in Fig. 9, the blocking temperature (T_{B2}) of the adjacent antiferromagnetic layer to sensing layer has to be lower than the blocking temperature (T_{B1}) of the

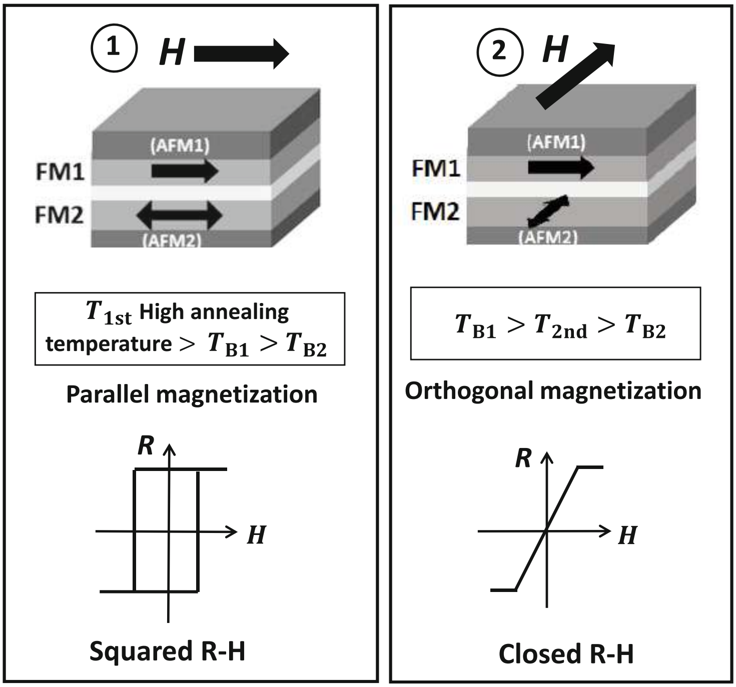

Fig. 9 MTJ with soft-pinning free layer (FM2/AFM2). The annealing temperature during the first step T_{1st} is greater than blocking temperatures of AFM1 and AFM2, and then the exchange-bias directions of the top pinning (AFM1/FM1) and bottom pinning (FM2/AFM2) will be directed through the external magnetic field, showing a squared R-H change. During the second step, annealing temperature T_{2nd} is greater than the blocking temperature of AFM2 only; therefore, the direction of exchange bias at the bottom pinning (FM2/AFM2) will be rotated along applied field direction. (Copyright 2018, MDPI publisher, and Ref. [47])

adjacent antiferromagnetic layer to reference layer. The cross-magnetization configuration can be therefore adjusted through two consecutive annealing steps under application of magnetic field. In the first step, the annealing temperature ($T_{1st} > T_{B1} > T_{B2}$) is high enough to crystallize the layer structure and set the direction of magnetizations though a certain direction. In the second step, the annealing temperature (T_{2nd}) is only higher than T_{B2} to reset the direction of magnetization of sensing layer along an orthogonal direction.

Blocking temperature (T_B) is the temperature at which the exchange-bias field disappears, closely reaching the Neel temperature (T_N) for raised thickness antiferromagnetic films having an increased grain size, whereas for thin films $T_B << T_N$ because of finite size influences. Consequently, as the T_b is tremendously dependent on the AFM material as well as its thickness, therefore, for bottom pinned layers, a specific temperature stability is needed. The same or different AFM materials can be employed to achieve the sensing layer blocking temperature, utilizing its thickness to verify that T_{B1} (reference layer) > T_{B2} (sensing layer). Consequently, two successive annealing stages through an orthogonal in-plane applied magnetic field at dissimilar temperatures, the crossed formation among the magnetization of the sensing, and the pinned layers can be defined properly. The initial annealing step, executed at an increased temperature $T_{1st} > T_{B1} > T_{B2}$, assigns both reference and sensing layer magnetizations in the identical orientation, whereas the subsequent annealing stage is conducted at a lesser temperature $T_{B1} > T_{2nd} > T_{B2}$ which orients the magnetization of the softly pinned sensing layer with a normal configuration to the lower one.

Two-Step Annealing Technique

In this technique, researchers set the orthogonal-magnetization configuration by applying two-consecutive annealing steps, in which orthogonal annealing magnetic fields should be adapted at different annealing temperatures. The easy-axis of magnetization of the sensing layer is set first by the first annealing step. For that, top-pinned MTJs are very suitable multilayer structures, such that the sensing layer must be completely free from the demagnetization effect, e.g., not patterned as shown in Fig. 10. Thereafter, a second annealing step is needed to set the pinning direction orthogonal to the sensing layer magnetization.

Sensor Design

The magnetic sensor design relies on multiple criteria that must be taken into consideration in order to have a functional device for different applications. Sensor design and structure depend to a large extent on the type of application. The overall performance of the magnetic sensor will be affected by the constituents of its parts. For example, the structure of the sensing layer in addition to the sensor's packaging can affect the linearity and thermal behavior of the sensor. These parameters have a direct effect on the sensor's performance; hence, precise knowledge must be acquired before starting the improvement of the sensor. Hereinafter, the bridge and in array structure of TMR will be discussed.

Array Sensor

The background noise level is a serious implication when using MTJ sensors in numerous applications because of their voltage bias dependence and reduced electrical robustness. A proposed approach to decrease the influence of the voltage bias requirement is to employ an array of serially connected MTJ sensors as shown in Fig. 11. Under such a configuration, the effect of the high bias voltage would be reduced across each junction, maintaining a high TMR ratio. However, the main disadvantages of array sensors are the broadening in linear transfer curve (low spatial resolution), and also they possess a higher noise level in comparison with noise of a single MTJ sensor.

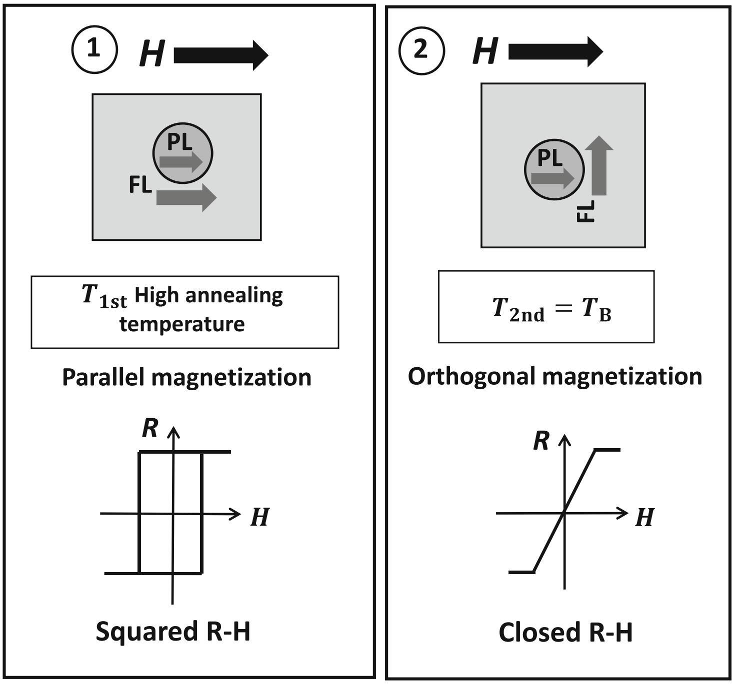

Fig. 10 MTJ with un-patterned (flat) free layer. The first annealing step will result in parallel magnetization, where the induced magnetocrystalline anisotropy of the free layer (FL) in the bottom electrode will be parallel to the pinning direction of the pinned layer (PL). Thereafter, the sample will be rotated by 90^0 and then reannealed at a temperature equal to blocking temperature of AFM. This results in an orthogonal-magnetization configuration between free and pinned layers. (Adapted with permission from Ref. [47], Copyright 2018, MDPI, and Ref. [45], Copyright 2021, IOP science)

Among all, these sensors are sometimes utilized in severe environments, where temperature drifts may affect the output voltage (V_{out}). Like any other resistive sensor, the electrical resistance of MTJs and spin-valves commonly changes as the temperature changes. Thus, any fluctuations in the output voltage that originated from temperature drift must be differentiated from those originated from the sensing magnetic field. One possible solution for these issues is to integrate sensors into Wheatstone bridge architecture as shown in Fig. 12.

Bridge Sensor

Wheatstone bridges are a specific type of electrical circuit used mainly to measure the value of unknown resistance and are composed of four resistances. The TMR sensor can be implemented in the Wheatstone bridge using TMR devices with different topologies, and the merit is that the output voltage of the bridge can be adapted to be independent of the change in the ohmic resistance (thermal-drift

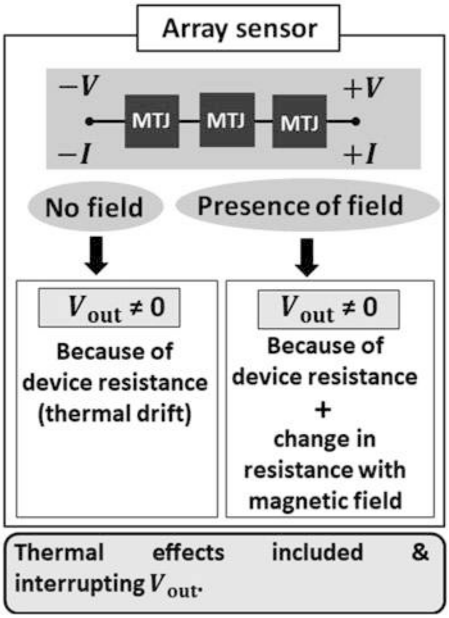

Fig. 11 Output signal of MTJ array sensor with and without external magnetic field; thermal-drift current contributing the output voltage/resistance change in the two cases. (Adapted with permission from Ref. [48], Copyright 2022, MDPI)

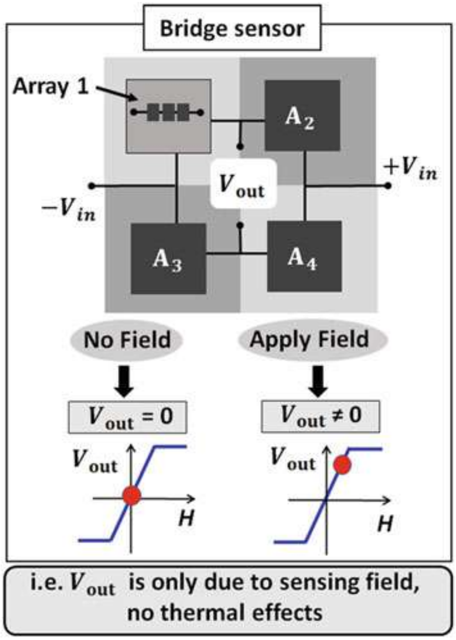

Fig. 12 Output signal of MTJ bridge sensor with and without external magnetic field; thermal-drift current not affecting the output voltage/resistance change in the two cases. (Adapted with permission from Ref. [49], Copyright 2018, MDPI)

current) of those devices. To carry out such a configuration, the bridge may contain four congruent TMR sensors (A_1, A_2, A_3, and A_4) as shown in Fig. 14, and each two opposing elements must have a symmetric dR/dH. It means that each two TMRs (A_1 and A_4) exhibits $dR/dH > 0$ and the other two (A_2 and A_3) exhibit $dR/dH < 0$. Then, unlike an individual TMR sensor or array, if R of each TMR array changes, the contribution of such a change to the output voltage (V_{out}) has nonsense.

The most-straightforward approach to implement a bridge TMR sensor is to connect all four TMR elements mechanically, either through wire bonding or at the PCB level, and align the matching elements in the similar direction but in the reverse sense. However, this technique has three significant drawbacks:

1. Alignment mistakes will always be introduced during mechanical assembly of the individual components; in turn, it will limit the performance of the device.
2. The mass production is not cost-effective for the mechanical assembly of individual components.
3. In compact applications demanding strong spatial regularity, mechanical rotation cannot be functioned because the separate parts will be relatively small to manipulate. A procedure to create entire Wheatstone bridges at the wafer level is necessary when such restrictions are present.

Sensor Evaluation Parameters

Sensitivity, electronic noise level, and limits of detection are three critical parameters that must be considered for any type of sensor, because those parameters involve a deterministic role in the sensors' application areas. Magnetic anisotropy has a vital impact on sensor sensitivity and limits of detection. Generally, uniaxial and unidirectional magnetic anisotropies are preferable because they provide a coherent rotation of magnetization and a reversible mechanism of magnetization, therefor a repeatable voltage response [50, 51]. Here the uniaxial magnetic anisotropy can stem from shape of a material (shape anisotropy) [52] and/or material's structure (magnetocrystalline anisotropy) [50], while the unidirectional anisotropy can be induced either by exchange bias (in FM/AFM bilayers and in FM/NM/AFM trilayers) or Ruderman–Kittel–Kasuya–Yosida (RKKY) interaction between two ferromagnetic materials (separated by a nonmagnetic material: FM/NM/FM) [51]. The type and magnitude of a magnetic anisotropy can influence a sensor's sensitivity and limits of detection, particularly for materials that have uniaxial and unidirectional magnetic anisotropies.

Sensitivity

The sensor's sensitivity is stated as the occurring resistance derivative (as an output) divided by the magnetic field (as an input). Consequently, presuming the response in a linear way, the sensitivity attributed to MTJ sensors (S) is determined by the linear span's slope, which might be normalized by least resistance value (R_{min}) of the sensor to contrast the sensitivity of diverse sensors [53, 54]:

$$S = \frac{(R_{\max} - R_{\min})}{(R_{\min})} \frac{1}{\Delta H} = \frac{TMR}{\Delta H} \tag{8}$$

where $R_{\max}$ is the maximum sensor resistance value and ΔH represents the linear operating range. Thus, an elevated sensitivity is realized by limiting the field of saturation and raising the ratio for TMR. Though, the TMR ratio relies on the applied voltage magnitude, being roughly constant when the biasing voltage is reduced than 30 mV, until it begins to reduce nearly linearly approaching a magnitude which signifies 50% of the optimum TMR ratio (TMR_0). $V_{(1/2)}$ is the designation for the corresponding voltage magnitude where the signal reduces to half of its optimal value. Accordingly, the relation governing the dependence of TMR and biasing voltage values is introduced as follows:

$$[\mathrm{TMR(V)}] = \left[\mathrm{TMR}_0\left(1 - \frac{V}{2V_{\frac{1}{2}}}\right)\right] \tag{9}$$

Defects in the insulating barrier, which initiate to appear as the voltage elevates, are the main reason for the TMR reduction. Thus, an elevated-quality barrier is essential to diminish TMR−voltage reliance and advance junction specifications. An insulating barrier as a dielectric which might be disturbed electrically when the bias voltage exceeds the breakdown voltage ($V_{\mathrm{break}} \approx 1.5$ V) is introduced. This restriction can be overcome by employing a sensor array since it increases the entire voltage by dropping the voltage throughout every junction.

The magnitude of the applied voltage impacts the TMR amount; likewise, the sensor sensitivity owes a dependence on the biasing voltage amount represented mathematically as follows [55]:

$$[S(V)] = \left[S_0\left(1 - \frac{V}{2V_{\frac{1}{2}}}\right)\right] \tag{10}$$

where S_0 is the supreme sensitivity, acquired at reduced bias voltages. Within the linear section of the output curve, the resistance of the sensor can be labeled as a summation of a nominal resistance R_0 and an adjustable resistance ΔR_{H} which is affected by the magnetic field application H and the sensitivity of the sensor [55]:

$$R(H) = R_0 + \Delta R_{\mathrm{H}} = R_0 + S(V)R_{\min}H \tag{11}$$

where R_0 is the sensor resistance in the absence of the magnetic field, which might be designated as an offset term. Accordingly, the signal discrepancy ΔV because of an external magnetic field alteration $\Delta V = H_2 - H_1$ is assumed by

$$\Delta V = (R(H_2) - R(H_2))I \approx S(V)\, R_{\min} I \Delta H \tag{12}$$

Noise

Frequency-independent white noise (i.e., thermal noise and shot noise) and noise that is frequency-reliant on (1/*f* flicker noise and random telegraphic noise [RTN]) are two forms of noise that are present in magnetic sensors. Also, the measurement circuit comprising amplification and electronics parts contributes with background noise, which influences the intrinsic signal of the sensors.

White Noise

Nyquist noise or thermal noise is the first typical sort of white noise. Any resistance at a temperature more than zero is a potential cause of electrical noise. When the electromotive force is absent, the electron velocity tends to be zero. However, Brownian motion delivers nonzero resistance fluctuations.

At a specific temperature T, the voltage spectral density specified with the thermal noise $S_{V,th}^{1/2}$ is given by the Nyquist formula (15), where k_B is Boltzmann constant, T is the temperature, and R is the magnetic sensor resistance. Nyquist noise (also known as thermal noise) is the first type of white noise. Electrical noise can come from any resistance at any temperature other than zero. In the absence of electromotive force, electrons have no velocity. However, Brownian motion causes resistance fluctuations to be nonzero. The Nyquist formula (13) gives the voltage spectral density of thermal noise S (V,th) at a constant temperature T: [55]

$$S_{V,th}^{1/2} = \sqrt{4k_B TR} \tag{13}$$

As clearly seen from Eq. 15, thermal noise does not depend on the applied voltage or magnetization characteristic of the device, but on the resistance (R). Compared to longitudinal resistances in AMR, GMR, and TMR devices, the transverse resistance in PHE-based sensors is very small. Therefore, thermal noise is very low in PHE-based magnetic field sensors.

Shot Noise

Shot noise is the second variety of white noise. It is an electrical noise that the Poisson law can simulate. Shot noise is a distinct carrier charge reflection. An electric current is produced by each charge carrier being transported when exposed to an electric field. Dissimilar to thermal noise, this noise is directly correlated with the electric current I and the carrier's charges. The following equation can be used to get the spectral noise density [36, 55]:

$$S_{V,\mathrm{shot}}^{1/2} = \sqrt{2eIR} \tag{14}$$

Herein, e represents the electron charge, I is the applied current, and R is the resistance under study. This term is very low in AMR- and GMR-based sensors and virtually missed in PHE-based sensors. However, shot noise becomes important in

TMR-based sensors since the insulating layer causes a discontinuity in a conduction medium.

Flicker Noise

Flicker ($1/f$) noise is present in any type of material, and it is very rich in information about the quality of materials and layer structures. Particularly in low frequency applications of MR-based sensors, it is the major contributor to electronic noise. It can stem from the fluctuations of energy around equilibrium and is determined through the shape, size, and materials specifications For example, in magnetic materials, the presence of magnetic domains may cause a fluctuation of magnetization around the equilibrium energy (due to thermal activation, or stress, or vibrations). Flicker noise can be described by a general formula [36]:

$$S_{V,\frac{1}{f}}(f) = \frac{\alpha_H}{N} \cdot \frac{V^2}{f} \tag{15}$$

The terms in this Eq. N and V are designated as the overall charge carriers number and the potential difference within the conductor, respectively. The value of the nondimensional α_H known as the Hooge constant is varied with defect density and material purity, making it feasible to compare the noise levels of various sensors. Below the overlap (cutoff) frequency, the $1/f$ noise is responsible for the white noise (characteristically in GMR and TMR). For the small GMR magnetic sensor, the generated noise as a result of the magnetic domains is elevated and is closely correlated with the structural characteristics and magnetic configuration of the GMR. Increased sensor volume lowers the $1/f$ noise since it owes an inverse proportion to the number of carriers.

Random Telegraphic Noise

One of the most dynamic and significant source of variation in digital circuits is the random telegraph noise (RTN). The RTN arises as a result of random variation among magnetic domains of metastable states of the free layers. The RTN phenomenon inducing undesirable fluctuations in the electrical resistance is largely related to the working circumstances of the used device and also on the induced polarization current. The spectral density of RTN is given in Eq. 16:

$$S_{V,RTN}(f) = S_{V,RTN}(0) / \cosh\left(\frac{\Delta E}{k_B T}\right)\left[\cosh^2\left(\frac{\Delta E}{k_B T}\right) + (2\pi f \tau)^2\right] \tag{16}$$

where $\tau^{-1} = \sum_{i=1}^{2} \tau_i{}^{-1}$ with $\tau_i = \tau_{i,0} \exp\left(\frac{E_i}{K_B T}\right)$ and E_i corresponds to the energy level residing at state i. In magnetoressitive sensors, appearance of RTN is mainly due to magnetic fluctuations associated with magnetic instability of the magnetic layers and particularly fluctuations during the magnetization reversal process at the pinning sites.

Detectivity

The threshold magnitude, which designates the lowest external magnetic field that the sensor can detect at a specific frequency with a specified bandwidth, is used to express the sensor's detectability. Thus, a signal beyonds the threshold range will not produce an output alternation because of the limit of detection and the sensor noise. The sensor detectivity is expressed in magnetic field units corresponding to the noise level as in the following equation [36, 56]:

$$D = \frac{S_{\mathrm{V}}^{\mathrm{total}}}{S\, I_{\mathrm{bias}}\, R_0}\ (\mathrm{Oe/Hz}) \tag{17}$$

$S_{\mathrm{V}}^{\mathrm{total}}$ is the entire magnitude of noise and S is the sensitivity for the sensor, being together determined at a specified bias voltage through an external magnetic field H.

Magnetic Sensor Applications

Recently, the fast development of the micro- and nanotechnology related areas impacts an immense portion of the scientific development delivering an elevated life quality experience [57]. A variety of sensing systems demonstrate an extensive assortment of thoughts and phenomena from the of physics and material science fields [3]. The rapid acquisition of the test results, reduced cost fabrication and processing, and feasibility of usage are significant requirements for the biological systems diagnostics [21]. The following section covers briefly the most common industrial and medical applications for magnetic sensors. Figure 13 represents major magnetic sensing applications.

Magnetocardiography (MCG)

Inaccessible health monitoring has developed a need because of limited healthcare access arising from lockdowns for pandemic and elevated aging populations [59]. Medical applications relying on magnetic sensing appliances might be divided into two major categories: the measurements of exerted fields delivered by the organs in humans and the monitoring of the magnetically labeled beads and macromolecules. The potential evolution of the magnetic field sensors directed toward medical applications demands a specific focus on the noise reduction and enhancing the entire device to be smaller, affordable, and cheaper while at the same time maintaining the desired amounts of the detection limit [21]. Figure 14 presents versatile magnetic sensing selectivities. Here, magnetic cardiography as a medical application for magnetic sensors is introduced. Magnetocardiography refers to the

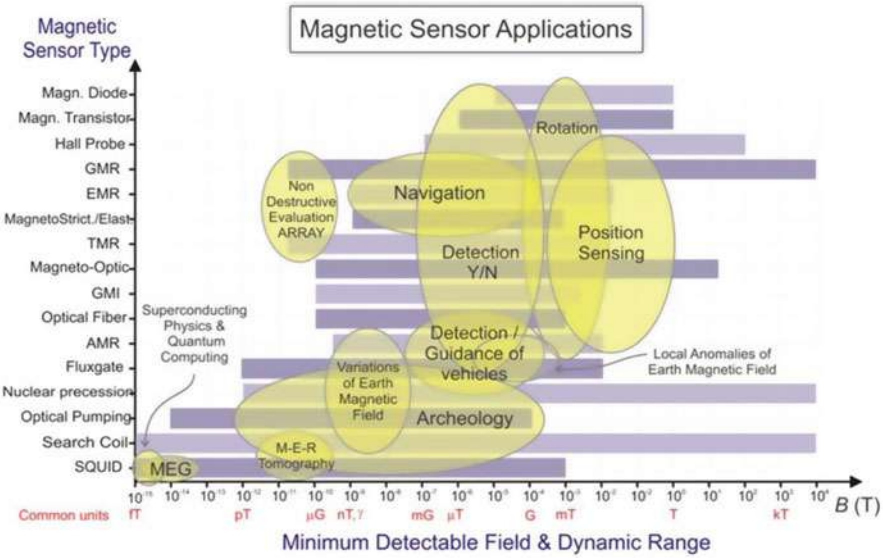

Fig. 13 Major magnetic sensing technologies and their linked application areas. (Reproduced with permission from Ref. [58], Copyright (2009), MDPI publisher)

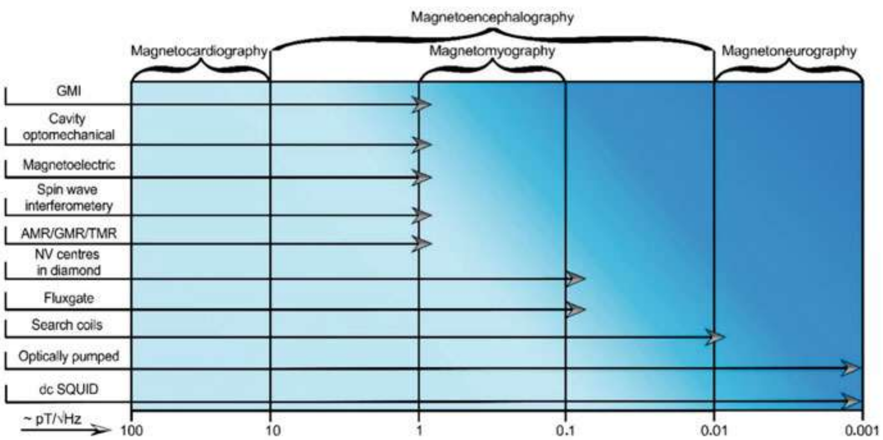

Fig. 14 Different magnetic sensors technologies reflected on the vertical axis with respect to the biomagnetic detection signals on the horizontal axis. (Adapted with permission from Ref. [21], Copyright 2020, MDPI)

technique which detects the appraising magnetic fields arising from the heart's electric currents and activities which cardiomyocytes generate. This process employs highly sensitive devices like the SQUID [60]. Magnetic cardiography provides early data for the conduction disturbances during the human fetal period.

Table 1 Advantages of MCG compared to ECG [60]

Parameter	MCG	ECG
The contribution of the basic currents	High	Low
Volume currents portion	Low	High
Effect of body tissues on conductivity	Low	High
Required attachment to the skin	No	Yes
The interference between the skin and electrode	No	Yes
Required filtering for straight current	No	Yes
The usage of fetal study	Yes	No

This might support in taking an early decision-making by physicians. Magnetocardiography (MCG) outcomes the electrocardiography (ECG) in terms of the performance and desired results due to their significant diagnostic potentials. Table 1 summarizes the completeness between MCG and ECG. Both ECG and MCG rely on the same phenomena; however, MCG are superior. This superiority emerges from the nature that MCG records direct magnetic fields from the primary current, while ECG results are recorded from the derived current from the primary one [60]. This nature delivers enhanced and less distorted information. Besides, conductivity is constant and independent of the body compositions in the case of MCG, while it fluctuates with dissimilar body compositions in ECG detected currents case [61]. The contactless, noninvasive MCG monitoring technique reduces skin electrode influence while simultaneously speeding up examinations. Last but not the least, the currents for MCG do not need any filtration; therefore, the MCG can assess the heart current absolute magnitude. The common benefits of the MCG over ECG are represented in Table 1. Versatile works have employed the magnetic cardiography for medical field, for instance, Sadman Sakib et al. have established a model that relied on artificial intelligence (AI) which merges two designs intending to simulate arrhythmia detection. The authors concluded that the designated AI architecture is auspicious for keeping the ultra-edge sensing appliances in the medical sector [59]. In another report, the authors have developed precise TMR sensors to evaluate both MCG and MEG at ambient conditions with a decent SNR and high spatial resolution [62]. The real on-time estimation and mapping of MCG affords a significant enhancement in heart disease diagnostic tools. The introduction of magnetocardiograms without the need for a magnetically shielded room has been recently developed by researchers [63]. In their work, they have delivered a setup which allows the clear detection of the magnetic field for the heart at ambient temperature in the absence of a shielded room. The authors have employed the TMR sensors to acquire low detection limits and precision by limiting the device and surrounding noise with a mathematical algorithm. In comparison with SQUID, it is more efficient due to less cost and time. These recent reports with a focus on the merging and combining of electronics, modeling, and basic physics could provide insights on grasping very promising selectivities and conditions for operation to assist in the detection of risks and potential dangers for human life.

Neural Signal Detection

The conducted massive research on the structure, behavior, and functions of our brain has been increased in the past few decades. These researches unable us to get more information and deep understanding of our brain; hence, a lot of funded programs are directed to this field.

Particular attention has been paid to healthcare and medical diagnosis fields; the analysis of brain signals can be helpful for identifying some diseases. Additionally, modern technology based on the brain–computer interface (BCI) that receives and processes real-time signals from our brain contributes to identifying some diseases and other different fields. For instance, neuroprosthetics can substitute a disabled person's nonfunctional arm or leg and be employed in neural repair and rehabilitation. The real-time signals of our brain could be used in many applications including video game interaction. The very complicated weak electrical signals generated from our brain in a very short period of time cause variation in the magnetic field of our brain.

Highly sensitive and accurate sensor arrays composed of superconducting quantum interferential devices (SQUIDs) were used for neural signal measuring and analyzing since early times, thanks to elevated ratio for accuracy and sensitivity. Nevertheless, the SQUIDs require a very low temperature to sustain the superconducting property during measurements; thereby, complicated and large scale devices are required.

From other point of view, the magnetic tunnel junction (MTJ) sensor based on the CMOS can be operated at room temperature and has a simple structure and low cost.

The alpha rhythm, one of the brain oscillations, has a frequency range of 8–13 Hz and reaches its maximum amplitude over the occipital area. Besides, it typically manifests in REM sleep, sleepiness, and peaceful wakefulness with the eyes closed, with an amplitude that diminishes when the eyes are opened. Based on this function, it can be used to monitor levels of wakefulness or identify drowsiness while driving. Additionally, the alpha rhythm can have a significant impact on other measurements of the brain activities like event-related field (ERF) due to its high amplitude. The ERF is a collection of brain activity that has been time-locked to an event, such as a sensory stimulus or the identification of a target stimulus, and is captured using magnetic tunnel junctions. It is the measurable brain activity that follows a particular sensory, cognitive, or motor event. In this regard, recording brain signals using linear MR sensors has been examined [64–67].

Nondestructive Detection (NDT)

Magnetic NDT technologies have been widely implemented in manufacturing to guarantee the functioning protection of ferromagnetic assemblies and apparatuses [68]. Ferromagnetic materials are composed of magnetic domains at the microstructural level. One characteristic property of these ferromagnetic materials is the existing coupling through the emerging stress and the magnetic field where the magnetization might promote a distortion in the FM dimensions known as magnetostriction [68]. Conversely, applied stress and mechanical forces also alter the FM magnetization referred to as the piezomagnetic effect [68]. These phenomena are attributed to the rotation of magnetic moments and subsequent domain wall movement upon the experience of external magnetic fields or mechanical forces. The latter (i.e., piezomagnetic effect) has seized raised interest due to the suitability of evaluating stress status by magnetic measurement devices. Consequently, noteworthy efforts and techniques have been focused on this section in the preceding decades such as magnetic flux leakage (MFL) and Barkhausen noise. The concept of the MFL working principle is based on the leakage of the magnetic field whenever magnetic field is applied to ferromagnetic material. This leakage is pursued by the potential existence of any geometrical asymmetry. The arising leakage can be monitored by magnetic sensors to report the dimensions of the defect [69, 70]. The important parameters to consider for this leakage are as follows: 1) The flux should be large enough, systematic, and homogenous to enable the variation at the defect place. 2) The appropriate positioning of the sensor is necessary to differentiate between the arising leakage due to the defect and the background noise. Hoke first revealed the MFL phenomenon in 1918, and the initial application of the MFL technology was conducted by Watts in 1933 for evaluating welded joints [68]. The pipeline pig is considered as a successful application of MFL where it was functioned for the corrosion of metals in oil pipelines. Figure 15 represents this design. Despite the facility provided for the MFL as a nondestructive testing approach, two parameters need more investigation and optimization. The first is the changed dimensions of the defect (i.e., width, depth, length) and so forth which impact the measurement signals, and second is the burden of dealing with elastic-plastic regions close to the cracks. Therefore, more research is demanded on these points [68, 71]. The nondestructive analysis covers a wide range of areas including magnetic flux leakage, magnetic particle inspection, and recently the protection of cultural heritage. The nondestructive process is achievable with a neural network design introduced by Doulmais in 2012 [72]. This design has the capability for detecting the artistic styles involved in paintings. NDT can also be incorporated for delivering messages on the initial case of a building or a construction to aid in realizing the

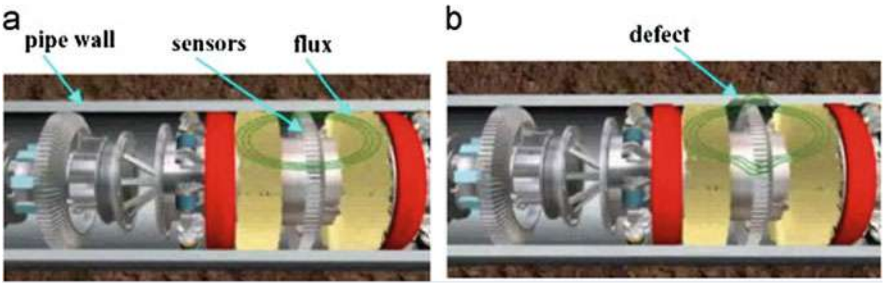

Fig. 15 The design of the called pipeline pig. (**a**) No defect is detected in the pipeline, and (**b**) the defected site is monitored. (Adapted with permission from Ref. [68], Copyright 2012, Elsevier)

errors beforehand. This way limits the loss of life [73]. Like so, this technique is beneficial for preserving cultural heritage and national treasures.

Monitoring of Pollutants in Water Resources

Water treatment for the groundwater and available water resources has been greatly demanded in the recent decades. This necessity is specifically vital in water-rich countries and communities [74]. The resulting contaminations from industrial factories, pesticides, and other sources might raise the potential of diseases and deliver undesired risks for human health and the environment including animals. Additionally, food industry might contain various sorts of pollutants such as water organic pollutants (e.g., cationic and anionic dyes). The progress of low-cost and label-free sensors is demanded to mitigate the influences of water limitation and contamination. Agriculture and other related fields' productivity is elevated as the sensors can regulate the environmental situations by reducing the inputs and allowing the employment of pesticides and water more affordably. Besides, these sensors are beneficial in digitizing irrigation concepts [75]. The most common sources for water pollutants are illustrated in Fig. 16. The detection and estimation of these contaminations assists in designing proactive solutions to provide higher quality water. The manipulation of these pollutions as an applied answer and sensing and gaging the capacities of these toxic materials can profit designing a practical consequence to eradicate the toxins and enhance the water value. Versatile approaches have been paved to determine the pollutants in water such as spectroscopic analysis [76],

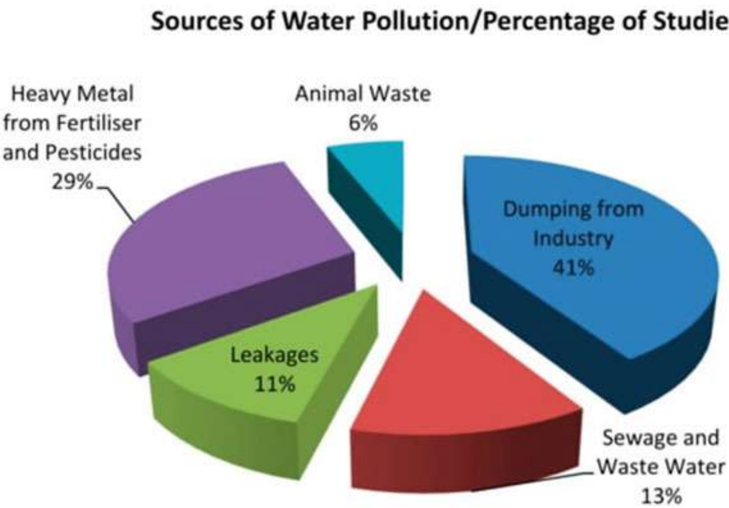

Fig. 16 Various surrounding sources for water contamination. (Adapted with permission from Ref. [80], Copyright 2021, MDPI)

chromatographic studies [77], or more [78]. For the application of determining heavy metals, pollutants, and contaminations, there might be few undesirable disadvantages like side toxicity, prolonged time process, reduced sensitivity, and costly methods. The electrochemical sensing approach is introduced for the removal of toxins and contaminations [9, 11, 79]. However, the benefits offered by magnetic sensing technologies using sensors and composites are superior and provide insights on the needed application, and it is remotely controlled by the external applied field. The common sources of water pollution are introduced in Fig. 16.

Magnetic materials include three subcategories which are ceramics, alloys, and composites. Among them, ferrite- and iron-based composites as magnetite and hematite are widely exploited for the pollutant removal from water resources in various sensing technological aspects [74]. Magnetic materials possess a few desirable merits such as the ability for functionalization, biocompatibility, separation, and cost [74]. The challenge is generally to control the synthesis process to acquire tailored morphology, size, and stability conditions. In this contest, 2D transition-metal carbide materials stated as nanocomposites are auspicious entrants with various striking features. They have widely spanned versatile sorts of applications including cancer therapy, imaging processes, and particularly water treatment. On the one side, MXenes tend to agglomerate as major magnetic materials behave and it can be oxidized. Besides, separation in aqueous media is harsh because of the high colloidal ability. The increased size of the MXene molecules hinders transfer of the electrons at the interface and suppresses the formation of a suitable contact surface for electron transfer. Being said, the MXene based magnetic materials act as an environmental remedy for the removal of toxins and heavy metals. Though, the functionalization of the surface is beneficial and requested for the upsurge of efficiency and disadvantages elimination, as well as to avoid wasted time and cost. Thus, the functionalization of the surface has evolved to afford metal oxide nanocomposites for the eradication of pollutants and contaminations [81]. The hybridization of $Fe_2O_3/Ti_3C_2T_x$ which is a magnetic MXene nanocomposite was synthesized using the hydrothermal process to purify the mercury (Hg^{2+}) ions accompanied by other metal ions (Na^+, K^+, Ca^{2+}) from the medium. Inherently, the metal ions were reduced by this composite as an adsorber, and the mercury concentration approached 0.02 mg^{-1} after starting at 2.29 mg^{-1}. This removal proficiency might be attributed to the presence of extra anion groups such as O^{2-} and OH^- which are negatively charged on the surface [82]. Reported in another research, Shahzad et al. synthesized nanosheets of MXene to eradicate copper from water. The results indicate that MXene has the ability for removal according to excellent surface area and hydrophilicity. That mechanism was evaluated by the contributing functional groups of O, OH, and F on the MXene surface as potential locations to absorb the heavy metal ions [83]. Many other combinations based on MXene and other nanocomposites [84] have functioned for the remediation of water. In summary, several desirable specifications and merits as the hydrophobic attitude, less toxicity, and raised area of the surface nominate the MXene and their combined nanocomposites for water treatment. Generally, there are three sorts of applications, for membranes, electrodes, and adsorbents. To keep the flow of the work and the progress of the magnetic materials-based sensing routes, the hazardous pollutants in water resources might be eradicated by other routes besides the already published ones, suggesting the combination of magnetic materials with other nonmagnetic matrices to limit the agglomeration incident and upsurge the efficiency of application. The other possible direction is to hit the manipulation and control of waterborne pathogens and bacteria. The evolution of potential materials for detecting waterborne viruses and bacteria in various aqueous environments could elevate the evaluation quality as these bacteria and viruses are generally resisting the antimicrobial agents. Besides, it is also necessary to fabricate innovative designs that could simultaneously assess various sorts of contaminants in water resources efficiently and precisely to save time, cost, and effort. Finally, machine learning and artificial intelligence are impacting everything in our progressively propagating life activities; therefore, the simulation models using these machine learning and artificial intelligence methods for the hazardous are also demanded. Few reports are inspected in this regard [85]. The employment of smart wearable tools for the prediction and monitoring of these pollutants is highly suggested.

Conclusion

The magnetic sensors are widely spread in various types and sorts, based on the orientation of the field and magnetization along with the magnetic moments. The classification as AMR, GMR, TMR, PHE or other is grasped. The parameters optimizing the performance of the sensor are mainly the sensitivity, the detection limit or the resolution, the exchange-bias field, as well as the magnetic anisotropy and noise. Depending on the specific area of application, these parameters can be manipulated and optimized. Magnetic sensor applications have the advantage of being tracked and employed in a wireless method. Therefore, they are applied on a wide scale of everyday life activities such as computer heads, microbead detection, MRI, automobile industry, magnetic cardiography, and more. Magnetic sensors are beneficial and need further investigation in the upcoming years along with the modeling and simulation devices supported with artificial intelligence and machine learning for the progress in the upcoming era.

Future Perspective

According to the sensor development roadmap published in 2019 [86], a research milestone is the development of stand-alone TMR sensors with magnetic field detectivity ≈ 1 pT/$\sqrt{\text{Hz}}$ at 10 Hz by 2027. For ultraprecise applications such as detection of neural signals, magnetocardiography, and quantum computing systems, subpT magnetic field detectivity is also mandatory. For that, extensive research efforts have been done to achieve such a detection limit. Old-style research applies additional techniques as magnetic flux concentrator (MFC) to improve sensor sensitivity and hence improve detectivity. However, this technique is incompatible with continuous minimization of electronic devices. Recently, great efforts have been made to optimize the shape, size, and aspect ratio of tunneling junctions. Also, the number of integrated junctions as an array or bridge sensor has also been investigated. However, there are still imitating parameters as the device footprint and background noise. Therefore, these techniques are considered as artificial ways to improve the limit of detection and are not treating the fundamental origin of the noise in multilayer spintronic stacks. Therefore, very recent attention has been paid to optimize the soft-magnetic properties and the crystal structure of magnetic materials especially in the free layers. For instance, utilizing amorphous phase of CoFeBTa, with high crystallization temperature ≥ 500 °C, helps to improve the bcc texture and minimize source of crystal defects at MgO/CoFeB interface as discussed in section "Sensor Materials." This improves the signal-to-noise ratio and thereby improves the detection limit. However, polycrystalline magnetic materials such as NiFe have better soft-magnetic properties than amorphous magnets. Therefore, materials engineering, integrating the properties of amorphous and polycrystalline magnetic materials, and introducing newly functional free layers are the future approaches to push the limit of detection towards subpico Tesla range. These types of magnetic sensors might provide a supportive apparatus for the upcoming era and the next generations.

References

1. Wilson JSBT-STH (2005) Chapter 1 – sensor fundamentals. Newnes, Burlington, pp 1–20
2. Rout CS, Hegde M, Govindaraj A, Rao CNR (2007) Ammonia sensors based on metal oxide nanostructures. Nanotechnology 18:205504. https://doi.org/10.1088/0957-4484/18/20/205504
3. Lenz J, Edelstein S (2006) Magnetic sensors and their applications. IEEE Sensors J 6:631–649. https://doi.org/10.1109/JSEN.2006.874493
4. Morsy M, Abdel-Salam AI, Mostafa M, Elzwawy A (2022) Promoting the humidity sensing capabilities of titania nanorods/rGO nanocomposite via de-bundling and maximizing porosity and surface area through lyophilization. Micro Nano Eng 17:100163. https://doi.org/10.1016/j.mne.2022.100163
5. Morsy M, Elzwawy A, Abdel-Salam AI, Mokhtar MM, El Basaty AB (2022) The humidity sensing characteristics of PANI-titania nanotube-rGO ternary nanocomposite. Diam Relat Mater 126:109040. https://doi.org/10.1016/j.diamond.2022.109040
6. Morsy M, Ibrahim M, Yuan Z, Meng F (2020) Graphene foam decorated with ZnO as a humidity sensor. IEEE Sensors J 20:1721–1729. https://doi.org/10.1109/JSEN.2019.2948983
7. Morsy M, Elzwawy A, Oraby M (2022) Carbon nano based materials and their composites for gas sensing applications. Egypt J Chem 65:1–2
8. Elzwawy A, Mansour AM, Magar HS, Hammad ABA, Hassan RYA, El Nahrawy AM (2022) Exploring the structural and electrochemical sensing of wide bandgap calcium phosphate/$CuxFe_3$-xO_4 core-shell nanoceramics for H_2O_2 detection. Mater Today Commun 33:104574. https://doi.org/10.1016/j.mtcomm.2022.104574
9. El Nahrawy AM, Abou Hammad AB, Elzwawy A, Alam MM, Asiri AM, Uddin J, Kabir MH, Rahman MM (2022) Development of 4-aminophenol sensor probe based on co(0.8-x) $ZrxNa_{0.2}Fe_2O_4$ nanocomposites for monitoring environmental toxins. Emergent Mater 5: 431–443. https://doi.org/10.1007/s42247-021-00342-y
10. El Nahrawy AM, Elzwawy A, Alam MM, Hemdan BA, Asiri AM, Karim MR, Hammad ABA, Rahman MM (2021) Synthesis, structural analysis, electrochemical and antimicrobial activities

of copper magnesium zirconosilicate ($Cu_{20}Mg_{10}Si_{40}Zr(30\text{-}x)O$:(x = 0,5,7,10) Ni^{2+}) nanocrystals. Microchem J 163:105881. https://doi.org/10.1016/j.microc.2020.105881

11. Abou Hammad AB, Elzwawy A, Mansour AM, Alam MM, Asiri AM, Karim MR, Rahman MM, El Nahrawy AM (2020) Detection of 3,4-diaminotoluene based on $Sr_{0.3}Pb_{0.7}TiO_3$/$CoFe_2O_4$ core/shell nanocomposite: via an electrochemical approach. New J Chem 44: 7941–7953. https://doi.org/10.1039/d0nj01074j
12. Mishra RB, El-Atab N, Hussain AM, Hussain MM (2021) Recent Progress on flexible capacitive pressure sensors: from design and materials to applications. Adv Mater Technol 6: 2001023. https://doi.org/10.1002/admt.202001023
13. Masihi S, Panahi M, Maddipatla D, Hanson AJ, Bose AK, Hajian S, Palaniappan V, Narakathu BB, Bazuin BJ, Atashbar MZ (2021) Highly sensitive porous PDMS-based capacitive pressure sensors fabricated on fabric platform for wearable applications. ACS Sens 6:938–949. https://doi.org/10.1021/acssensors.0c02122
14. Morsy M, Darwish AG, Mokhtar MM, Elbashar Y, Elzwawy A (2022) Preparation, investigation, and temperature sensing application of rGO/SnO_2/Co_3O_4 composite. J Mater Sci Mater Electron. https://doi.org/10.1007/s10854-022-09247-w
15. Chen H, Zhang L, Hu Y, Zhou C, Lan W, Fu H, She Y (2021) Nanomaterials as optical sensors for application in rapid detection of food contaminants, quality and authenticity. Sensors Actuators B Chem 329:129135. https://doi.org/10.1016/j.snb.2020.129135
16. Fang L, Jia M, Zhao H, Kang L, Shi L, Zhou L, Kong W (2021) Molecularly imprinted polymer-based optical sensors for pesticides in foods: recent advances and future trends. Trends Food Sci Technol 116:387–404. https://doi.org/10.1016/j.tifs.2021.07.039
17. Philip A, Kumar AR (2022) The performance enhancement of surface plasmon resonance optical sensors using nanomaterials: a review. Coord Chem Rev 458:214424. https://doi.org/10.1016/j.ccr.2022.214424
18. Qin J, Jiang S, Wang Z, Cheng X, Li B, Shi Y, Tsai DP, Liu AQ, Huang W, Zhu W (2022) Metasurface micro/nano-optical sensors: principles and applications. ACS Nano 16: 11598–11618. https://doi.org/10.1021/acsnano.2c03310
19. Heidari H, Nabaei V (2019) Magnetic sensors for biomedical applications. Wiley-IEEE Press, Hoboken
20. Coey JMD (2010) Magnetism and magnetic materials. Cambridge University Press, Cambridge
21. Murzin D, Mapps DJ, Levada K, Belyaev V, Omelyanchik A, Panina L, Rodionova V (2020) Ultrasensitive magnetic field sensors for biomedical applications. Sensors (Switzerland) 20: 1569. https://doi.org/10.3390/s20061569
22. Elzwawy A, Piskin H, Akdoğan N, Volmer M, Reiss G, Marnitz L, Moskaltsova A, Gurel O, Schmalhorst J (2021) Current trends in planar Hall effect sensors: evolution, optimization, and applications. J Phys D Appl Phys. https://doi.org/10.1088/1361-6463/abfbfb
23. Volmer M, Neamtu J (2012) Optimisation of spin-valve planar Hall effect sensors for low field measurements. IEEE Trans Magn 48:1577–1580. https://doi.org/10.1109/TMAG.2011.2173671
24. Lin G, Makarov D, Schmidt OG (2017) Magnetic sensing platform technologies for biomedical applications. Lab Chip 17:1884–1912. https://doi.org/10.1039/C7LC00026J
25. Damsgaard CD, Freitas SC, Freitas PP, Hansen MF (2008) Exchange-biased planar Hall effect sensor optimized for biosensor applications. J Appl Phys 103:07A302. https://doi.org/10.1063/1.2830008
26. Mahfoud M, Tran QH, Wane S, Ngo DT, Belarbi EH, Boukra A, Kim M, Elzwawy A, Kim C, Reiss G, Dieny B, Bousseksou A, Terki F (2019) Reduced thermal dependence of the sensitivity of a planar Hall sensor. Appl Phys Lett 115:072402. https://doi.org/10.1063/1.5110671
27. Elzwawy A, Kim S, Talantsev A, Kim C (2019) Equisensitive adjustment of planar Hall effect sensor's operating field range by material and thickness variation of active layers. J Phys D Appl Phys 52:285001. https://doi.org/10.1088/1361-6463/ab18f2
28. Talantsev A, Elzwawy A, Kim C (2018) Effect of NiFeCr seed and capping layers on exchange bias and planar Hall voltage response of NiFe/Au/IrMn trilayer structures. J Appl Phys 123: 173902. https://doi.org/10.1063/1.5023888

29. Freitas PP, Ferreira R, Cardoso S (2016) Spintronic sensors. Proc IEEE 104:1894–1918. https://doi.org/10.1109/JPROC.2016.2578303
30. Binasch G, Grünberg P, Saurenbach F, Zinn W (1989) Enhanced magnetoresistance in layered magnetic structures with antiferromagnetic interlayer exchange. Phys Rev B 39:4828–4830. https://doi.org/10.1103/PhysRevB.39.4828
31. Baibich MN, Broto JM, Fert A, Van Dau FN, Petroff F, Etienne P, Creuzet G, Friederich A, Chazelas J (1988) Giant magnetoresistance of (001)Fe/(001)Cr magnetic superlattices. Phys Rev Lett 61:2472–2475. https://doi.org/10.1103/PhysRevLett.61.2472
32. Rifai D, Abdalla AN, Ali K, Razali R (2016) Giant magnetoresistance sensors: a review on structures and non-destructive Eddy current testing applications. Sensors 16:298
33. Giouroudi I, Keplinger F (2013) Microfluidic biosensing systems using magnetic nanoparticles. Int J Mol Sci 14:18535–18556
34. Tripathy D, Adeyeye AO (2008) Current-perpendicular-to-plane giant magnetoresistance in half-metallic pseudo-spin-valve structures. J Appl Phys 103:07D702. https://doi.org/10.1063/1.2828617
35. Hirohata A, Yamada K, Nakatani Y, Prejbeanu L, Diény B, Pirro P, Hillebrands B (2020) Review on spintronics: principles and device applications. J Magn Magn Mater 509:166711. https://doi.org/10.1016/j.jmmm.2020.166711
36. Freitas PP, Ferreira R, Cardoso S, Cardoso F (2007) Magnetoresistive sensors. J Phys Condens Matter 19:165221. https://doi.org/10.1088/0953-8984/19/16/165221
37. Wang M, Zhang Y, Zhao X, Zhao W (2015) Tunnel junction with perpendicular magnetic anisotropy: status and challenges. Micromachines *6*(8):1023–1045
38. Lee D-Y, Lee S-E, Shim T-H, Park J-G (2016) Tunneling-magnetoresistance ratio comparison of MgO-based perpendicular-magnetic-tunneling-junction spin valve between top and bottom $Co_2Fe_6B_2$ free layer structure. Nanoscale Res Lett 11:433. https://doi.org/10.1186/s11671-016-1637-9
39. Matos F, Macedo R, Freitas PP, Cardoso S (2023) CoFeBX layers for MgO-based magnetic tunnel junction sensors with improved magnetoresistance and noise performance. AIP Adv 13: 25108. https://doi.org/10.1063/9.0000559
40. Rasly M, Nakatani T, Li J, Sepehri-Amin H, Sukegawa H, Sakuraba Y (2021) Magnetic, magnetoresistive and low-frequency noise properties of tunnel magnetoresistance sensor devices with amorphous CoFeBTa soft magnetic layers. J Phys D Appl Phys 54:95002. https://doi.org/10.1088/1361-6463/abc2f5
41. Cardoso S, Leitao DC, Gameiro L, Cardoso F, Ferreira R, Paz E, Freitas PP (2014) Magnetic tunnel junction sensors with pTesla sensitivity. Microsyst Technol 20:793–802. https://doi.org/10.1007/s00542-013-2035-1
42. Wiśniowski P, Almeida JM, Cardoso S, Barradas NP, Freitas PP (2008) Effect of free layer thickness and shape anisotropy on the transfer curves of MgO magnetic tunnel junctions. J Appl Phys 103:07A910. https://doi.org/10.1063/1.2838626
43. Almeida JM, Freitas PP (2009) Field detection in MgO magnetic tunnel junctions with superparamagnetic free layer and magnetic flux concentrators. J Appl Phys 105:07E722. https://doi.org/10.1063/1.3077228
44. Leitao DC, Silva AV, Ferreira R, Paz E, Deepack FL, Cardoso S, Freitas PP (2014) Linear nanometric tunnel junction sensors with exchange pinned sensing layer. J Appl Phys 115: 17E526. https://doi.org/10.1063/1.4869163
45. Oogane M, Fujiwara K, Kanno A, Nakano T, Wagatsuma H, Arimoto T, Mizukami S, Kumagai S, Matsuzaki H, Nakasato N, Ando Y (2021) Sub-pT magnetic field detection by tunnel magneto-resistive sensors. Appl Phys Express 14(12):123002. https://doi.org/10.35848/1882-0786/ac3809
46. Lu Y, Altman RA, Marley A, Rishton SA, Trouilloud PL, Xiao G, Gallagher WJ, Parkin SSP (1997) Shape-anisotropy-controlled magnetoresistive response in magnetic tunnel junctions. Appl Phys Lett 70:2610–2612. https://doi.org/10.1063/1.118933
47. Endoh T, Honjo H (2018) A recent progress of spintronics devices for integrated circuit applications. J Low Power Electron Appl 8(4):44

48. Zhao W, Tao X, Ye C, Tao Y (2022) Tunnel magnetoresistance sensor with AC modulation and impedance compensation for ultra-weak magnetic field measurement. Sensors 22:1021
49. Yan S, Cao Z, Guo Z, Zheng Z, Cao A, Qi Y, Leng Q, Zhao W (2018) Design and fabrication of full wheatstone-bridge-based angular GMR sensors. Sensors 18:1832
50. Schuhl A, Van Dau FN, Childress JR (1995) Low-field magnetic sensors based on the planar Hall effect. Appl Phys Lett 66:2751–2753. https://doi.org/10.1063/1.113697
51. Hung TQ, Oh S, Sinha B, Jeong J-R, Kim D-Y, Kim C (2010) High field-sensitivity planar Hall sensor based on NiFe/Cu/IrMn trilayer structure. J Appl Phys 107:09E715. https://doi.org/10.1063/1.3337739
52. Das PT, Nhalil H, Schultz M, Amrusi S, Grosz A, Klein L (2021) Detection of low-frequency magnetic fields down to sub-pT resolution with planar-Hall effect sensors. IEEE Sens Lett 5:1–4. https://doi.org/10.1109/LSENS.2020.3046632
53. Kim KW, Torati SR, Reddy V, Yoon SS (2014) Planar Hall resistance sensor for monitoring current. J Magn 19:151–154. https://doi.org/10.4283/JMAG.2014.19.2.151
54. Donolato M, Dalslet BT, Damsgaard CD, Gunnarsson K, Jacobsen CS, Svedlindh P, Hansen MF (2011) Size-dependent effects in exchange-biased planar Hall effect sensor crosses. J Appl Phys 109:064511. https://doi.org/10.1063/1.3561364
55. Ripka P, Arafat MMBT-RM in MS and ME (2019) Magnetic sensors: principles and applications. Elsevier, Oxford
56. Hung TQ, Oh S, Jeong JR, Kim CG (2010) Spin-valve planar Hall sensor for single bead detection. Sensors Actuators A Phys 157:42–46. https://doi.org/10.1016/j.sna.2009.11.033
57. Vitol EA, Novosad V, Rozhkova EA (2012) Microfabricated magnetic structures for future medicine: from sensors to cell actuators. Nanomedicine 7:1611–1624. https://doi.org/10.2217/nnm.12.133
58. Díaz-Michelena M (2009) Small magnetic sensors for space applications. Sensors 9:2271–2288
59. Sakib S, Fouda MM, Al-Mahdawi M, Mohsen A, Oogane M, Ando Y, Fadlullah ZM (2022) Deep learning models for magnetic Cardiography edge sensors implementing noise processing and diagnostics. IEEE Access 10:2656–2668. https://doi.org/10.1109/ACCESS.2021.3138976
60. Watanabe S, Yamada S (2008) Magnetocardiography in early detection of electromagnetic abnormality in ischemic heart disease. J Arrhythmia 24:4–17. https://doi.org/10.1016/S1880-4276(08)80002-6
61. Nousiainen J, Oja S, Malmivuo J (1994) Normal vector magnetocardiogram: II. Effect of constitutional variables. J Electrocardiol 27:233–241. https://doi.org/10.1016/S0022-0736(94)80007-3
62. Fujiwara K, Oogane M, Kanno A, Imada M, Jono J, Terauchi T, Okuno T, Aritomi Y, Morikawa M, Tsuchida M, Nakasato N, Ando Y (2018) Magnetocardiography and magnetoencephalography measurements at room temperature using tunnel magneto-resistance sensors. Appl Phys Express 11:23001. https://doi.org/10.7567/APEX.11.023001
63. Kurashima K, Kataoka M, Nakano T, Fujiwara K, Kato S, Nakamura T, Yuzawa M, Masuda M, Ichimura K, Okatake S, Moriyasu Y, Sugiyama K, Oogane M, Ando Y, Kumagai S, Matsuzaki H, Mochizuki H (2023) Development of magnetocardiograph without magnetically shielded room using high-detectivity TMR sensors. Sensors 23:646
64. Amaral J, Cardoso S, Freitas PP, Sebastião AM (2011) Toward a system to measure action potential on mice brain slices with local magnetoresistive probes. J Appl Phys 109:07B308. https://doi.org/10.1063/1.3562915
65. Amaral J, Gaspar J, Pinto V, Costa T, Sousa N, Cardoso S, Freitas P (2013) Measuring brain activity with magnetoresistive sensors integrated in micromachined probe needles. Appl Phys A Mater Sci Process 111:407–412. https://doi.org/10.1007/s00339-013-7621-7
66. Caruso L, Wunderle T, Lewis CM, Valadeiro J, Trauchessec V, Trejo Rosillo J, Amaral JP, Ni J, Jendritza P, Fermon C, Cardoso S, Freitas PP, Fries P, Pannetier-Lecoeur M (2017) In vivo magnetic recording of neuronal activity. Neuron 95:1283–1291.e4. https://doi.org/10.1016/j.neuron.2017.08.012
67. Sharma PP, Gervasoni G, Albisetti E, D'Ercoli F, Monticelli M, Moretti D, Forte N, Rocchi A, Ferrari G, Baldelli P, Sampietro M, Benfenati F, Bertacco R, Petti D (2017) Towards a

magnetoresistive platform for neural signal recording. AIP Adv 7:56706. https://doi.org/10.1063/1.4973947
68. Wang ZD, Gu Y, Wang YS (2012) A review of three magnetic NDT technologies. J Magn Magn Mater 324(4):382–388. https://doi.org/10.1016/j.jmmm.2011.08.048
69. Pham HQ, Le VS, Vu MH, Doan DT, Tran QH (2019) Design of a lightweight magnetizer to enable a portable circumferential magnetic flux leakage detection system. Rev Sci Instrum 90: 74705. https://doi.org/10.1063/1.5090938
70. Pham HQ, Tran BV, Doan DT, Le VS, Pham QN, Kim K, Kim C, Terki F, Tran QH (2018) Highly sensitive planar Hall magnetoresistive sensor for magnetic flux leakage pipeline inspection. IEEE Trans Magn 54:1–5. https://doi.org/10.1109/TMAG.2018.2816075
71. Gupta M, Khan MA, Butola R, Singari RM (2022) Advances in applications of non-destructive testing (NDT): a review. Adv Mater Process Technol 8:2286–2307. https://doi.org/10.1080/2374068X.2021.1909332
72. Aggelis DG, Soulioti DV, Barkoula NM, Paipetis AS, Matikas TE (2012) Influence of fiber chemical coating on the acoustic emission behavior of steel fiber reinforced concrete. Cem Concr Compos 34:62–67. https://doi.org/10.1016/j.cemconcomp.2011.07.003
73. Clausen JS, Nikolaos Z, Knudsen A (2012) Onsite measurements of concrete structures using impact-echo and impulse response. Emerg Technol Non-Destr Test V:117–122
74. Hojjati-Najafabadi A, Mansoorianfar M, Liang T, Shahin K, Karimi-Maleh H (2022) A review on magnetic sensors for monitoring of hazardous pollutants in water resources. Sci Total Environ 824:153844. https://doi.org/10.1016/j.scitotenv.2022.153844
75. Mahmoud AED, Fawzy M (2021) Nanosensors and nanobiosensors for monitoring the environmental pollutants BT. In: Makhlouf ASH, Ali GAM (eds) Waste recycling technologies for nanomaterials manufacturing. Springer International Publishing, Cham, pp 229–246
76. Jung B, Safan A, Batchelor B, Abdel-Wahab A (2016) Spectroscopic study of se(IV) removal from water by reductive precipitation using sulfide. Chemosphere 163:351–358. https://doi.org/10.1016/j.chemosphere.2016.08.024
77. Allpike BP, Heitz A, Joll CA, Kagi RI, Abbt-Braun G, Frimmel FH, Brinkmann T, Her N, Amy G (2005) Size exclusion chromatography to characterize DOC removal in drinking water treatment. Environ Sci Technol 39:2334–2342
78. Holkar CR, Jadhav AJ, Pinjari DV, Mahamuni NM, Pandit AB (2016) A critical review on textile wastewater treatments: possible approaches. J Environ Manag 182:351–366. https://doi.org/10.1016/j.jenvman.2016.07.090
79. Alam MK, Rahman MM, Elzwawy A, Torati SR, Islam MS, Todo M, Asiri AM, Kim D, Kim CG (2017) Highly sensitive and selective detection of Bis-phenol A based on hydroxyapatite decorated reduced graphene oxide nanocomposites. Electrochim Acta 241:353–361. https://doi.org/10.1016/j.electacta.2017.04.135
80. Antwi HA, Zhou L, Xu X, Mustafa T (2021) Progressing towards environmental health targets in China: an integrative review of achievements in air and water pollution under the "ecological civilisation and the beautiful China" dream. Sustainability 13:3664
81. Hojjati-Najafabadi A, Mansoorianfar M, Liang T, Shahin K, Wen Y, Bahrami A, Karaman C, Zare N, Karimi-Maleh H, Vasseghian Y (2022) Magnetic-MXene-based nanocomposites for water and wastewater treatment: a review. J Water Process Eng 47:102696. https://doi.org/10.1016/j.jwpe.2022.102696
82. Shahzad A, Rasool K, Miran W, Nawaz M, Jang J, Mahmoud KA, Lee DS (2018) Mercuric ion capturing by recoverable titanium carbide magnetic nanocomposite. J Hazard Mater 344: 811–818. https://doi.org/10.1016/j.jhazmat.2017.11.026
83. Shahzad A, Rasool K, Miran W, Nawaz M, Jang J, Mahmoud KA, Lee DS (2017) Two-dimensional Ti_3C_2Tx MXene nanosheets for efficient copper removal from water. ACS Sustain Chem Eng 5:11481–11488. https://doi.org/10.1021/acssuschemeng.7b02695
84. Aylaz G, Kuhn J, Lau ECHT, Yeung C-C, Roy VAL, Duman M, Yiu HHP (2021) Recent developments on magnetic molecular imprinted polymers (MMIPs) for sensing, capturing, and

monitoring pharmaceutical and agricultural pollutants. J Chem Technol Biotechnol 96: 1151–1160. https://doi.org/10.1002/jctb.6681

85. Li X, Yang Y, Yang J, Fan Y, Qian X, Li H (2021) Rapid diagnosis of heavy metal pollution in lake sediments based on environmental magnetism and machine learning. J Hazard Mater 416: 126163. https://doi.org/10.1016/j.jhazmat.2021.126163
86. Zheng C, Zhu K, de Freitas SC, Chang J, Davies JE, Eames P, Freitas PP, Kazakova O, Kim C, Leung C, Liou S, Ognev A, Piramanayagam SN, Ripka P, Samardak A, Shin K, Tong S, Tung M, Wang SX, Xue S, Yin X, Pong PWT (2019) Magnetoresistive sensor development roadmap (non-recording applications). IEEE Trans Magn 55:1–30. https://doi.org/10.1109/TMAG.2019.2896036

electronics

Article

Designing a Spintronic Based Magnetoresistive Bridge Sensor for Current Measurement and Low Field Sensing

Cristian Mușuroi [1], Marius Volmer [1,*], Mihai Oproiu [1], Jenica Neamtu [2] and Elena Helerea [1]

1 Department of Electrical Engineering and Applied Physics, Transilvania University of Brasov, Blvd. Eroilor 29, 500036 Brasov, Romania
2 National Institute for Research and Development in Electrical Engineering, Splaiul Unirii 313, 030138 Bucharest, Romania
* Correspondence: volmerm@unitbv.ro

Abstract: An exchanged-biased anisotropic magnetoresistance bridge sensor for low currents measurement is designed and implemented. The sensor has a simple construction (single mask) and is based on results from micromagnetic simulations. For increasing the sensitivity of the sensor, the magnetic field generated by the measurement current passing through the printed circuit board trace is determined through an analytical method and, for comparative analysis, finite elements method simulations are used. The sensor performance is experimentally tested with a demonstrator chip. Four case studies are considered in the analytical method: neglecting the thickness of the trace, dividing the thickness of the trace in several layers, and assuming a finite or very long conductive trace. Additionally, the influence of several adjacent traces in the sensor area is evaluated. The study shows that the analytical design method can be used for optimizing the geometric selectivity of a non-contacting magnetoresistive bridge sensor setup in single trace, differential, and multi-trace (planar coil) configurations. Further, the results can be applied for developing highly performant magnetoresistance sensors and optimizations for low field detection, small dimensions, and low costs.

Keywords: magnetoresistive sensors; anisotropic magnetoresistance; current sensors; planar Hall effect; exchange bias; magnetic field modeling; micromagnetic simulations

check for updates

Citation: Mușuroi, C.; Volmer, M.; Oproiu, M.; Neamtu, J.; Helerea, E. Designing a Spintronic Based Magnetoresistive Bridge Sensor for Current Measurement and Low Field Sensing. *Electronics* **2022**, *11*, 3888. https://doi.org/10.3390/electronics11233888

Academic Editor: Gianpaolo Vitale

Received: 11 October 2022
Accepted: 22 November 2022
Published: 24 November 2022

1. Introduction

Measurement of the electric current is a key element in electrical systems, even more so with the continuous development and full-scale implementation of Industry 4.0 and 5.0 technologies in an Internet of things era. Some key characteristics can be identified for modern current measurement applications, such as high accuracy and sensitivity, linear response, DC/AC operation, low thermal drift, immunity to interferences, IC packaging, reduced costs, and power consumption.

Resistive-based current-sensing techniques are adequate for some applications but they present a lot of disadvantages, such as power loss, no galvanic isolation, and low bandwidth [1], issues that are not present with non-contacting current sensing techniques.

Typical non-contacting current sensor technologies are AC/DC current transformers, fluxgate magnetometers [2,3], or those that utilize Hall effect [4–7], anisotropic magnetoresistive (AMR) sensors [2,5,8], giant magnetoresistive (GMR) [4,9–11], and tunnelling magneto-resistance (TMR) sensors [12,13]. Current sensors based on magnetoresistive effects offer high accuracy, endurance, low temperature drift, low offset, and are suitable for low volume production together with tight integration capabilities with integrated circuits (ICs). An overview detailing their properties, performance characteristics, magnetic field behavior, as well as specific advantages and drawbacks was performed in [14,15]. Thus, for superior sensor characteristics (immunity to some electromagnetic interferences, high sensitivity, linearity), a double differential implementation of magnetoresistive current sensors should be used together with a multi-trace planar coil setup for improving low field response with a biasing system utilizing coils or permanent magnets. Versatility of the sensing system can be improved with a coil biasing system, but power consumption increases in this case.

Besides the general desirable characteristics for a sensor (sensitivity, low linearity error, low offset, and stability over time), in order to better define the requirements for a high performant current sensor, specific parameters for magnetic sensors have to be taken into account: hysteresis, perming, and geometric selectivity. Hysteresis is related to the magnetic material behavior and is usually defined as the current changing between the maxima of the full-scale range. Perming is the change in the sensor offset caused by a high intensity external magnetic field. Geometric selectivity refers to sensitivity of the sensor in function of the characteristics of the conductor through which the measured current is passing and the influence of crosstalk from non-measured currents or external magnetic fields [16]. Other practical characteristics are desirable, depending on the application in which they are implemented: immunity to high electric field variations, frequency response from DC to MHz, cost, weight, and size requirements.

The electrical resistivity of magnetic thin films (usually Fe, Co, Ni, or alloys like Permalloy—$Ni_{80}Fe_{20}$) is anisotropically dependent on the direction of the applied magnetic field [17]. Thus, the layer resistivity depends on the angle between the magnetization and direction of current flow. Moreover, the magnetization rotation direction and angle depend on the applied external field's amplitude. The electrical resistance change can be measured as roughly the square of the cosine of the angle between the magnetization and the direction of current flow. This constitutes the basis for effects such as planar Hall effect (PHE), which is a consequence of the AMR effect.

Regarding the layout of AMR sensors, the basic approach is to utilize several magnetic thin film resistive elements that have a large aspect ratio (about 10 nm thin, a few μm wide, and tens of μm long), such that the magnetization is aligned on the longitudinal (easy) axis, connected in a Wheatstone bridge configuration for increased thermal stability and sensitivity around zero field. The maximum sensitivity and linearity are achieved when the magnetization is at 45° with respect to the current direction. This is commonly achieved using the Barber pole biasing technique [18] or other biasing techniques, such as herringbone [19].

In terms of classification, AMR sensors can be divided into two classes: those that are similar to Hall sensors and AMR bridges. [20]. The first class are those that share a geometry with Hall sensors, where the current is injected along one direction in the sensor cross and the voltage is measured orthogonally, these are referred as PHE sensors. In the second class, the AMR elements are combined in a Wheatstone bridge, such that the current is injected along one direction and the voltage is measured in the orthogonal direction. To further differentiate between the two classes, the term "PHE bridge (PHEB) sensors" was introduced to distinguish between other AMR bridge sensors, the more correct term being "exchange-biased AMR bridge sensors [21]. A comprehensive study for the geometry influence and structure of AMR/PHE sensors was performed in [22].

We demonstrated that both DC and AC currents through linear stripes can be measured down to μA using GMR sensors [15], however, some limitations in terms of sensor sensitivity, size, and setup complexity were found. For achieving lower detection limits, this study aims to consider some possible sources of electromagnetic interferences and trace current dimensional effects that can have adverse effects on the response of the magnetoresistive sensor. An analytical method can be used to estimate the response of the sensor, but such an approach is dependent on the number of dimensional parameters that are taken into account when modeling the magnetic field in the sensor area. This can be especially important for low currents which are producing magnetic fields that have to be measured. The method implemented in [15] did not take into account the length or thickness of the trace or specific trace geometries.

This work aims to improve the analytical method from [15], to include trace length and thickness as dimensional parameters. A comparative study is performed with different versions of the analytical method and finite elements simulations with COMSOL Multiphysics to study the influence of trace geometry and sensor placement on the magnetic field intensity in the sensor area. Results are applied for the design and implementation of a proof-of-concept exchange-biased AMR bridge sensor: often called planar Hall resistance (PHR) in the literature. The mode of operation of the sensor is proven using multi-domain micromagnetic simulations. Focus is placed on design optimizations by sensor placement and trace configurations that can be applied for various non-contacting current sensors. Experimental results from the PHR bridge sensor setup and a previously implemented GMR sensor setup are performed to validate the results. The main purpose of this study is to serve as the basis for designing optimized magnetoresistive sensor designs, improved mostly through geometric selectivity and experimental setup.

2. Materials and Methods

Materials and methods is structured into several sections. Firstly, the basic principles of the AMR, PHE (Section 2.1), and GMR effects (Section 2.2) are detailed, which are utilized in the experimental setup. Secondly, the analytical method for estimating the magnetic field intensity in the sensor area by a single or multiple printed circuit board (PCB) traces through which a current is flowing is shown in Section 2.3. Section 2.4 describes the layout of the PHR bridge sensor and critical analysis is performed using a single domain and multi-domain micromagnetic method to justify the specific layout influences for the sensing elements as well. Section 2.5 and part of Section 2.6 show the influence of thermal and magnetic annealing processes on the sensor performance to optimize sensitivity of the sensors. Exchange bias field effects on sensor response are justified throughout Sections 2.4 and 2.5. Finally, Section 2.6 also describes the experimental setup and manufacturing steps for the demonstrator chip. Various sensor design steps and best practices can be extracted from all sections.

2.1. Principle of Operation–AMR and PHE Effects

The AMR effect appears in ferromagnetic bulk materials or thin films from Ni, Co, Fe, and their alloys [23]. The AMR effect comes from the dependence of the electrical resistivity of a material on the angle between the direction of electric current and direction of magnetization inside the material. In other words, the physical origin of AMR can be attributed to the anisotropic s–d scattering of electrons due to the spin–orbit coupling on 3d orbitals of ferromagnetic materials. [24,25]. The result of this effect is that in most magnetic materials, the resistivity of the material increases when the direction of the current is parallel to the applied magnetic field and minimum when the direction of the current is perpendicular. The AMR ratio can be expressed by:

$$\frac{\Delta\rho}{\rho_\perp} = \frac{\rho_\parallel - \rho_\perp}{\rho_\perp} \tag{1}$$

where both resistivities $\rho_\parallel$ and $\rho_\perp$ are expressed at saturation field, parallel, and perpendicular to the current direction, respectively.

Usually, for magnetic materials, this ratio is not larger than 5%, while for typical ferromagnetic NiFe films, the AMR value is in the order of 2–2.2% for magnetic fields of a few Oe [12]. Commonly, $Ni_{80}Fe_{20}$ (Permalloy) is used due to close to zero magnetostriction constants in all directions. For a schematic representation of the AMR effect, we can consider a thin film of ferromagnetic material (Figure 1). Note that for actual devices, an easy axis of magnetization is defined through the shape anisotropy ($l > w$) and the uniaxial anisotropy field H_K. If an electrical current passes through the film along x direction and the magnetization, M, which makes an angle θ with the current, the longitudinal, E_x, and transverse, E_y, components of the electric field can be derived by considering the angular dependency of the resistivity tensor components ρ_{xx} and ρ_{xy} [7,18]:

$$E_x = j_x \cdot \rho_{xx} = j_x\rho_\perp + j_x\left(\rho_\parallel - \rho_\perp\right)\cos^2\theta \tag{2}$$

$$E_y = j_x \rho_{xy} = j_x \left(\rho_{\parallel} - \rho_{\perp}\right) \sin\theta \cos\theta \tag{3}$$

with $\left|\vec{j}\right| = j_x$ and $\rho_{\parallel}$ and $\rho_{\perp}$ as defined above.

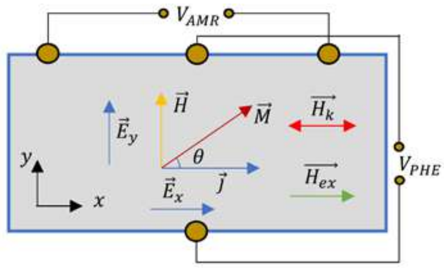

Figure 1. Schematic representation of the AMR and PHE effects on a Permalloy thin film through which a current is flowing along the x axis; $\vec{M}$ is the magnetization which makes an angle θ with the current direction due to the applied field, $\vec{H}$ which is perpendicular on the applied current.

The variation of the longitudinal resistivity, given by ρ_{xx} and measured through $U_x = E_x \times l$, characterizes the AMR effect. The second term, E_y, shows generation of a signal perpendicular to the current direction in a geometry typical for Hall effect but with the applied field contained in the film plane. This is the PHE signal, V_{PHE}, which is also defined in Figure 1:

$$V_{PHE} = l \frac{\left(\rho_{\parallel} - \rho_{\perp}\right)}{t} \sin\theta \cos\theta \tag{4}$$

2.2. Principle of Operation–GMR Effect

The GMR effect takes place in multilayered magnetic structures of the type FM/NM/FM coupled by exchange interaction. Here, FM denotes ferromagnetic layers of $Ni_{80}Fe_{20}$, Co, CoFeB layers with thicknesses between 1–100 nm and NM represents nonmagnetic layers, usually from Cu or Ag with thickness of about 1 nm, that mediate the exchange interaction between the FM layers. The basis of this effect is that a change in the electrical resistance of the magnetic multilayers is produced in response to an applied external magnetic field. The resistance change is dependent on the angle between the direction of the magnetizations of adjacent layers. Thus, when the ferromagnetic layers are magnetized in parallel, the resistance is at a minimum value, R_P- while at antiparallel orientation, the resistance is at a maximum value. The electrical resistance dependency between the angle and direction of the electric current and the magnetization in the magnetic layers can be expressed by [26–29]:

$$R = \frac{R_{AP} + R_P}{2} + \frac{R_P - R_{AP}}{2} cos\theta \tag{5}$$

Thus, for antiparallel configuration and parallel, we obtain:

$$\theta = 180^\circ \rightarrow cos\theta = -1 \rightarrow R = R_{AP} = R_{High} \tag{6}$$

$$\theta = 0^\circ \rightarrow cos\theta = 1 \rightarrow R = R_P = R_{Low} \tag{7}$$

The magnitude of the GMR effect is around 5–20% and is expressed by:

$$GMR = \frac{R_{AP} - R_P}{R_{AP}} 100\ [\%], \tag{8}$$

The AA003-02 sensor was used in the experimental setup, which contains two active GMR elements, and two magnetically shielded identical sensors, together forming a Wheatstone bridge with an average sensitivity 25–40 µV/(V × A/m) [15,30].

2.3. Design Optimization of the Non-Contacting Current Sensor Based on Analytical Method for Current Stripes

Electromagnetic field modeling can offer great insight into the behavior, operation, and possible improvements for devices that rely on specific configuration of the magnetic field for proper operation, especially if these devices are susceptible to interferences or very high sensitivity is required. Applying software and mathematical methods for analyzing high-sensitivity magnetic sensors is a very a useful tool for improving their characteristics: reducing susceptibility to electromagnetic interferences, improving the signal-to-noise ratio, reducing size or costs. Several approaches from the literature have proposed modeling of the field produced by various configurations of single or multiple loops of wire in the same plane [31,32]. Most solutions focus on complex integral solutions that are usually solved with numerical methods [33], through FEM simulations [34], or serve application-specific purposes [35]. Although most methods that can be found in the literature are accurate up to a certain point, they are not adapted for the specificity required for field estimation in common setups in which magnetoresistive sensors are involved. However, many solutions shown in the literature, either lack automation or require intense computation steps. In this study, several specific optimizations are performed which reduce complexity significantly and do not require computationally intensive FEM simulations. For ease of use and integration with other instrumentation functionalities, the analytical method was implemented in a LabView application.

The basic principle of the proposed setup is to increase the intensity of the magnetic field in the non-contacting current sensor area, and thus the accuracy and sensitivity by a proper design of the current stripes from which the magnetic field to be measured is generated. This was achieved by integrating a planar coil below the magnetoresistive sensor which will increase the magnetic field intensity in the sensitive area of the sensor, essentially increasing sensor sensitivity for the same input current. In the current measurement setup, the MR sensors act as magnetometers, thus if a current, I, passes through a wire, the magnetic field, B, will produce a change in the output of the MR sensor. The working principle of the non-contacting current measurement setup for both single and multi-trace configurations is illustrated in Figure 2.

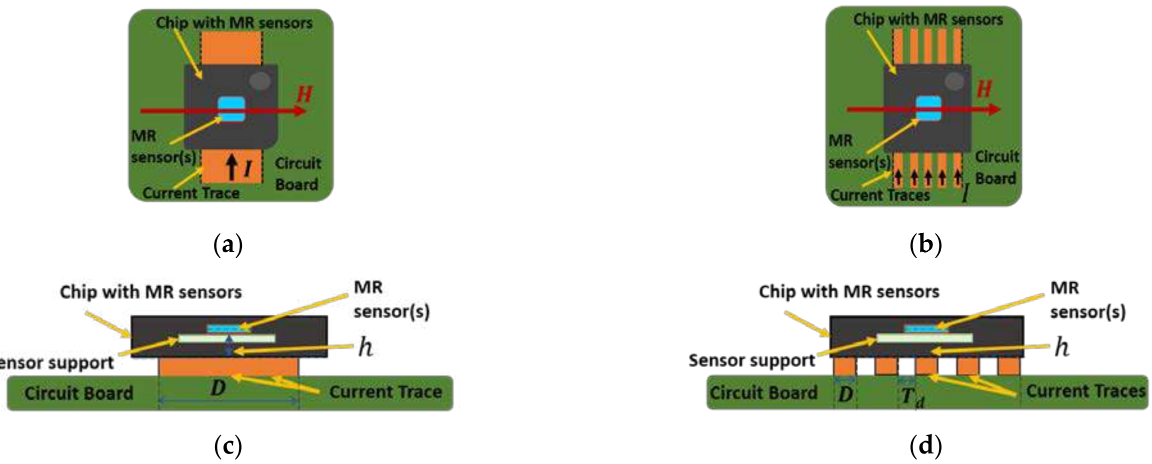

Figure 2. Working principle of the non-contacting current measurement setup utilizing current traces and a MR-based chip: (**a**) Single trace plane section; (**b**) Multi-trace plane section; (**c**) Single trace cross section; (**d**) Multi-trace cross section (adapted from [15]).

An approach optimized for low field detection by utilizing multiple current traces, in a double differential system, and implemented in a custom printed circuit board was demonstrated [15].

In order to estimate B_x, an analytical model based on Biot–Savart law was derived, which assumes that the sensor is centered above the multiple trace at distance h (Figure 3).

Note that the thickness of each trace is divided by an m number of layers, consequently, h changes for each individual layer (from the center of each layer). For the finite length correction, we introduced the sum of the sine functions of the angles between the sensor area (above central trace) and for each end of the linear current trace (Figure 3a). Note that some geometric correction can still be introduced, especially for a large number of adjacent traces or nonlinear trace configurations.

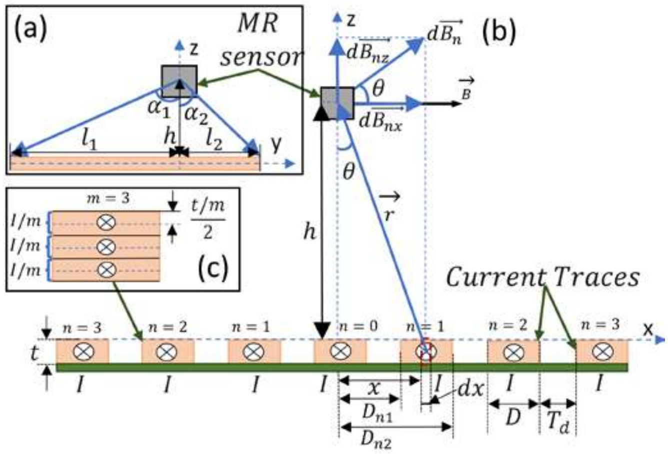

Figure 3. Analytical model to compute the magnetic field present in the sensor area: (**a**) Length correction of the magnetic field in the sensor area based on the distance from the linear trace ends; (**b**) Magnetic field components generated by the current through the trace and dimensional parameters; (**c**) Layered trace thickness parameters. Note that the model takes into account that there is an odd number of traces that generate the magnetic field and the central trace is denoted as n = 0.

For calculating the magnetic field, the Biot–Savart equation was applied to the geometry shown in Figure 3 and integrated:

$$d\vec{B} = \frac{\mu_0 I d\vec{l} \times \vec{r}}{4\pi \cdot r^3} 100\ [\%], \tag{9}$$

By assuming a very long conductive trace (Figure 2d, the elementary current produced by the current I, can be expressed, using the Biot–Savart law by:

$$dB_n = \mu_0 \frac{dI}{2\pi r} = \mu_0 \frac{Idx}{D} \cdot \frac{1}{2\pi\sqrt{h^2 + x^2}}\ ; dI = \frac{I}{D} dx, \tag{10}$$

$$dB_{nx} = dB_n \cdot cos\theta = \mu_0 \frac{Idx}{2\pi D} \cdot \frac{1}{\sqrt{h^2 + x^2}} \cdot \frac{h}{\sqrt{h^2 + x^2}}\ , \tag{11}$$

where $\mu_0 = 4\pi \times 10^{-7}$ H/m is the vacuum magnetic permeability, D is the trace width, t is the trace thickness (not used in the equation), T_d is the distance between the traces, h is the height on which the sensing element is placed above the trace, and θ is the angle shown in Figure 3a used to estimate the B_x component of the magnetic field.

By assuming a uniform linear current density, *I/D*, and integrating equation 11 from D_{n1} to D_{n2}, the x component of the magnetic field generated by a trace n = 1, 2, 3, . . . , in the sensor area is determined corresponding for $2n + 1$ traces for a planar coil (Equation (12)). If now, we introduce the length correction factor and divide the thickness of the trace in m layers, we get equation 13. If we take into account MR chip dimensions, usually the maximum value of n can be up to 6 (13 total traces).

$$B_{nx} = \frac{\mu_0 I}{2\pi D}\left[\arctan\left(\frac{D_{n2}}{h}\right) - \arctan\left(\frac{D_{n1}}{h}\right)\right] [\mathrm{T}], \tag{12}$$

$$B_{nx} = \sum_{i=0}^{m} \left(\frac{\mu_0 \frac{I}{m}}{2\pi D} \left[\arctan\left(\frac{D_{n2}}{h_i}\right) - \arctan\left(\frac{D_{n1}}{h_i}\right) \right] \cdot (sin\alpha_1 + sin\alpha_2) \right) [\mathrm{T}] \quad (13)$$

For a single trace (n = 0), from equation 13 it follows:

$$B_{0x} = \sum_{i=0}^{m} \left(\frac{\mu_0 \frac{I}{m}}{\pi D} \left[\arctan\left(\frac{D}{2h_i}\right) \right] \cdot (sin\alpha_1 + sin\alpha_2) \right) [\mathrm{T}] \quad (14)$$

A study based on four possible cases for this analytical method was performed: Case I- Infinite trace length, with a single layer (trace thickness neglected), Case II- Infinite trace length, with m = 35 layers (1 µm each layer), Case III, finite trace length, with a single layer (trace thickness neglected), and Case IV- finite trace length, with m = 35 layers (1 µm each layer). For Case II and Case IV, layered trace thickness means that the thickness of each trace is divided on a number of layers through which we assume a constant current, I/m is flowing (where m is the number of layers). The analytical method is in such a way implemented that the results of the final field is the sum of the field produced by the individual layers.

Moreover, for a comparative analysis of the results obtained with the analytical method, two use cases were studied using finite elements method simulations. Firstly, for a singular trace, results were compared with a single trace U-shaped current trace (Figure 4a) modeled to simulate the behavior in a double differential configuration. The specific dimensions of the U-shaped trace are chosen based on the ability to integrate highly sensitive and miniature magnetoresistive sensors, for example [36], in a double differential configuration in a very small package. Secondly, comparative analysis with experimental results is performed for the case of a multi-trace planar coil. The results of this comparison are shown in the Results and Discussion section.

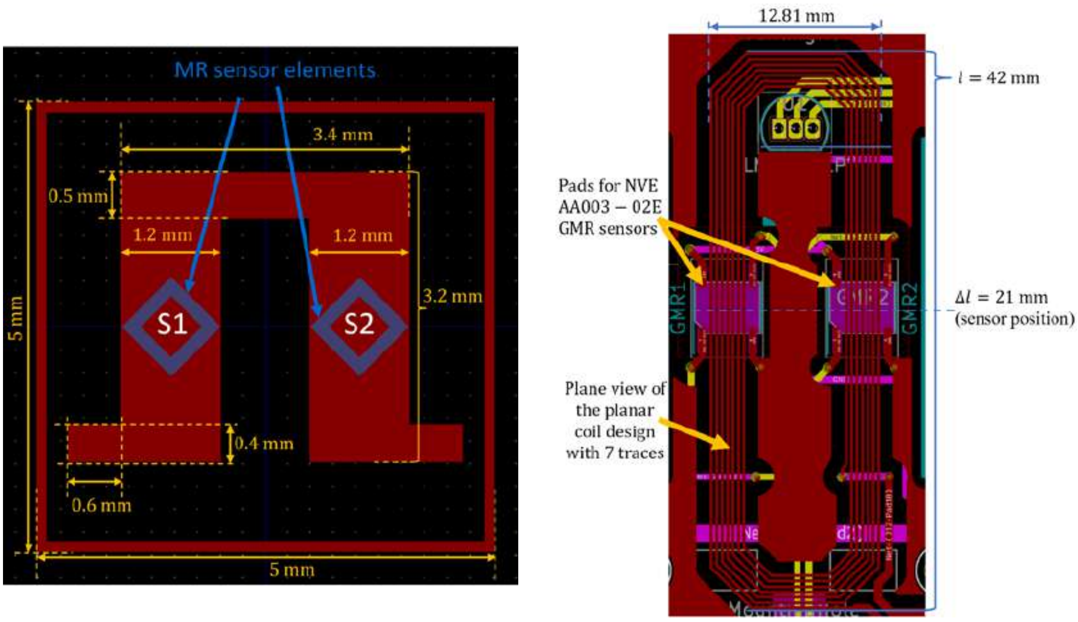

(**a**) (**b**)

Figure 4. Design and experimental implementation of (**a**) Geometry and parameters for the U-shaped trace; (**b**) Plane view of the planar coil with seven traces.

2.4. Principle of Operation of the Exchange Bias AMR Bridge Sensor

The design that serves as the layout for the demonstrator chip is shown in Figure 5. This design, which has two identical sensors is aimed at defining magnetoresistive structures adapted to the magnetic field produced by electric currents in the conditions of minimizing the effects created by temperature variations and interferences from external magnetic fields. The two sensors chip shows a double differential measurement system, in the sense that each of the AMR bridges is a differential sensor. On top of the sensor, a U-shaped Silver band is placed. The U-shaped trace was printed on top of a Kapton band with a thickness of 45 µm, by using a prototyping system (Voltera V-One) [37]. This band was placed on top of the sensors.

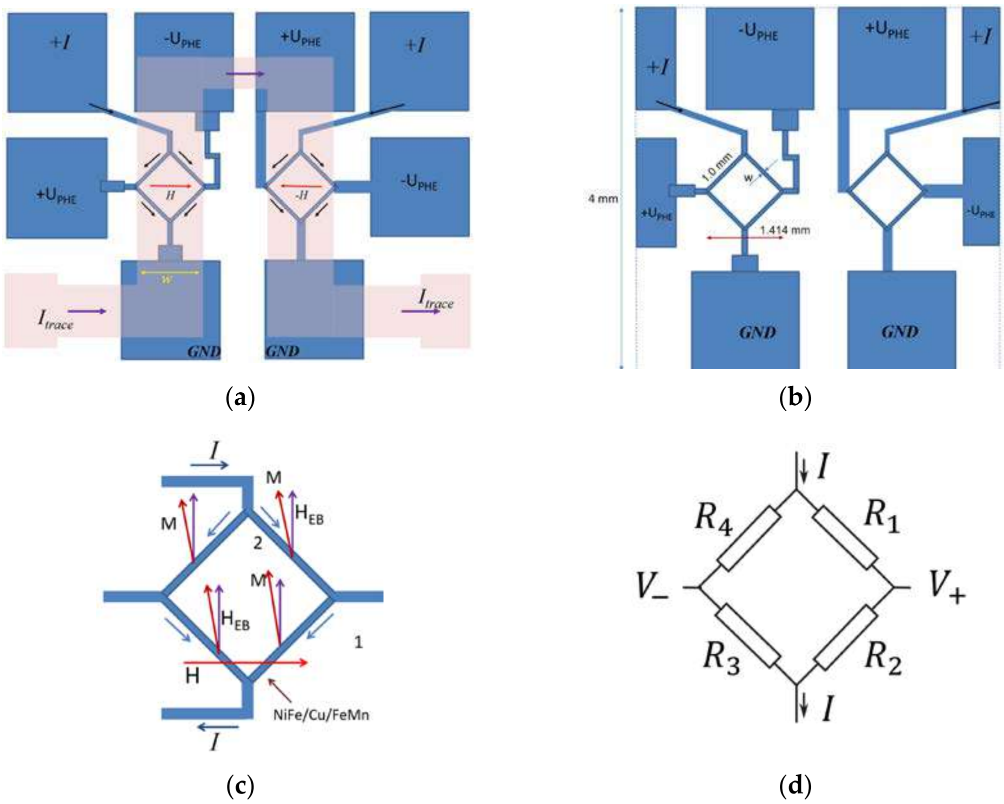

Figure 5. Layout of the exchange biased AMR bridge sensor chip: (**a**) Chip layout with over imposed U-shaped current trace on top of the AMR bridges; (**b**) Dimensions of the chip; (**c**) Working principle of the AMR bridge sensor; (**d**) Equivalent circuit of a single AMR bridge sensor. Note that the structured is within a square of 4 × 4 mm^2 and was realized on a 5 × 5 mm^2 chip. The margins are 0.5 mm while the arm of the bridge has a length L = 1 mm and a width of either 0.1 or 0.2 mm. The contacting pads size can be reduced such that the chip can fit inside a 3 × 3 mm^2 footprint.

Based on the equivalent circuit for one AMR bridge sensor (Figure 5d), we can note that the four AMR chip elements are in a Wheatstone bridge configuration (arms of the bridge R_1-R_4). Note that each resistor arm of the bridge can be constituted from multiple stripes for specific configurations [20]. Thus, the resistance of each arm is dependent on the number of stripes. If there is a positive applied current though the resistor, the output voltage (potential increase in the y-direction) from the bridge is:

$$V = I\,\frac{R_2R_3 - R_1R_4}{R_1 + R_2 + R_3 + R_4} \approx \frac{1}{2}I(R_3 - R_1) \tag{15}$$

where the result of the expression is valid when $R_1 + R_2 \approx R_3 + R_4$, thus when $I_{\text{stripe}} = I/2$.

In [20], a single domain approach was used to model the response and field contributions on the resistance of a single stripe (in our case, equivalent to one arm of the AMR bridge). The expression that was obtained for the resistance of a single sensor construction element (single stripe) was:

$$R(\alpha) = R_0 - sin(2\alpha)\left(S_0B_y^{ext} + S_0B^{sf}cos\alpha\right) \tag{16}$$

where R_0 is the stripe resistance when θ = 0 (θ is the magnetization rotation angle for a single domain stripe), α is the angle of a positive current passing through the stripe on the x-axis, S_0 is the single stripe low field sensitivity, B_y^{ext} is the field contribution due to homogenous external applied fields along the y-axis, and B^{sf} is the contribution of the magnetic field induced by the bias current passing though the sensor (the self-field).

The single stripe low-field sensitivity S_0 is [20]:

$$S_0 \equiv -\frac{l\Delta\rho}{wt(B_{ex} + B_K)} \tag{17}$$

where w is the width, l is the length, t is thickness of the stripe, $\Delta\rho = \rho_{\|} - \rho_{\perp}$, B_{ex} is the exchange pinning field, and B_K is the anisotropy field.

In order to validate the AMR bridge (PHR) sensor mode of operation for actual operation, we used a multi-domain simulation approach using LLG micromagnetics v4 [22,38]. The mask required for the simulation was obtained by editing a SEM image of the sensor and performing a black/white cleanup (Figure 6). The magnetic layer and spacing layer are situated in a 1000 × 2000 × 10 nm structure. The parameters used for the simulation are: saturation magnetization M_S = 710 kA/m [14,22], exchange constant $A = 1.3 \times 10^{-11}$ J/m, anisotropy constant K_u = 500 J/m^3 [39], the exchange bias field (pinning field) H_{ex} = 150 Oe, temperature T = 0 K; discretization cell 10 × 10 × 10 nm^3. The convergence condition was maintained at 1×10^{-4}. Note that between K_u and the anisotropy field H_k, there is the following relation $H_K = 2K_u/M_S$. Generally, micromagnetic simulators model structures at 0 K such that thermal fluctuations do not influence the results. These fluctuations make obtaining convergence difficult, especially for models with a high number of magnetic spins. Structures larger than 2 × 2 µm^2 are usually not simulated because results are not significantly different and the computation time requirements are high. The magnetization distribution for different applied field values (H = 0 Oe, H = −150 Oe, H = 150 Oe, H = 250 Oe) is shown in Figure 7. From Figure 7 and the magnetization distribution along the x and y axis for the entire structure compared with the central area of the AMR bridge at low field values (Figure 8), it can be denoted that the contacting pads and traces have very little influence on the magnetization characteristic of the sensor as the magnetic moments of the vertical stripes almost do not change at different applied fields and thus no additional hysteretic behavior is added to the central area of the structure.

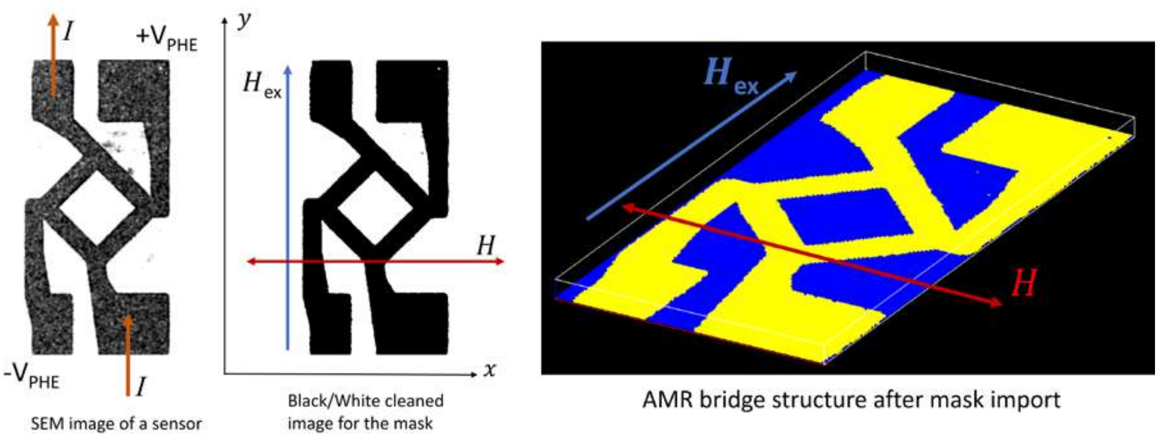

(**a**) (**b**)

Figure 6. AMR bridge sensor, multi-domain simulation mask layout: (**a**) SEM image of the sensor with obtained mask image after editing; (**b**) Overview of the imported mask in the software with the marked direction of the applied field and exchange bias field.

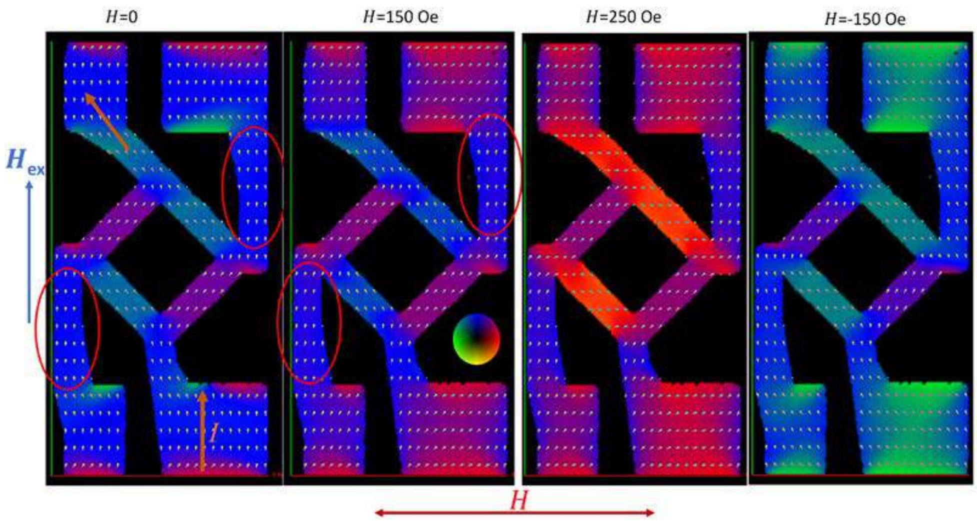

Figure 7. Simulated multi-domain magnetization distribution of the AMR bridge structure at different field values (H = 0 Oe, H = −150 Oe, H = 150 Oe, H = 250 Oe). The red arrow signifies the direction of the applied field while the blue arrow shows the orientation of the exchange bias field. The encircled areas show that no matter the field value, the orientation of the magnetic moments does not change and does not influence the behavior of the central area of the structure, thus there is no signal change with the applied field for these areas.

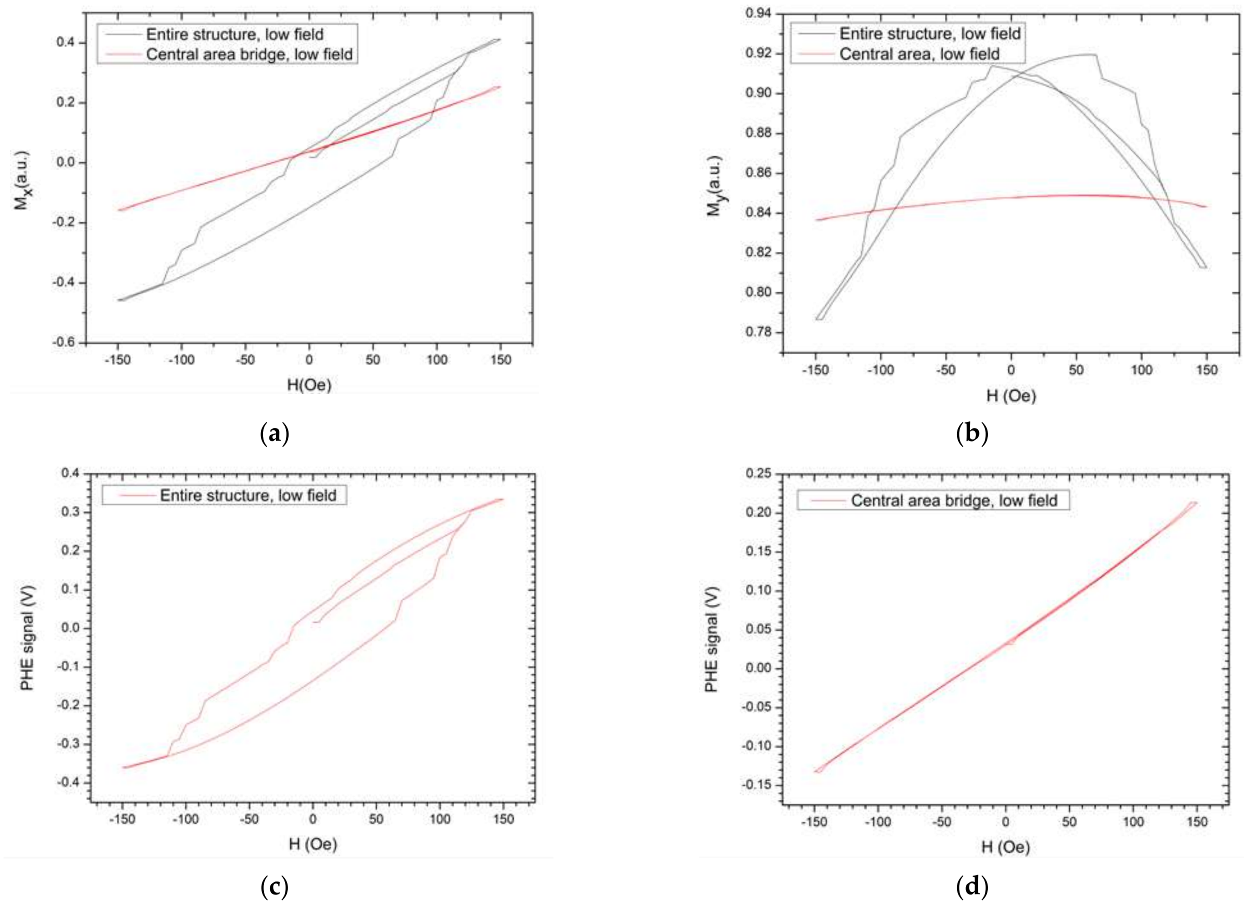

Figure 8. AMR bridge sensor, multi-domain simulation results for low field values: (**a**) Magnetization distribution along the x-axis; (**b**) Magnetization distribution along the y-axis; (**c**) PHE signal for the entire structure; (**d**) PHE signal for the central area of the structure (bridge).

2.5. Fabrication of Exchange Bias AMR Bridge Sensor Demonstrator

The AMR bridge sensors use spintronic structures of the type $Ni_{80}Fe_{20}$(10 nm)/FeMn (1 nm) and were deposited at ICPE-CA Bucharest though magnetron sputtering on an oxidized silicon substrate and microfabricated through the liftoff method. Given the particularities of the deposition method, the structures are amorphous and have a very low electrical conductivity. Additionally, the deposited structures do not show an established magnetocrystalline anisotropy axis or an exchange bias field, H_{ex}, between the antiferromagnetic layer (FeMn) and the permalloy ($Ni_{80}Fe_{20}$) magnetic layer. Finally, 5×5 mm^2 chips were cut. Of note is that a single mask was used for the chip, thus reducing complexity of the microfabrication process significantly. A scanning electron microscope image of the chip can be seen in Figure 9a. Several chips were thermally treated, Figure 9bc, with the purpose of enhancing the crystalline structures of the deposited layers and thus the electric conductivity. The thermal treatment was made in an argon (Ar, 99.99%) atmosphere, 2 mbarr pressure at a temperature of 450 °C for two hours [40].

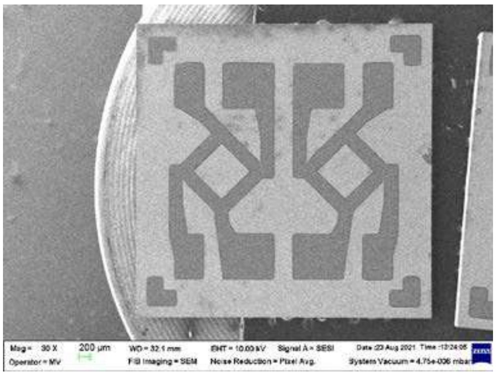

(**a**)

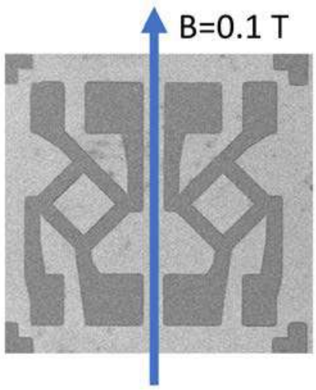

(**b**)

Figure 9. (**a**) SEM image of the AMR bridge sensor; (**b**) Direction and intensity of the applied field, *B* over the structure during the magnetic annealing process.

The magnetic annealing system was comprised of: (1) Electronically controlled heated air blower (40–300 °C), (2) Vacuum pump (2 mbarr), (3) Electronic thermometer with K-type thermocouple; (4) Support Copper (Cu) sheet at the end of which a chip is fixed for the magnetic annealing, (5) Stainless steel tube connected to the vacuum pump, (6) Neodymium permanent magnets. The chip is placed at the end of a copper sheet which is introduced into a stainless-steel tube, which is connected to the vacuum pump. Given the small volume, a 2 mbarr pressure is obtained in approximately 15 min. Initially, the system is not placed between the poles of the magnets. After 15 min of vacuum, tube (5) is heated to 100 °C with the air blower for 10 min, in order to degas the interior walls, the Cu sheet, and the probe. The temperature is increased to 200 °C and the system is introduced within the poles of the magnets which generate a field of B = 0.1 T in the area of the tip of the tube where the chip is located. The temperature is maintained for 5 min after which it is dropped to 30 °C within 10 min. Field measurements were made with a Lake Shore 475 DSP Gaussmeter.

In order to produce the U-shaped current trace, Figure 4a, on the surface of the sensor, the utilized method was to print directly on a Flexible Kapton band, with silver ink, Voltera Adorable Anchovy, Flex 2 ink type [41], which remains flexible after thermal treatment for eliminating organic compounds. This ink is kept between 4–10 °C and is also compatible with polyethylene terephthalate (PET) and other flexible polymer substrates. The resistivity of the ink is around 1.36×10^{-7} Ωm after thermal treatment. The U-shaped trace was realized utilizing the dedicated PCB printer, Voltera V-One, Figure 10 [37]. A 6 mm wide and 45 µm (micrometer measured) Kapton band was used. For maintaining mechanical integrity and flatness during printing, the Kapton tape was temporarily fixed on a standard FR4 PCB board. The printer was configured to print a 35–40 µm layer from a distance of 0.08 mm from the surface and for the printing head, a 150 µm metallic tip was used. Immediately after printing, the entire ensemble was thermally treated at 160 °C for 30 min. By using a scalpel, a strip containing a single trace was cut and placed on the surface of the sensor. On the ends of the U-shaped trace, two wires were bonded using silver paste. The electrical resistance of the conductive trace was measured with the Keithley 2700 digital multimeter using a 4-wire method: $R_{4w} = 0.096\ \Omega$.

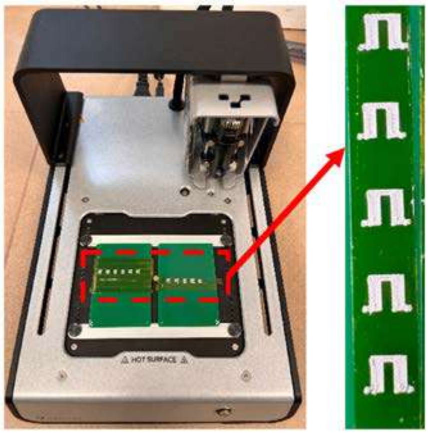

Figure 10. Voltera V-One printer with printed U-shaped traces and printed traces detail.

2.6. Galvanomagnetic Characterization of the Exchange-Biased AMR Bridge Sensor

2.6.1. Experimental Setup

The functional block diagram of the setup can be seen in Figure 11. Evaluating the performance of the sensor is necessary as they should be able to detect low magnetic fields, under 1 Oe (10^{-4} T in air). Note that given the identical layout, results for a single sensor on the chip are shown.

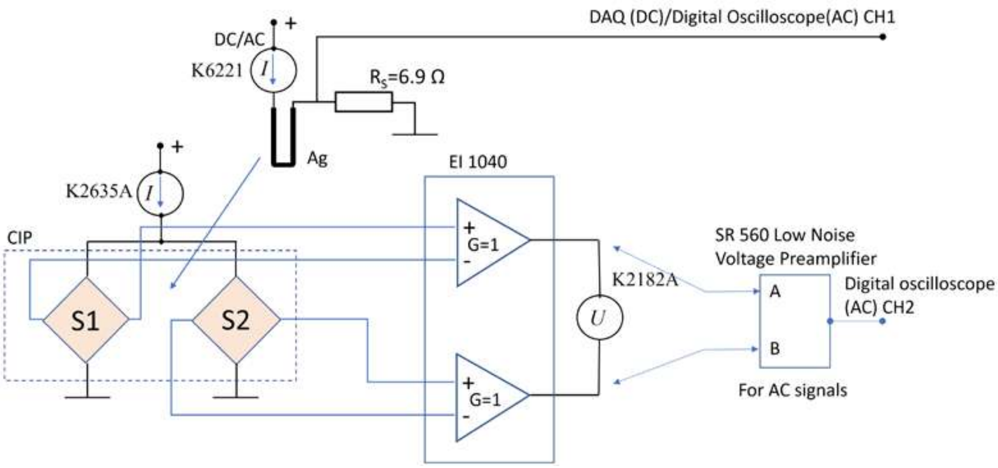

Figure 11. Functional block diagram of the experimental setup for the AMR bridge sensor demonstrator chip.

The chip measurement setup for both cases is shown in Figure 12. The magnetic field is applied in the sensor plane. A Keithley 6221 power supply is used to supply the sensors and a Keithley 2182 A nanovoltmeter for measuring the voltage output. As a magnetic field source, a Helmholtz coil was used, able to generate fields up to 200 Oe, which was powered by a programmable current source, Kepco BOP 100–10 MG. The coil was calibrated using the Lakeshore 475 DSP digital gaussmeter while data acquisition was done on a PC. For some tests, a biasing field was applied, H_{bias}, in order to linearize the characteristic of the sensor and to highlight the necessity for magnetic annealing; H is applied on the direction of the field which will be generated by the conductive trace, Figure 5. The sensor was supplied with a 1 mA current, DC.

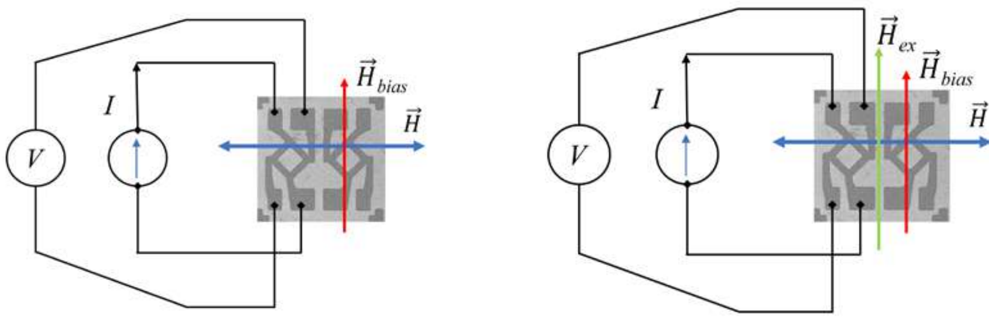

(**a**) (**b**)

Figure 12. Measurement schematic for the AMR bridge sensors: (**a**) For the thermally annealed chip; (**b**) For the thermally and magnetically annealed chip.

Before testing, the chip was contacted with silver plated Cu wires. The wire-bonding was done with Ag paste from Sigma-Aldrich with a 24 h curing time at room temperature. The contacted chip was placed on a connecting PCB board, SO8, MSOP8 which allows placement in a DIP PIN 8 socket with gold plated pins, Figure 13a. Over the chip, the printed U-shaped trace was placed. Thus, a compact structure was obtained, which can be considered a hybrid integrated circuit that can be manipulated and characterized to allow great versatility. A second U-shaped trace was placed beneath the sensor to show the setup implementation for higher currents testing. Since the response of the sensor for low field values is of interest, a small size Helmholtz coil system was placed next to the chip, Figure 13b. The entire setup is placed in a ferromagnetic enclosure for magnetic shielding. The chip was introduced in a DIP PIN 16 socket where necessary connections were made to the connection grid while remaining pins was used to connect the current traces. An additional two ferrite permanent magnets were used to compensate the effect of the exchange bias field, H_{ex} (noted as H_{bias}, Figure 12b).

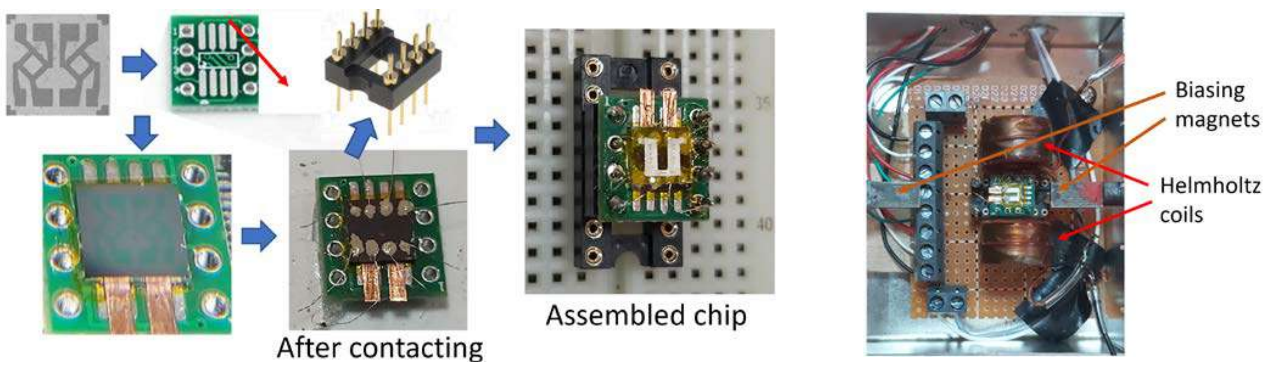

(**a**) (**b**)

Figure 13. Demonstrator setup: (**a**) Steps for assembling the demonstrator chip; (**b**) The sensor mounted in the shielded box, as implemented for characterization and testing.

2.6.2. Characterization of the Demonstrator Chip—After Thermal and Magnetic Annealing

For comparison purposes, the field characteristics for a chip with only thermal treatment applied and for a chip that went through the magnetic annealing process are shown.

For the chip with only the thermal treatment, we can note, Figure 13a, the nonlinear, hysteretic characteristic, typical for AMR structures with no magnetic anisotropy and defined direction for H_{ex}. By applying a prepolarization field, H_{bias}, like in Figure 12a, the nonlinearity of the response characteristic can be reduced, Figure 14b. This field has the same effect such as H_{ex} which can be induced through magnetic annealing; H_{EB} depends on the nature of the FM and AFM layers, the quality of the interface between these layers, and the magnetic annealing process.

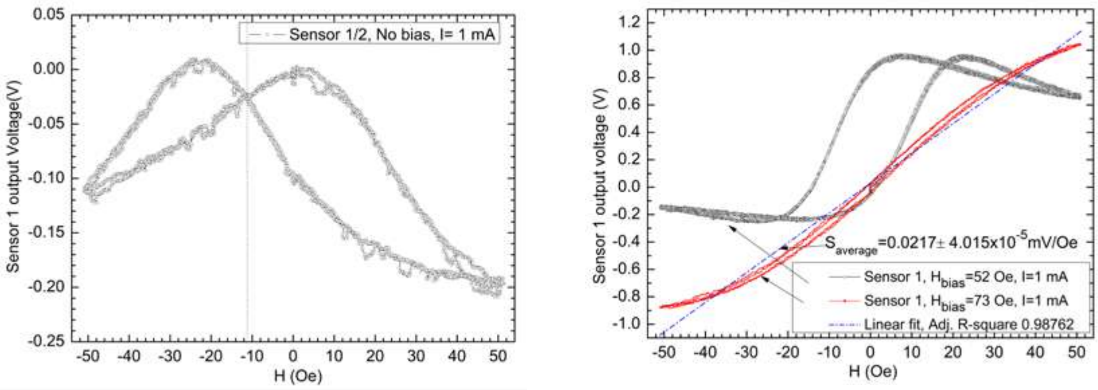

(**a**) (**b**)

Figure 14. Thermally annealed AMR bridge sensor, field characteristics: (**a**) No applied biasing field; (**b**) Field characteristics for different H_{bias} values.

For the chip with both the thermal treatment and magnetic annealing, the results can be seen in Figure 14b for sensor "1": and Figure 15b for sensor "2", connected as shown in Figure 11b. The Helmholtz coils field characteristic (Figure 16) was obtained by placing, instead of the chip in the setup, the Hall probe of the Lakeshore 475 DSP gaussmeter.

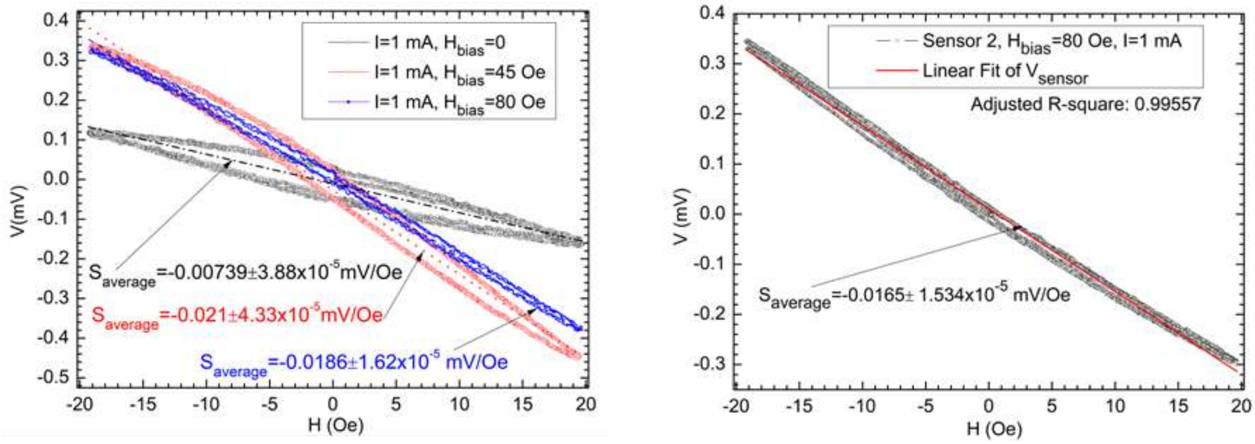

(**a**) (**b**)

Figure 15. Thermally and magnetically cured AMR bridge sensor, field characteristics at different biasing levels (H_{bias} = 0, 45, 80 Oe): (**a**) Field characteristics for sensor 1; (**b**) Field characteristics for sensor 2 H_{bias} = 80 Oe bias level.

By comparing the results from Figures 14a and 15a, for H_{bias} = 0, we can note the emergence of the H_{ex} field in the magnetically cured probe. In order to reduce hysteretic behavior and nonlinearity, two permanent magnets were placed on the wall of the metallic shielded box. Due to the box being ferromagnetic, the field from the magnets closes through it. Figure 15b shows the characteristics $V = f(H)$ for two values of the biasing field H_{bias} = 45, respectively, 80 Oe. Additionally, the positions of the two magnets were modified such that a compromise is obtained between sensitivity and linearity. The H_{bias} = 80 Oe was considered optimal as higher values will reduce sensitivity. Note that the two sensors have a 1 mm gap between them. The light asymmetries between the response of the sensors will be compensated in the differential measurement system. By taking into account the distribution of the current through the U-shaped band and the magnetic field orientation created by the sensors, the output voltage will be of type: $V_{\text{diff}} = V_{\text{sensor1}} - V_{\text{sensor2}}$, as discussed in detail in [14,15].

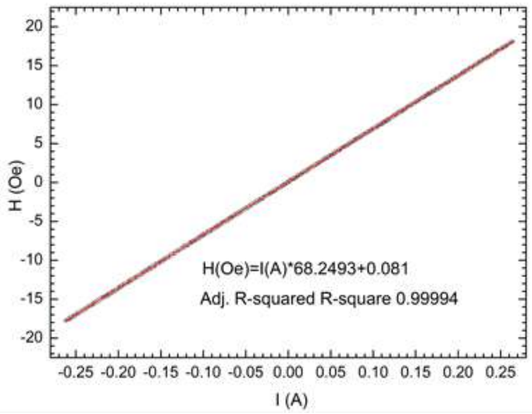

Figure 16. Helmholtz coil supply current-field dependency, H(I) characteristic in the sensor area.

3. Results and Discussion

3.1. Case Study Utilizing Analytical Model and Finite Elements Method Simulations for Currrent Stripes Optimization

For the finite elements method (COMSOL) simulation, a single trace "U-shaped" current trace was modeled (Figure 4b) to simulate the behavior in a double differential configuration. The specific dimensions of the U-shaped trace are chosen based on the ability to integrate highly sensitive and miniature magnetoresistive sensors. The specific parameters utilized for both the COMSOL simulation and the analytical model are shown in Table 1. Note, that in COMSOL, the U-shaped trace was modeled using Ag material properties but with a reduced resistivity of 1.36×10^{-7} Ωm to correspond to the experimental measurement, while the planar coil was modeled with Cu material properties with a resistivity of 1.72×10^{-8} Ωm. Note that the thickness of the U-shaped trace was 35 µm in the simulation for direct comparison with the planar coil thickness.

Table 1. Parameters utilized for the analytical model and COMSOL simulation (U-shaped trace and planar coil).

Symbol	Name	Quantity
D	Trace width	Planar coil with 7 traces: 0.22 mm
		U-shaped trace: 1.2 mm
T_d	Distance between traces	Planar coil with 7 traces: 0.19 mm
		U-shaped trace: N/A
I	Current through trace	0.1 A
h	Distance between sensor and trace	Planar coil with 7 traces: 0.045 [mm] to 3.58 [mm]
		U-shaped trace: 0.045 mm to 2.08 mm
t	Trace thickness	35 µm
m	Number of layers in which t is divided	35 (1 µm each layer)

Table 1. *Cont.*

Symbol	Name	Quantity	
L	Trace length	Planar coil with 7 traces: 42 mm	
		U-shaped trace: 3.2 mm	
Δl	Sensor position on trace length [1]	Planar coil with 7 traces: 21 mm	
		U-shaped trace: 1.6 mm	
V_s	Sensor input voltage	U-shaped trace setup: 4.399 V Planar coil setup: 4.096 V	
S	Sensor sensitivity	U-shaped trace sensor setup:	S_1: 159 μV/(V × A/m) (0.01268 mV/V-Oe)
			S_2: 188.54 μV/(V × A/m) (0.0150034 mV/V-Oe)
			$S_{\text{differential}}$: 347.94 μV/(V × A/m) (0.0277 mV/V-Oe)
		Planar coil sensor setup:	$S_{\text{differential}}$: 32.67 μV/(V × A/m)

[1] The sensor position on the trace length is given by $\frac{\Delta l}{L} \cdot 100$ [%].

Figure 17a shows the magnetic field intensity distribution along the x-axis, H_x obtained from the COMSOL simulation of the U-shaped trace, and Figure 17b of the Multitrace from Figure 4b. In order to better illustrate the field values at specific points, at height h above the sensor, data were extracted for points of interest along transverse (Figures 18a and 19) and longitudinal lines, Figure 18b (note the insets).

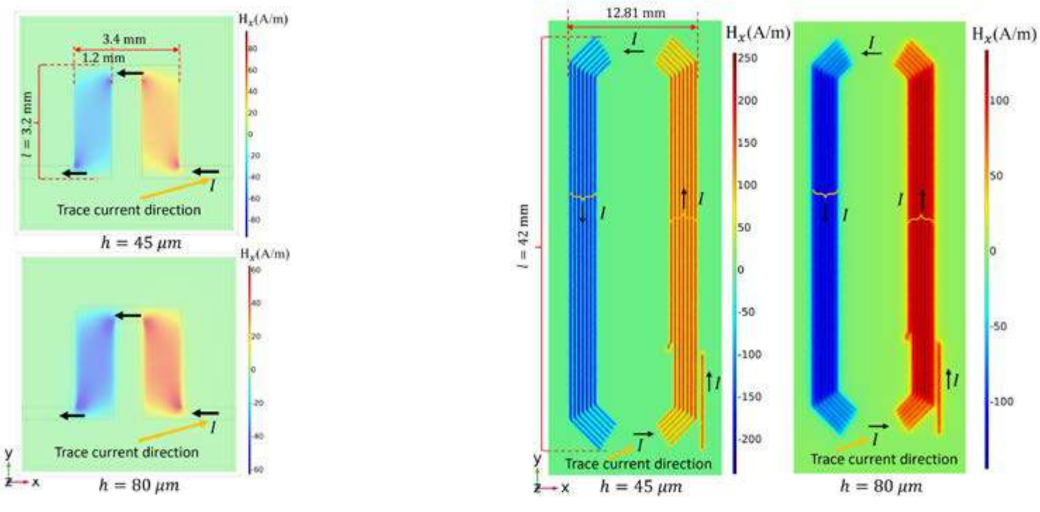

(**a**) (**b**)

Figure 17. Magnetic field distribution on the x-axis for the U-shaped trace and planar coil for a 100 mA current according to COMSOL simulations: (**a**) U-shaped current trace: H_x field distribution at height h = 45 μm (H_{x_sensor} = 40.630 A/m) and h = 80 μm (H_{x_sensor} = 39.056 A/m) from the current trace; (**b**) Multitrace (7 traces): H_x field distribution at height h = 45 μm (H_{x_sensor} = 126.67 A/m) and h = 80 μm (H_{x_sensor} = 121.94 A/m) from the current trace.

From Figures 18 and 19, we can notice that, as expected, the magnetic field intensity is maximum at the center of the trace and there is a minimum magnetic field intensity between the traces. Figure 20a results show that the analytical model converges towards the COMSOL simulation results in the following way (for the U-shaped trace): for higher field values and consequently closer distance from the trace, the cases where a very long conductive trace is assumed (Case I and Case II) are closer to the results obtained from COMSOL while for the finite model (Case III and Case IV), results more closely converge to the results from the simulation at larger distances from the trace. Moreover, for the planar coil configuration, the analytical model provides results similar to the simulation for distances closer to the coil (Case I and Case II) while Case III and IV converge more closely at further distances which is the opposite behavior as in the case of just a single trace. We suspect some of the inaccuracies of the finite length models can be corrected by further geometric corrections. Additionally, more studies can be performed at various distances and trace configurations as the specific magnetic field at further trace distances can also contain y and z components, which can affect the sensor response, thus the analytical method can be improved to also account for those changes. Table 2 shows validation data for the central point (note inset from Figure 18a) between the COMSOL simulation results and the analytical method, after which the analytical method for the seven traces planar coil is compared with experimental results from [15]. The parameters from Table 1 were used for the results shown is Table 2. Note that the field values are calculated for 45 μm (thickness of the Kapton tape on which the trace is printed) and 80 μm distance between the sensor and the trace for the U-shaped trace and 0.8 mm or 0.08 mm for the planar coil as the planar coil experimental setup utilized the AA003-02 encapsulated sensors [31].

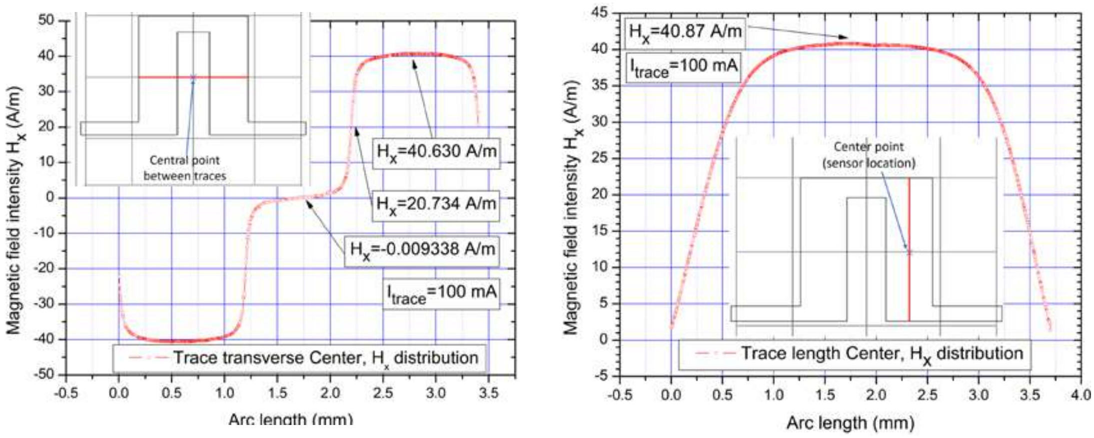

(**a**) (**b**)

Figure 18. Magnetic field intensity on the *x* direction, variation for the U-shaped trace at height h = 45 μm according to results from COMSOL simulation: (**a**) transverse center line (note the inset); (**b**) longitudinal center line (note the inset).

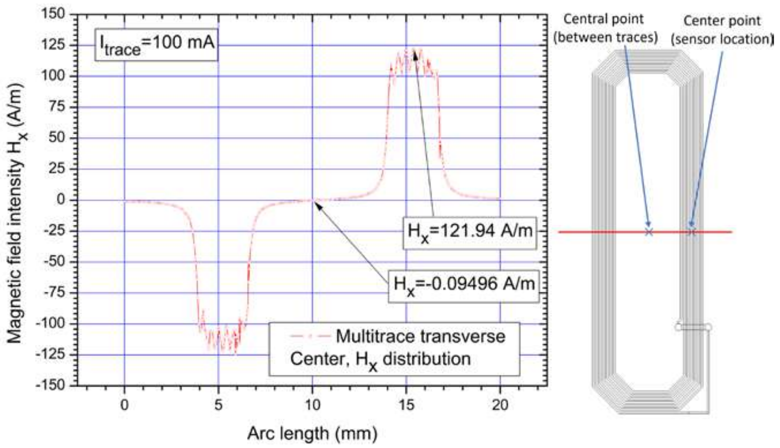

Figure 19. Magnetic field intensity on the *x* direction, variation for the Multitrace planar coil with 7 traces at height h = 80 μm from the trace according to results from COMSOL simulation: transverse center line (note the inset).

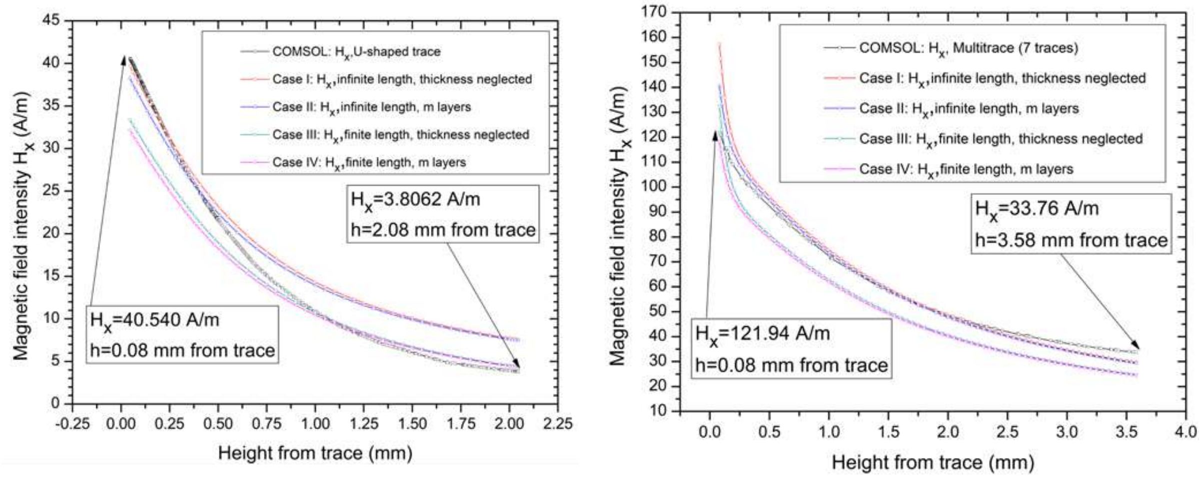

(**a**) (**b**)

Figure 20. (**a**) Magnetic field intensity H_x, variation for different h (0.08 mm to 2.08 mm) for the "U-shaped current trace according to results from COMSOL simulation and from the analytical model; (**b**) Magnetic field intensity H_x, variation for different h (0.08 mm to 3.58 mm) for the "Planar coil with 7 traces" according to results from COMSOL simulation and from the analytical model; The current through the trace was 100 mA.

Table 2. Comparative analysis between COMSOL simulation, analytical model, and experimental data.

Trace Type	Validation Case		h [1] [mm]	H_x [A/m]	V_{out} [2] [mV]	$V_{differential}$ [2] [mV]
U-shaped trace (Figure 4a) I_{trace} = 100 mA V_s = 4.399 V [3]	COMSOL simulations		0.08	39.056	-	-
			0.045	40.630	-	-
	Analytical method	Case I: Infinite length, t neglected	0.08	38.150	S_1: 0.02675 S_2: 0.03164	0.05839
			0.045	39.680	S_1: 0.02782 S_2: 0.03291	0.06073
		Case II: Infinite length, m = 35 layers (1 µm each layer)	0.08	36.7321	S_1: 0.02575 S_2: 0.03046	0.05622
			0.045	38.2408	S_1: 0.02681 S_2: 0.03171	0.05853
		Case III: Finite length, t neglected	0.08	32.0769	S_1: 0.02249 S_2: 0.0266	0.04910
			0.045	33.3818	S_1: 0.02341 S_2: 0.02768	0.05109
		Case IV: Finite length, m = 35 layers (1 µm each layer)	0.08	30.8842	S_1: 0.02165 S_2: 0.02561	0.04727
			0.045	32.1704	S_1: 0.02255 S_2: 0.02668	0.04924
	Experimental results		0.045	31.7423	S_1: 0.0198 S_2: 0.022	0.042
Planar coil with 7 traces (Figure 4b) I_{trace} = 100 mA V_s = 4.096 V [3]	COMSOL simulation		0.8	79.780	-	-
			0.08	121.94	-	-
	Analytical method	Case I: Infinite length, t neglected	0.8	82.5885	11.8702	23.7404
			0.08	157.422	22.6257	45.2514
		Case II: Infinite length, m = 35 layers (1 µm each layer)	0.8	81.2428	11.6768	23.3536
			0.08	140.624	20.2115	40.423
		Case III: Finite length, t neglected	0.8	67.9498	9.9838	19.9676
			0.08	132.465	19.0388	38.0776
		Case IV: Finite length, m = 35 layers (1 µm each layer)	0.8	66.8427	9.821	19.642
			0.08	118.331	17.0073	34.0146
	Experimental results		0.8	-	10.716	21.432

[1] Distance between the sensing element and the current trace. Note that 0.045 mm is the distance between the sensors and the U-shaped trace in the experimental setup and 0.8 mm is the distance between the sensing element and the current trace in the experimental setup for the planar coil with the AA003-02 encapsulated sensors [31]. [2] Output voltage for a single sensor (V_{out}) and for the two sensors in differential configuration ($V_{differential}$). [3] Sensors supply voltage in differential configuration.

Figure 21 shows results obtained with the analytical method for a multi-trace configuration–different numbers of trace configurations (from 1 to 21 traces). We can denote, that the field intensity in the sensor area increases up until 13 traces, after which the field increase is minor. From tests, we determined that this number is consistent no matter the trace configuration of the planar coil (D, T_d) and the current flowing through the trace. We consider that at a higher number of traces, other field parameters on the y and z axis also play a role in the field distribution, thus accuracy of the results can be affected with the current implementation.

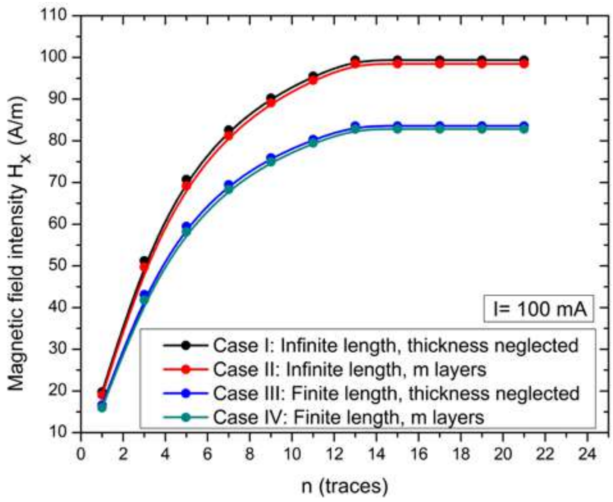

Figure 21. Magnetic field intensity obtained according to the analytical method in the sensor area, dependency on the number of traces in the case of a planar coil (the same parameters as for the 7 traces planar coil were used in this case). Note that m = 35 layers (1 µm each layer).

By analyzing the data from Table 2, for the U-shaped trace, we can note that the estimated value of the surface parallel component of the magnetic field in the sensor area varies between 30 and 39.68 A/m (between 0.4 and 0.48 Oe), depending on the chosen model. Given that the U-shaped trace is a relatively short trace (3.2 mm), with a length/width ratio = 2.66, and h is comparable with the thickness of the layer, we consider that the estimation corresponding to Case IV is closer to reality. With these data, an estimation of the signal level which will be obtained from the sensors can be made for a 100 mA current through the metallic band and considering a 3 mA current through the sensors: $V_{sensor1} = 0.0186 * 3 * 0.4 = 0.022$ mV, respectively, $V_{sensor2} = 0.0165 * 3 * 0.4 = 0.0198$ mV. In differential regime, an output voltage of around 0.042 mV for an $I = 100$ mA current through the current trace, which means 0.084 mV for a signal variation of 200 mA_{pp}. Furthermore, for the planar coil with 7 traces, the experimental value is between those of Case II and Case III of the analytical model. Thus, it can be denoted that for a very long current trace compared with the location and size of the sensor, the length of the trace can be neglected while for shorter traces (like for the U-shaped trace), length correction is necessary for adequate magnetic field estimation.

In terms of electrical parameters from the COMSOL simulation, there is not a very good correlation between the simulation and experimental results: the electrical resistance is close enough to the experimental parameters for the planar coil ($R_{simulated} = 1.422\ \Omega$ and $R_{measured} = 2\ \Omega$) considering not all parameters are taken into account (such as the entire length of the planar coil as implemented in the experimental setup) and the inductance is ~13 times lower ($L_{simulated} = 1.9895\ \mu$H, and $L_{measured} = 26.3\ \mu$H), while for the U-shaped trace, the electrical resistance is ~11 lower ($R_{simulated} = 0.008455\ \Omega$ and $R_{measured} = 0.096\ \Omega$).

3.2. Demonstrator Chip with AMR Bridge (PHR) Sensors

By taking into account the setup (Figure 11), the option to supply the sensors with a constant voltage source was tested but the response proved to be unstable. Given that the two sensors have very similar resistances, the option to supply the sensors with a constant current source was chosen as in Figures 14 and 16. The K2635A current source was set to 6 mA. The current was evenly distributed between the two sensors as confirmed by the offset voltages measured for each sensor, which are very close to those when the sensors were separately supplied at 3 mA. In the conditions described above, the K2635A source determined:

- The voltage at the terminals of the bridge: 4.399 V;
- The total resistance of the bridge: 0.734 kΩ;
- The power dissipated by the bridge: 13.1 mW.

The output voltages from the two sensors were applied to the LabJack EI1040 conditioning system [42], Figure 11, which supplies two voltages at the output, equal with the input voltages but ground referenced. The obtained signal is applied to the K2182A nanovoltmeter. The current through the Ag band is generated by the K6221 source set to generate a sine waveform with 0.04 Hz (thus, quasi-stationary regime). The band current passes through the ground through a R = 6.903 Ω load resistance. The output from this resistor is read by a data acquisition system such that $V_{\text{diff}} = V_{\text{sensor1}} - V_{\text{sensor2}} = \text{f}(I)$ data are acquired. Figure 22 shows the response characteristic of the sensor in differential configuration in function of the current through the printed Ag band. We can note a good linearity of the system with a sensitivity between 4–4.67 $\cdot\ 10^{-4}$ mV/mA. Additionally, from Figure 20b, we can note that the experimental results are in good qualitative agreement with the output signal estimated in Section 3.1.

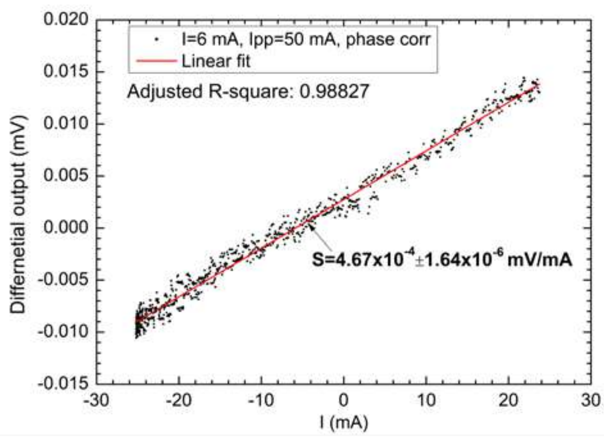

(**a**)

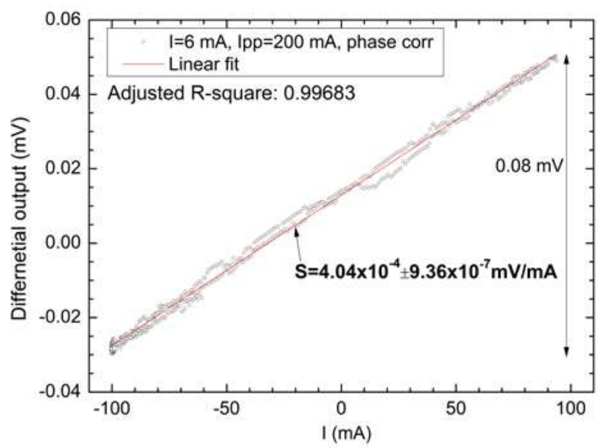

(**b**)

Figure 22. Response characteristics of the differential sensor, depending on the value of the current through the printed Ag trace for: (**a**) Low currents up to 25 mA; (**b**) Currents up to 100 mA.

The demonstrator chip was tested in AC conditions. The total current through the sensors remained 6 mA. The K6221 source was programmed to generate alternative current through the U-shaped trace, Figure 11. The signal was amplified by the SR 560 low noise voltage amplifier from Standford Research; the gain was set to $2\cdot10^4$ and filters were used that cut frequencies higher than 1 kHz and lower than 5 Hz. The signal from the load resistor R = 6.903 Ω is applied on channel 1 and the one corresponding to the current sensor is applied on channel 2 of the HDO 4000 Lecroy Teledyne digital oscilloscope, which allows the analysis of the signal supplied by the chip.

In the Ag band, the current was injected with the following amplitudes: 5, 10, 15, 25, 25, 50, 75 și 100 mA at a 100 Hz frequency. With the HDO 4000 digital oscilloscope, the waveforms of the signal generated by the chip and the effective signal value were measured.

The calibration curve was obtained (Figure 23a). Additionally, the frequency response of the sensor was tested in this case, Figure 23b. Finally, in Figure 24, the waveforms obtained for a sinewave current with the amplitude I_{peak} = 5, 25, and 50 mA at 100 Hz are shown. From Figure 24, it can be noted that for I_{peak} > 15 mA, the waveform of the output voltage shows minimal distortions, following closely the sinusoidal waveform of the current, also confirmed by the Fourier analysis.

The detection limit of the setup is around 2 mA (both DC and AC). The linearity error was determined from Figure 22b by determining a 0.006 mV error for a signal variation of 0.078 mV, which constitutes around a 7.5% linearity error. The sensor was tested between a range of 0–100 mA to avoid any significant thermal effects on the conductive band which can influence the signal stability. Note that the setup aims to serve as a proof of concept and cannot be compared directly with commercial solutions but is now subject to new developments, especially concerning the multilayer structure used to deposit the sensors.

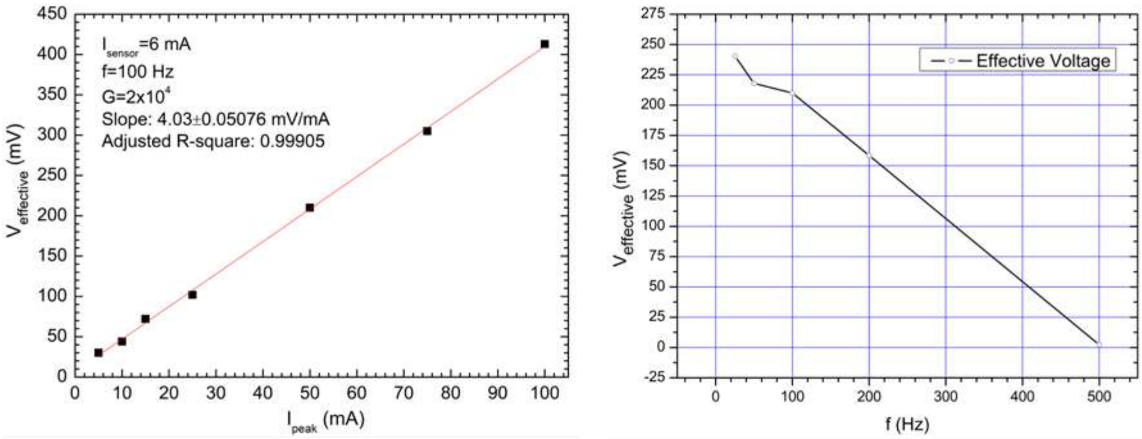

(**a**) (**b**)

Figure 23. (**a**) AC calibration curve in the 0–100 mA range for a 100 Hz sinewave; (**b**) Frequency response of the output voltage for a 50 mA amplitude (peak-to-peak) sinewave.

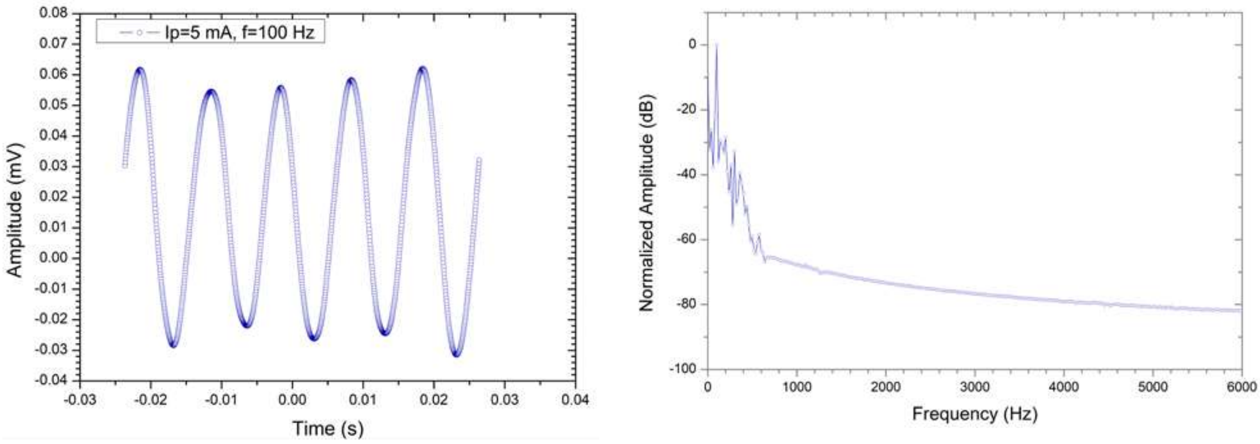

(**a**) (**b**)

Figure 24. *Cont.*

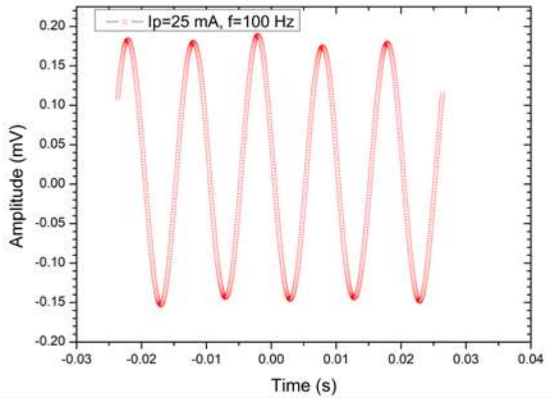

(**c**)

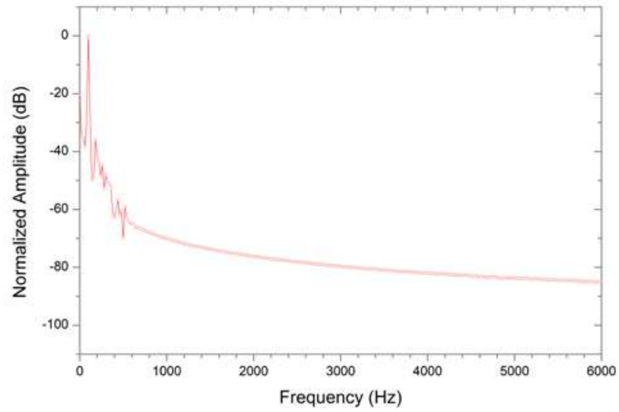

(**d**)

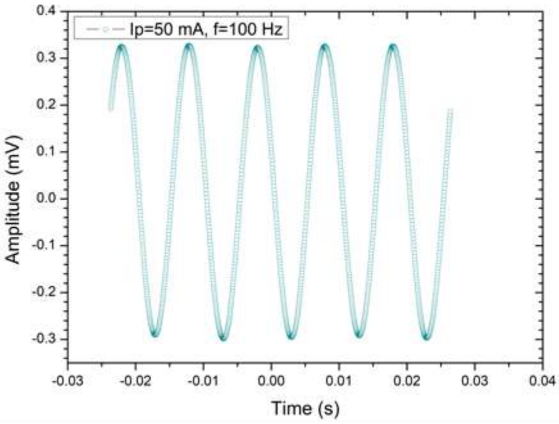

(**e**)

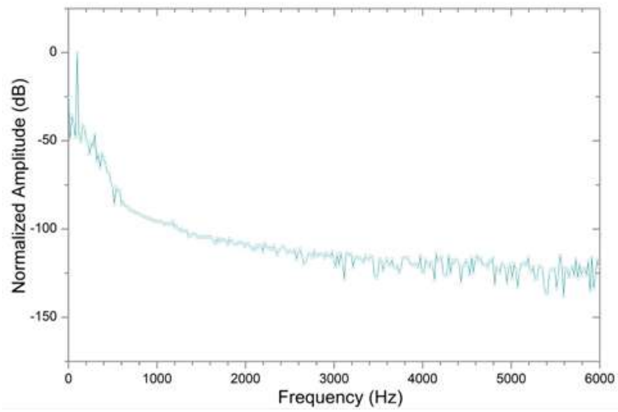

(**f**)

Figure 24. Demonstrator chip: Time-domain characteristics (**a**,**c**,**e**) and Fourier transforms (**b**,**d**,**f**) for the output voltage when a 5 mA, 100 Hz, sinusoidal waveform current is injected into the U-shaped trace, f = 100 Hz, with the amplitude of: (**a**,**b**) 5 mA; (**c**,**d**) 25 mA; (**e**,**f**) 50 mA.

4. Conclusions

The aim of this study is to serve as a basis in designing and optimizing a magnetoresistive bridge sensor for current measurement and low magnetic field sensing. Focus was placed on improving the geometric selectivity of the setup by employing an analytical model which can be used to optimize sensor placement and configuration to achieve the best ratio in terms of sensitivity, complexity, and physical size. The optimization process means: appropriate biasing of the sensor, adequate spacing of components to avoid parasitic magnetic fields, thus greatly improving the sensitivity of the sensor by increasing the useful magnetic field present in the sensor area. This can be applied, for example, for non-destructive testing of electronic circuits when measuring the current in different regions of a printed circuit board.

The magnetic field modeling study of conductive traces for sensing applications has shown that the implemented analytical method can serve as an essential tool for designing high-sensitivity magnetoresistive sensor applications.

The analytical method included four study cases: neglecting the thickness of the trace, dividing the thickness of the trace in several layers, finite or very long conductive trace, and several adjacent traces in the sensor area. It was established that, in terms of accuracy with experimental data, the case of the analytical model when the trace is finite in length and the thickness of the trace is taken into account and divided in an appropriate number of layers, is the most accurate. However, for longer trace lengths, models which neglect the length of the trace can prove more accurate and are closer to the COMSOL FEM model.

A detailed overview of the layout, behavior, and fabrication steps for a demonstrator AMR bridge sensor setup focused on low fields was performed. The behavior of the magnetoresistive structure that comprise the sensor was demonstrated through both equations from a single domain micromagnetic model and simulations using a multi-domain micromagnetic approach. Through micromagnetic simulations, it was proved that only the AMR bridge sensor generates the output depending on the applied field. Other parts of the structure (such as the contacting pads or connecting traces) do not influence the magnetization dynamics of the bridge with the proposed setup.

Very useful data were obtained, such as the optimal number of traces in a planar coil setup to increase the field in the sensor area or the field distribution, depending on the distance from the trace. This method was proven to be accurate when compared with COMSOL simulations and experimental measurements for the implemented AMR bridge sensor and for a giant magnetoresistive (GMR)-based current sensor. Several specific optimizations were performed to the model, which reduce complexity significantly and do not require computationally intensive FEM simulations compared with other solutions shown in the literature [31,33–35], which either lack automation or require computationally intense steps. Further developments of the analytical method can focus on geometric corrections for multi-trace or non-linear trace configurations.

Furthermore, the proposed setup aims to create a highly versatile and sensitive sensor setup by taking advantage of inherent benefits in terms of sensor treatment and design (exchange bias field, geometry) and setup advantages (differential configuration, optimized U-shaped trace design, sensors placed in a magnetically shielded box). Given the relatively simple fabrication steps and procedure for the AMR bridge sensor, the proposed sensor design is for proof-of concept purposes only. This approach has some advantages, such as: simple fabrication, reduced costs, ease of use, and integration possibilities and disadvantages, such as: nonlinearity, increased resistivity, and limited sensitivity compared to commercial solutions [43–45]. Thus, the novelty of our approach is focused on modeling-setup optimizations and single mask chip microfabrication.

Results were shown for both thermally and magnetically annealed sensors illustrated into a complex testing device for DC/AC testing. From the analysis of the experimental results, a detection limit of approximately $\pm$ 2 mA can be estimated. An almost linear characteristic was obtained in the 0–200 Hz range, with an estimated 7.5% linearity error. Results can be significantly improved by utilizing more complex structures based on the GMR or TMR effect, with cross-axis anisotropy, which can lead to significantly enhanced performance of this type of sensor. The findings from this study can also be applied for magnetic nanoparticles detection placed on branches of the PHR sensor instead of the U-shaped stripe. They can be seen as additional sources of the magnetic field which can unbalance the bridge. Future studies can also focus on more complex sensor layouts together with refined analytical modeling in xyz directions and simulations for more complex sensor layouts in multiple axis orientations.

Author Contributions: Conceptualization, C.M., J.N. and M.V.; methodology, C.M, M.V. and M.O.; software, M.O. and M.V.; validation, M.V. and E.H.; formal analysis, M.O.; investigation, C.M. and M.O.; resources, M.V. and J.N.; data curation, E.H.; writing—original draft preparation, C.M.; writing—review and editing, C.M., M.V. and E.H.; visualization, C.M. and M.V.; supervision, M.V. and E.H.; project administration, M.V. and M.V.; funding acquisition, M.V. and J.N. All authors have read and agreed to the published version of the manuscript.

Funding: This research was funded for C.M., M.O., M.V by a grant of the Romanian Ministry of Education and Research, CCCDI-UEFISCDI, project number PN-III-P2-2.1-PED-2019-3514, 510PED/2020, within PNCDI III.

Data Availability Statement: Not applicable.

Conflicts of Interest: The authors declare no conflict of interest.

References

1. Patel, A.; Ferdowsi, M. Current Sensing for Automotive Electronics—A Survey. *IEEE Trans. Veh. Technol.* **2009**, *58*, 4108–4119. [CrossRef]
2. Ripka, P.; Mlejnek, P.; Hejda, P.; Chirtsov, A.; Vyhnánek, J. Rectangular Array Electric Current Transducer with Integrated Fluxgate Sensors. *Sensors* **2019**, *19*, 4964. [CrossRef] [PubMed]
3. Snoeij, M.F.; Schaffer, V.; Udayashankar, S.; Ivanov, M.V. Integrated Fluxgate Magnetometer for Use in Isolated Current Sensing. *IEEE J. Solid-State Circuits* **2016**, *51*, 1684–1694. [CrossRef]
4. Weiss, R.; Mattheis, R.; Reiss, G. Advanced giant magnetoresistance technology for measurement applications. *Meas. Sci. Technol.* **2013**, *24*, 082001. [CrossRef]
5. Nhalil, H.; Givon, T.; Das, P.T.; Hasidim, N.; Mor, V.; Schultz, M.; Grosz, A.; Amrusi, S.; Klein, L. Planar Hall effect magnetometer with 5 pT resolution. *IEEE Sens. Lett.* **2019**, *3*, 1–4. [CrossRef]
6. Hung, T.Q.; Oh, S.; Sinha, B.; Jeong, J.R.; Kim, D.Y.; Kim, C. High field-sensitivity planar Hall sensor based on NiFe/Cu/IrMn trilayer structure. *J. Appl. Phys.* **2010**, *107*, 9. [CrossRef]
7. Granell, P.N.; Wang, G.; Cañon Bermudez, G.S.; Kosub, T.; Golmar, F.; Steren, L.; Makarov, D.; Fassbender, J. Highly compliant planar Hall effect sensor with sub 200 nT sensitivity. npj Flex. *Electron* **2019**, *3*, 10–1038. [CrossRef]
8. Du, W.Y. *Resistive, Capacitive, Inductive and Magnetic Sensor Technologies*; CRC Press: Boca Raton, FL, USA, 2014; pp. 239–253.
9. Poon, T.Y.; Tse, N.C.F.; Lau, R.W.H. Extending the GMR Current Measurement Range with a Counteracting Magnetic Field. *Sensors* **2013**, *13*, 8042–8059. [CrossRef]
10. Soliman, E.; Hofmann, K.; Reeg, H.; Schwickert, M. Noise study of open-loop direct current-current transformer using magnetoresistance sensors. In Proceedings of the 2016 IEEE Sensors Applications Symposium (SAS), Catania, Italy, 20–22 April 2016; IEEE: Piscataway, NJ, USA, 2016; pp. 1–5. [CrossRef]
11. Li, Z.; Dixon, S. A Closed-Loop Operation to Improve GMR Sensor Accuracy. *IEEE Sens. J.* **2016**, *16*, 6003–6007. [CrossRef]
12. Ziegler, S.; Woodward, R.C.; Iu, H.H.C.; Borle, L.J. Current sensing techniques: A review. *IEEE Sens. J.* **2009**, *9*, 354–376. [CrossRef]
13. Vidal, E.G.; Muñoz, D.R.; Arias, S.I.R.; Moreno, J.S.; Cardoso, S.; Ferreira, R.; Freitas, P. Electronic Energy Meter Based on a Tunnel Magnetoresistive Effect (TMR) Current Sensor. *Materials* **2017**, *10*, 1134. [CrossRef]
14. Mușuroi, C.; Oproiu, M.; Volmer, M.; Firastrau, I. High Sensitivity Differential Giant Magnetoresistance (GMR) Based Sensor for Non-Contacting DC/AC Current Measurement. *Sensors* **2020**, *20*, 323. [CrossRef] [PubMed]
15. Mușuroi, C.; Oproiu, M.; Volmer, M.; Neamtu, J.; Avram, M.; Helerea, E. Low Field Optimization of a Non-Contacting High-Sensitivity GMR-Based DC/AC Current Sensor. *Sensors* **2021**, *21*, 2564. [CrossRef] [PubMed]
16. Ripka, P. Contactless measurement of electric current using magnetic sensors. *Tm-Tech. Messen* **2019**, *86*, 586–598. [CrossRef]
17. Volmer, M.; Neamtu, J. Micromagnetic analysis and development of high sensitivity spin-valve magnetic sensors. *J. Phys. Conf. Ser.* **2011**, *268*, 012032. [CrossRef]
18. Sreevidya, P.V.; Khan, J.; Barshilia, H.C.; Ananda, C.M.; Chowdhury, P. Development of two axes magnetometer for navigation applications. *J. Magn. Magn. Mater.* **2018**, *448*, 298–302. [CrossRef]
19. Hauser, H.; Tondra, M. Magnetoresistors. In *Magnetic Sensors and Magnetometers*; Ripka, P., Ed.; Artech house: Norwood, MA, USA, 2001; pp. 136–144.
20. Hansen, M.F.; Rizzi, G. Exchange-biased AMR bridges for magnetic field sensing and biosensing. *IEEE Trans. Magn.* **2016**, *53*, 1–11. [CrossRef]
21. Henriksen, A.D.; Dalslet, B.T.; Skieller, D.H.; Lee, K.H.; Okkels, F.; Hansen, M.F. Planar Hall effect bridge magnetic field sensors. *Appl. Phys. Lett.* **2010**, *97*, 013507. [CrossRef]
22. Elzwawy, A.; Pişkin, H.; Akdoğan, N.; Volmer, M.; Reiss, G.; Marnitz, L.; Schmalhorst, J.M.; Moskaltsova, A.; Gurel, O. Current trends in planar Hall effect sensors: Evolution, optimization, and applications. *J. Phys. D Appl. Phys.* **2021**, *54*, 353002. [CrossRef]
23. McGuire, T.; Potter, R.L. Anisotropic magnetoresistance in ferromagnetic 3d alloys. *IEEE Trans. Magn.* **1975**, *11*, 1018–1038. [CrossRef]
24. Lin, G.; Makarov, D.; Schmidt, O.G. Magnetic sensing platform technologies for biomedical applications. *Lab A Chip* **2017**, *17*, 1884–1912. [CrossRef] [PubMed]
25. West, F.G. Rotating-field technique for galvanomagnetic measurements. *J. Appl. Phys.* **1963**, *34*, 1171–1173. [CrossRef]
26. Tumanski, S. *Thin film Magnetoresistance Sensors*; CRC Press: Boca Raton, FL, USA, 2001.
27. Jogschies, L.; Klaas, D.; Kruppe, R.; Rittinger, J.; Taptimthong, P.; Wienecke, A.; Wurz, M.C.; Rissing, L. Recent developments of magnetoresistive sensors for industrial applications. *Sensors* **2015**, *15*, 28665–28689. [CrossRef] [PubMed]
28. Hauser, H.; Stangl, G.; Fallmann, W.; Chabicovsky, R.; Riedling, K. Magnetoresistive Sensors, Preparation, Properties, and Applications of Thin Ferromagnetic Films, June 2000. Available online: http://educypedia.karadimov.info/library/Hauser.pdf (accessed on 23 November 2022).
29. Jander, A.; Smith, C.; Schneider, R. Magnetoresistive sensors for nondestructive evaluation. *Adv. Sens. Technol. Nondestruct. Eval. Struct. Health Monit.* **2005**, *5770*, 1–13. [CrossRef]
30. NVE Sensors Catalogue. Available online: https://www.nve.com/Downloads/catalog.pdf (accessed on 23 November 2022).
31. Misakian, M. Equations for the magnetic field produced by one or more rectangular loops of wire in the same plane. *J. Res. Natl. Inst. Stand. Technol.* **2000**, *105*, 557. [CrossRef]

32. Nicolaide, A. *Electromagnetics. General Theory of the Electromagnetic Field. Classical and Relativistic Approaches*, 3rd ed.; Transilvania University Press: Brașov, Romania, 2012; pp. 170–173.
33. Minnaert, B.; Stevens, N. Evaluation of The Vertical Magnetic Field Generated By A Spiral Planar Coil. In Proceedings of the Nordic Circuits and Systems Conference (NORCAS), Oslo, Norway, 26−28 October 2015; NORCHIP & International Sympo-sium on System-on-Chip (SoC). pp. 1–3. [CrossRef]
34. Hrabovský, P.; Kravets, O. The Design and Simulation of Spiral Planar Coil in COMSOL Multiphysics. In *IEEE International Conference on Modern Electrical and Energy Systems (MEES)*; IEEE: Piscataway, NJ, USA, 2019; pp. 374–377. [CrossRef]
35. Gupta, M.; Agarwal, P. To model magnetic field of RF planar coil for portable NMR applications. In Proceedings of the International Conference on Inventive Computing and Informatics (ICICI), Coimbatore, India, 23−24 November 2017; pp. 490–494. [CrossRef]
36. NVE ALTxxx-10 TMR Catalogue. Available online: https://www.nve.com/Downloads/ALTxxx-10.pdf (accessed on 23 November 2022).
37. Voltera V-One Printer Overview. Available online: https://f.hubspotusercontent30.net/hubfs/5264434/Sales-Docs/Product-Development.pdf (accessed on 23 November 2022).
38. Leliaert, J.; Mulkers, J. Tomorrow's micromagnetic simulations. *J. Appl. Phys.* **2019**, *125*, 180901. [CrossRef]
39. Yin, L.F.; Wei, D.H.; Lei, N.; Zhou, L.H.; Tian, C.S.; Dong, G.S.; Jin, X.F.; Guo, L.P.; Jia, Q.J.; Wu, R.Q. Magnetocrystalline anisotropy in permalloy revisited. *Phys. Rev. Lett.* **2006**, *97*, 067203. [CrossRef]
40. Roshchupkina, O.D.; Strache, T.; McCord, J.; Mücklich, A.; Bähtz, C.; Grenzer, J. Structural modifications of thin magnetic Permalloy films induced by ion implantation and thermal annealing: A comparison. *Acta Mater.* **2014**, *74*, 278–284. [CrossRef]
41. Voltera Flexible Conductor Ink Datasheet. Available online: https://assets.ctfassets.net/e6vf9wdhbae5/2z1lTqP8uRIxYLRCSZ9hCQ/839deb49846f3e75878cea856297f7eb/Voltera-Flexible-Conductive-Ink.pdf (accessed on 23 November 2022).
42. LabJack EI1040 Instrumentation Amplifier. Available online: https://labjack.com/products/ei1040-dual-instrumentation-amplifier (accessed on 23 November 2022).
43. Mlejnek, P.; Vopalensky, M.; Ripka, P. AMR current measurement device. *Sens. Actuators A* **2008**, *141*, 649–653. [CrossRef]
44. Aceinna Current Sensors Catalogue. Available online: https://www.aceinna.com/current-sensors (accessed on 23 November 2022).
45. Sensitec Current Sensors Catalogue. Available online: https://www.sensitec.com/products-solutions/current-measurement/cfs1000 (accessed on 23 November 2022).

IOP Publishing Journal of Physics D: Applied Physics
J. Phys. D: Appl. Phys. 54 (2021) 353002 (29pp) https://doi.org/10.1088/1361-6463/abfbfb

Topical Review

Current trends in planar Hall effect sensors: evolution, optimization, and applications

Amir Elzwawy[1,*], **Hasan Pişkin**[2], **Numan Akdoğan**[3], **Marius Volmer**[4], **Günter Reiss**[5], **Luca Marnitz**[5], **Anastasiia Moskaltsova**[5], **Ogan Gurel**[6,7] **and Jan-Michael Schmalhorst**[5]

[1] Ceramics Department, Inorganic Chemistry Industries and Mineral Resources Division, National Research Centre, El-Bohouth Str., Cairo 12622, Egypt
[2] Department of Physics, Boğaziçi University, Istanbul, 34342, Turkey
[3] Department of Physics, Gebze Technical University, Gebze, Kocaeli 41400, Turkey
[4] Electrical Engineering and Applied Physics Department, Transilvania University of Brasov, Brasov 500036, Romania
[5] Thin Films & Physics of Nanostructures, Center for Spinelectronic Materials and Devices, Department of Physics, Bielefeld University, Bielefeld 33615, Germany
[6] College of Transdisciplinary Studies, DGIST, Daegu 42988, Republic of Korea
[7] Flite Material Sciences, Montreal, Canada

E-mail: elzwawy1@gmail.com and aa.elzwawy@nrc.sci.eg

Received 18 February 2021, revised 15 April 2021
Accepted for publication 27 April 2021
Published 30 June 2021

Abstract
The advantages of planar Hall effect (PHE) sensors—their thermal stability, very low detection limits, and high sensitivities—have supported a wide range of advanced applications such as nano-Tesla (nT) magnetometers, current sensing, or low magnetic moment detection in lab-on-a-chip devices. In this review we outline the background and implications of these PHE sensors, starting from fundamental physics through their technological evolution over the past few decades. Key parameters affecting the performance of these sensors, including noise from different sources, thermal stability, and magnetoresistance magnitudes are discussed. The progression of sensor geometries and junctions from disk, cross-to-bridge, ring, and ellipse configuration is also reviewed. The logical sequence of these structures from single magnetoresistive layers to bi-, tri-layers, and spin-valves is also covered. Research contributions to the development of these sensors are highlighted with a focus on microfluidics and flexible sensorics. This review serves as a comprehensive resource for scientists who wish to use PHE for fundamental research or to develop new applications and devices. The conclusions from this report will benefit the development, production, and performance evaluation of PHE-based devices and microfluidics, as well as set the stage for future advances.

Keywords: planar Hall effect, sensors, permalloy, magnetoresistance, thin films, NiFe/IrMn

(Some figures may appear in colour only in the online journal)

* Author to whom any correspondence should be addressed.

1. Introduction

Technologies that improve life are always in increasing demand. Spintronics—also known as spin electronics—which combines the charge and spin characteristics of electrons, offers a variety of novel and powerful device possibilities to provide such solutions. These devices find use in several key applications such as magnetometers, magnetic compasses, magnetic memories, or as sensing elements in conjunction with lab-on-a-chip (LOC) devices and point-of-care systems. Different types of sensors may be employed in these devices, as with electrochemical sensors [1–9], pressure sensors [10–13], temperature sensors [14, 15], gas sensors [16, 17], and humidity sensors [18–20] These familiar classes of sensors directly detect changes in the surrounding environment, whereas magnetic sensors do not directly measure such properties. Instead, these magnetic sensors measure disturbances in the applied magnetic field which can be converted into an electrical output voltage [21–23]. Basically, the information attained from the magnetic sensors (variations and fluctuations of the field) can be exploited to track the directions, locations, angles and rotations of items, the existence of an electric current, in nondestructive testing, and so on [24]. The working principle, then, for magnetic sensors does not involve direct, physical contact. This property, along with the fact that magnetic sensing has reduced noise in biological media, positions magnetic sensors ideally in the area of biodetection [25–27]. In this review we focus on magnetic sensors based on ferromagnetic (FM) materials, not semiconducting material-based sensors. The key advantages for these sensors are improved response time, field linearity, reliability, reproducibility, sensitivity, selectivity, stability, ease of fabrication, and lower detection limits [28–37].

The market for magnetic field sensors is growing rapidly, estimated at ~$20B (USD) in 2019 [38, 39]. Various physical phenomena are employed to develop magnetic field sensors, which include search-coil, micro (fluxgate) sensors [40], magnetoresistive, and Hall effect sensors, as based on galvanomagnetic effects in semiconductors and magnetic thin films [41]. Despite their high sensitivity, search-coil and fluxgate magnetometers require complex electronic circuitry to deliver a useful voltage and are not compatible with integrated circuit (IC) technology, which, in turn, allows miniaturization, portability, and low power consumption. On the other hand, magnetoresistance (MR) and Hall effect sensors offer many benefits because they both compatible with and readily interfaced with IC technology, and thus can be integrated on the same chip in both analog and digital electronic circuits. With respect to sensor performance, their application areas are well established and distinct. MR sensors made from magnetic layers are considered to be highly sensitive and ideal for small magnetic fields between 10^{-9} T to 10^{-2} T, whereas Hall sensors, constructed from semiconductors, are less sensitive and more optimal for magnetic fields greater than 10^{-6} T [42]. In contrast, however, with MR sensors, semiconductor-based Hall sensors show no saturation effects at high magnetic fields. It should be noted that, for MR-based sensors, these limits are strongly influenced by the magnetic properties of the materials and the layout of the microfabricated sensors. There is an increasing number of applications that require magnetic field sensors with improved performances like high sensitivity, low hysteretic behavior, low noise, and low thermal drift. Also, some special applications require magnetic sensors with tunable properties to fine adapt their field characteristics to the specific use. The planar Hall sensors based on magnetoresistance has diverse applications. These include biosensing [43], flux leakage inspection [44], current sensing [45], and others [46]. Furthermore, from the field of wearable sensors for remote health monitoring, which has developed significantly in recent years, has given rise to many studies on the magnetic and electrical properties of structures deposited over flexible substrates [47–52].

The evolution of the number of publications and their total citations within 2002–2020 for the keyword, planar Hall effect (PHE) is screened in figure 1 based on the Web of Science core collection. However, in many other research papers, the PHE is used both as a tool for fundamental research or for sensing applications, so, the total number of published papers and citations regarding with this subject can be much higher.

In this review, we review the fundamentals of PHE sensors with respect to their origin, evolution, and configuration. From this, we proceed to FM and FM/antiferromagnetic (FM/AF) exchange-biased multilayer structures, discussing the optimizations performed for key parameters such as junction configuration, thermal stability, and signal-to-noise ratio (S/N). Finally, we highlight the major areas of application such as bio-detection, low magnetic moment sensing, and inspection of flux leakage for pipelines. We then offer perspectives on the future outlook and directions for the field.

In what follows we give a brief description of the most important MR effects that are used for fundamental research, i.e. investigation of magnetization processes and other related phenomena in nanostructured thin films, and to build magnetic sensors for applications such as high sensitivity magnetometers [47, 53], rotation encoders and micro compasses [54–58], current sensors [45, 59, 60], and magnetic nanoparticles (MNPs) detection for biosensing [61–64] in LOC devices.

2. Fundamentals of MR effects

The MR effect refers to a change in the electrical resistivity of a material depending on the externally applied magnetic field. For non-magnetic materials, the MR effect can be expressed by [29]:

$$\mathrm{MR}\,(H)\,\% = \frac{R\,(H) - R\,(H=0)}{R\,(H=0)} \times 100\% \tag{1}$$

where $R(H)$ and $R(H=0)$ being the resistance of the material for an applied field, (H), and $H=0$, respectively. In non-magnetic metals, for magnetic fields up to 1 T, the MR ratio is larger than 0 but is less than 1% and the effect is due to Lorentz forces that act on moving electrons.

For magnetic materials, $H=0$ describes the remanent state which can depend on the magnetization history. For this

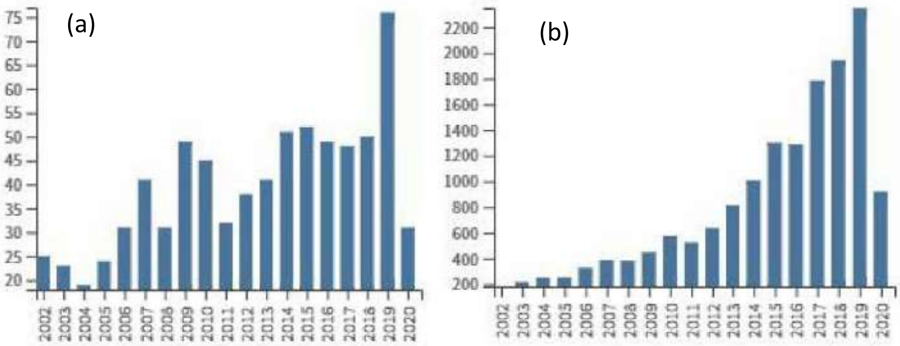

Results,	958 publications
Total no. of	citations, 16753
Average citation	per item 17.49

Figure 1. The evolution of number of papers dealing with planar Hall effect since 2002 according to Web of Science core collection (accessed 6-5-2020) (a) number of publications using the keyword 'planar Hall effect', (b) the total number of citations within the same years range.

reason, a more reliable state to describe the reference resistance is at saturation, H_{sat}, such that, for FM materials, a more appropriate description of the MR field dependence is [65, 66]:

$$\mathrm{MR}\,(H) = \left(\frac{R\,(H) - R\,(H_{sat})}{R\,(H_{sat})}\right). \tag{2}$$

Note that the applications enumerated above are mostly based on Giant MR (GMR), Tunneling MR (TMR), Anisotropic MR effect (AMR), and PHE effects which will be briefly presented in what follows. Special attention will be paid to AMR and PHE.

2.1. GMR and TMR effects

The GMR effect was discovered in 1988 by Albert Fert [67], and Peter Grünberg [68] in exchange-coupled magnetic multilayered structures of the type $(Fe/Cr)_n$. Briefly, the resistance of a multilayer stack with an antiparallel magnetization configuration is larger in size as compared to that of a parallel magnetization configuration as shown in figure 2. The physical mechanism of the GMR effect is the spin-dependent scattering at the interfaces and in FM layers for spin-up (spin parallel to layer magnetization) and spin-down (spin antiparallel to layer magnetization) electrons [69, 70]. The exchange coupling between the FM layers (like Co, Fe, NiFe, etc) has an oscillatory behavior and for some specific values of the non-magnetic (NM) interlayer thickness is AF [71, 72]. Therefore, when aligning the magnetization directions of the FM layers from the initial antiparallel state, at zero field, to a parallel configuration by applying an external magnetic field, the electrical resistance of the layer stack decreases.

Figure 2(a) illustrates a simple GMR structure of the type FM1/NM/FM2 for $H = -H_{sat}$ and $H = 0$ and $H = H_{sat}$ t respectively for which the magnetic moments in both layers are parallel. The field behavior of the MR effect is quadratic, very similar to the AMR effect but the amplitude of the GMR effect is larger, up to 15% at room temperature. Figure 2(b)

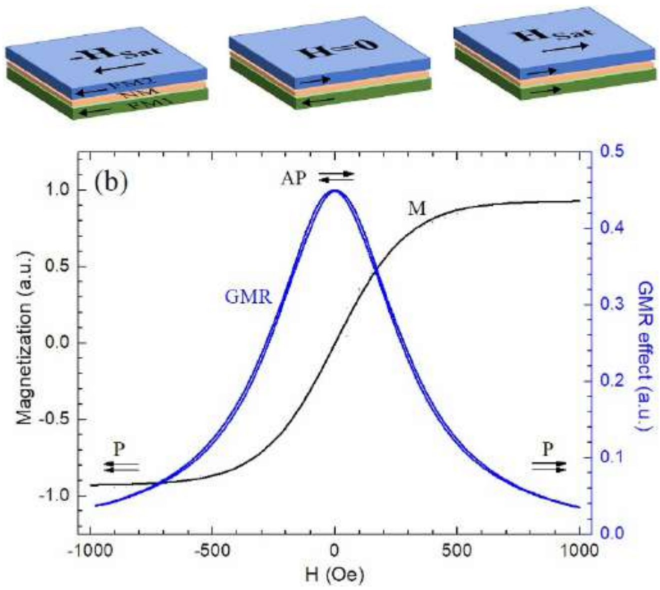

Figure 2. (a) Simple GMR 3-layer structure for three distinct states. i.e. for $H{=}-H_{sat}$, $H{=}$o, and and $H{=}H_{sat}$ respectively, and (b) typical field dependence of the structure magnetization and GMR by micromagnetic simulations.

shows the typical field behavior of the structure magnetization and the GMR effect obtained by micromagnetic simulations. Details regarding the parameters used for simulations are presented in [60].

A more convenient way to build a GMR sensor is to pin one of the FM layers with an adjacent AF layer through a unidirectional interface coupling effect named exchange bias [73, 74] while the other FM layer's magnetization remains free to be switched by an externally applied magnetic field [39, 61, 75]. This is an exchange-biased spin-valve structure of the type FM/NM/FM/AF.

TMR is found in magnetic tunnel junctions (MTJs) with a structure very similar to that of spin valves where the conducting NM layer is replaced by a thin layer (around 1 nm) of insulating oxide like Al_2O_3 or MgO [39, 76, 77]. The tunneling current through the insulating barrier of MTJs depends on the relative orientation of the magnetizations of the FM layers, which gives rise to a TMR effect. The field dependence of the TMR effect is similar to that of the GMR effect but with a MR ratio up to 200% at room temperature [61, 77]. MTJ structures are used as magnetic sensors, spin tunnel read heads, and biomedical applications for detection of magnetic markers [78]. Now, MTJs are used as building blocks for magnetoresistive random access memories because of their small spatial footprint, which allows nanofabrication of high-density non-volatile memory cells [79].

Although TMR sensors can provide much larger signals when compared to GMR devices, the microfabrication processes of the TMR sensors are more complicated and expensive due to the need for 'an upper contact.' Therefore, a proper choice of device type is necessary for certain applications, as with, for example biosensing applications [77, 79]. For biosensing applications this means a larger distance between the magnetic nanoparticles (MNPs) and the free layer in the sensor which can lower the effective detection sensitivity of the field created by the MNPs. Moreover, the effective surface of the TMR sensors that can be exposed to MNPs is much lower than for GMR and PHE sensors and this affects the dynamic range in terms of the number of magnetic particles detected [80]. Finally, the resistance of TMR sensors is usually much larger as compared with GMR devices, and the corresponding noise is increased subsequently. For the detection of very low magnetic moments, elimination of noise requires an extended measuring period.

2.2. AMR and PHE effects

The AMR effect was discovered by William Thomson (Lord Kelvin) in 1856 and appears in FM bulk materials or thin films such as Ni, Co, Fe and their alloys [81, 82]. The AMR effect comes from the dependence of the electrical resistivity (hence the resistance as a measurable value) of a material on the angle between the direction of electric current and the direction of magnetization inside the material. In short, the physical origin of AMR can be attributed to the anisotropic s–d scattering of electrons due to the spin–orbit coupling on 3d orbitals of FM materials [56, 61, 83–85] The net effect (in most magnetic materials) is that the electrical resistance has a maximum value when the direction of current is parallel to the magnetization and it has a minimum value when the direction of the current is perpendicular to the magnetization.

Thus, the AMR ratio that can be achieved in a magnetic material is expressed by [64, 86]

$$\frac{\Delta\rho}{\rho_{\perp}} = \left(\frac{\rho_{||} - \rho_{\perp}}{\rho_{\perp}}\right) \times 100\% \qquad (3)$$

where both resistivities $\rho_{||}$ and $\rho_{\perp}$ are expressed at saturation field, parallel and perpendicular to the current direction respectively.

AMR devices, as single resistors, are more susceptible to thermal noise and thermal drift around zero fields [57]. However, as we can see from figure 3(a), when M rotates around $\pm 45^{\circ}$ with the current direction, the AMR effect has linear variation. This has inspired the barber pole (BP) biasing where the current is forced to flow in a direction that makes an angle of $\pm 45^{\circ}$ with M [58]. Now, when H is applied over y-axis, the AMR effect will show a linear field dependence. The thin film elements are usually connected in a Wheatstone bridge configuration in order to compensate temperature drift and to double the signal output. This means that the AMR elements on the opposite arms are biased in the same way (at 45° and −45° respectively) creating, in this way, a differential sensor. Ideally, the bridge resistances have the same value forming diagonal pairs of identical elements that react oppositely to one another to an external magnetic field. We must remark that this setup is equivalent, from an electric point of view, with a PHE structure [87, 88]. Several suppliers offer a large variety of commercially available devices based on AMR effect [54, 59, 89] and sensitivities of about 0.35 (mV/V) Oe^{-1} have been reported for Wheatstone bridges with BP-biased AMR sensors [58].

For most bulk magnetic materials this ratio is not larger than 5% whereas for typical FM NiFe films, the AMR value is in the order of 2%–2.2% in fields of a few Oe [58]. A widely used material is the $Ni_{80}Fe_{20}$ (Permalloy) the magnetostriction and magnetocrystalline anisotropy both pass through zero near this composition [90].

To quantify the AMR and PHE, we may consider the measurement configuration given in figure 3(a). Here a thin film of FM material is presented. For functional devices, an easy axis of magnetization is defined by an anisotropy field (H_K) through the shape anisotropy ($l > w$) and the intrinsic anisotropy field due to the crystalline structure of the magnetic layer and microfabrication process.

The PHE output voltage is delivered as [91, 92]:

$$V_{PHE} = I\frac{(\rho_{||} - \rho_{\perp})}{t}\,\sin\theta\cos\theta \qquad (4)$$

where t is the thickness of the FM layer, and I is the constant current applied along the x-axis of the FM layer.

It can be mentioned here that the magnetization rotation can be due to a rotating magnetic field or to a magnetic field, (H), which is applied along y-axis. The equilibrium state of magnetization angle (θ) in the sensing layer, can be calculated by minimizing the system's free energy density (E_M) expressed by [93–96]

$$E_M = K_u\sin^2\theta - M_S H\cos(\alpha - \theta) - M_S H_{ex}\cos(\beta - \theta) \qquad (5)$$

where K_u is the effective anisotropy constant, M_S is the saturation magnetization and H_{ex} is the exchange biasing field, which acts like an external biasing (unidirectional) field applied to the sensing layer. α is the angle between the external field, (H), and the easy axis (anisotropy axis). β is the angle between the direction of the exchange bias field and the easy axis of the magnetic layer. Usually, in PHE sensors β is adjusted as 0º. Thus, under the zero magnetic field ($H = 0$), the magnetization can be aligned along the current direction (along $+x$-axis), figure 3(a). For this device configuration, because $\theta = 0$, theoretically, the V_{PHE} given in equation (4) provides

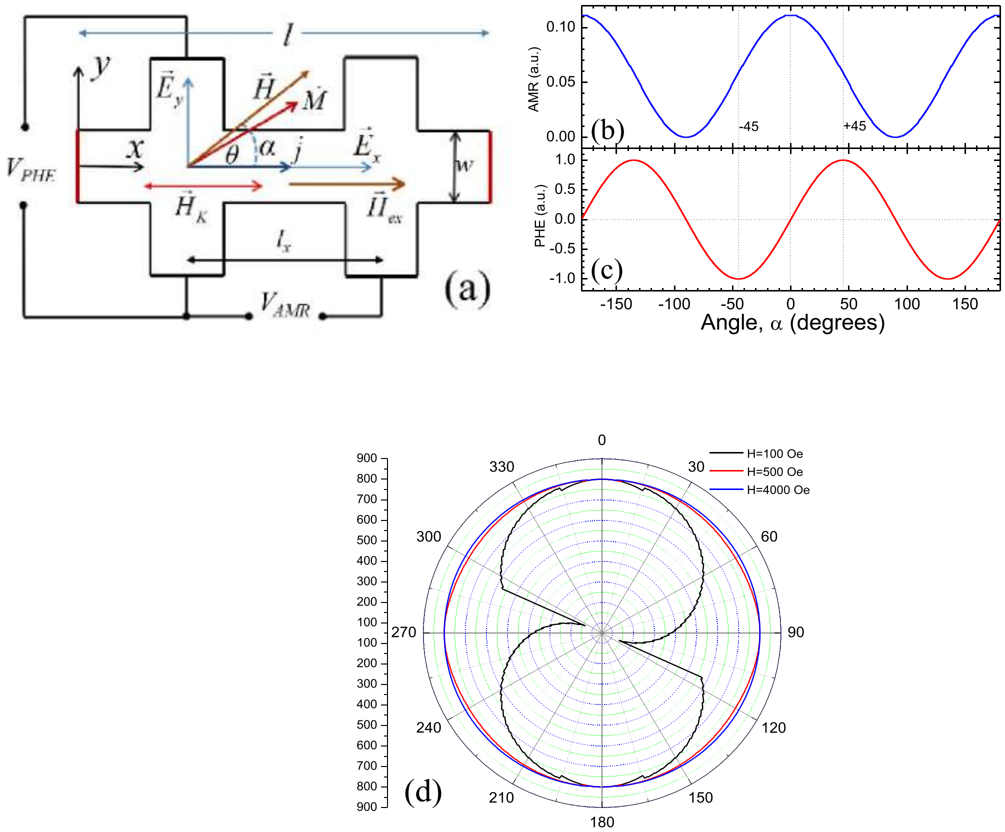

Figure 3. (a) Schematic representation of a Permalloy thin film through which is flowing a current along x-axis; M is the magnetization which makes an angle θ with the current direction due to the applied field, H. A uniaxial magnetic anisotropy, defined by H_K may be present; (b), (c) the angular dependencies of the AMR and PHE respectively; (d) the angular dependence of magnetization along the rotating field $H = 100$, 500, and 4000 Oe.

zero voltage, therefore the PHE sensors are providing zero offset voltage. In addition, in many cases, the effect of the anisotropy can be described by an anisotropy field of (H_K) rather by the anisotropy constant of (K_u), (where $H_K = 2K_u/M_S$) [97].

The position at the equilibrium of magnetization, and hence the angle θ, is calculated from the energy minimum condition, $dE_M/d\theta = 0$, using a semi-analytical Stoner–Wohlfarth (SW) model implemented in SimulMag [55, 98].

Figures 3(b) and (c) show the dependencies of the AMR effect and PHE, respectively, on the angle α between the rotating field H and j. These plots, which have a qualitative character, were obtained by considering a single domain of Permalloy ($Ni_{80}Fe_{20}$), with $l \times w \times t = 1000 \times 500 \times 10$ nm^3 (t being the film thickness), $M_S = 800$ emu cm^{-3} and $H_K = 90$ Oe. A rotating field $H = 4000$ Oe was employed in these simulations. The position at the equilibrium of magnetization, and hence the angle θ between M and j, was obtained by minimizing the system's free energy using a semi-analytical SW model implemented in SimulMag [55, 98]. Figure 3(d) shows that if H is large enough, i.e. larger than the effective anisotropy field, M follows accurately the field orientation, i.e. $\alpha = \theta$, and this suggests the application of AMR and PHE for rotation sensors.

As mentioned above, the magnetization can rotate, also, because of a field H applied over y-axis, i.e. $\alpha = 90°$ in figure 3(a). This is the typical setup used for field sensing we present, in figure 4(a) and in figure 4(b) the field dependencies of the AMR effect and PHE simulated in the single domain approach. Now, comparing the results from figures 3 and 4 we can draw some conclusions: (a) the sensitivity of the AMR effect around zero-field (which can mean also, $\theta = 0$) is very small and is 0 for $H = 0$ whereas the response of the PHE is linear around zero-field, with a constant sensitivity; (b) the AMR signal is unipolar, with a quadratic field dependence, whereas the PHE signal is bipolar both for angular and field dependencies and (c) by applying a biasing field, H_{ex}, along the easy axis we can fine tune the AMR and PHE field response [56, 62]. The peak field-H_P (for which $\theta = 45°$) expresses the maximum value of the applied field for which the sensor can deliver a useful signal, figure 4(b). This field can be expressed as [93]:

$$H_p = H_{ex} + H_K/\sqrt{2}. \tag{6}$$

With H_K, the effective anisotropy field which includes uniaxial anisotropy, the shape anisotropy, etc; H_{ex} is the exchange biasing field present in exchange biased and spin-valve structures or can be an external field, H_{ex}, applied along the current direction, figure 3(a) [62].

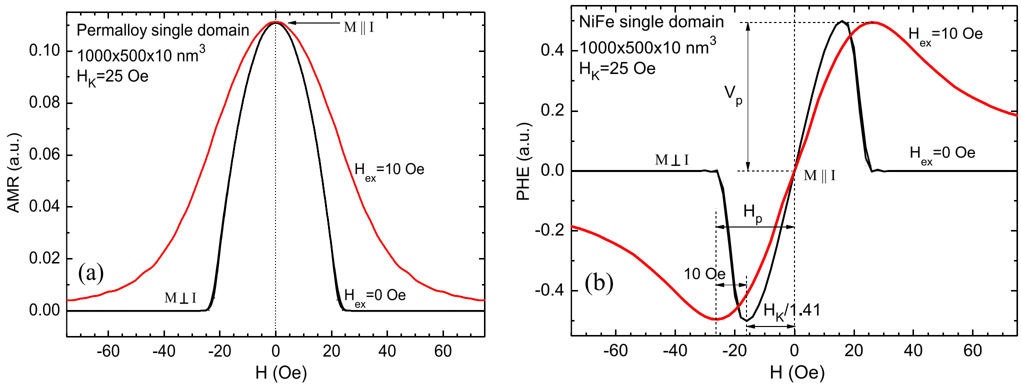

Figure 4. Field dependencies for (a) AMR effect and (b) PHE; H is directed along y-axis. The simulations were done, using the parameters presented above, for $H_{ex} = 0$ and $H_{ex} = 10$ Oe.

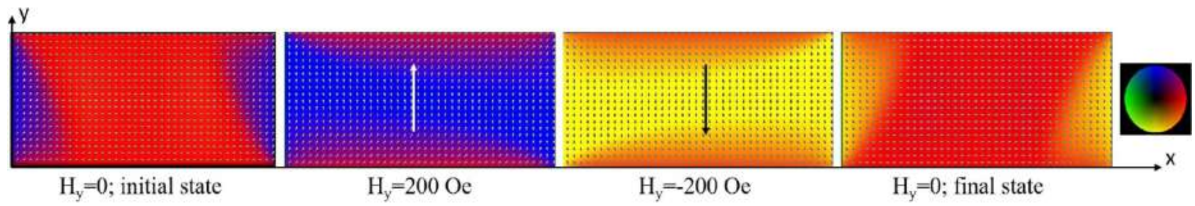

Figure 5. Illustration of magnetic moments orientation in a thin film of Permalloy $1000 \times 500 \times 10$ nm^3. The used parameters are: cell dimension 5 nm, $M_S = 710$ emu cm^{-3}, exchange constant $A = 1.3 \times 10^{-11}$ J m^{-1}, and the anisotropy constant $K_u = 500$ J m^{-3} along the x-axis; $T_{abs} = 0$ K. The color legend illustrates the magnetic moments orientation.

These data show that PHE signals can be used to build low magnetic field sensors but can also be used as a sensitive tool to characterize magnetic thin films. As we will show later, PHE sensors are more sensitive to catch fluctuations in the direction of FM layer magnetization. Exactly controlling the magnetization state is key to the operation of PHE sensors. Ideally, the magnetization must be confined to a certain direction in zero field, and the application of a field perpendicular to this direction rotates the magnetization in such a way that the output signal, V_{PHE}, is linear with respect to the magnitude of the applied field. This is true for applied fields smaller than a fourth of the intrinsic effective anisotropy field, given for magnetocrystalline anisotropy, uniaxial anisotropy induced during the film deposition and the shape anisotropy. Magnetoelastic anisotropy becomes important when tension is present in the substrate. Such cases can be found when, for example, a piezoelectric material or a flexible material, like Kapton is used as substrate [47].

PHE sensors acquire the advantages of high linearity at small applied fields, elevated S/N ratio, reduced noise and zero-offset, as well as enhanced thermal stability and low power consumption [32, 64, 99–105]. Generally the sensitivity can be referred to as the ratio of the response to cause, hence the PHE sensitivity can be expressed as the ratio between the noticed output voltage and the operating field range, simply denoted as: $S_{PHE} = \Delta V/\Delta H$ [97, 106].

From equation (6) and figure 4(b) it appears that higher sensitivities can be achieved for lower values of H_p. However, for real structures, smaller values for H_K and H_{ex} means magnetic domains in the sensing layer, figure 3, that imply nonlinear field dependence and hysteretic behavior of the PHE signal [62]. On the other hand, larger values of H_{ex} and H_K bring the sensing layer close to a single domain structure with the cost of magnetic field sensitivity [93].

Finally, we must note that AMR and PHE dependencies may be affected by hysteretic effects in real structures, like NiFe films, which are far from single domain behavior, even if an easy axis of magnetization is defined through shape and uniaxial anisotropy. Figure 5 presents the results of micromagnetic simulations using LLG Micromagnetics simulator [107], performed on a Permalloy thin film of $1000 \times 500 \times 10$ nm^3 where the structure arrives in a final state which is slightly different from the initial state. This is translated into a different AMR or PHE signal at the sensor output.

Note that, the internal magnetization has no preferred direction along the longitudinal axis and flipping of 180° can occur due to spikes or to exposure to some external magnetic fields. This flipping of the magnetization results in a different sensitivity of the system. To overcome this problem an internal coil (KMZ51) or external controlled magnetic field should be used to reset and set the magnetization to the initial orientation. Other methods to keep the initial magnetization state, for $H = 0$, is to use exchange-biased structures like bilayers FM/AF, trilayers FM/NM/AF, or spin valves of the type FM/NM/FM/AF where FM is a FM layer (NiFe, NiFeCo, etc.), NM is a NM layer like Cu, Ag, Pt and AF is an AF layer like FeMn or IrMn [93]. These methods with their advantage and drawbacks will be discussed, later.

In this review article we focus on the use of NiFe as FM layer and IrMn as AF layer, as being representative for applications of PHE sensors. Other FM materials were studied with these bi- and tri-layer structures such as NiCo [108, 109], NiFeMo [100], CoFe [110], and others [91, 109, 111]. NiFe is a better candidate according to its MR value, diminished magnetostriction, and anisotropy, along with an easier domain rotation depending on excellent soft properties with reduced coercive field and increased saturation [112]. Previous studies were dedicated to using various AF materials as FeMn [113], NiMn [114, 115], NiO [116, 117], to exchange bias the NiFe layer. Presently, IrMn is the better choice to be used with NiFe, as it gives a higher exchange bias field, elevated thermal stability, and higher Néel temperature [118, 119].

2.3. A brief history of the PHE

Earlier studies of the PHE were reported more than five decades ago [120–124]. The term itself was first mentioned as a new galvanomagnetic effect by Goldberg, *et al* [121], where the authors introduced a new term 'planar Hall field', which is observed by measuring the induced voltage normal to the direction of current flow as in the conventional Hall effect configuration but with the magnetic field in the current–voltage plane. No earlier discussions or reports can be found regarding this topic. Sometimes this effect is cited as "pseudo Hall effect," as the design of the experimental measurement mimics the conventional Hall effect excluding the field orientation [104, 115]. The study of theoretical basics of PHE was conducted by Ky [123, 124]. Additionally, PHE in a single Ni layer was introduced in (1966) [125, 126]. The quadratic dependence of the PHE output voltage on magnetization was demonstrated.

Afterwards, Ky in 1968 reported the PHE in Co, Fe, Ni, and NiFe FM materials with layers thicknesses within 10–150 nm, and a wide temperature range of 77–293 K [120]. The author concluded that the output voltage slightly increases with a decreasing film thickness at low temperature, which was attributed to the increased defects and impurities concentration in the film. Another report by Yau *et al.* [122] discusses the PHE in NiFe alloys with 50%, 80%, and 100% Ni content. The output voltage varies noticeably with the Ni content, and it shows a parabolic dependence on the field for fields above saturation. This result was explained by the existence of an inertial field, the domain structure. The exploitation of PHE to explore the thin films rotational hysteresis, was developed by Vatskichev, *et al* [127], where they concluded that PHE voltage hysteresis area calculations can produce a uniaxial anisotropy magnitude in thin films. Berger [128], displayed that for PHE, the voltage which is proportional to the thickness of domain wall is shaped when the DC current transverses the domains.

Later on, Schuhl *et al.,* fabricated a sensor for low magnetic field detection relying on the PHE principle in ultrathin Permalloy film. A reachable 10 nT detection limit and 100 V $A^{-1}T^{-1}$ sensitivity was acquired [129–131]. A sensor designed for microcompass applications introduced by Montaigne *et al* based on the Permalloy thin film has a reachable 200 V $A^{-1}T^{-1}$ sensitivity and 10 nT detection limit within a 1–1000 Hz frequency [57]. The investigation of the perpendicular anisotropy in Co thin film was also performed using the PHE with a perpendicularly applied magnetic field on the film surface by Ogrin *et al* [132]. The offset voltage is also explained in terms of origin and its suppression tactics. Following up on this, Santos *et al* [96] prepared Permalloy films where they investigated the propagation of the PHE, and concluded that the transverse voltage possesses a strong variation where the field is perpendicular to the films plane. A model to express this was proposed, thus it is convenient for angular positioning. The exchange bias systems with FM/AFM bilayers with the PHE was firstly proposed by Kim *et al* where NiO/NiFe system was used and an optimization of the PHE using biaxial currents was employed [116].

After 1999, Baselt *et al.,* showed a potential detection of biomaterials by using a GMR-based sensor, the PHE-is also investigated for the biosensing by several groups [43, 133–136]. It was found that the facile fabrication and unique properties of PHE sensors were very useful in detecting magnetic labels/beads with a very good S/N ratio. Afterwards, these researchers tried to enhance the sensor sensitivity and resolution either by changing the sensor structure [65, 93, 108] or sensor geometry [108, 137]. During these investigations, new sensor application fields have emerged such as current monitoring [137], oil and gas pipeline inspection [44], and non-volatile logic gates functionalization [138]. Recent investigations of PHE sensors have focused on the different sources of noise and thermal stability [94, 139], as well as integration with wearable devices [137, 140, 141]. The implications of sensor structure and sensor geometry on PHE sensor sensitivity is provided in detail under sections 3 and 4. Flexible PHE-based sensors are discussed in section 7. The historical timetable for the evolution of the PHE is displayed in figure 6.

3. Effect of sensor structures on PHE sensitivity

In this section, we cover different layers composing the PHE sensors and their correlation with the sensitivity and MR magnitude with more focus on Permalloy based structures of PHE as well as seed and capping layers contributions to the sensitivity.

3.1. PHE in a single FM layer

PHE can be observed in the Hall voltage of single layer FM materials [46, 120, 122, 129, 142–144]. When the conditions given in theoretical background (figure 3(a)) have been supplied, the PHE signal exhibits a quite linear region as shown in figure 3(b). This linear region can be used for measuring/-detecting magnetic fields in the range of millitesla (mT) and picotesla (pT). In order to detect low magnetic fields down to the pT level, the FM sensing layer must be magnetically soft with a good AMR ratio. Therefore, the FM materials such as NiFe, CoFe and NiCo are good candidates to be a sensing layer

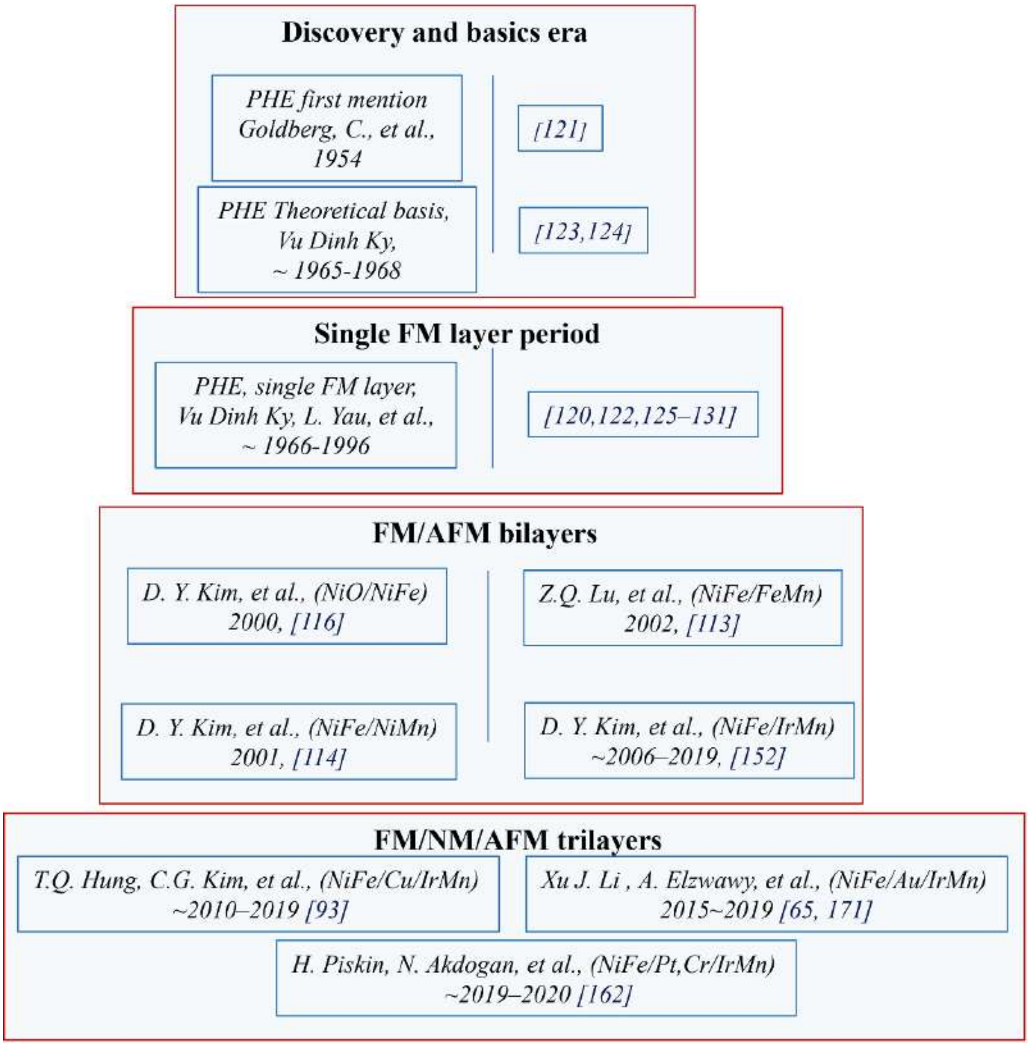

Figure 6. The evolution of the planar Hall effect related work with the appropriate timing for each phase, with their related references.

of PHE sensors [108, 110, 145, 146]. Also, the uniaxial magnetic anisotropy property of these materials makes it easier to control the output signal of the PHE sensors for applications. In the FM layers, such as NiFe, the magnetization favors to lie along a particular axis (or several axes) called the easy axis of magnetization, leading to magnetic anisotropy. The application of an external magnetic field on the FM layer causes the rotation of the magnetization from its original direction by an angle θ. The values of angle θ depend on the value of the external magnetic field and the properties of the FM layer. Applying sufficient magnetic field perpendicular to the easy axis causes the rotation of the magnetization from its original direction $\theta = 0°$ to the direction of the applied magnetic field $\theta = 90°$ (usually called the hard axis of the magnetization). The cancellation of the applied magnetic field causes the rotation of the magnetization from $\theta = 90°$ to $\theta = 180°$. When the FM layer is employed as a planar Hall sensor, the voltage corresponding to this rotation (from $\theta = 0°$ to $\theta = 90°$ and from $\theta = 90°$ to $\theta = 180$) will show a large hysteresis due to the linear dependence of the planar Hall voltage on the sinus of the angle 2θ ($V_{\mathrm{PHE}} \sim \sin(2\theta)$). This hysteresis can be avoided by coupling the FM layer to an AF layer which induces a unidirectional anisotropy of the magnetization due to a fundamental interfacial property called the exchange bias interaction.

In the early studies, Dau *et al* have demonstrated that the PHE signal of a single layer of NiFe grown on Fe/Pd buffer can detect low magnetic fields below 10 nT [131]. Recently, Nhalil *et al* have illustrated that the elliptical shaped NiFe layer can detect low magnetic fields down to 5 pT level and they have reported that the micro-structured magnetoresistive sensor based on PHE can be used instead of fluxgate sensor which is larger and more expensive [147]. However, the PHE signal of a single NiFe layer (without an exchange bias field, H_{ex}) exhibits hysteresis due to the switching behavior of magnetization during magnetic field sweeping [57, 131]. Since the hysteresis of the PHE signal is undesirable for many sensor applications, it can be removed by considering exchange biased FM/AF bilayer or double biased FM/AF/FM sensor structures.

3.2. Bilayers

The phenomenon of the exchange bias was discovered 63 years ago by Meiklejohn and Bean during their work on nanoparticles of the core–shell structure (Co/CoO) [73]. From a macroscopic point of view, the effect of the exchange interaction between the two FM and AF layers appears clearly in the shift of the hysteresis cycle M (H) from zero for a single FM layer to non-zero values for the FM/AF bilayer structure. The value of the field shift is called the exchange bias field (H_{ex}). The application of an external magnetic field to the hard axis of the bilayer structure incites the rotation of the magnetization form $\theta = 0°$ to $\theta = 90°$ and when the applied field has removed the magnetization of the bilayer structure rotates from $\theta = 90°$ to $\theta = 0°$ which eliminates the hysteresis of the planar Hall voltage.

Besides, the exchange bias compels the magnetic moments in the FM layer to rotate coherently towards the applied magnetic field, and by consequence, it improves the thermal stability of the planar Hall sensor and reduces the Barkhausen noise. Due to these advantages, the planar Hall sensor based on a bilayer structure is a good candidate for the detection of small magnetic fields. However, a deep understanding of the effects of the thickness, shape, material compounds, and the size of magnetic layers were required to develop a bilayer planar Hall magnetic sensor that combines high sensitivity, low noise, high thermal stability, and a low limit of detection.

In the FM/AF bilayer or double biased sensor structures, the exchange bias effect induces a unidirectional magnetic anisotropy which results in a reversal behavior of magnetization without switching [91, 145, 148–150]. Thus, the hysteresis behavior of the PHE signal can be removed. In the literature, IrMn material has commonly been used as an AF layer due to its high electrical resistivity and high Néel temperature [151]. Besides, Thanh *et al* and Damsgaard *et al* have worked on the FM thickness dependence of the PHE sensitivity (S_{PHE}) in the bilayer structure of NiFe(t)/IrMn for the thickness ranges between 3–20 nm and 20–50 nm, respectively [43, 152, 153], the similar direction is applied on (NiO (30 nm)/NiFe(t)) bilayer by Kim *et al,* within 5–30 nm thickness [154]. They have observed an increase in S_{PHE} as the thickness of the NiFe layer increased. The sensitivity increase in the PHE signal has been explained by considering two main effects:

(a) the exchange bias field (H_{ex}) has decreased as a function of increasing thickness of the NiFe sensing layer. Thus, the magnetic moments of the NiFe sensing layer can be rotated more freely toward the applied magnetic field which results in higher magnetic field sensitivity.
(b) the observed resistivity difference ($\Delta\rho = \rho_{||} - \rho_{\perp}$) of the FM sensing layer has increased when the thickness of the NiFe layer is increased. This results in a maximum voltage increase of the PHE signal which provides increased sensitivity. The reported resistivity trends as two regimes, one less than 10 nm NiFe thickness where the resistivity increases, and one higher than 10 nm NiFe thickness where it decreases. This is explained by the surface interaction contributions in the multilayer, when NiFe is a few nm thickness, IrMn and Ta dominate. For further increase of NiFe thickness, it obtains enough surface contributions to affect and reduce the resistivity magnitude following the Funchs–Sondheimer theory [153].

However, the strong pinning of the exchange bias interaction in the NiFe/IrMn bilayer system restricts the magnetic field sensitivity (S_{PHE}) of the PHE signal compared to a single NiFe layer. To increase the S_{PHE} further, the exchange bias field (H_{ex}) must be further reduced. This can be accomplished by using a trilayer structure of FM/NM/AF or a spin-valve structure of FM/NM/FM/AF.

3.3. Trilayers

The exchange bias field (H_{ex}) can be reduced by inserting a NM thin spacer layer between FM and AF layers [93, 97, 155, 156]. Thus, the H_{ex} can be well-tuned in FM/NM/AF trilayer sensor structures by varying the thickness of the NM spacer layer. The exchange bias decreases exponentially with the increase of the spacer layer thickness and vanishes around 1 nm thickness while this thickness is enough to completely separate the FM/AF layers [65, 93, 157–161]. In the literature, mostly the Cu material has been used as a spacer layer. When a very thin Cu spacer layer has been inserted between NiFe and IrMn layers, a significant increase in S_{PHE} has been observed [93, 112]. However, although the exchange bias field (H_{ex}) can be reduced by inserting a thicker Cu spacer layer, the PHE sensor's sensitivity (S_{PHE}) has not been further increased due to the decreased maximum output voltage of the PHE signal. The decrease in the maximum output voltage of the PHE signal can be explained by recalling the V_{PHE} expression given in equation (4). When the sensor structure consists of different layers than the FM sensing layer, the applied current I, is separated into I_{FM} and I_{shunt}. Thus, the I_{FM} decreases in the presence of other layers (shunt layers) depending on their resistivities. Furthermore, the good conductivity of Cu spacer layer results in a large decrease in I_{FM} as the thickness of the Cu layer increased. Therefore, the sensor's maximum output voltage is reduced. In the literature, there are also few efforts to investigate the effect of different types of spacer layers such as Au, Pt, and Cr materials in the trilayer structures of NiFe/NM/IrMn [65, 162–164]. Li *et al* has reported a very good enhancement of PHE sensitivity by using Au spacer layer up to 1 nm thickness, So far the prominent thickness of the spacer layer for sensitivity is around $0.5-0.6$ nm [65]. Surprisingly, they have observed a maximum voltage increase despite the Au spacer thickness being increased. This is attributed to the enhancement of resistivity difference $(\rho_{||} - \rho_{\perp})$ of the NiFe layer when it is interfaced with the Au spacer. A similar enhancement of resistivity difference has been observed in the NiFe/Pt/IrMn sensor structure by Pişkin *et al* using a Pt spacer layer up to 1 nm [162, 165]. This indicates that both Au and Pt spacer layers repair the negative effect of Cu. Thus, the S_{PHE} can be further increased in NiFe/NM/IrMn (NM: Au, Pt) trilayer structures compared to the NiFe/Cu/IrMn structure. Moreover, Elzwawy *et al* have reported that the power consumption of PHE sensors can be minimized without sacrificing sensitivity [100]. In their study, equisensitive PHE sensors have been successfully fabricated by varying the thicknesses of spacer and capping layers. It is shown that the output voltage of the PHE sensor can be tuned by varying the thickness of capping layer, while the exchange bias field (H_{ex}) can be tuned by adjusting the thickness of the spacer layer.

In connection with the use of Au and Pt layers, we can mention a special class of structures of the type FM/HM where a large spin Hall MR (SMR) can appear [1–3]; HM represents a heavy metal thin layer like Pt, Au_xPt_{1-x} alloy [166], W [167], PtHf and PtAl alloys [168] or Pt/Hf multilayer [169] whereas FM is a FM layer like NiFe, CoFeB [166–168]. When the current flows through the multilayered structure, the NM layer acts as a spin orbit torque (SOT) biasing layer [166–168] for the FM layer. The current-induced magnetization due to SOT effect eliminates the need of a biasing field from an external source or from an exchange coupling with an AF layer. We must note that SMR is based on the spin Hall effect (SHE) and on the inverse SHE (ISHE) in NM [167]. A typical PHE setup is used for sensing applications with such structures [166, 167]. Using a Wheatstone bridge comprising of four ellipsoidal NiFe(2.5 nm)/$Au_{0.19}Pt_{0.81}$(3.2 nm) sensing elements with a long axis length of 800 μm and short axis of 200 μm, a SMR sensor with nearly zero DC offset and negligible hysteresis was reported in [166]. The sensitivity is up to 1.10 mV V^{-1} Oe^{-1} at 20 °C within a linear region of ±0.86 Oe and the field detectivity can reach 0.71 nT $Hz^{-1/2}$ at 1 Hz. Despite the simplicity of such structures, work has to be done on HM and FM layers to increase the SMR effect, the linear range and to improve the stability of the sensitivity with temperature [166, 170]. Also, it must be noted that PHE setup or the Wheatstone bridge configuration can also be used to characterize SOT effective fields and the MR effect in FM/HM structures.

Another improvement in the NiFe/Au/IrMn trilayer based PHE sensors has been introduced by substituting the Ta capping layers with NiFeCr layer [171]. When the NiFeCr material has been used instead of Ta capping layer, a better condition for domain wall pinning in the NiFe sensing layer has been observed. This results in a lower value of Barkhausen noise. Thus, a 50% higher S/N ratio has been reported compared to a sensor structure that contains the Ta capping layer. Besides, it is important to mention here that the higher S/N ratio enables the detection of lower magnetic fields.

Recently, Mahfoud *et al* have presented a very interesting method to stabilize the magnetic field sensitivity of PHE sensors by using a trilayer sensor structure of NiFe/Cu/IrMn in an unstable thermal environment [94]. In this study, they have found a special case that the sensor's magnetic field sensitivity does not significantly change with varying temperature. It has been reported that the PHE sensors with the thermal stability of sensitivity can be used for the characterization of low volume and low dimension magnetic materials like single molecular magnets. The NiFe thickness effect is explained as well for NiFe/Cu/IrMn trilayer structure with a varied NiFe thickness 10–30 nm and Cu thickness 0−0.6 nm, in summary, 20–30 nm thickness of NiFe accompanied by 0.6 nm thickness of Cu layer gives around 90% elevated signal [172], few reports interconnect with AF materials conjugated with NiFe for PHE sensors [113, 114] However, up to the authors best knowledge, no IrMn layer thickness effect on PHE sensors is investigated in this bi- and tri-layer structures.

3.4. Spin-valves

The spin-valve structure typically consists of two FM layers separated by a NM conducting (spacer) layer. It is important to note that when the thickness of the spacer layer is smaller than the mean free path of the electrons, the two FM layers can affect each other via Ruderman–Kittel–Kasuya–Yosida (RKKY) interaction. The RKKY interaction between two FM layer is known to cause a unidirectional magnetic anisotropy when one of the FM layers is pinned by an AF layer. Thus, the other almost free FM layer can be used as sensing layer for PHE sensors [110, 173–177]. The RKKY interaction can also be used to tune the H_{ex} of the NiFe sensing layer by varying the thickness of a spacer layer or varying the thickness of FM layers. In order to optimize the magnetic field sensitivity of spin-valve based PHE sensors, Hung *et al* has investigated systematically the effect of thickness of FM free (t_f) layers in Ta(5)/NiFe (t_f)/Cu(1.2)/NiFe (2)/IrMn(15)/Ta(5) (nm) ($t_f = 4$–16 nm) structure [178]. They have observed a sensitivity increase as the t_f increased up to 16 nm. However, the magnetic field value of the peak in PHE signal did not change a lot as the t_f was increased. Thus, they have explained the enhancement of sensitivity by decreasing the shunt current from other layers. A similar systematic study has been done by Tu *et al* considering the effect of thicknesses of the FM pinned (t_p) and the FM free (t_f) layers in Ta(5)/NiFe (t_f)/Cu(1.2)/NiFe (t_p)/IrMn(15)/Ta(5) (nm) ($t_f = 4$–26 nm, $t_p = 1$–12 nm) structure [179]. They have observed the same shunt current effect with similar magnetic anisotropy behavior when the t_f varied in the working range. In addition, they have reported that the PHE sensor sensitivity increases as the thickness of t_f increased and t_p decreased. Thus, the highest PHE sensitivity has been reported in the spin-valve configuration with $t_f = 26$ nm and $t_p = 1$ nm.

3.5. Seed and capping layer effect

The seed layer in general affects the MR ratio [149] as a better-smoothed seed layer promotes a lowered grain boundary and a larger grain size that increases (111) texture for the subsequent layers. This leads to a longer mean free path affected by scattering of the conduction band electrons and finally, an elevation of the MR value can be noticed. According to Wang *et al* the optimum MR ratio value (3.5%) of the seed layer was at ≈5 nm thickness and 400 °C for Ta as the most commonly used seed layer with the Permalloy FM layer [180], whereas the NiFeCr was found as a superior alternative for Ta seed layer [181–185]. Contrary to the Ta seed layer which encounters a thermally preferred interaction between Ta and NiFe leading to a magnetically dead layer and a reduced magnetic moment magnitude, NiFeCr does not experience this interaction. The $(NiFe)_{1-x}Nb_x$ seed layer is also used and has a reported 3.76% MR ratio at x ≈ 20% of NiFeNb alloy at 450 °C, while Ta has a 3.27% MR ratio at the same conditions [186, 187]. The capping layer effect in general is a protective layer of the humidity and surroundings. Vastly, the capping layer affects the overall resistance of the stacking which subsequently affects the effective output voltage [188], of the sensors. Lately, another point of view on the capping layer contribution is discussed and depicted [171], in terms of the mechanical energy changes. A threefold elevation of the exchange bias value is maintained upon introducing a NiFeCr capping layer in contrast with the usual Ta layer. Since the collision probability of sputtered atoms with different masses, a change in momentum transfer can be acquired. The transfer is linked to coupled/decoupled areas in the FM/AF interface leading to the increase in exchange bias magnitude.

4. Effect of the sensor geometry on PHE sensitivity

The PHE sensors are patterned with different geometries in relation to the desired application. The most usual geometries are: cross-shaped, elliptical, and disk-shaped. Other geometries, which mimic the PHE, exist as ring shaped or diamond shaped AMR resistors connected in a Wheatstone bridge. These resistors are named PHE bridge (PHEB) and, to sustain the correct orientation of the magnetization inside of these arms, an exchange-biased stack is used [137]. Some results regarding the development of Permalloy based PHE sensors are presented as follows.

4.1. Cross junctions

Theoretically, the PHE voltage does not depend on the length or width of a cross junction, but is affected by the thickness of the FM layer as expressed in equation (4). Until the year ~2010 the planar Hall sensors were manufactured based on cross-shaped architectures. The widespread use of this shape is due to the ease of its manufacture as well as the existence of a large body of research that has studied the various magnetic interactions occuring in these shapes. Also, these shapes appeared to be an appropriate option for some technological applications especially those related to biological detection as increasing the active surface of the sensor could increase the possibility of detecting biological molecules. Hung *et al* has experimentally investigated the effect of cross size on the PHE voltage by fabricating a spin-valve structure of Ta(5)/NiFe(6)/Cu(3)/NiFe(3)/IrMn(15)/Ta(5) (nm) with the cross sizes of 50 × 50 μm^2, 50 × 70 μm^2 and 50 × 100 μm^2 [189]. They have observed the same PHE voltage profiles when the cross size has been varied. A similar experimental study has been carried out by Donolato *et al* They have fabricated a bilayer structure of Ta(3)/NiFe(30)/IrMn (20)/Ta(3) (nm) with the cross sizes varied between 40 × 40 μm^2 and 3 × 3 μm^2 [190]. They have observed the same PHE voltage profiles when they used the 40 × 40 μm^2 and 20 × 20 μm^2 crosses. This finding was very similar to the results observed by Hung *et al* However, when the cross size has been reduced below 10 × 10 μm^2, they have observed hysteresis in the PHE voltage profile with an increasing trend. They have investigated this hysteresis behavior of the PHE signal by taking a magnetic force microscopy (MFM) images of crosses and by micromagnetic simulations. They concluded that when the cross size is reduced a new magnetic easy axis has occurred due to the shape anisotropy. The presence of a new easy axis has resulted in a hysteresis behavior in the PHE voltage profile. The importance of this work lies in highlighting the effect of the sensor's dimensions on its magnetic behavior, especially for magnetic sensors that have small dimensions. The low dimensional sensors could be the next generation of planar Hall magnetic sensors due to the urgent need to reduce the size of the sensor to detect small magnetic materials. In another study, Hung *et al* have successfully fabricated a spin-valve structure of Ta(5)/NiFe(16)/Cu(1.2)/NiFe(2)/IrMn(15)/Ta(5) nm with a cross junction size of 3 × 3 μm^2 [174]. But they have reported no hysteresis in the PHE voltage profile. It is well understood, when the exchange anisotropy is well enough to overcome the shape anisotropy, the PHE signal does not exhibit hysteresis. These investigations have shown that the cross junctions can be successfully fabricated in different sizes according to the requirement of an application.

For the cross junctions, if a single FM layer, like a NiFe material, has been used, several tens of μV (Oe·mA)$^{-1}$ PHE sensitivity can be obtained [57, 131, 146]. However, the exchange biased sensor structures (bilayer, trilayer and spin-valve) can provide a sensor sensitivity typically some of μV (Oe·mA) due to the presence of exchange bias field (H_{ex}) and increased shunt current (I_{shunt}).

In [129, 131], early results in microfabrication of high sensitivity PHE sensors, with a sensitivity of 100 V/AT and a minimum detectable field below 10 nT were reported. The sensing layer consists of Permalloy and is 6 nm thick, epitaxially grown by molecular beam epitaxy. Uniaxial magnetic anisotropy is induced in the film through FM coupling with a Fe/Pd bilayer epitaxially grown on MgO (001). A large enhancement of the PHE sensitivity was reported in a NiO/NiFe/NiO heterostructure figure 7 [92].

This sensitivity improvement derives from (a) the increase of resistivity change ($\Delta\rho$) and (b) the decrease of the saturation field (H_{sat}). A sensitivity up to 1200 V A^{-1}T^{-1} was reported in this study for an optimal stack of the type Ta(5)/NiO(3)/NiFe(8)/NiO(2)/Ta(3 nm). This remarkable enhancement of the sensitivity is strongly related to the strengthened electron scattering by the flat oxide/metal interfaces and the easier magnetization rotation because of the reduced intermixing of Ta and NiFe [92].

In [191], the PHE in NiFe films was studied using MgO as the buffer and capping layer in order to reduce the shunt effect. A sensitivity of about 865 V A^{-1}T^{-1} was reported in a MgO (3 nm)/NiFe (5 nm)/MgO (3 nm)/Ta (3 nm) structure after thermal annealing at 500 °C 2 h^{-1}. After this annealing smooth MgO/NiFe and NiFe/MgO interfaces were found and the shunting effect due to Ta layer was decreased. The smooth interfaces lower the diffusive scattering of electrons at MgO/NiFe and NiFe/MgO interfaces.

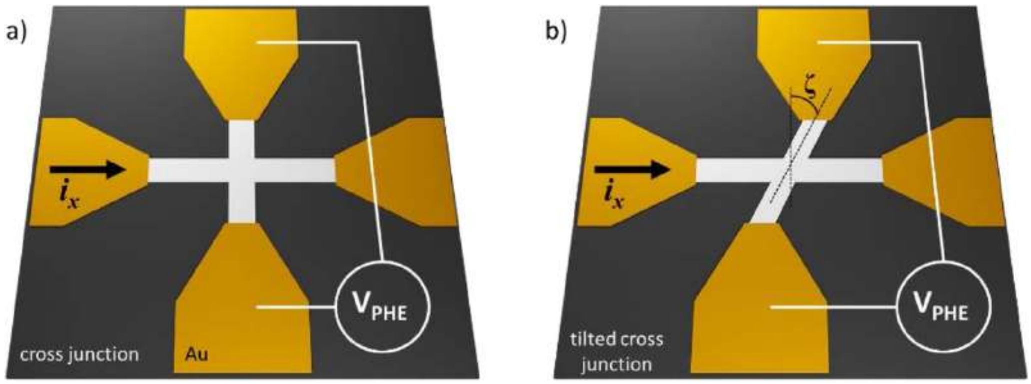

Figure 7. (a) Typical cross-shaped Permalloy based PHE sensor (reproduced from [64]. CC BY 3.0.), and (b) tilted cross junction as sketched in [189] (reproduced from [189]. © IOP Publishing Ltd. All rights reserved).

4.2. Tilted-cross junctions

The main idea behind the fabrication of tilted-cross junctions is to combine the longitudinal MR effects such as AMR, GMR with the PHE which is the transverse AMR component [189, 192]. This combination of MR effects in one sensor remarkably increases the magnetic field sensitivity compared to a cross junction fabricated with the same sensor structure. Hung *et al* have systematically investigated the sensor's magnetic field sensitivity in 100 μm $\times$ 50 μm crosses fabricated with a spin-valve structure of Ta(5)/NiFe(6)/Cu(3)/NiFe(3)/IrMn(15)/Ta(5) (nm) by varying the tilt angle between 0° and 45° [189]. They have observed that the magnetic field sensitivity has been gradually increased as the tilt angle changed to 45°. Furthermore, they reported that this tilted configuration exhibited not only better sensitivity, but also better linearity as compared with the typical PHE cross junction sensor. It is important to note that the shape of the output signal of the tilted cross junctions changes due to the contribution of other MR effects. Therefore, the working range (linear region) of this type of magnetic field sensor shifts. In sensor applications of tilted cross junctions, this shift of linear region must be considered.

4.3. Bridge junctions

A very interesting development of the PHE sensor has been realized by replacing the traditional cross junction with a Wheatstone bridge design by using the exchange biased bilayer, trilayer, and spin-valve sensor structures [103, 108, 193–199]. Since the output voltage characteristic for this configuration of the Wheatstone bridge has the same angle dependence of magnetization as the PHE signal of cross junctions, they were termed PHEB sensors to distinguish them from other types of AMR bridge sensors. Figures 8(a)–(d) present diamond-shaped and ring-shaped bridge sensors, respectively [193, 194], where l is the length, and w is the line width of the resistor elements. It is important to mention that, the exchange bias and anisotropy fields have been aligned along the x-axis and the magnetic field has been applied along the y-axis. The constant current of i_x has been applied from the a–b terminals and the voltage has been recorded from the

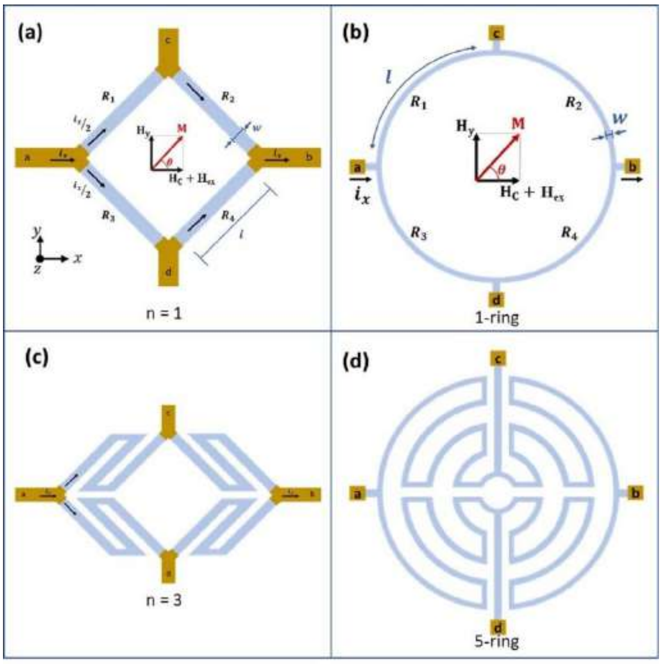

Figure 8. PHE bridge designs in diamond-shaped (a), (c) reprinted from [193], with the permission of AIP Publishing, and ring-shaped (b), (d) geometries reprinted from [194], Copyright (2011), with permission from Elsevier.

c–d terminals. For this configuration of Wheatstone bridges, a magnetic field profile of PHE signal given in figure 3(b) can be obtained.

The output voltage of the Wheatstone bridges should be well understood before proceeding with the findings of the experiments. The output voltage of a Wheatstone bridge (V_{out}) can be expressed by the following function when the bridge has been biased with a constant current of i_x [200]:

$$V_{out} = i_x \frac{R_2R_3 - R_1R_4}{R_1 + R_2 + R_3 + R_4} \tag{7}$$

where the R_1, R_2, R_3 and R_4 stand for the resistance elements of the Wheatstone bridge, which is produced by using an exchange biased PHE sensor structure. It is important to note

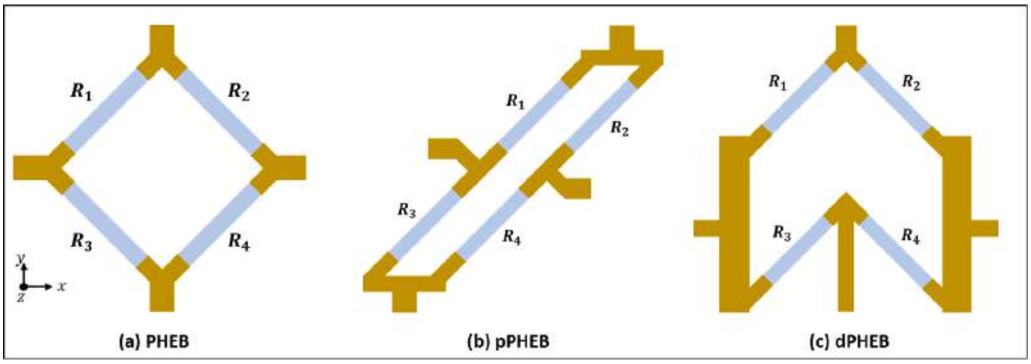

Figure 9. Wheatstone bridges with different configurations. (a) PHEB (b) parallel-PHEB (pPHEB) (c) differential-PHEB (dPHEB) reprinted from [200], with the permission of AIP Publishing.

that the $R_1 = R_4$ and $R_2 = R_3$ when the PHEB has been symmetrically designed by using a diamond or ring shape. If this condition replaced into equation (7), the V_{out} can be written in the following form:

$$V_{\text{out}} = \frac{i_x}{2}\left(R_2 - R_1\right). \tag{8}$$

It is very clear that the V_{out} is not zero when a difference has occurred between R_2 and R_1 resistances. In addition, the resistance elements (R_1 and R_2) of a diamond shape can be expressed individually by considering the AMR properties of FM materials as follows:

$$R_\theta = \frac{l}{wt}\left[\rho_\perp + \left(\rho_{||} - \rho_\perp\right)\cos^2\theta\right]. \tag{9}$$

If equation (9) replaced into equation (8), the V_{out} will be related to the (l/w) ratio.

In early studies of PHEB sensors, Henriksen *et al* and Oh *et al* have experimentally and theoretically demonstrated that the sensor's output voltage can be enhanced by a geometric factor of (l/w) [193, 194]. Thus, the magnetic field sensitivity of PHEB sensors can be largely enhanced when the (l/w) has been increased. In the study of Henriksen *et al*, they have fabricated an exchange-biased bilayer structure of Ta(5)/NiFe(30)/IrMn(20)/Ta(5) (nm) with various size of Wheatstone bridges in a diamond shape [193]. When the geometric factor of (l/w) has been experimentally tuned as 20 with the $n = 7$ repeats (which means $l/w = 140$), they observed a 102 times improvement in the sensitivity compared to the cross junction fabricated with the same sensor structure. The detectability of the planar Hall sensor in low-frequency regime was improved by one order by using the bridge geometry instead of using the cross geometry [195]. Furthermore, it has been reported that the magnetic field sensitivity of PHEB sensors can be further increased by altering the sensor structure with a lower exchange biased one such as the spin-valve or the trilayer sensor structures [193, 194, 197].

Parallel to the development of the bilayer bridge sensor, another development in the geometry of the bilayer planar Hall sensor which was based on ring architecture was proposed by Kim's group [201]. Ring architecture bilayer sensors with differing width (w = 5 μm and 10 μm) and radius (r = 30 μm, 60 μm, 90 μm, and 120 μm) and multiring sensors were investigated. Theses studies showed that the sensitivity and the output voltage of the sensor increase with the increase of the radius of the ring and/or with the decrease of the width of the ring. Additionally, the study showed that the sensitivity and the output voltage increase with the number of rings also. A high sensitivity of the multiring sensor of 3.3 mV mT^{-1} was achieved for the multiring sensor compounded by seven rings with a width of 5 μm. This sensitivity was improved when the magnetic field was applied with an angle of 20° to the easy axis, the sensitivity of the multiring sensor at this angle increased 2.5 times. For example, the use of NiCo FM layer as a sensitive layer instead of NiFe for planar Hall sensor based on the ring shape was introduced, which improved the signal voltage and the dynamic range of the sensor [108]. When compared to the ring geometry, the diamond geometry has been found theoretically 41%, and experimentally 30% more sensitive to the low magnetic fields [137]. The difference between theory and experiment has been explained as the diamond shaped sensors can be more affected by demagnetization effects than ring sensors. As a result, both the diamond and ring designs of bridge sensors have largely enhanced the magnetic field sensitivity and seemed to offer higher performance levels compared to those provided by the conventional cross junction PHE sensors.

In another study, Østerberg *et al.,* have provided and optimized two more configurations of PHEB sensor which is shown in figure 9. They have termed the new Wheatstone bridge designs as parallel PHEB (pPHEB) and differential PHEB (dPHEB) sensors [200, 203]. It is evident that the ($R_2R_3 - R_1R_4$) term in equation (7) is always zero for the pPHEB and dPHEB sensor designs. Therefore, the pPHEB and dPHEB sensor designs are not sensitive to the homogenous external magnetic fields, unlike the PHEB. But these sensors can provide a signal caused by only the MNPs when one of the resistance elements has been used for the sensing. Furthermore, in the pPHEB design, the sensor's self-fields (Oersted fields) caused by the applied current is additive due to the parallel shape of the sensor. It has been demonstrated that the sensor's self-fields can also be eliminated in dPHEB design.

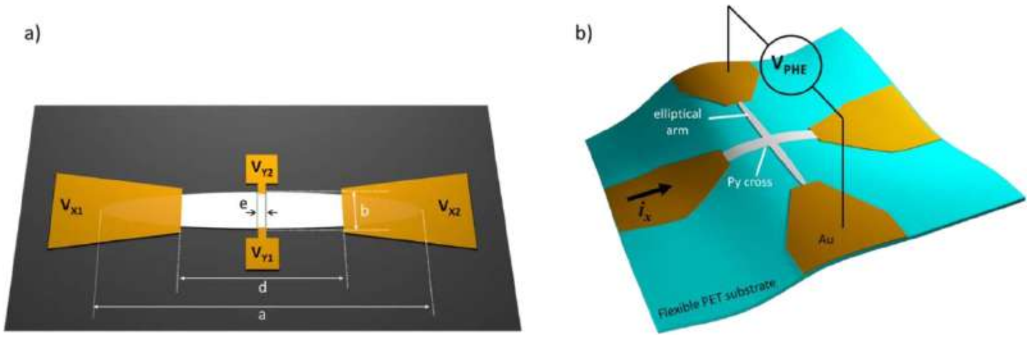

Figure 10. (a) Elliptical shaped Permalloy based PHE sensors deposited on rigid substrate reprinted from [202], with the permission of AIP Publishing, and (b) on flexible substrate reproduced from [47]. CC BY 4.0.

Besides, Henriksen *et al* have reported that the sensor's self-field (Oersted field) due to the applied current can also be used to detect the MNPs [172, 198]. This allows MNP detection without the need for external magnetic fields. With these fascinating properties of bridge junctions, they have been found very promising in many sensor applications.

4.4. Elliptical-shaped PHE sensors

A straightforward method to keep the initial orientation of the magnetization along the current direction is to microfabricate elliptical-shaped Permalloy based PHE sensors with a very large aspect ratio 10:1 (figure 10(a)) to induce a preferred magnetization axis can be induced by the shape anisotropy. In [47] was reported such a sensor deposited on polyethylenterephthalat (PET) substrate, figure 10(b) with a sensitivity of 0.86 V T^{-1}, for a bias current of 5 mA, and a detection limit of 20 nT. Such a sensor presents, also, the ability to work as a rotation sensor, as we showed in figures 3(c) and (d). PHE sensors deposited on flexible substrate can be used in the field of flexible electronics with applications in health monitoring. Using the same geometry of elliptical shape PHE sensor (5 mm long axis and 0.625 mm short axis), but integrated within flat trapezoidal magnetic field concentrators, a 5 pT magnetometer at room temperature has been reported [147].

In [62], disk-shaped structures were used to microfabricate Permalloy based PHE sensors. Because no anisotropy axis is defined in this case, a biasing field was used to align the magnetization parallel with current direction when the applied field is zero. Sensitivity up to 6 μV $(\mathrm{Oe.mA})^{-1}$ was found for a field range of about ± 10 Oe. The superb linearity of the measured signal for H_{ex} higher than 25 Oe suggests that the main mechanism of the magnetization reversal processes is based on the magnetic moment's rotation.

However, the main application for which these sensors were microfabricated is devoted to MNPs detection using the surface-based detection technique [62]. The choice is motivated by the relatively *large detection area*, typical for this geometry, large S/N, and a superior thermal stability. For these sensors, the detection technique is based on *localized reversal nucleation induced by MNPs in the sensing layer*. Such a method was studied, also, for GMR sensors. Micromagnetic simulations and experiments were conducted in order to increase the dynamic range of these sensors, in terms of MNPs detected [56]. It was shown that micrometre sized structures, with large aspect ratio, have a limited dynamic range, which affects their applicability [56].

In the sensing setup presented in [46], a magnetic field, H_{ex}, up to 100 Oe, which is used to polarise the MNPs, is *applied perpendicular* to the sensor surface. By this, can be increased the amplitude of the magnetic field generated by the MNPs *without the risk to saturate the sensor* which is less sensitive to perpendicular fields. A second external magnetic field, *scanning field H*, no larger than 30 Oe, is applied *in the film plane along the sensor's driving current, I*. It was found that the presence of the MNPs above the sensor surface affects the magnetization switching behavior of the sensing layer, therefore, a change in the amplitude of the output signal can be observed. These changes of the output signal occur at *small applied fields H*, between 6 and 10 Oe. Maghemite nanoparticles, 10 nm in diameter, functionalized with PEG 6000 were used for experiments, and detection sensitivities, up to 0.116×10^{-3} emu mV^{-1}, can be achieved.

4.5. Impact of junction dimensions (l/w) *on sensor performance*

Another factor that impacts the performance and figure of merits of the PHE sensor is the junction dimensions, (i.e. *l/w* ratio). A higher ratio of *l/w* around ten conjugated with less thickness of NiFe FM layer for cross shape, leads to triple increase of sensitivity, attributed to shape anisotropy elevation as reported [53]. Different square, rectangle, rhombus and circle Permalloy films are introduced with a varied length to width ratio from 1 to 29, where square shape shows the maximum sensitivity [204, 205]. The impact of the width of the junction arm is stipulated in terms of shape anisotropy. Briefly, PHE is studied with a varied width, for larger magnitude, a hysteresis free accompanied by a single domain model is acquired. While, for smaller width, a remarkable hysteresis behavior is introduced to the sensor profile and magnetization reversal occurs as one step [190, 206, 207]. Moreover, a tilting angle of the cross junction by 45º can raise the sensor sensitivity by 30% [189]. An earlier work demonstrated the PHE in NiO/NiFe bilayer system with a changed width of the junction from 200–400 nm.

The exchange coupling magnitude possesses a reversal proportionality with the arm width for all changed temperatures within 5–300 K. This suggests that the sensitivity is higher for larger width [117]. Attention is also paid to the Wheatstone bridge configuration:. as the ratio of *l/w* is increased, the output profile curves are noticed to alter by a scaling factor with a linear dependence of sensitivity on this ratio, and depict insignificant hysteresis, a slight voltage offset increase is also observed. In general, a 100× sensitivity elevation is obtained for the bridge topology in comparison with the conventional cross junction [193]. An increased sensitivity aligned with reduced noise is gained with the higher length to width ratio along with a higher repeated number of the meander-like resistor in the bridge configuration [195].

5. Thermal drift and noise

Thermal stability and thermal drift for the sensors are vital parameters for operation and integration onto devices. Temperature constancy performance features for AMR and PHR sensors are controlled by double kinds of drifts: baseline drift and signal amplitude fluctuation. As reported by Jeon *et al* [103], the significance of PHE sensors performance relative to AMR is explained within the 25 °C–90 °C range for NiFe/IrMn bilayer structure. The thermal drift is three orders of magnitude lower in PHE than AMR. Limited thermal dependence of the sensitivity in planar Hall sensor is also demonstrated. Mahfoud *et al* [94], attributed the achievable stability of the sensitivity by controlling the interplay between the usual exchange bias, Zeeman energy, and anisotropy energy as a function of the temperature of the sensor. Manifested high thermal stability for NiFe/Cu/IrMn trilayer structure is amongst ±2 mT applied magnetic field magnitude with an extremely low variation of sensitivity of about 4.5×10^{-3} V/A/T/K for an extensive temperature span of −163 °C–86 °C. In addition, the change of the temperature during the biosensing process may affect the sensitivity of the sensor. Damsgaard *et al* studied the thermal behavior of the bilayer planar Hall sensor in the range of temperature between 10 °C and 70 °C corresponding to the typical change of temperature in the biological environment [151]. The temperature coefficient of the sensitivity at room temperature shows a relatively high value of 0.32%/°C. The approach proposed for solving this problem involves the use of a second PHE sensor as a reference sensor to correct the drift of the sensitivity.

Although PHE sensors, fabricated from Permalloy thin films, have been long studied [87, 88, 129, 131], they still have the potential to generate more applications with valuable results [47, 53, 57, 62, 94]. For the thermal stability studies, usually, the PHE sensors have a cross-shaped geometry investigated, but other geometries that allow a specific control of the magnetic properties in the sensing layer can be found [47, 56, 62]. As shown in the previous section, the PHE, which is a consequence of the AMR effect, comes with some advantages like linear behavior around zero field, figure 4(b), and the native equivalent electrical behavior like a Wheatstone bridge which brings higher thermal stability. The temperature drift appears to be the main factor limiting the low field performance of magnetoresistive detectors where the voltage is measured along the current. Instead, the PHE is actually a measurement of the transverse magnetoresistivity, figure 3. The transverse measurement is sensitive only to the anisotropic part of the resistivity. The suppression of the term $j_x\rho_\perp$ from AMR expression $E_x = j_x\rho_{xx} = j_x\rho_\perp + j_x\left(\rho_{||} - \rho_\perp\right)\cos^2\theta$ [83] in PHE setup leads to a drastic reduction, with at least four orders of magnitude, of the thermal drift for a Permalloy based sensor [129, 131]. Such that, nano-Tesla sensitivity can be achieved in the low-frequency range [47, 64, 129].

Noise is an important parameter that can affect the low field detection limit of the MR sensors. Such that, we can enumerate the noises, typically associated with MR-based sensors: thermal noise (Johnson noise), shot noise, and 1/*f* noise [47, 61, 64]. Thermal noise arises from thermal fluctuations of electrons and is given by the Nyquist formula [195]:

$$S_{\mathrm{Johnson}} = 4k_{\mathrm{B}}T_{\mathrm{abs}}R. \tag{10}$$

With k_{B} being the Boltzmann constant, T_{abs} the absolute temperature and R the resistance under test. Thermal noise has no magnetic origin which is independent of the applied voltage but directly associated with the electrical resistance of a sensor. For AMR, GMR and TMR sensors, R is larger than R_y, which is the resistance between the measurement arms where PHE is measured; usually R_y is in the range of tens to hundreds of ohms. If $R_y = 100\ \Omega$, the thermal noise is ∼1.3 nV $(\mathrm{Hz}^{1/2})^{-1}$ at 300 K that is equivalent with a magnetic field noise of 1–1.5 nT $(\mathrm{Hz}^{1/2})^{-1}$ [47, 94]. This noise level is much lower than the noise of signal conditioning circuits.

Shot noise is important in MTJs where the existence of an insulating barrier produces discontinuities in the conduction path. Shot noise is expressed by [208]:

$$S_{\mathrm{Shot}} = 2qIR^2 \tag{11}$$

where q is the electron charge, I is the current through the structure and R is the resistance between the measurement contacts.

This term is lower in AMR and GMR but virtually absent in PHE structures.

However, an important component of noises of MR sensors is given by 1/*f* noise which has a major contribution on low-frequency signals. For example, in magnetic materials, this noise comes from the fluctuations of energy around equilibrium due to the presence of magnetic domains; their movement in Permalloy films can be thermally activated or by mechanical stress induced through vibrations in substrate. The dynamics of magnetic domains are dependent on the sensor shape, size and materials properties [61]. A larger effective anisotropy field due to crystalline anisotropy, uniaxial induced anisotropy, and an exchange biasing field [93], and/or a high aspect ratio of the sensor (shape anisotropy) can bring the sensing layer close to a single domain state. However, a larger anisotropy has the cost of a lower sensitivity. Sensors that exhibit

Table 1. The comparison of the most common magnetoresistive sensors (Reproduced from [64]. CC BY 3.0).

Sensor type	I (mA)	Resolution $\mu_0 H_{\mathrm{min}}$ (nT)	Signal to noise ratio (S/N)
Spin valve	10	54	442
Planar Hall effect (PHE)	10	32	1453
Anisotrpoic magnetoresistance (AMR)—ring	10	26	50
Giant magnetoresistance (GMR)	5	93	382
Magnetic tunneling junction (MTJ)	1	202	114

hysteresis show much higher field sensitivity [80], so a compromise must be chosen in accordance with the application envisioned. The $1/f$ noise of the current source can have, also its own contribution, but this can be lower in the case of PHE sensors because of the equivalent differential setup. Using low noise electronics, and integration time up to 10 s, the detection limits can reach levels of nT.

In [64] the main detection characteristics for AMR, GMR, PHE and TMR sensors for MNPs detection are compared. Some useful data adapted from [64] is summarized in Table 1.

The comparison results show that the PHE used for sensing applications has many advantages over others such as a very high S/N and a very high ($\mu_0 H_{\mathrm{min}}$) in the detection of the magnetic field. Furthermore, the voltage profile of a PHE sensor responds linearly to the magnetic field at the small values and the thermal drift of the output signal is better than for other sensors as we stressed above.

6. Comparison of the PHE sensitivity

Hung *et al.,* compared the PHE sensitivity for a bilayer of Ta(3)/NiFe(10)/IrMn(10)/Ta(3), a trilayer of Ta(3)/NiFe(10)/Cu(0.12)/IrMn(10)/Ta(3) and a spin-valve of Ta/NiFe(10)/Cu(1.2)/NiFe(2)/IrMn(10)/Ta(3) structures [93]. It is worth noting that the thickness of the NiFe sensing layers has been chosen as 10 nm in all sensor structures. Among these, the highest PHE sensitivity has been obtained from the trilayer structure. They have reported that the magnetic field sensitivity of the trilayer is about one order larger than the bilayer and two times greater than the spin-valve structure. They explained this result as the trilayer structure has the advantages of weak exchange coupling and the high active current passing through the FM sensing layer due to the very thin Cu spacer layer. Thus, the trilayer structure of NiFe/Cu/IrMn has overcome the disadvantages of the bilayer and spin-valve structures resulting in the highest PHE sensitivity. It is stressed that the PHE sensitivity of the trilayer structures can be further increased by using the Au and Pt spacer layers since both enhance the maximum output voltage of the PHE signal unlike the Cu spacer. The comparison of most familiar PHE structures is delivered in Table 2. Figure 11 represents a visualization of the acquired sensitivity with altered junction geometry.

In this literature, in addition to the structural and geometrical effects on PHE sensor, several studies can be found that investigate the substrate effects [210], etching effects [211], exchange bias field direction dependence [212], magnetization angle dependence [213], reversible and irreversible temperature-induced changes [214], and so on. [112, 188, 215, 216].

7. Applications

Systems for the detection of biomolecules are presently moving towards LOC devices that often integrate the sensing ofmagnetic micro/nano-sized particles within a microfluidic environment. In these systems, the MNPs are functionalized to serve as carriers or labels for the biomolecules, and they provide a magnetic stray field. The latter can be detected by sensors that need to be integrated in the microfluidic environment. Thus, the combination of such sensors with microfluidics is a longstanding topic for research on LOC systems for various applications, as with medical diagnostics or food testing. As sensing technology, the magnetoresistive effects are promising candidates. A wide variety of anticipated sensing technologies have been already reviewed by Freitas *et al* [31], Tamanaha *et al* [217] and Wang and Li [218]. One of the first demonstrations that the GMR can be utilized for the detection of MNPs was discussed by Baselt *et al* [219]. This concept was used to demonstrate single MNP positioning and detection later on by Graham *et al* [220], and a comparison of Schotter *et al* [221] with fluorescent labels demonstrated the potential of magnetoresistive sensors in biotechnology. The PHE as sensing technology was discussed in 2004 and 2005 by Ejsing *et al* [91, 145]. This research opened the way for the wide use of NiFe/IrMn structure as a planar Hall sensor, especially for biological applications. To combine the high sensitivity and the high area of detection, Tu, *et al* developed an array of 24 planar Hall sensors, each sensor has a size of $w \times w = 9\ \mu\mathrm{m}^2$ based on NiFe (20 nm)/IrMn (10 nm) bilayer structure. The sensors in the middle of the array showed a sensitivity of 2.5 mΩ Oe^{-1} and the sensor at the edge showed a sensitivity of 2.3 mΩ Oe^{-1}. These sensitivities allow the sensors to detect a single micromagnetic bead with a signal significantly higher compared to the signals of the micro magnetic beads in that period [148]. Although magnetic beads can be detected by placing them directly on the top of the sensor. The development of on-chip magnetic biosensors that provide easily repeatable results, may require the use of microfluidic systems. In order to compare the performance of the bridge and the cross planar Hall sensors for biological applications, Dalslet *et al* measured the Browning relaxation of magnetic nanobeads using both sensors [209]. The study showed that the signals measured by the bridge sensor are six times higher than those measured by the cross sensor.

Table 2. Illustration of the numerical value of sensitivity for the most common structures for planar Hall effect-based sensors.

Sensor architecture	Sensor structure	Sensitivity	Authors	Reference
Cross 3 × 3 μm^2	bilayer NiFe(20 nm)/IrMn(10 nm)	25 V/AT	Tu *et al*	[148]
Cross 5 × 5 μm^2	Trilayer NiFe(10)/Pt(0.8)/IrMn(8 nm)	38 V/AT	Pişkin *et al*	[162]
Cross 20 × 20 μm^2	Bilayer NiFe (30 nm)/IrMn(20 nm)	49.4 V/AT	Dalslet *et al*	[209]
Tilted cross-junction 5 × 5 μm^2	Trilayer NiFe(10 nm)/Pt(0.8 nm)/IrMn(8 nm)	58 V/AT	Pişkin *et al*	[162]
Cross 3 × 3 μm^2	Spin valve NiFe(16 nm)/Cu(1.2 nm)/NiFe(2 nm)/IrMn(15 nm)	72 V/AT	Hung *et al*	[174]
Tilted cross-junction 100 × 50 μm^2	Spin valve NiFe(6 nm)/Cu(3 nm)/NiFe(3 nm)/IrMn(15 nm)	95 V/AT	Hung *et al*	[189]
Cross 50 × 50 μm^2	Spin valve NiFe(16 nm)/Cu(1.2 nm)/NiFe(2 nm)/IrMn(15 nm) Spin valve	76.15 V/AT	Hung *et al*	[178]
Cross 50 × 50 μm^2	Trilayer NiFe(10 nm)/Cu(0.2 nm)/NiFe(10 nm)	120 V/AT	Hung *et al*	[93, 112]
Cross 50 × 50 μm^2	Trilayer NiFe(10 nm)/Au(0.6 nm)/IrMn(10 nm)	236 V/AT	Li *et al*	[65]
dPHEB (bridge) $n = 1$ arms $l = 250$ (length) μm, $w = 25$ μm	Bilayer NiFe(30 nm)/IrMn(20 nm)	181 V/AT	Østerberg *et al*	[200]
dPHEB (bridge) $n = 2$ arms $l = 250$ (length) μm, $w = 25$ μm	Bilayer NiFe(30 nm)/IrMn(20 nm)	369 V/AT	Østerberg *et al*	[200]
dPHEB $n = 3$ arms $l = 250$ (length) μm, $w = 25$ μm	Bilayer NiFe(30 nm)/IrMn(20 nm)	555 V/AT	Østerberg *et al*	[200]
Ring $n = 1$ (radius = 150 μm, width w = 5 μm)	Trilayer NiFe(10 nm)/Pt(0.8 nm)/IrMn(8 nm)	960 V/AT	Pişkin *et al*	[162]
Ring $n = 5$ (radius = 150 μm, width $w = 5$ μm)	Trilayer NiFe(10 nm)/Pt(0.8 nm)/IrMn(8 nm)	2990 V/AT	Pişkin *et al*	[162]
Multi bridge (mPHEB) $n = 3$ $w = 30$ μm, $l = 600$ μm	bilayer NiFe (30 nm)/IrMn (20 nm)	1757	Henriksen *et al*	[193]
Multi bridge (mPHEB) $n = 5$ $w = 30$ μm, $l = 600$ μm	bilayer NiFe (30 nm)/IrMn (20 nm)	2825	Henriksen *et al*	[193]
Multi bridge (mPHEB) $n = 7$ $w = 30$ μm, $l = 600$ μm	bilayer NiFe (30 nm)/IrMn (20 nm)	3790 V/(AT)	Henriksen *et al*	[193]
Ring $n = 7$ $w = 5$ μm $r = 120$ μm. (the outer radius)	Trilayer NiFe(10)/Cu(0.2)/NiFe(10 nm) trilayer	6350 V/(AT)	Hung *et al*	[197]
Ring $n = 5$ $w = 5$ μm $r = 120$ μm. (the outer radius)	Trilayer NiFe(10 nm)/Cu(0.1 nm)/IrMn(10 nm)	12000 V/AT	Hung *et al*	[196]

Also, the bridge sensors were used in this study to measure the Browning relaxation of nano beads that were hybridized with DNA coil, and the obtained measurements are similar to those found when using a commercial AC susceptometer. The influence of temperature effects and the possibility of exchange biasing have been evaluated by Damsgaard *et al* [43, 151]. The compensation of parasitic magnetic fields by compensation layers was demonstrated by Dalslet *et al* [222]. The effect of the sensor's dimensions, stack, and the applied current on the self-heating of the sensor has been studied by Henriksen *et al* [198]. However, to our knowledge, no study has considered the effect of self-heating on the magnetic state of the beads. Based on these improvements and optimizations on the planar Hall sensor, several papers have been published on the biological uses of such sensors, such as the detection of point mutations in DNA [223], the investigation of DNA denaturation under the effect of temperature or salt [224, 225], and the detection of DNA formed by the rolling circle amplification from a *Vibrio cholerae* DNA target and from a Bacillus globigii bacterial spore target [226]. Recently, PHE sensors have been integrated on flexible substrates, and a sensitivity better than 200 nT was shown by

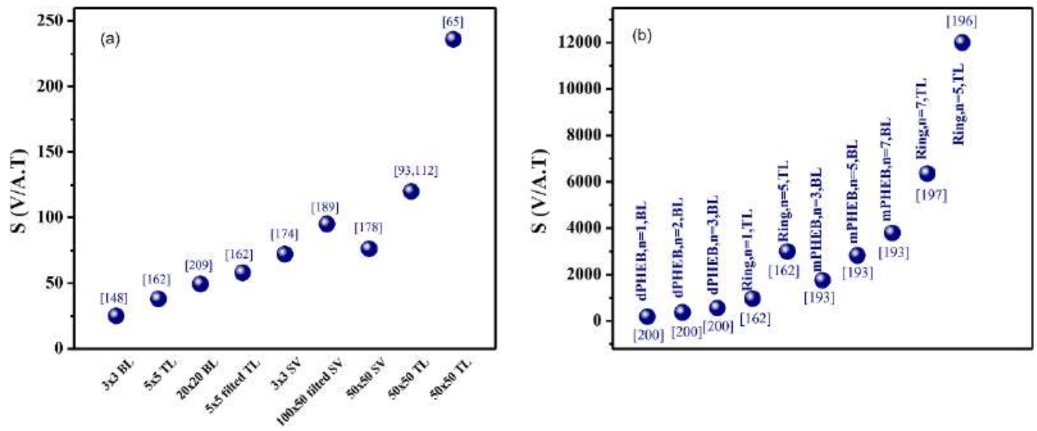

Figure 11. The graphical illustration of the varied sensitivity magnitudes with the junction geometry. (a) the sensitivity of the cross junction where SV, BL, and TL stand for spin valve, bilayer, and trilayer respectively attributed to their references, and (b) The bridge configuration junction sensitivities.

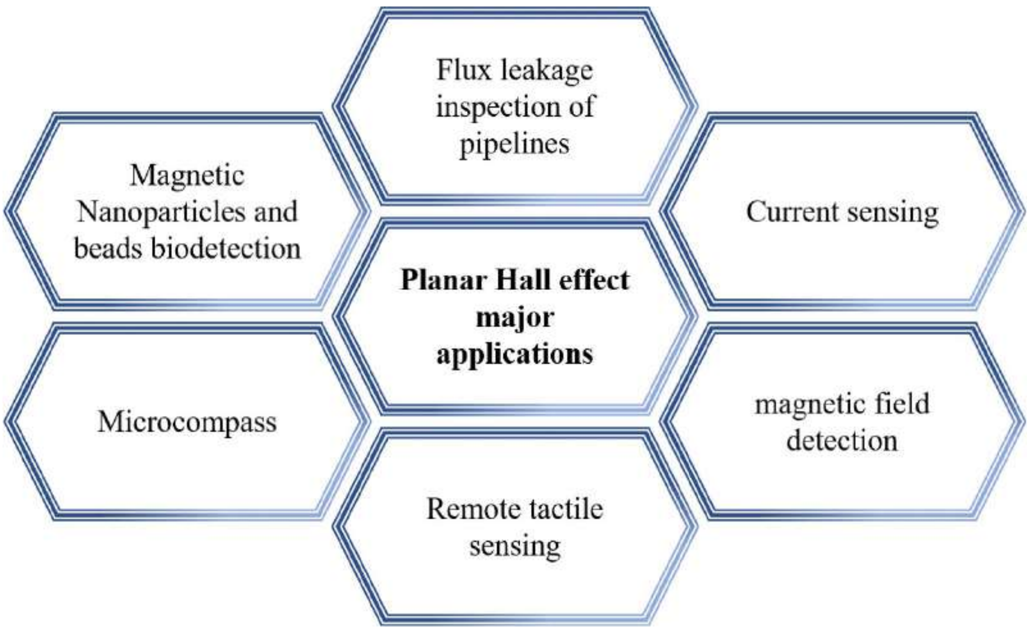

Figure 12. Major areas of application for the planar Hall effect-based sensors.

Granell *et al* [47], which is critically important for wearable devices or other such sensors otherwise attached to the body.

In addition to the detection of biomaterials [227–232], the use of PHE based sensors have been investigated in various application areas, such as magnetic micro/nano-sized particle detection/characterization [233–240], current sensing [241], very low magnetic field detection [53, 129, 242, 243], microelectronic compasses [57, 244], remote tactile sensing [140], and flux leakage inspection of pipelines [44]. Several studies on flexible sensorics also show that flexible PHE sensors can be used in these application areas. These major application areas for PHE-based sensors are presented in figure 12. In the following section, we briefly discuss the MNP detection capability of the PHE sensor with a new technique which can be integrated with a microfluidic channel. Furthermore, the frontier studies of flexible PHE sensors will be addressed.

7.1. PHE sensors for MNPs detection integrated with microfluidic channels

The planar Hall sensor integrated into a microfluidic system was used to inspect the capturing of micromagnetic beads on the sensor [245, 246], and to measure the Browning relaxation of nanomagnetic beads at room temperature [247, 248]. In previous studies, the magnetic beads are magnetized by the electromagnetic field created from the bias current that passes through the sensor. The advantage of this technique is that the magnetic field created from the beads has the same sign wherever the magnetic bead is located [249]. Therefore, the application of a high current inside the sensor increases the magnetic field created by the bead on the active area of the sensor. However, a high applied current can breakdown the sensor or even change the magnetic state of the magnetic bead or the magnetic particles. In contrast to the self-field technique, when an external magnetic field is applied on the magnetic beads, the magnetic field created from beads located outside the sensor has an opposite sign to the magnetic field created by the beads inside the sensor [250], which reduces the total magnetic field created on the sensor.

Here, a new technique is briefly discussed, that was recently developed within an EU H2020 project (MADIA [251]). There MNPs are transported close to the sensors by the microfluidics. Then, in order to avoid external magnetic fields, they are magnetized by the sense current's magnetic field $\vec{H}_{Oe}$ and the stray field of the MNPs is detected by the sensor. As discussed in [31], there are different types of sensors, that can be used for this purpose such as GMR-, TMR- or PHE-sensors that consist of a multilayered thin film stack with magnetic reference and other layers. Because the sensors are located in fluidics, they must be protected by a passivation layer deposited after lithography.

These sensors need to pick up the dipolar stray fields $\vec{H}_S$ of the MNPs, which depend strongly on the magnetic moment of the MNP and the distance between MNP and sensor. Figure 13 shows the calculated strength of $\vec{H}_S$ of a typical MNP as a function of this distance. It is obvious, that the sensors must be able to detect magnetic fields down to some mOe (10^{-7} T), and that the passivation layer between the sensor and the microfluidics should be as thin as possible. The red line indicates the cut-off for a 100 nm thick passivation layer

The most important test for evaluating the potential of different sensor types is, therefore, to measure the sensor response down to ≈0.1 mOe. To exploit the full sensitivity, an AC-measurement technique is used: There, the current through the sensor is driven at a frequency *f*. Simultaneously, the magnetic field is also applied with the same frequency and phase. Then, the resistance of the sense layer will change with the frequency *f*, too. This gives rise to a second harmonic component (frequency 2*f*) of the GMR, TMR and PHE-sensor signal. The basic idea behind this is to magnetize the MNPs directly by the Oersted-field created by the sense current. The major advantage behind this scheme is that the 2*f*-component arises only, if magnetic material is above the sensor.

Figure 14, shows the first and second harmonic response of a PHE sensor operated in this mode to an external DC-field. The sense layer in this example is 10 nm Permalloy, that is weakly RKKY-coupled by 1.8 nm of Ru to a strongly exchange biased Permalloy layer. The 2*f*-signal in this example saturates at ±10 Oe and is slightly shifted to a positive external field by the weak RKKY-coupling. Thus, this coupling has two major advantages: first, it suppresses domain formation in the sense layer, and, second, at zero external field the response is close to linear. It shall be mentioned that a DC sensitivity of 10 μV Oe^{-1} has been reached. The 1*f* signal (left axis in figure 14) shows a signal change of about 20 μV Oe^{-1} in zero field.

The potential to detect fields down to 1 mOe is demonstrated in figure 15, where the results of the sensitivity tests for an exchange biased PHE sensor with a stack sequence $Ru^{5\,nm}$/Mn-$Ir^{10\,nm}$/Ni-$Fe^{4\,nm}$/$Ru^{1.8\,nm}$/Ni–$Fe^{10\,nm}$/$Ta^{2\,nm}$ are shown.

Figure 15 demonstrates the potential of the PHE-sensors to detect small fields down to the range of mOe. Similar results have been obtained for the sensitivity of TMR- and GMR-sensors (not shown).

In addition to mOe sensitivity of the sensor, a magnetic field of some tens of Oersteds is needed to be generated to partially magnetize the MNPs in a microfluidic channel. On the other hand, this external magnetic field must NOT saturate the sensor, because then the detection of the mOe stray fields of the MNPs would be impossible. One approach is to use a single or a pair of highly conducting layers, which upon current loading would generate a magnetic field. This, however, requires additional insulating layers, making the lithographic process complicated and decreasing the yield of working sensor systems. In contrast to TMR-sensors, it is generally possible to use the sensor layers themselves as a field line. In figure 16, we show the calculated magnetic field as a function of the distance to the sensor surface for a typical sensor layout.

It becomes clear, that within a distance that is comparable to the wire width, the field decays only weakly with increasing distance and has amplitudes of some 10 Oe. Taking this into account, the PHE sensor is most probably the best choice. The stray field of the sense current is enough to produce a 1% magnetization in the MNPs that in turn leads to a stray field of some 10 mOe at distances of some μm from the MNP's center. Thus, the scheme to use the sense current itself for magnetizing the MNPs and then apply the 2*f*-Lock-in technique for detection is based on a realistic scenario for sensing MNPs within microfluidics.

An additional critical issue is the passivation layer that must protect the sensors against the fluids in the microfluidic channels. The passivation layer must be free of pinholes and as thin as possible to minimize the distance between the sensor and the MNP (see figure 13). This surface chemistry must be compatible with the requirements for the bonding to the microfluidic channels. For reactively sputtered TaO_X or Al_2O_3 at least about 200 nm thickness is necessary to protect in particular the edges of the sensor. Al_2O_3 layers deposited by atomic layer deposition (ALD) are more promising for protection. There, a $Al(CH_3)_3$-precursor and H_2O gas are let into a reaction chamber in alternating cycles. The precursors can reach all surfaces of a sample and thus can cover edges by a homogeneous Al_2O_3 layer. To evaluate the reliability of the ALD grown passivation layers, stressing by voltage ramping (0 V–10 V) and constant voltage (between 0 V and 10 V) was applied for thicknesses between 5 nm and 50 nm. An Al_2O_3 layer of 20 nm thickness deposited by ALD turned out to provide a reliable protection of the sensors, which is by a factor of 10 thinner than sputter-deposited protections.

For real-world sensor operation, the magnetic field created by the sense current ($\vec{H}_{Oe}$) has to be taken into account. In the case of a multilayer system, the net torque acting on the sense layer's magnetization depends on its position in the stack

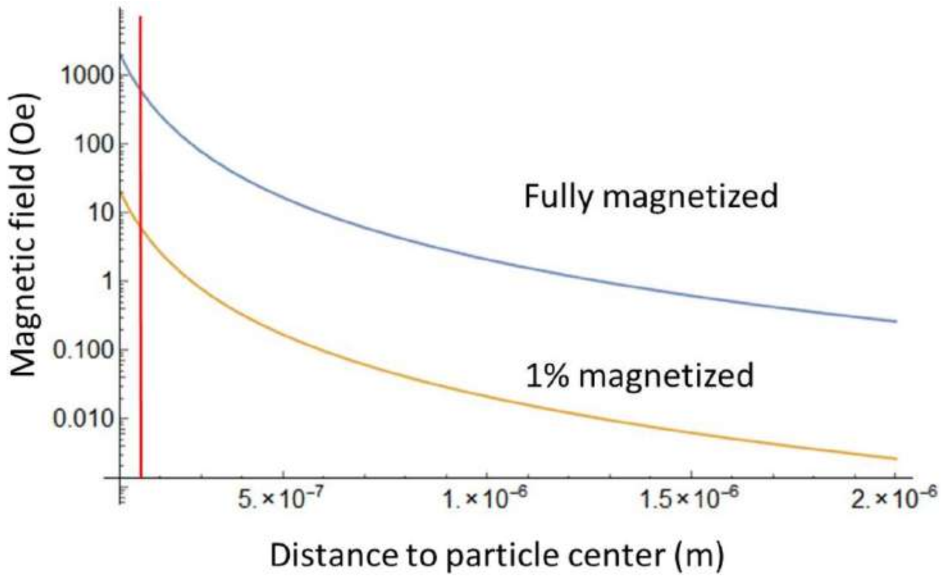

Figure 13. The magnetic stray field of a MNP with saturation magnetization of 500 kA m^{-1} and a diameter of 20 nm as a function of the distance from the particle's center for full magnetization and for 1% of the saturation magnetization.

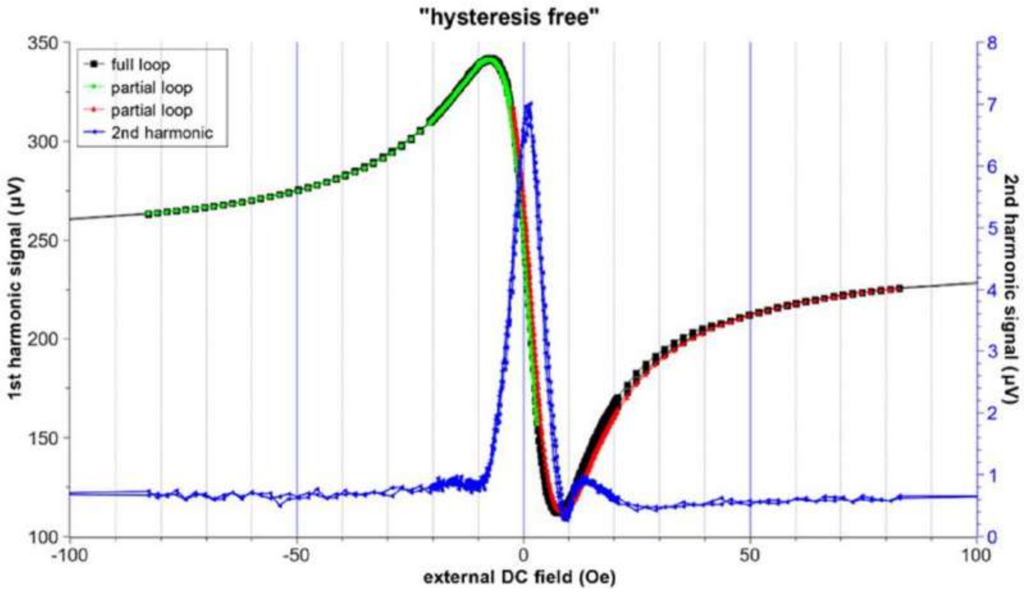

Figure 14. Hysteresis loop in first and second harmonic lock-in detection ($Ru^{5\,nm}$/$Mn–Ir^{10\,nm}$/$Ni–Fe^{4\,nm}$/$Ru^{1.8\,nm}$/**$Ni–Fe^{10\,nm}$**/$Ta^{2\,nm}$ PHE stack) in second harmonic mode. The sense layer FM of the stack is marked in bold.

and on the thicknesses and the electrical conductivities of all layers involved. The influence of the Oersted field in asymmetric PHE stacks on the signal is shown in figure 17. The Oersted field of a DC sensor current of ±20 mA shifts the sensor response by ±2.5 Oe in this particular case.

If one uses an AC sensor current, the resulting $\vec{H}_{\mathrm{Oe}}$ will be an AC field, accordingly. For a quantitative evaluation of the ac $1f$- and $2f$-sensor signal, one needs to understand all contributions to the $1f$ and $2f$ components: As is known, the PHE is intimately related to the AMR. If $\rho_{||}$ is the longitudinal resistivity of a FM material for parallel (orthogonal) alignment of its magnetization and the current, one can define the AMR amplitude as $\left(\rho_{||}-\rho_{\perp}\right)$. The sensor current is taken as an AC current in x-direction: $I_x = I_0 \sin\omega t$. Furthermore, the normalized hysteresis loop of the PHE sensor as a function of an external DC magnetic field in y-direction is described by $f\left(H_y^{\mathrm{DC}}\right)$. The AC sensor current is then directly connected to an AC Oersted field in y-direction: $H_y^{\mathrm{Oe}} = \gamma_y^{\mathrm{Oe}} \mathrm{I}_0 \sin\omega t$, where γ_y^{Oe} is a constant depending on the effective asymmetry of the stack. As the sensor current generates $\vec{H}_{\mathrm{Oe}}$ for partially magnetizing the MNPs and as the stray field of the MNPs will have the same time dependence as their magnetic moment, a similar ansatz can be made for the stray field of the MNPs seen by the sense layer: $H_y^{\mathrm{MNP}} = \gamma_y^{\mathrm{MNP}} I_0 \sin\omega t$, where γ_y^{MNP} is a proportionality factor depending on the susceptibility of

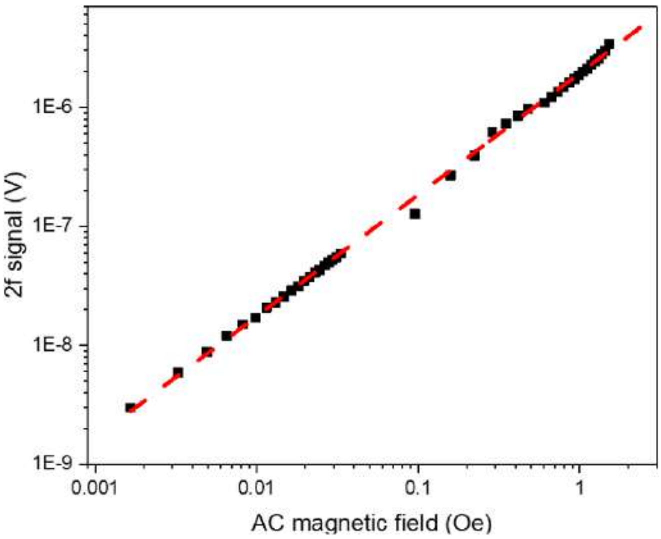

Figure 15. Sensitivity test of the $2f$-signal of a PHE sensor described in the text.

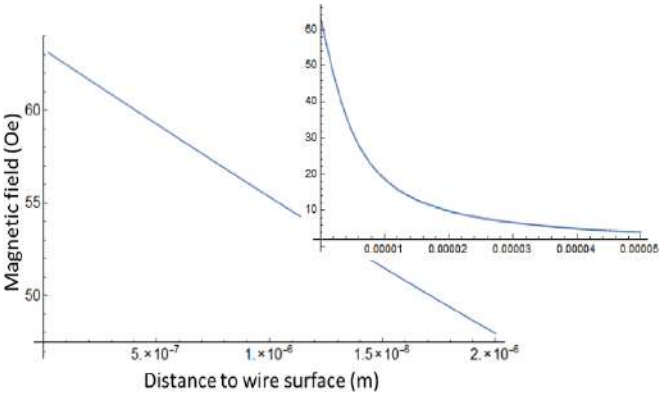

Figure 16. The magnetic field created by a 40 nm thick and 10 μm wide wire at a current of 100 mA as a function of the distance to the wire surface. The inset shows the same up to a distance of 50 μm (calculation by Biot–Savart's law), where the 1/distance dependence appears for distances larger than the wire width.

the MNPs and their lateral distribution in the vicinity of the senor. Finally, a geometric factor Ω_{sensor} takes into account the layer sequence, the sensor width and the total thickness of the sensor. Thus, the voltage analyzed by a lock-in amplifier with respect to the first and second harmonic term becomes:

$$
\begin{aligned}
V_y = {} & \Omega_{\text{sensor}} \left(\rho_{||} - \rho_{\perp}\right) I_0 f\left(H_y^{\text{DC}}\right) \sin\omega t \\
& + \Omega_{\text{sensor}} \left(\rho_{||} - \rho_{\perp}\right) I_0^2 \frac{\partial f\left(H_y^{\text{DC}}\right)}{\partial H_y^{\text{DC}}} |_{H_y^{\text{DC}}} \\
& \times \left(\gamma_y^{\text{MNP}} + \gamma_y^{\text{Oe}}\right) \sin^2\omega t. \qquad (12)
\end{aligned}
$$

The first term is the first harmonic signal which will not change in the presence of MNPs and might be useful for controlling the temperature. The second term includes the signal of the MNPs. If $\vec{H}_{\text{Oe}}$ is balanced ($\gamma_y^{\text{Oe}} = 0$), the second harmonic signal consists of some constants and the proportionality factor of the MNPs in the vicinity of the sensor. This is the required direct signal that can be fed to data processing. A large advantage is, that this signal is equal to zero if no MNPs are present.

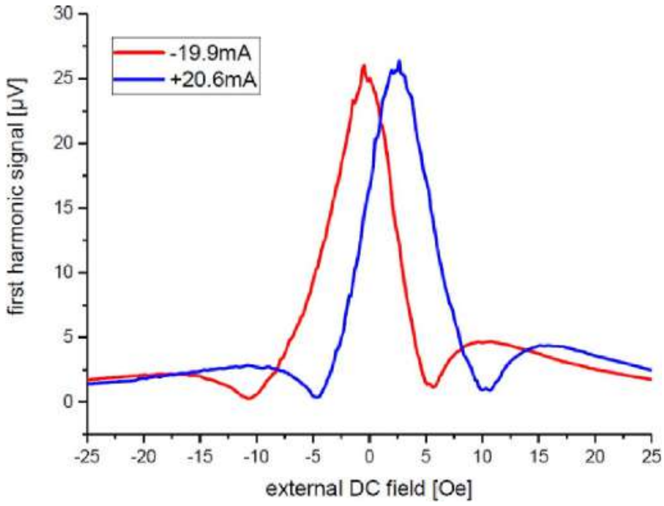

Figure 17. Derivative of hysteresis loops of a PHE sensor. The external DC field is applied in y-direction. As the current flow is in x-direction, the Oersted field must also be aligned in y-direction. We used DC currents of $\pm$20 mA in this case which results in a net Oersted field of about $\pm$2.5 Oe. The derivative has been taken by applying a small additional external AC field in y-direction and by taking the first harmonic lock-in signal.

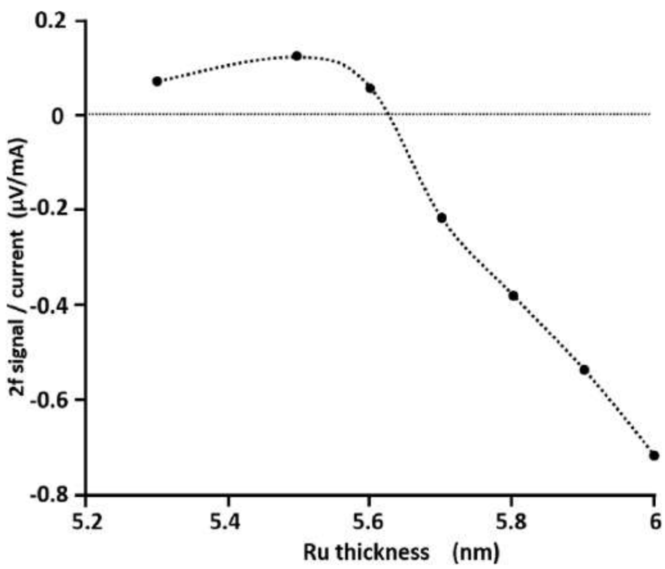

Figure 18. The measured second harmonic signal response of a PHE sensor normalized to the sense current as a function of the thickness of a Ru cap layer. The AC Oersted field in the sense layer is compensated at a Ru thickness between 5.6 nm and 5.7 nm. The dotted curve is a guide for the eye.

The compensation of the Oersted field can be obtained by varying the current distribution in the film stack. In figure 18, as an example the $2f$-signal of a PHE sensor stack is shown normalized to the sense current as a function of the thickness of a Ru-cover layer that is needed for contacting.

Thus, this example shows, that PHE-sensors fulfill the major requirements for detecting MNPs in microfluidics:

Within a Lock-in detection scheme, they can provide a thorough sensitivity and in the $2f$-component, they can be selective to magnetic entities close to the sensor if these entities are magnetized by $\vec{H}_{\mathrm{Oe}}$. In combination with a thin ALD passivation layer, this layout and measurement technique provides optimum conditions for further developing magnetic LOC systems for biotechnology.

7.2. Flexible sensorics based on PHE

Healthcare is a vital area for consideration with new and more powerful types of sensors [252–257]. The integration of PHE-based sensors with wearable devices has increased in recent years. A flexible MR device referring to the PHE was constructed by Oh *et al* [51] using a hybrid process of embedding an Ag nanoparticle electrode with thermal imprinting and magnetic multilayer sensor through sputtering on polyethylene naphthalate substrate. The comparison of the root mean square (RMS) and magnetic properties showed that exchange bias was reduced with the rise in roughness, and that the temperature holds no noteworthy impact on sensor performance. The Ag NP-paste was stable up to $\theta \approx 90°$ during convex bending while the Au electrode was stable up to $\theta \approx 45°$ only. Yet, sensor sensitivity was decreased due to the position of the sensor at the center during bending. The field sensitivity decrement is due to induced stress which increases linearly with the bending up to $\theta = 45°$. Overall, the strain at the sensor position disturbs the field sensitivity of the MR signal that makes it essential to calibrate the signal when subjecting the sensor to static stress. Oh *et al* [50], developed a point-of-care analytic system to spot pathogenic bacteria. The system comprises a PHE sensor in conjunction with a magnetic bead coated by a specific antibody to a bacterial antigen. The sensor with Teflon passivation layer was fabricated over an organic substrate for conferring both flexibility and low-cost. Bacteria thus bound to the magnetic bead was readily distinguished with this sensor with no preceding preparatory steps. The response was measured for *Magnetospirillum magneticum* AMB-1 at a minimum concentration of 1.3×10^8 cells ml^{-1}. Furthermore, *Escherichia coli* was captured by immobilized anti-*E. coli* antibodies on the surface of the sensor and detected using magnetic bead labelled with anti-*E. coli* antibody. The detection limit of *E. coli* was found to be 1.2×10^3 cells ml^{-1}. The design of a new temperature sensor able to detect body temperature by encompassing a magnetic sensor polymer relying on the PHE and a growing polymer was presented by Jeong *et al* [258]. Reliable repeatability, increased sensitivity and precision, and free thermal hysteresis, were demonstrated specifications for the proposed sensor. A differential planar Hall resistive (PHR) sensor was employed for the high precision open-type current sensor. The current sensor was designed to quantify a 1 A current, and nonlinearity of current $\pm 0.5\%$, as an example of a single-chip current sensor using the PHE sensor [45]. With a bioinspired robotic hand designed for tactile sensing, the system mimicked the natural joints of three fingers with both high sensitivity and the capability of grasping diverse items [259]. The application of the PHE for the angle orientation and distance sensors of low fields triggered by magnetic objects was also developed in which a 20 nT limit of detection and high bendability was demonstrated confirmed [47]. The introduction of stable sensitivity through repeatable bending cycles of the PHE sensors was demonstrated. The subjected sensor is very sensitive to stress and strain fluctuations while sensitivity was maintained, thus showing the potential of such sensors for tactile sensing [52]. The bending consequences on the performance of the PHR sensors were considered, in which deformation has a reversible/irreversible threshold point depending on the substrate composition, thus paving the way to applications in medical diagnostics and wearable electronics [141].

8. Conclusion and perspectives

In this review, we have highlighted the most significant research on PHE sensors and their major potential applications. These results can be categorized into four basic sections: firstly, the origin of the AMR effect and theoretical background of PHE and magnetoresistive sensors. Secondly, dissimilar structures, such as simple Permalloy thin film, exchange biased structures (bilayers, trilayers) or spin-valve structures and their implications on the sensor sensitivity, field behavior, and stability. Thirdly, the effects of the sensor geometry on PHE sensitivity, and finally, the integration of these sensors into microfluidics and wearable devices. Micromagnetic simulations that describe the AMR, GMR and PHE in magnetic thin films were presented in order to have a better understanding of the presented data and sensors behavior at very low fields. Besides the aforementioned sections, a demonstration of the basic milestones for the evolution of PHE is displayed. Sensitivity comparison for various structures and junctions was introduced. Sensitivities between 25 V/AT for cross junctions to 12000 V/AT for structures with special sensor geometry such as ring shaped PHR were reported in this paper. It should be mentioned that the advantages of these sensors include higher sensitivity, lower detection limits, lower noise, with consequent increased S/N; hence, the consequences of junction aspect ratio, noise at different frequencies, and thermal stability were presented and discussed. Even though many groups worldwide have investigated these PHE sensors from different points of view, there are still some limitations regarding field sensitivity compared with GMR and TMR sensors, Further studies on new materials with better thermal stability and innovative junction geometries should be considered in order to improve the field sensitivity and to lower the detection limit. The reduction of noise with its different sources in the composed construction of the sensor was discussed. For example, when NiFeCr material was used instead of a Ta capping layer, decreased Barkhausen noise was observed with a S/N ratio increase of 50%. Operation at a wider temperature range is desirable for sensing applications. By careful microfabrication of NiFe/Cu/IrMn trilayer structures, an extremely low variation of a sensitivity of about 4.5×10^{-3} V/A/T/K for an extensive temperature span of -163 °C to 86 °C was reported. However, better sensitivities are offered by other NM spacer layers such as Au, Al_2O_3

deposited by ALD offers better passivation for practical bioapplications. Currently, no reports highlight the consequence of the self-heating on the magnetic state of the beads. For commercial development, further studies are needed on the integration procedures considering the advantages and disadvantages for lower cost and increased feasibility of the prototype devices. All of these areas need to be completely surveyed and monitored for more reliable, faster, and less costly devices for the next generation magnetic sensing technologies.

Data availability statement

All data that support the findings of this study are included within the article (and any supplementary files).

Acknowledgments

Our thanks to Hayden Clement of Charleston, South Carolina, in the United States for reviewing this work for grammatical and syntactic errors. His help is appreciated.

ORCID iDs

Amir Elzwawy https://orcid.org/0000-0003-2206-1616
Hasan Pişkin https://orcid.org/0000-0001-9927-4930
Numan Akdoğan https://orcid.org/0000-0001-8469-5919
Marius Volmer https://orcid.org/0000-0002-1160-9650
Günter Reiss https://orcid.org/0000-0002-0918-5940

References

[1] Mekawy M M, Hassan R Y A, Ramnani P, Yu X and Mulchandani A 2018 Electrochemical detection of dihydronicotinamide adenine dinucleotide using Al_2O_3-GO nanocomposite modified electrode *Arab. J. Chem.* **11** 942–9

[2] Abou Hammad A B, Elzwawy A, Mansour A M, Alam M M, Asiri A M, Karim M R, Rahman M M and El Nahrawy A M 2020 Detection of 3,4-diaminotoluene based on $Sr_{0.3}Pb_{0.7}TiO_3/CoFe_2O_4$ core/shell nanocomposite via an electrochemical approach *New J. Chem.* **44** 7941–53

[3] Alam M K, Rahman M M, Elzwawy A, Torati S R, Islam M S, Todo M, Asiri A M, Kim D and Kim C G 2017 Highly sensitive and selective detection of Bis-phenol A based on hydroxyapatite decorated reduced graphene oxide nanocomposites *Electrochim. Acta* **241** 353–61

[4] Alam M K, Rahman M M, Abbas M, Torati S R, Asiri A M, Kim D and Kim C 2017 Ultra-sensitive 2-nitrophenol detection based on reduced graphene oxide/ZnO nanocomposites *J. Electroanal. Chem.* **788** 66–73

[5] Salih E, Mekawy M, Hassan R Y A and El-Sherbiny I M 2016 Synthesis, characterization and electrochemical-sensor applications of zinc oxide/graphene oxide nanocomposite *J. Nanostruc. Chem.* **6** 137–44

[6] Sedki M, Hassan R Y A, Hefnawy A and El-Sherbiny I M 2017 Sensing of bacterial cell viability using nanostructured bioelectrochemical system: rGO-hyperbranched chitosan nanocomposite as a novel microbial sensor platform *Sens. Actuators* B **252** 191–200

[7] Yang X and Cheng H 2020 Recent developments of flexible and stretchable electrochemical biosensors *Micromachines* **11** 243

[8] Jeerapan I and Poorahong S 2020 Review—flexible and stretchable electrochemical sensing systems: materials, energy sources, and integrations *J. Electrochem. Soc.* **167** 37573

[9] Mani V, Beduk T, Khushaim W, Ceylan A E, Timur S, Wolfbeis O S and Salama K N 2021 Electrochemical sensors targeting salivary biomarkers: a comprehensive review *TrAC Trends Anal. Chem.* **135** 116164

[10] Zhou X, Zhang Y, Yang J, Li J, Luo S and Wei D 2019 Flexible and highly sensitive pressure sensors based on microstructured carbon nanowalls electrodes *Nanomater* **9** 496

[11] Sharma S, Chhetry A, Sharifuzzaman M, Yoon H and Park J Y 2020 Wearable capacitive pressure sensor based on MXene composite nanofibrous scaffolds for reliable human physiological signal acquisition *ACS Appl. Mater. Interfaces* **12** 22212–24

[12] Jeong Y, Park J, Lee J, Kim K and Park I 2020 Ultrathin, biocompatible, and flexible pressure sensor with a wide pressure range and its biomedical application *ACS Sens.* **5** 481–9

[13] Nguyen T, Dinh T, Phan H-P, Nguyen T-K, Md Foisal A R, Nguyen N-T and Dao D V 2020 Opto-electronic coupling in semiconductors: towards ultrasensitive pressure sensing *J. Mater. Chem.* C **8** 4713–21

[14] Cui Z, Poblete F R and Zhu Y 2019 Tailoring the temperature coefficient of resistance of silver nanowire nanocomposites and their application as stretchable temperature sensors *ACS Appl. Mater. Interfaces* **11** 17836–42

[15] Roriz P, Silva S, Frazão O and Novais S 2020 Optical fiber temperature sensors and their biomedical applications *Sensors* **20** 2113

[16] Morsy M, Yahia I S, Zahran H Y, Meng F and Ibrahim M 2019 Portable and battery operated ammonia gas sensor based on CNTs/rGO/ZnO nanocomposite *J. Electron. Mater.* **48** 7328–35

[17] Zhao Z-J, Ko J, Ahn J, Bok M, Gao M, Hwang S H, Kang H-J, Jeon S, Park I and Jeong J-H 2020 3D layer-by-layer Pdcontaining nanocomposite platforms for enhancing the performance of hydrogen sensors *ACS Sens.* **5** 2367–77

[18] Morsy M, Ibrahim M, Yuan Z and Meng F 2020 Graphene foam decorated with ZnO as a humidity sensor *IEEE Sens. J.* **20** 1721–9

[19] Jang J, Kang K, Raeis-Hosseini N, Ismukhanova A, Jeong H, Jung C, Kim B, Lee J-Y, Park I and Rho J 2020 Self-powered humidity sensor using chitosan-based plasmonic metal–hydrogel–metal filters *Adv. Opt. Mater.* **8** 1901932

[20] Kapic A, Tsirou A, Verdini P G and Carrara S 2020 Humidity sensors for high energy physics applications: a review *IEEE Sens. J.* **20** 10335–44

[21] Kuang K 2012 *Magnetic Sensors: Principles and Applications* (BoD–Books on Demand)

[22] Ripka P and Závěta K 2009 Chapter three magnetic sensors: principles and applications Handbook of Magnetic Materials vol 18, ed K H J B T-H of M M Buschow (Amsterdam: Elsevier) pp 347–420 (www.sciencedirect.com/science/article/pii/S1567271909018034)

[23] Karsenty A 2020 A comprehensive review of integrated Hall effects in macro-, micro-, nanoscales, and quantum devices *Sensors* **20** 1–33

[24] Ripka P, Arafat M M B T-R M in M S and M E 2019 *Magnetic Sensors: Principles and Applications* (Amsterdam: Elsevier)

[25] Issadore D, Park Y I, Shao H, Min C, Lee K, Liong M, Weissleder R and Lee H 2014 Magnetic sensing technology for molecular analyses *Lab Chip* **14** 2385–97

[26] Cao B, Wang K, Xu H, Qin Q, Yang J, Zheng W, Jin Q and Cui D 2020 Development of magnetic sensor technologies for point-of-care testing: fundamentals, methodologies and applications *Sens. Actuators* A **312** 112130

[27] Murzin D, Mapps D J, Levada K, Belyaev V, Omelyanchik A, Panina L and Rodionova V 2020 Ultrasensitive magnetic field sensors for biomedical applications *Sensors* **20** 1569

[28] Rizzi G, Lee J-R, Guldberg P, Dufva M, Wang S X and Hansen M F 2017 Denaturation strategies for detection of double stranded PCR products on GMR magnetic biosensor array *Biosens. Bioelectron.* **93** 155–60

[29] Du W Y 2014 *Resistive, Capacitive, Inductive, and Magnetic Sensor Technologies* (Boca Raton, FL: CRC Press)

[30] Su D, Wu K, Saha R, Peng C and Wang J-P 2019 Advances in magnetoresistive biosensors *Micromachines* **11** 34

[31] Freitas P P, Ferreira R, Cardoso S and Cardoso F 2007 Magnetoresistive sensors *J. Phys.: Condens. Matter.* **19** 165221

[32] Tumanski S 2001 *Thin Film Magnetoresistive Sensors* (Boca Raton, FL: CRC Press)

[33] Pannetier M, Fermon C, Le Goff G, Simola J and Kerr E 2004 Femtotesla magnetic field measurement with magnetoresistive sensors *Science* **304** 1648–50

[34] Schotter J, Kamp P B, Becker A, Puhler A, Brinkmann D, Schepper W, Bruckl H and Reiss G 2002 A biochip based on magnetoresistive sensors *IEEE Trans. Magn.* **38** 3365–7

[35] Denmark D J, Bustos-Perez X, Swain A, Phan M H, Mohapatra S and Mohapatra S S 2019 Readiness of magnetic nanobiosensors for point-of-care commercialization *J. Electron. Mater.* **48** 4749–61

[36] Mehrotra P 2016 Biosensors and their applications—a review *J. Oral Biol. Craniofacial Res.* **6** 153–9

[37] Hussein H A, Hassan R Y A, Chino M and Febbraio F 2020 Point-of-care diagnostics of COVID-19: from current work to future perspectives *Sensors* **20** 4289

[38] Anon 2027 Permanent magnets market size & share Industry Report

[39] Hirohata A, Yamada K, Nakatani Y, Prejbeanu L, Diény B, Pirro P and Hillebrands B 2020 Review on spintronics: principles and device applications *J. Magn. Magn. Mater.* **509** 166711

[40] Primdahl F 1979 The fluxgate magnetometer *J. Phys.* E **12** 241–53

[41] Nalwa H S 2002 *Handbook of Thin Film Materials* (New York: Academic)

[42] Weiss R, Mattheis R and Reiss G 2013 Advanced giant magnetoresistance technology for measurement applications *Meas. Sci. Technol.* **24** 082001

[43] Damsgaard C D, Freitas S C, Freitas P P and Hansen M F 2008 Exchange-biased planar Hall effect sensor optimized for biosensor applications *J. Appl. Phys.* **103** 07A302

[44] Pham H Q, Tran B V, Doan D T, Le V S, Pham Q N, Kim K, Kim C, Terki F and Tran Q H 2018 Highly sensitive planar hall magnetoresistive sensor for magnetic flux leakage pipeline inspection *IEEE Trans. Magn.* **54** 1–5

[45] Lee S, Hong S, Park W, Kim W, Lee J, Shin K, Kim C-G and Lee D 2018 High accuracy open-type current sensor with a differential planar hall resistive sensor *Sensors* **18** 2231

[46] Bason Y, Klein L, Yau J B, Hong X, Hoffman J and Ahn C H 2006 Planar Hall-effect magnetic random access memory *J. Appl. Phys.* **99** 08R701

[47] Granell P N, Wang G, Cañon Bermudez G S, Kosub T, Golmar F, Steren L, Fassbender J and Makarov D 2019 Highly compliant planar Hall effect sensor with sub 200 nT sensitivity *Npj Flex Electron.* **3** 3

[48] Turner A P F 2013 Biosensors: sense and sensibility *Chem. Soc. Rev.* **42** 3184–96

[49] Zhou W, JimmyHuang P J, Ding J and Liu J 2014 Aptamer-based biosensors for biomedical diagnostics *Analyst* **139** 2627–40

[50] Oh S, Jadhav M, Lim J, Reddy V and Kim C 2013 An organic substrate based magnetoresistive sensor for rapid bacteria detection *Biosens. Bioelectron.* **41** 758–63

[51] Oh S, Yu J, Lim J, Jadhav M, Lee T, Kim D and Kim C 2013 Highly flexible magnetoelectronic device integrated with embedded Ag nanoparticle electrode *IEEE Sens. J.* **13** 3957–61

[52] Özer B, Pişkin H and Akdoğan N 2019 Shapeable planar hall sensor with a stable sensitivity under concave and convex bending *IEEE Sens. J.* **19** 5493–8

[53] Quynh L K, Hien N T, Binh N H, Dung T T, Tu B D, Duc N H and Giang D T H 2019 Simple planar Hall effect based sensors for low-magnetic field detection *Adv. Nat. Sci. Nanosci. Nanotechnol.* **10** 025002

[54] Anon Products and solutions for intelligent sensor technology Sensitec GmbH

[55] Volmer M and Neamtu J 2010 Electrical and micromagnetic characterization of rotation sensors made from permalloy multilayered thin films *J. Magn. Magn. Mater.* **322** 1631–4

[56] Volmer M and Neamtu J 2012 Optimisation of spin-valve planar Hall effect sensors for low field measurements *IEEE Trans. Magn.* **48** 1577–80

[57] Montaigne F, Schuhl A, Van Dau F N and Encinas A 2000 Development of magnetoresistive sensors based on planar Hall effect for applications to microcompass *Sens. Actuators* A **81** 324–7

[58] Sreevidya P V, Khan J, Barshilia H C, Ananda C M and Chowdhury P 2018 Development of two axes magnetometer for navigation applications *J. Magn. Magn. Mater.* **448** 298–302

[59] Aceinna current sensors—aceinna: leader in MEMS sensor technology (https://www.aceinna.com/current-sensors)

[60] Mușuroi C, Oproiu M, Volmer M and Firastrau I 2020 High sensitivity differential giant magnetoresistance (GMR) based sensor for non-contacting DC/AC current measurement *Sensors* **20** 323

[61] Lin G, Makarov D and Schmidt O G 2017 Magnetic sensing platform technologies for biomedical applications *Lab Chip* **17** 1884–912

[62] Volmer M and Avram M 2015 Using permalloy based planar hall effect sensors to capture and detect superparamagnetic beads for lab on a chip applications *J. Magn. Magn. Mater.* **381** 481–7

[63] Gooneratne C P, Kodzius R, Li F, Foulds I G and Kosel J 2016 On-chip magnetic bead manipulation and detection using a magnetoresistive sensor-based micro-chip: design considerations and experimental characterization *Sensors* **16** 1369

[64] Quang T, Young D, Parvatheeswara B and Kim C 2013 Novel planar Hall sensor for biomedical diagnosing lab-on-a-chip *State of the Art in Biosensors—General Aspects* (Rijeka: InTech)

[65] Li X J, Feng C, Chen X, Zhang J Y, Liu Y W, Jiang S L, Liu Y, Li M H and Yu G H 2015 Enhanced planar hall sensitivity with better thermal stability by introducing interfacial modification of Au spacer *J. Magn. Magn. Mater.* **381** 386–9

[66] Bagherzadeh R, Gorji M, Sorayani Bafgi M S and Saveh-Shemshaki N 2017 Electrospun conductive nanofibers for electronics *Woodhead Publishing Series in*

Textiles ed M B T-E N Afshari (Amsterdam: Woodhead Publishing) pp 467–519
[67] Baibich M N, Broto J M, Fert A, Van Dau F N, Petroff F, Etienne P, Creuzet G, Friederich A and Chazelas J 1988 Giant magnetoresistance of (001)Fe/(001)Cr magnetic superlattices *Phys. Rev. Lett.* **61** 2472–5
[68] Binasch G, Grünberg P, Saurenbach F and Zinn W 1989 Enhanced magnetoresistance in layered magnetic structures with antiferromagnetic interlayer exchange *Phys. Rev.* B **39** 4828–30
[69] Prinz G A 1998 Magnetoelectronics *Science* **282** 1660–3
[70] Yin Z, Bonizzoni E and Heidari H 2018 Magnetoresistive biosensors for on-chip detection and localization of paramagnetic particles *IEEE J. Electromagn. RF Microwaves Med. Biol.* **2** 179–85
[71] Chang C-H, Dou K-P, Chen Y-C, Hong T-M and Kaun C-C 2015 Engineering the interlayer exchange coupling in magnetic trilayers *Sci. Rep.* **5** 16844
[72] Grünberg P A 2001 Exchange anisotropy, interlayer exchange coupling and GMR in research and application *Sens. Actuators* A **91** 153–60
[73] Meiklejohn W H and Bean C P 1956 New magnetic anisotropy *Phys. Rev.* **102** 1413–4
[74] Nogués J and Schuller I K 1999 Exchange bias *J. Magn. Magn. Mater.* **192** 203–32
[75] Vedmedenko E Y *et al* 2020 The 2020 magnetism roadmap *J. Phys. D: Appl. Phys.* **53** 453001
[76] Moodera J S, Kinder L R, Wong T M and Meservey R 1995 Large magnetoresistance at room temperature in ferromagnetic thin film tunnel junctions *Phys. Rev. Lett.* **74** 3273–6
[77] Vidal E G, Muñoz D R, Arias S I R, Moreno J S, Cardoso S, Ferreira R and Freitas P 2017 Electronic energy meter based on a tunnel magnetoresistive effect (TMR) current sensor *Materials* **10** 1134
[78] Ribeiro P, Cardoso S, Bernardino A and Jamone L Highly sensitive bio-inspired sensor for fine surface exploration and characterization
[79] Nishi Y and Magyari-Kope B 2019 *Advances in Non-volatile Memory and Storage Technology* (Cambridge: Woodhead Publishing)
[80] Feng Y, Liu J, Klein T, Wu K and Wang J-P 2017 Localized detection of reversal nucleation generated by high moment magnetic nanoparticles using a large-area magnetic sensor *J. Appl. Phys.* **122** 123901
[81] Thomson W 1857 XIX. On the electro-dynamic qualities of metals:—effects of magnetization on the electric conductivity of nickel and of iron *Proc. R. Soc.* A **8** 546–50
[82] Tumanski S 2016 *Handbook of Magnetic Measurements* (Boca Raton, FL: CRC press)
[83] West F G 1963 Rotating-field technique for galvanomagnetic measurements *J. Appl. Phys.* **34** 1171–3
[84] McGuire T and Potter R 1975 Anisotropic magnetoresistance in ferromagnetic 3d alloys *IEEE Trans. Magn.* **11** 1018–38
[85] Ky V D 1967 Theory of the anisotropy of resistance in ferromagnetic metals *Sov. Phys. JETP* **24** 995–9
[86] Rüffer D, Huber R, Berberich P, Albert S, Russo-Averchi E, Heiss M, Arbiol J, Fontcuberta I M A and Grundler D 2012 Magnetic states of an individual Ni nanotube probed by anisotropic magnetoresistance *Nanoscale* **4** 4989–95
[87] Stavroyiannis S 2003 Planar Hall effect and magnetoresistance in $Ni_{81}Fe_{19}$ and Co square shaped thin films *Solid State Commun.* **125** 333–6
[88] Zhao B, Yan X and Pakhomov A B 1997 Anisotropic magnetoresistance and planar Hall effect in magnetic metal-insulator composite films *J. Appl. Phys.* **81** 5527–9
[89] Anon Low-cost, high-performance angular measurement
[90] O'Handley R C 2003 Magnetic materials *Encyclopedia of Physical Science and Technology* ed R A B T-E of P S and Third E Meyers (Amsterdam: Elsevier) pp 919–44
[91] Ejsing L, Hansen M F, Menon A K, Ferreira H A, Graham D L and Freitas P P 2005 Magnetic microbead detection using the planar Hall effect *J. Magn. Magn. Mater.* **293** 677–84
[92] Li X J *et al* 2014 Large enhancement of planar Hall sensitivity in NiO/NiFe/NiO heterostructure by interfacial modification *Mater. Lett.* **126** 101–4
[93] Hung T Q, Oh S, Sinha B, Jeong J-R, Kim D-Y and Kim C 2010 High field-sensitivity planar Hall sensor based on NiFe/Cu/IrMn trilayer structure *J. Appl. Phys.* **107** 09E715
[94] Mahfoud M *et al* 2019 Reduced thermal dependence of the sensitivity of a planar Hall sensor *Appl. Phys. Lett.* **115** 072402
[95] Antonov I, Vatsktichev L and Vatskitcheva M 1997 Planar Hall effect in thin magnetic films with domain structure *J. Magn. Magn. Mater.* **169** 25–30
[96] Santos J A M, Kakazei G N, Pereira A M, Pogorelov Y G, Carpinteiro F S and Sousa J B 2001 Galvanomagnetic effects in $Ni_{81}Fe_{19}$ thin films under in-plane and out-of-plane magnetic field *Mater. Sci. Forum* **373–376** 509–12
[97] Kim H, Reddy V, Kim K W, Jeong I, Hu X H and Kim C G 2014 Single magnetic bead detection in a microfluidic chip using planar hall effect sensor *J. Magn.* **19** 10–14
[98] Anon PC micromagnetics simulator release 2.0
[99] Oh S J, Le T T, Kim G W and Kim C G 2007 Size effect on NiFe/Cu/NiFe/IrMn spin-valve structure for an array of PHR sensor element *Phys. Status Solidi Appl. Mater. Sci.* **204** 4075–8
[100] Elzwawy A, Kim S, Talantsev A and Kim C 2019 Equisensitive adjustment of planar Hall effect sensor's operating field range by material and thickness variation of active layers *J. Phys. D: Appl. Phys.* **52** 285001
[101] Ngan Luong T Q, Cao T A and Cao Dao T 2013 Low-concentration organic molecules detection via surface-enhanced Raman spectroscopy effect using Ag nanoparticles-coated silicon nanowire arrays *Adv. Nat. Sci. Nanosci. Nanotechnol.* **4** 015017
[102] Épshtein É M 2002 Planar hall effect in ferromagnets *Phys. Solid State* **44** 1327–9
[103] Jeon T, Lee J H, Talantsev A and Kim C G 2019 Planar Hall resistance sensor with improved thermal stability *IEEE Magn. Lett.* **10** 1–5
[104] Hunte F 2004 *Determination of Exchange Anisotropy by ac-AMR and Planar Hall Effect* (Minneapolis: University of Minnesota)
[105] Lee K J *et al* 2018 Magnetization reversal in trilayer structures consisting of GaMnAs layers with opposite signs of anisotropic magnetoresistance *Sci. Rep.* **8** 2288
[106] Vig J R and Walls F L 2000 A review of sensor sensitivity and stability *Proceedings of the 2000 IEEE/EIA Int. Frequency Control Symp. and Exhibition (Cat. No.00CH37052)* pp 30–33
[107] Scheinfein M R and Price E A 1997 LLG user manual v2. 50 code LLG simulator can be found (available at: http://llgmicro.home.mindspring.com)
[108] Lim J, Sinha B, Ramulu T S, Kim K, Kim D-Y and Kim C 2013 NiCo sensing layer for enhanced signals in planar hall effect sensors *Met. Mater. Int.* **19** 875–8
[109] Bason Y, Klein L, Yau J-B, Hong X and Ahn C H 2004 Giant planar Hall effect in colossal magnetoresistive $La_{0.84}Sr_{0.16}MnO_3$ thin films *Appl. Phys. Lett.* **84** 2593–5

[110] Thanh N T, Kim K W, Kim C O, Shin K H and Kim C G 2007 Microbeads detection using planar Hall effect in spin-valve structure *J. Magn. Magn. Mater.* **316** e238–41
[111] Won J, Shin J, Lee S, Lee H, Yoo T, Lee S, Liu X and Furdyna J K 2013 Planar Hall effect in a single GaMnAs film grown on Si substrate *J. Cryst. Growth* **378** 361–4
[112] Hung T Q, Oh S, Anandakumar S, Jeong J R, Kim D Y and Kim C 2009 Optimization of the multilayer structures for a high field-sensitivity biochip sensor based on the planar Hall effect *IEEE Trans. Magn.* **45** 4518–21
[113] Lu Z Q, Pan G, Lai W Y, Mapps D J and Clegg W W 2002 Exchange anisotropy in NiFe/FeMn bilayers studied by planar Hall effect *J. Magn. Magn. Mater.* **242–245** 525–8
[114] Lu Z Q, Pan G and Lai W Y 2001 Planar Hall effect in NiFe/NiMn bilayers *J. Appl. Phys.* **90** 1414–8
[115] Li G, Yang T, Hu Q and Lai W 2000 Exchange coupling in NiFe/NiMn films studied by pseudo-Hall effect *Appl. Phys. Lett.* **77** 1032–4
[116] Kim D Y, Park B S and Kim C G 2000 Optimization of planar Hall resistance using biaxial currents in a NiO/NiFe bilayer: enhancement of magnetic field sensitivity *J. Appl. Phys.* **88** 3490–4
[117] Nemoto A, Otani Y, Kim S G, Fukamichi K, Kitakami O and Shimada Y 1999 Magnetoresistance and planar Hall effects in submicron exchange-coupled NiO/$Fe_{19}Ni_{81}$ wires *Appl. Phys. Lett.* **74** 4026–8
[118] Chen Y-T 2008 The effect of interface texture on exchange biasing in $Ni_{80}Fe_{20}/Ir_{20}Mn_{80}$System *Nanoscale Res. Lett.* **4** 90
[119] Anderson G, Huai Y and Miloslawsky L 2000 CoFe/IrMn exchange biased top, bottom, and dual spin valves *J. Appl. Phys.* **87** 6989–91
[120] Ky V D 1968 Planar Hall effect in ferromagnetic films *Phys. Status Solidi* **26** 565–9
[121] Goldberg C and Davis R E 1954 New galvanomagnetic effect *Phys. Rev.* **94** 1121–5
[122] Yau K L and Chang J T H 1971 The planar Hall effect in thin foils of Ni-Fe alloy *J. Phys.* F **1** 38–43
[123] Ky V D 1965 N IA 2-Dimension galvanomagnetic effect in thin ferromagnetic films *Ser. Fiz.* **29** 576
[124] Ky V D 1967 Planar Hall and nernst effect in ferromagnetic metals *Phys. Status Solidi* **22** 729–36
[125] Ky V D 1966 Plane Hall effect in ferromagnetic metals *Sov. Phys. JETP* **23** 809–13
[126] Ky V D 1966 The nernst effect in permalloy films *Phys. Status Solidi* **17** K203–5
[127] Vatskichev L, Mucha J, Georgiev Z and Vatskicheva M 1990 Measurements of the rotational hysteresis losses in magnetic films by the planar hall effect *Phys. Status Solidi* **118** K95–7
[128] Berger L 1991 Galvanomagnetic voltages in the vicinity of a domain wall in ferromagnetic thin films *J. Appl. Phys.* **69** 1550–5
[129] Schuhl A, Van Dau F N and Childress J R 1995 Low-field magnetic sensors based on the planar Hall effect *Appl. Phys. Lett.* **66** 2751–3
[130] Schuhl A, Van Dau F N and Childress J R 1995 Nanotesla detection using the planar hall effect *Mater. Res. Soc. Symp. Proc.* **384** 15–20
[131] Van Dau F N, Schuhl A, Childress J R and Sussiau M 1996 Magnetic sensors for nanotesla detection using planar Hall effect *Sens. Actuators* A **53** 256–60
[132] Ogrin F Y, Lee S L and Ogrin Y F 2000 Investigation of perpendicular anisotropy of a thin film using the planar Hall effect *J. Magn. Magn. Mater.* **219** 331–9
[133] Rizzi G 2014 Planar Hall effect sensors for biodetection Ph.D. Thesis Technical University of Denmark
[134] Volmer M and Avram M 2013 Signal dependence on magnetic nanoparticles position over a planar Hall effect biosensor *Microelectron. Eng.* **108** 116–20
[135] Ejsing L W 2006 *Planar Hall Sensor for Influenza Immunoassay* (Kongens Lyngby: MIC-Department of Micro and Nanotechnology, Technical University of Denmark)
[136] Oh S, Anandakumar S, Lee C, Kim K W, Lim B and Kim C 2011 Analytes kinetics in lateral flow membrane analyzed by cTnI monitoring using magnetic method *Sens. Actuators* B **160** 747–52
[137] Henriksen A D, Rizzi G and Hansen M F 2015 Experimental comparison of ring and diamond shaped planar Hall effect bridge magnetic field sensors *J. Appl. Phys.* **118** 103901
[138] Lee S, Bac S-K, Choi S, Lee H, Yoo T, Lee S, Liu X, Dobrowolska M and Furdyna J K 2017 Non-volatile logic gates based on planar Hall effect in magnetic films with two in-plane easy axes *Sci. Rep.* **7** 1115
[139] Elzwawy A, Talantsev A and Kim C G 2018 Free and forced Barkhausen noises in magnetic thin film based cross-junctions *J. Magn. Magn. Mater.* **458** 292–300
[140] Oh S, Jung Y, Kim S, Kim S, Hu X, Lim H and Kim C 2017 Remote tactile sensing system integrated with magnetic synapse *Sci. Rep.* **7** 16963
[141] Kim M, Oh S, Jeong W, Talantsev A, Jeon T, Chaturvedi R, Lee S and Kim C 2020 Highly bendable planar Hall resistance sensor *IEEE Magn. Lett.* **11** 1–5
[142] Ky V-D 1966 Plane hall effect in ferromagnetic metals *J. Exp. Theor. Phys.* **23** 809
[143] Chang C-R 2000 A hysteresis model for planar Hall effect in thin films *IEEE Trans. Magn.* **36** 1214–7
[144] Battarel C and Galinier M 1969 Optimization of the planar hall effect in ferromagnetic thin films for device design *IEEE Trans. Magn.* **5** 18–22
[145] Ejsing L, Hansen M F, Menon A K, Ferreira H A, Graham D L and Freitas P P 2004 Planar hall effect sensor for magnetic micro- and nanobead detection *Appl. Phys. Lett.* **84** 4729–31
[146] Roy A, Sampathkumar P and Anil Kumar P S 2020 Development of a very high sensitivity magnetic field sensor based on planar Hall effect *Measurement* **156** 107590
[147] Nhalil H, Givon T, Das P T, Hasidimn N, Mor V, Schultz M, Amrusi S, Klein L and Grosz A 2019 Planar Hall effect magnetometer with 5 pT resolution *IEEE Sens. Lett.* **3** 1–4
[148] Tu B D, Hung T Q, Thanh N T, Danh T M, Duc N H and Kim C G 2008 Planar Hall bead array counter microchip with NiFe/IrMn bilayers *J. Appl. Phys.* **104** 1–5
[149] Chui K M, Adeyeye A O and Li M H 2008 Effect of seed layer on the sensitivity of exchange biased planar Hall sensor *Sens. Actuators* A **141** 282–7
[150] Qejvanaj F, Zubair M, Persson A, Mohseni S M, Fallahi V, Sani S R, Chung S, Le T, Magnusson F and Akerman J 2014 Thick double-biased IrMn/NiFe/IrMn planar hall effect bridge sensors *IEEE Trans. Magn.* **50** 4006104
[151] Damsgaard C D, Dalslet B T, Freitas S C, Freitas P P and Hansen M F 2009 Temperature effects in exchange-biased planar hall sensors for bioapplications *Sens. Actuators* A **156** 103–8
[152] Thanh N T, Chun M G, Ha N D, Kim K Y, Kim C O and Kim C G 2006 Thickness dependence of exchange anisotropy in NiFe/IrMn bilayers studied by planar Hall effect *J. Magn. Magn. Mater.* **305** 432–5
[153] Thanh N T *et al* 2007 Thickness dependence of parallel and perpendicular anisotropic resistivity in Ta/NiFe/IrMn/Ta multilayer studied by anisotropic magnetoresistance and planar Hall effect *J. Appl. Phys.* **101** 53702

[154] Kim D Y, Kim C G, Park B S and Park C M 2000 Thickness dependence of planar Hall resistance and field sensitivity in NiO(30 nm)/NiFe(t) bilayers *J. Magn. Magn. Mater.* **215** 585–8

[155] Zhao Z D, Li M H, Kang P, Zhao C J, Zhang J Y, Zhou L J, Zhao Y C, Jiang S L and Yu G H 2015 The influence of ultrathin Cu interlayer in NiFe/IrMn interface on rotation of the magnetic moments *Appl. Surf. Sci.* **332** 710–5

[156] Li X J, Feng C, Chen X, Liu Y, Liu Y W, Li M H and Yu G H 2014 Effects of interfacial roughness on the planar Hall effect in NiFe/Cu/IrMn multilayers *Appl. Phys.* A **118** 505–9

[157] Morgunov R B, Talantsev A D, Bakhmet'ev M V and Granovskii N V 2020 Exchange interactions in NiFe/Ta/IrMn heterostructures under conditions of tantalum deficiency *Phys. Solid State* **62** 1033–8

[158] Gökemeijer N J, Ambrose T and Chien C L 1997 Long-range exchange bias across a spacer layer *Phys. Rev. Lett.* **79** 4270–3

[159] Yoo Y-G-G, Min S-G-G and Yu S-C-C 2006 Influence of spacer layer in exchange coupled NiFe/Cu/IrMn trilayer structure *J. Magn. Magn. Mater.* **304** e718–20

[160] Thomas L, Kellock A J and Parkin S S P 2000 On the exchange biasing through a nonmagnetic spacer layer *J. Appl. Phys.* **87** 5061–3

[161] Li K, Guo Z, Han G, Qiu J and Wu Y 2003 Abnormal temperature dependence of exchange bias in the NiFe5/Ta0.2/IrMn8 system *J. Appl. Phys.* **93** 6614–6

[162] Pişkin H and Akdoğan N 2019 Interface-induced enhancement of sensitivity in NiFe/Pt/IrMn-based planar hall sensors with nanoTesla resolution *Sens. Actuators* A **292** 24–29

[163] Pişkin H 2020 Fabrication and Characterization of NiFe/X/IrMn (X: Cu, Cr, Pt)-Based Planar Hall Effect Sensors Ph.D Thesis (Gebze Technical University)

[164] Pişkin H and Akdoğan N 2020 Tuning the magnetic field sensitivity of planar Hall effect sensors by using a Cr spacer layer in a NiFe/Cr/IrMn trilayer structure *Turk. J. Phys.* **44** 554–63

[165] Demirci E 2020 Anisotropic magnetoresistance and planar Hall effect in magnetoresistive NiFe/Pt thin film *Turk. J. Phys.* **44** 77–84

[166] Xu Y, Yang Y, Xie H and Wu Y 2019 Spin Hall magnetoresistance sensor using Au_xPt_{1-x} as the spin-orbit torque biasing layer *Appl. Phys. Lett.* **115** 182406

[167] Cho S, Baek S C, Lee K-D, Jo Y and Park B-G 2015 Large spin Hall magnetoresistance and its correlation to the spin-orbit torque in W/CoFeB/MgO structures *Sci. Rep.* **5** 14668

[168] Nguyen M-H, Zhao M, Ralph D C and Buhrman R A 2016 Enhanced spin Hall torque efficiency in $Pt_{100-x}Al_x$ and $Pt_{100-x}Hf_x$ alloys arising from the intrinsic spin Hall effect *Appl. Phys. Lett.* **108** 242407

[169] Zhu L, Zhu L, Shi S, Sui M, Ralph D C and Buhrman R A 2019 Enhancing spin-orbit torque by strong interfacial scattering from ultrathin insertion layers *Phys. Rev. Appl.* **11** 61004

[170] Kim J, Sheng P, Takahashi S, Mitani S and Hayashi M 2016 Spin hall magnetoresistance in metallic bilayers *Phys. Rev. Lett.* **116** 97201

[171] Talantsev A, Elzwawy A and Kim C 2018 Effect of NiFeCr seed and capping layers on exchange bias and planar Hall voltage response of NiFe/Au/IrMn trilayer structures *J. Appl. Phys.* **123** 173902

[172] Henriksen A D, Rizzi G and Hansen M F 2016 Planar Hall effect bridge sensors with NiFe/Cu/IrMn stack optimized for self-field magnetic bead detection *J. Appl. Phys.* **119** 93910

[173] Thanh N T, Parvatheeswara Rao B, Duc N H and Kim C 2007 Planar Hall resistance sensor for biochip application *Phys. Status Solidi Appl. Mater. Sci.* **204** 4053–7

[174] Hung T Q, Oh S, Jeong J R and Kim C G 2010 Spin-valve planar Hall sensor for single bead detection *Sens. Actuators* A **157** 42–46

[175] Jeong I, Eu Y J, Kim K W, Hu X H, Sinha B and Kim C G 2012 Magnetic sensor-based detection of picoliter volumes of magnetic nanoparticle droplets in a microfluidic chip *J. Magn.* **17** 302–7

[176] Bui D T, Tran M D, Nguyen H D and Nguyen H B 2012 Influence of CoFe and NiFe pinned layers on sensitivity of planar Hall biosensors based on spin-valve structures *Adv. Nat. Sci. Nanosci. Nanotechnol.* **3** 045019

[177] Neamtu J, Volmer M and Neamtu M C 2018 Spin-valve structures with anisotropic magneto-resistance (AMR) for planar Hall effect (PHE) sensing applications *Optoelectron. Adv. Mater. Commun.* **12** 603–7

[178] Hung T Q, Oh S J, Tu B D, Duc N H, Phong L V, AnandaKumar S, Jeong J R and Kim C G 2009 Sensitivity dependence of the planar Hall effect sensor on the free layer of the spin-valve structure *IEEE Trans. Magn.* **45** 2374–7

[179] Tu B D, Cuong L V, Hung T Q, Giang D T H, Danh T M, Duc N H and Kim C 2009 Optimization of spin-valve structure NiFe/Cu/NiFe/IrMn for planar hall effect based biochips *IEEE Trans. Magn.* **45** 2378–82

[180] Wang S, Gao T, Wang C and He J 2013 Studies of anisotropic magnetoresistance and magnetic property of Ni81Fe19ultra-thin films with the lower base vacuum *J. Alloys Compd.* **554** 405–7

[181] Lee W-Y, Toney M F, Tameerug P, Allen E and Mauri D 2000 High magnetoresistance permalloy films deposited on a thin NiFeCr or NiCr underlayer *J. Appl. Phys.* **87** 6992–4

[182] Lee W Y, Toney M F and Mauri D 2000 High magnetoresistance in sputtered Permalloy thin films through growth on seed layers of $(Ni_{0.81}Fe_{0.19})_{1-x}Cr_x$ *IEEE Trans. Magn.* **36** 381–5

[183] Sheng S, Li W, Li M and Yu G 2012 Investigation on interface of NiFeCr/NiFe/Ta films with high magnetic field sensitivity *Rare Met.* **31** 22–26

[184] He J F and Wang S Y 2012 Effects of substrate temperature and buffer layer on the anisotropic magnetoresistance of Ni_{81} Fe_{19} ultra thin films *Optoelectron. Adv. Mater. Commun.* **6** 165–8

[185] Elzawawy A A I 2019 Fabrication and optimization of magnetoresistive thin film structure for improved spintronic sensors *Doctoral dissertation* DGIST

[186] Liu J, Duan C-K and Zheng R L 2005 Influence of seed layer NiFeNb on magnetic properties of nanometer permalloy films *Int. J. Mod. Phys.* B **19** 621–5

[187] Wang S, Wang C, Gao Y, Gao T, Hu G and Zhang H 2013 Anisotropic magnetoresistance of $Ni_{81}Fe_{19}$ films on NiFeNb buffer layer *J. Alloys Compd.* **575** 419–22

[188] Kim C G, Park B S, Kim D Y, Song J S and Min B K 2001 Combined effects of MR and PHR Using biaxial currents in NiO/NiFe *Mater. Sci. Forum* **373–376** 365–8

[189] Hung T Q, Jeong J-R, Kim D-Y, Duc N H and Kim C 2009 Hybrid planar Hall-magnetoresistance sensor based on tilted cross-junction *J. Phys. D: Appl. Phys.* **42** 55007

[190] Donolato M, Dalslet B T, Damsgaard C D, Gunnarsson K, Jacobsen C S, Svedlindh P and Hansen M F 2011 Size-dependent effects in exchange-biased planar Hall effect sensor crosses *J. Phys. D: Appl. Phys.* **109** 064511

[191] Li M, Zhao Z, Ma L, Yu G G, Lu X, Teng J, Yu G G, Zhou W, Amiri P K and Wang K L 2015 The influence of an MgO nanolayer on the planar Hall effect in NiFe films *J. Appl. Phys.* **117** 123908

[192] Hung T Q, Rao B P and Kim C 2009 Planar Hall effect in biosensor with a tilted angle of the cross-junction *J. Magn. Magn. Mater.* **321** 3839–41
[193] Henriksen A D, Dalslet B T, Skieller D H, Lee K H, Okkels F and Hansen M F 2010 Planar Hall effect bridge magnetic field sensors *Appl. Phys. Lett.* **97** 13507
[194] Oh S, Patil P B, Hung T Q, Lim B, Takahashi M, Kim D Y and Kim C 2011 Hybrid AMR/PHR ring sensor *Solid State Commun.* **151** 1248–51
[195] Persson A, Bejhed R S, Nguyen H, Gunnarsson K, Dalslet B T, Østerberg F W, Hansen M F and Svedlindh P 2011 Low-frequency noise in planar Hall effect bridge sensors *Sens. Actuators* A **171** 212–8
[196] Hung T Q, Terki F, Kamara S, Kim K, Charar S and Kim C 2015 Planar Hall ring sensor for ultra-low magnetic moment sensing *J. Appl. Phys.* **117** 154505
[197] Sinha B, Hung T Q, Ramulu T S, Oh S, Kim K, Kim D-Y, Terki F and Kim C 2013 Planar Hall resistance ring sensor based on NiFe/Cu/IrMn trilayer structure *J. Appl. Phys.* **113** 63903
[198] Henriksen A D, Rizzi G, Østerberg F W and Hansen M F 2015 Optimization of magnetoresistive sensor current for on-chip magnetic bead detection using the sensor self-field *J. Magn. Magn. Mater.* **380** 209–14
[199] Qejvanaj F, Mazraati H, Jiang S, Persson A, Sani S R, Chung S, Magnusson F and Åkerman J 2015 Planar hall-effect bridge sensor with NiFeX (X = Cu, Ag, and Au) sensing layer *IEEE Trans. Magn.* **51** 4005404
[200] Østerberg F W, Rizzi G, Henriksen A D and Hansen M F 2014 Planar Hall effect bridge geometries optimized for magnetic bead detection *J. Appl. Phys.* **115** 184505
[201] Sinha B, Oh S, Ramulu T S, Lim J, Kim D Y and Kim C G 2011 Planar hall effect ring sensors for high field-sensitivity *Adv. Mater. Res.* **317–319** 1136–40
[202] Mor V, Schultz M, Sinwani O, Grosz A, Paperno E and Klein L 2012 Planar Hall effect sensors with shape-induced effective single domain behavior *J. Appl. Phys.* **111** 07E519
[203] Hansen M F and Rizzi G 2017 Exchange-biased AMR bridges for magnetic field sensing and biosensing *IEEE Trans. Magn.* **53** 1–11
[204] Jen S U, Lee J Y, Yao Y D and Chen W L 2001 Transverse field dependence of the planar Hall effect sensitivity in permalloy films *J. Appl. Phys.* **90** 6297–301
[205] Hirohata A, Yao C C, Leung H T, Xu Y B, Guertler C M and Bland J A C 2000 Magnetic domain studies of permalloy wire-based structures with junctions *IEEE Trans. Magn.* **36** 3068–70
[206] Lima C S and Baibich M N 2016 Influence of sample width on the magnetoresistance and planar Hall effect of Co/Cu multilayers *J. Appl. Phys.* **119** 33902
[207] Chang Y C, Chang C C, Chang I, Wu J C, Wei Z-H, Lai M-F and Chang C-R 2006 Investigation of permalloy cross structure using magnetic force microscope and magnetoresistance measurement *J. Appl. Phys.* **99** 08B710
[208] Fermon C and Pannetier-Lecoeur M 2013 Noise in GMR and TMR sensors *Giant Magnetoresistance (GMR) Sensors* (Berlin: Springer) pp 47–70
[209] Dalslet B T, Damsgaard C D, Donolato M, Strømme M, Strömberg M, Svedlindh P and Hansen M F 2011 Bead magnetorelaxometry with an on-chip magnetoresistive sensor *Lab Chip* **11** 296–302
[210] Jen S U, Wang P J, Tseng Y C and Chiang H P 2009 Planar Hall effect of permalloy films on Si(111), Si(100), and glass substrates *J. Appl. Phys.* **105** 07E903
[211] Oh S J, Le T T, Kumar S A, Kim G W, Rao B P and Kim C 2007 Etching effect on exchange anisotropy in NiFe/Cu/NiFe/IrMn spin-valve structure for an array of PHR sensor element *2007 2nd IEEE Int. Conf. on Nano/Micro Engineered and Molecular Systems* pp 1183–5
[212] Hung T Q, Quang P H, Thanh N T, Sunjong O, Bajaj B and CheolGi K 2007 The contribution of the exchange biased field direction in multilayer thin films to planar Hall resistance *Phys. Status Solidi* **244** 4431–4
[213] Thanh N T, Chun M G, Schmalhorst J, Reiss G, Kim K Y and Kim C G 2006 Magnetizing angle dependence of planar Hall resistance in spin-valve structure *J. Magn. Magn. Mater.* **304** e84–7
[214] Rizzi G, Lundtoft N C, Østerberg F W and Hansen M F 2012 Reversible and irreversible temperature-induced changes in exchange-biased planar hall effect bridge (pheb) magnetic field sensors *Sens. Trans.* **15** 22–34
[215] Wesenberg D, Hojem A, Bennet R K and Zink B L 2018 Relation of planar Hall and planar Nernst effects in thin film permalloy *J. Phys. D: Appl. Phys.* **51** 244005
[216] Lu Z Q, Pan G, Li J and Lai W Y 2001 Planar Hall effect and magnetoresistance in spin valve multilayers *J. Appl. Phys.* **89** 7215–7
[217] Tamanaha C R, Mulvaney S P, Rife J C and Whitman L J 2008 Magnetic labeling, detection, and system integration *Biosens. Bioelectron.* **24** 1–13
[218] Wang S X and Li G 2008 Advances in giant magnetoresistance biosensors with magnetic nanoparticle tags: review and outlook *IEEE Trans. Magn.* **44** 1687–702
[219] Baselt D R, Lee G U, Natesan M, Metzger S W, Sheehan P E and Colton R J 1998 A biosensor based on magnetoresistance technology1This paper was awarded the biosensors & bioelectronics award for the most original contribution to the congress.1 *Biosens. Bioelectron.* **13** 731–9
[220] Graham D L, Ferreira H, Bernardo J, Freitas P P and Cabral J M S 2002 Single magnetic microsphere placement and detection on-chip using current line designs with integrated spin valve sensors: biotechnological applications *J. Appl. Phys.* **91** 7786–8
[221] Schotter J, Kamp P B, Becker A, Pühler A, Reiss G and Brückl H 2004 Comparison of a prototype magnetoresistive biosensor to standard fluorescent DNA detection *Biosens. Bioelectron.* **19** 1149–56
[222] Dalslet B T, Donolato M and Hansen M F 2012 Planar Hall effect sensor with magnetostatic compensation layer *Sens. Actuators* A **174** 1–8
[223] Rizzi G, Westergaard Østerberg F, Dufva M and Fougt Hansen M 2014 Magnetoresistive sensor for real-time single nucleotide polymorphism genotyping *Biosens. Bioelectron.* **52** 445–51
[224] Rizzi G, Østerberg F W, Henriksen A D, Dufva M and Hansen M F 2015 On-chip magnetic bead-based DNA melting curve analysis using a magnetoresistive sensor *J. Magn. Magn. Mater.* **380** 215–20
[225] Rizzi G, Dufva M and Hansen M F 2017 Two-dimensional salt and temperature DNA denaturation analysis using a magnetoresistive sensor *Lab Chip* **17** 2256–63
[226] Østerberg F W, Rizzi G, Donolato M, Bejhed R S, Mezger A, Strömberg M, Nilsson M, Strømme M, Svedlindh P and Hansen M F 2014 On-chip detection of rolling circle amplified DNA molecules from bacillus globigii spores and vibrio cholerae *Small* **10** 2877–82
[227] Rizzi G, Dufva M and Hansen M F 2017 Magnetoresistive sensors for measurements of DNA hybridization kinetics—effect of TINA modifications *Sci. Rep.* **7** 41940
[228] Oh S, Baek N S, Jung S D, Chung M A, Hung T Q, Anandakumar S, Rani V S, Jeong J R and Kim C 2011 Selective binding and detection of magnetic labels using PHR sensor via photoresist micro-wells *J. Nanosci. Nanotechnol.* **11** 4452–6

[229] Bui D T, Tran M D, Nguyen H D and Nguyen H B 2013 High-sensitivity planar Hall sensor based on simple gaint magneto resistance NiFe/Cu/NiFe structure for biochip application *Adv. Nat. Sci. Nanosci. Nanotechnol.* **4** 15017

[230] Sinha B, Ramulu T S, Kim K W, Venu R, Lee J J and Kim C G 2014 Planar Hall magnetoresistive aptasensor for thrombin detection *Biosens. Bioelectron.* **59** 140–4

[231] Kim S, Torati S R, Talantsev A, Jeon C, Lee S and Kim C 2020 Performance validation of a planar Hall resistance biosensor through beta-amyloid biomarker *Sensors* **20** 434

[232] Bajaj B, Thanh N T and Kim C G 2007 Planar Hall effect in spin valve structure for DNA detection immobilized with single magnetic bead *2007 7th IEEE Conf. on Nanotechnology (IEEE NANO)* pp 1033–6

[233] Østerberg F W, Rizzi G and Hansen M F 2013 On-chip measurements of brownian relaxation of magnetic beads with diameters from 10 nm to 250 nm *J. Appl. Phys.* **113** 154507

[234] Volmer M and Avram M 2012 Microbeads detection using spin-valve planar hall effect sensors *J. Nanosci. Nanotechnol.* **12** 7456–9

[235] Sinha B, Anandakumar S, Oh S and Kim C 2012 Micro-magnetometry for susceptibility measurement of superparamagnetic single bead *Sens. Actuators* A **182** 34–40

[236] Kim K W, Reddy V, Torati S R, Hu X H, Sandhu A and Kim C G 2015 On-chip magnetometer for characterization of superparamagnetic nanoparticles *Lab Chip* **15** 696–703

[237] Kamara S, Tran Q H, Davesne V, Félix G, Salmon L, Kim K, Kim C G, Bousseksou A and Terki F 2017 Magnetic susceptibility study of sub-pico-emu sample using a micromagnetometer: an investigation through bistable spin-crossover materials *Adv. Mater.* **29** 1–5

[238] Hung T Q *et al* 2013 Room temperature magnetic detection of spin switching in nanosized spin-crossover materials *Angew. Chem., Int. Ed.* **52** 1185–8

[239] Chui K M, Adeyeye A O and Li M-H 2007 Detection of a single magnetic dot using a planar Hall sensor *J. Magn. Magn. Mater.* **310** e992–3

[240] Volmer M, Avram M and Avram A M 2015 Simulation and experimental results on manipulation and detection of magnetic nanoparticles using planar hall effect sensors *2015 Int. Semiconductor Conf. (CAS)* pp 117–20

[241] Kim K W, Torati S R, Reddy V and Yoon S S 2014 Planar hall resistance sensor for monitoring current *J. Magn.* **19** 151–4

[242] Persson A, Bejhed R S, Østerberg F W, Gunnarsson K, Nguyen H, Rizzi G, Hansen M F and Svedlindh P 2013 Modelling and design of planar Hall effect bridge sensors for low-frequency applications *Sens. Actuators* A **189** 459–65

[243] Persson A, Bejhed R, Gunnarsson K, Nguyen H, Dalslet B T, Oesterberg F W, Hansen M F and Svedlindh P 2011 Low-frequency picotesla field detection with planar Hall effect bridge sensors *Mater. Sci.* 1–17 (www.diva-portal.org/smash/record.jsf?pid=diva2%3A416049&dswid=2652)

[244] Volmer M and Neamtu J 2008 Micromagnetic characterization of a rotation sensor based on the planar Hall effect *Phys.* B **403** 350–3

[245] Dalslet B T, Damsgaard C D, Freitasy S C, Freitas P P and Hansen M F 2008 Bead capture and release on a magnetic sensor in a microfluidic system *SENSORS, 2008 IEEE* pp 242–5

[246] Osterberg F W, Dalslet B T, Damsgaard C D, Freitas S C, Freitas P P and Hansen M F 2009 Bead capture on magnetic sensors in a microfluidic system *IEEE Sens. J.* **9** 682–8

[247] Østerberg F W, Rizzi G, De La Torre T Z G, Strömberg M, Strømme M, Svedlindh P and Hansen M F 2013 Measurements of Brownian relaxation of magnetic nanobeads using planar Hall effect bridge sensors *Biosens. Bioelectron.* **40** 147–52

[248] Osterberg F W, Dalslet B T, Snakenborg D, Johansson C and Hansen M F 2010 Chip-based measurements of brownian relaxation of magnetic beads using a planar Hall effect magnetic field sensor *AIP Conf. Proc.* **1311** 176–83

[249] Hansen T B G, Damsgaard C D, Dalslet B T and Hansen M F 2010 Theoretical study of in-plane response of magnetic field sensor to magnetic beads magnetized by the sensor self-field *J. Appl. Phys.* **107** 124511

[250] Damsgaard C D and Hansen M F 2008 Theoretical study of in-plane response of magnetic field sensor to magnetic beads in an in-plane homogeneous field *J. Appl. Phys.* **103** 064512

[251] Anon Magnetic diagnostic assay for neurodegenerative diseases MADIA Project H2020 CORDIS (European Commission)

[252] An B W, Shin J H, Kim S-Y, Kim J, Ji S, Park J, Lee Y, Jang J, Park Y-G and Cho E 2017 Smart sensor systems for wearable electronic devices *Polymers* **9** 303

[253] Dahiya A S *et al* 2020 Review—energy autonomous wearable sensors for smart healthcare: a review *J. Electrochem. Soc.* **167** 37516

[254] Lim H-R, Kim H S, Qazi R, Kwon Y-T, Jeong J-W and Yeo W-H 2020 Wearable flexible hybrid electronics: advanced soft materials, sensor integrations, and applications of wearable flexible hybrid electronics in healthcare, energy, and environment *Adv. Mater.* **32** 2070116

[255] Lee S, Yoon J, Lee D, Seong D, Lee S, Jang M, Choi J, Yu K J, Kim J and Lee S 2020 Wireless epidermal electromyogram sensing system *Electronics* **9** 269

[256] Kim K, Kim B and Lee C H 2020 Printing flexible and hybrid electronics for human skin and eye-interfaced health monitoring systems *Adv. Mater.* **32** 1902051

[257] Melzer M, Makarov D and Schmidt O G 2019 A review on stretchable magnetic field sensorics *J. Phys. D: Appl. Phys.* **53** 83002

[258] Jeong W, Kim M, Ha J-H, Binti Zulkifli N A, Hong J-I, Kim C and Lee S 2019 Accurate, hysteresis-free temperature sensor for health monitoring using a magnetic sensor and pristine polymer *RSC Adv.* **9** 7885–9

[259] Kim S, Oh S, Kim K B, Jung Y, Lim H and Cho K 2018 Design of a bioinspired robotic hand: magnetic synapse sensor integration for a robust remote tactile sensing *IEEE Robot. Autom. Lett.* **3** 3545–52

sensors

MDPI

Article

Low Field Optimization of a Non-Contacting High-Sensitivity GMR-Based DC/AC Current Sensor

Cristian Mușuroi [1], Mihai Oproiu [1], Marius Volmer [1,*], Jenica Neamtu [2], Marioara Avram [3] and Elena Helerea [1]

1 Department of Electrical Engineering and Applied Physics, Transilvania University of Brasov, Blvd. Eroilor 29, 500036 Brasov, Romania; cristian.musuroi@unitbv.ro (C.M.); mihai.oproiu@unitbv.ro (M.O.); helerea@unitbv.ro (E.H.)

2 National Institute for Research and Development in Electrical Engineering, Splaiul Unirii 313, 030138 Bucharest, Romania; jenica.neamtu@gmail.com

3 National Institute for Research and Development in Microtechnologies, Str. Erou Iancu Nicolae 32B, 72996 Bucharest, Romania; marioara.avram@imt.ro

* Correspondence: volmerm@unitbv.ro

Abstract: Many applications require galvanic isolation between the circuit where the current is flowing and the measurement device. While for AC, the current transformer is the method of choice, in DC and, especially for low currents, other sensing methods must be used. This paper aims to provide a practical method of improving the sensitivity and linearity of a giant magnetoresistance (GMR)-based current sensor by adapting a set of design rules and methods easy to be implemented. Our approach utilizes a multi-trace current trace and a double differential GMR based detection system. This essentially constitutes a planar coil which would effectively increase the usable magnetic field detected by the GMR sensor. An analytical model is developed for calculating the magnetic field generated by the current in the GMR sensing area which showed a significant increase in sensitivity up to 13 times compared with a single biased sensor. The experimental setup can measure both DC and AC currents between 2–300 mA, with a sensitivity between 15.62 to 23.19 mV/mA, for biasing fields between 4 to 8 Oe with a detection limit of 100 μA in DC and 100 to 300 μA in AC from 10 Hz to 50 kHz. Because of the double differential setup, the detection system has a high immunity to external magnetic fields and a temperature drift of the offset of about -2.59×10^{-4} A/°C. Finally, this setup was adapted for detection of magnetic nanoparticles (MNPs) which can be used to label biomolecules in lab-on-a-chip applications and preliminary results are reported.

Keywords: current sensors; GMR effect; magnetoresistive sensors; bias magnetic field; Biot-Savart law; magnetic nanoparticles

check for updates

Citation: Mușuroi, C.; Oproiu, M.; Volmer, M.; Neamtu, J.; Avram, M.; Helerea, E. Low Field Optimization of a Non-Contacting High-Sensitivity GMR-Based DC/AC Current Sensor. *Sensors* **2021**, *21*, 2564. https://doi.org/10.3390/s21072564

Academic Editor: Paul P. Sotiriadis

Received: 9 March 2021
Accepted: 4 April 2021
Published: 6 April 2021

1. Introduction

Current measurement is essential in modern electrical systems. Different current sensing methods have been developed and adapted for specific needs. Resistive-based current-sensing techniques, although acceptable to use in some applications, have a number of drawbacks such as low accuracy, power loss, low bandwidth, no galvanic isolation, and noise [1]. In contrast, electromagnetic-based current sensing techniques, mitigate most of these drawbacks, but present some specific challenges regarding their operation or application versatility.

However, many applications require galvanic isolation between the circuit where the current is flowing and the measurement device. Because of that, magnetic sensors are widely used in current measurements because they are non-intrusive and provide galvanic isolation. A good example of non-contact current detection, that can inspire many other applications, is presented in [2] where the ion beam equivalent current inside a particle accelerator, is measured through the magnetic field it creates. In this way, equivalent currents down to 100 μA can be measured. Typical current sensors include the AC/DC current transformers [2–4], fluxgate magnetometers [5,6], Hall effect sensors [3,7], anisotropic magnetoresistive (AMR) [3,8], giant magnetoresistance (GMR) [2,3,9,10] and tunnelling magneto-resistance (TMR) sensors [2,11].

For modern applications, some essential features for current sensors can be noted as necessary: enhanced accuracy and sensitivity, linear response, versatile DC/AC measurement, low thermal drift, immunity to interferences, integrated circuit (IC) packaging, low power consumption and low cost.

(Micro)fluxgate sensors [3,6] are an established solution for DC/AC currents detection since they offer good accuracy and stability. A fluxgate sensor [3] is typically comprised of high permeability magnetic cores around which coil windings are wrapped: a fluxgate coil (driven by a square wave current), compensation coil and pick-up coil which are used to determine the magnetization state of the core and, hence, the current to be measured. The necessary setup for managing the sensor's functionality, and conditioning the acquired signal is quite complex. While the classical setup is using discrete parts like magnetic core and coils wrapped on it [3], the modern solutions are using integrated microfluxgate sensors, which can be placed directly around the conductor [6].

By contrast, Hall microsensors can simplify the measurement setup and are compatible with IC technology [12] which means that both the sensing part and the electronics required for signal conditioning can be microfabricated on the same chip. Hall sensors do not saturate and can reach a sensitivity down to 10^{-6} T [13]. However, these sensors do require a closed magnetic core with a small air gap where the Hall sensor is placed [3,7]. The core surrounds the conductor through which the current is flowing. It must be mentioned that magnetic core becomes a source of non-linearity for the response characteristic due to hysteretic effects. Also, serious DC offset of the sensor's output can be caused by the remanence of the magnetic core. Some Hall current meters have an AC demagnetization circuit to overcome this issue [3]. There are manufacturers that integrate on the same chip the current trace, the Hall sensor and the conditioning circuits giving a compact solution, usually suitable for currents larger than 5 A.

On the other hand, magnetoresistive sensors (MR) made of magnetic thin films can exhibit much higher sensitivities, being able to detect magnetic fields in the 10^{-9}–10^{-2} T domain [13]. This can lead to simplification of the current measurement chain, the sensor being sensitive to in-plane magnetic fields, extending the current measurement range for values lower than 1 mA, allowing the possibility for developing special applications with reduced power consumption and price [8,9,11,14]. Also, it should be mentioned that for MR sensors the response characteristics like sensitivity, linearity, saturation field, noise, etc., are strongly affected by the magnetic properties of the utilized materials, the structure of their underlying multilayered and the layout of the microfabricated sensor. A short review of MR effects, underlying the physical origin of AMR, GMR and TMR, and the specific field behavior was presented in [10].

The GMR effect occurs in multilayered magnetic structures of the type FM/NM/FM coupled by exchange interaction; here FM denotes magnetic layers like $Ni_{80}Fe_{20}$, Co, CoFeB, etc., and NM denotes a nanometer thick conductive nonmagnetic layer as Cu, Ag. If the NM is a dielectric of the type Al_2O_3 or MgO_2 we talk about a TMR structure [10,11]. In GMR effect the resistance changes according to the angle between the directions of the magnetization of adjacent layers. When the layers are magnetized in parallel, the resistance is at a minimum value, R_p. When the magnetizations of the adjacent magnetic layers are antiparallel to each other, the resistance is at a maximum value, named R_{ap}. The magnitude of the GMR effect is expressed by Equation (1) [15], and is typically between 5–15%:

$$GMR = \frac{R_{ap} - R_p}{R_{ap}} 100 \ \ [\%], \tag{1}$$

Usually, one of the ferromagnetic layers is pinned by an anti-ferromagnetic (AFM) layer of FeMn or IrMn while the second FM layer has the magnetization free to rotate under the action of an external magnetic field. Such that, a GMR structure is of the type substrate/buffer layer (Ta)/FM(free layer)/NM/FM(pinned layer)/AFM/Cap layer [10].

Compared with AMR based sensors, the GMR sensors offer higher field sensitivity, wide frequency range, and do not require an internal coil (for example, of type KMZ51) or external controlled magnetic field to be used to reset the magnetization to the initial orientation [8]. However, most of the GMR sensors have a nonlinear behaviour around zero field and the output is unipolar which limits the application for bipolar and AC fields [9,10]. Until now, several methods of improving the response of a GMR sensor have been used. For example, using a bias field parallel to the sensitive axis can shift the operating point of the sensor in the linear region, thus reducing hysteresis behaviour and allowing detection of bipolar fields. In [10], we mentioned that this field can be created with a permanent magnet or a coil system with DC, AC, or short pulse currents which can have open or closed-loop control.

Several studies have presented the use of GMR sensors as current sensors, most detailing different methods to improve their performance and versatility. Some of the implemented methods are: magnetic shielding—for reduced susceptibility to interference magnetic fields [16], hysteresis modelling compensation [17], open loop operation [2,3,10], closed loop operation [18]—to reduce hysteresis and temperature dependency, low frequency capture—to increase the range of the GMR current sensor to ±800 A [19], negative feedback introduced by the Helmholtz coil—to increase the range of the sensor up to 5 times [9], or damping coil—to further increase the range by 5.23 times [20]. In [10], we demonstrated a novel method of improving the overall accuracy, thermal stability, power consumption and immunity to interference magnetic fields involving a double differential setup, adjustable permanent magnetic biasing and antiphase-operating GMR based sensors on top of a U-shaped current trace. As a general remark from the above enumeration, many current sensors are using: (i) a discrete solution, where the magnetic sensors, the current trace, coils and the corresponding electronics are implemented in a suitable setup to detect the current [2,3,8–11] or (ii) a compact solution as an integrated circuit where can be found inside the chip the current trace, the sensors [13] and the conditioning circuit [14].

In this paper, which continues the study presented in [10], an extremely sensitive GMR current sensor is designed and implemented, able to detect both DC and AC currents from 2 to 300 mA with a setup sensitivity between 15.62 to 23.19 mV/mA. The detection limit is 100 µA in DC and 100 to 300 µA in AC from 10 Hz to 50 kHz. We found this limitation to be due mainly to the signal processing chain and not due to the GMR sensors which have an operating frequency range from DC to 1 MHz. The basic approach is to use a multi-turn planar coil and a double differential GMR based detection system. To study the influence of the biasing field on the current sensor sensitivity and linearity and to fine balance the GMR sensors, a Helmholtz coil is used.

Finally, further applications of this measurement system will be discussed. We proved that this system is able to detect very low amounts of magnetic field generated by magnetic nanoparticles placed above the sensor surface.

2. Materials and Methods

2.1. Principle of Operation

The proposed setup relies on a practical method of significantly increasing the sensitivity and accuracy of a non-contacting current sensor by an appropriate design of the circuit which produces the magnetic field from the current that is intended to be measured. In order to validate this concept, GMR sensors were used. The novelty of the approach consists in utilizing multiple current traces, in a double differential system, implemented in a custom printed circuit board. In the current measurement setup, the GMR sensors act as a magnetometer, thus, if a current, I, passes through a wire, the magnetic field, B, will produce a change of the output voltage on the nearby GMR sensor. The working principle of the setup can be seen in Figure 1a,c. As a particular case, we can note the single trace variant, illustrated in Figure 1b,d and described in detailed in [10]. As shown in [10], the supposition for this setup is that the low current measurement capabilities can be significantly improved by utilizing a narrow trace. Moreover, by having multiple traces through which the same current to be detected passes, the system will become a planar coil (Figure 2b). The current, I, from the conducting traces (denoted as "Current traces"), generates a magnetic field, whose component, B_x, will be detected by the GMR sensor (note that this setup can be adapted to work with other types of sensors, for example, planar Hall effect sensors).

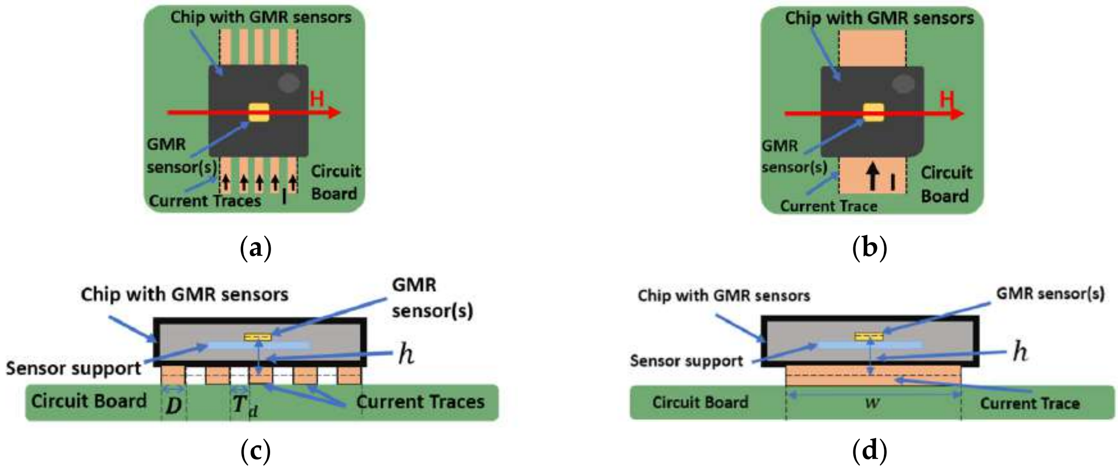

Figure 1. Working principle of the non-contacting current measurement setup utilizing current traces and a GMR based chip: (**a**) Multi-trace plane section; (**b**) Single trace plane section; (**c**) Multi-trace cross section; (**d**) Single trace cross section.

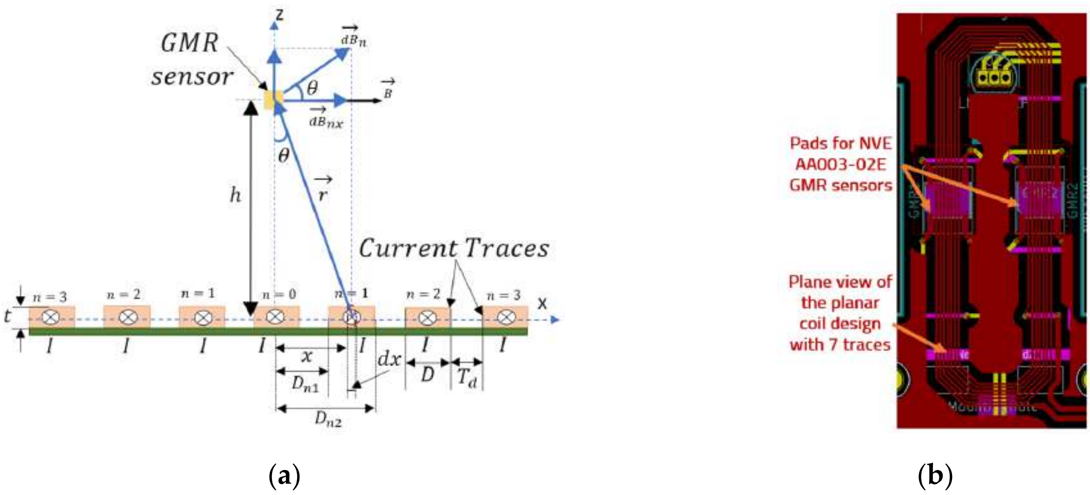

Figure 2. (**a**) Illustration of the geometry and parameters used in the analytical model to compute the magnetic field present in the sensor area. Note that the model takes into account that there is an odd number of traces that generate the magnetic field and the central trace is denoted as $n = 0$; (**b**) plane view of the planar coil with seven traces as designed for the actual implementation. $\vec{B}$ is the resulting field in the central position (the middle trace is centered just below the sensitive area of the sensor).

In order to estimate B_x, we derived an analytical model based on Biot-Savart law, which assumes that the sensor is centered above the multiple trace at distance h (Figure 2a).

Thus, by assuming a long conducting trace, as seen in the design from Figure 2b, the elementary field produced by the current I, can be expressed, using the Biot-Savart law, by Equations (2) and (3):

$$dB_n = \mu_0 \frac{dI}{2\pi r} = \mu_0 \frac{Idx}{D} \cdot \frac{1}{2\pi\sqrt{h^2 + x^2}}\,; dI = \frac{I}{D}dx, \tag{2}$$

$$dB_{nx} = dB_n \cdot \cos\theta = \mu_0 \frac{Idx}{2\pi D} \cdot \frac{1}{\sqrt{h^2+x^2}} \cdot \frac{h}{\sqrt{h^2+x^2}}\ , \tag{3}$$

where $\mu_0 = 4\pi \times 10^{-7}$ H/m is the vacuum magnetic permeability, D is the trace width, t is the trace thickness (not used in the equation, T_d is the distance between the traces, h is the height on which the sensing element is placed above the trace, and θ is the angle shown in Figure 2a used to estimate the B_x component of the magnetic field.

By assuming a uniform linear current density, I/D, and integrating Equation (3) from D_{n1} to D_{n2} we find the x component of field generated by a trace n = 1, 2, 3, . . . , in the sensor area:

$$B_{nx} = \frac{\mu_0 I}{2\pi D}\left[arctan\left(\frac{D_{n2}}{h}\right) - arctan\left(\frac{D_{n1}}{h}\right)\right]\ [\mathrm{T}] \tag{4}$$

Note that for the central trace (n = 0), B_{0x} was found in [10] to be:

$$B_{0x} = \frac{\mu_0 I}{\pi D} \cdot arctan\left(\frac{D}{2h}\right)\ [\mathrm{T}] \tag{5}$$

Taking into account the problem symmetry, the z component of the field in the sensor will be canceled by the fields from the left and right-side stripes, i.e., $B_{nz} = 0$. Such that, the total field generated in the sensor area can be expressed as:

$$B = B_0 + 2B_1 + 2B_2 + \ldots + 2B_n\ [\mathrm{T}] \tag{6}$$

For example, if we consider the situation illustrated in Figure 2a, for n = 3 it means that there will be seven linear stripes beneath the sensor that will produce the magnetic field (Figure 2b). In fact, this is the actual planar coil used in our practical implementation, where h = 0.8 mm, D = 0.22 mm and T_d = 0.19 mm. For these parameters we find that (note that the current I is expressed in [A]):

$$B = 10.3784 \cdot I \cdot 10^{-4}[\mathrm{T}] = 10.3784 \cdot I\ [\mathrm{G}] \tag{7}$$

Note that even though the results from Equations (4)–(6) are expressed in Tesla, they can be transformed into Gauss (which is equivalent to Oe in air) by multiplying by 10^4.

For ease of use as well as testing various scenarios, meaning different values for n, h, D and T_D, this analytical method was implemented in a LabVIEW application. Note that for only one trace (n = 0), the result is detailed in [10]. An analysis was performed with this method for two different trace structures (defined by the D and T_d parameters, Figure 2a). The field dependency between the two cases, for different number of traces, as obtained with the analytical algorithm can be seen in Figure 3. An example of the detailed calculus for one of the structures (Case II, Figure 3) is shown in Appendix A, while the parameters involved are shown in Table A1 and Equations (A1) and (A2), the example calculation being shown in Equations (A3)–(A13).

From Figure 3, we can note that the magnetic field in the sensor area is increased significantly from the case with just one trace (the results were obtained with a 0.5A current passing through each trace). The best balance between the obtained field and practicality of implementation was found to be at the five and seven traces structure as there is an asymptotic dependency. Thus, a prototype PCB for current sensing with the specifications from Case II (for higher magnetic field output), Figure 3, was be developed. The values of D and t_D were chosen such that to get the maximum field in sensors region and to allow a higher current to pass through the planar coil. The values of D and t_D used to plot Figure 3 show that: (i) the developed analytical method can take into account different trace widths and spacing to estimate the produced magnetic field and (ii) a large number of traces with a lower value of D give higher value for B in the sensor region. The lower value for t_D was 0.19 mm due to technological limitations. Because our work was focused on measuring low currents down to 1 mA, with a high dynamic range, up to 300 mA, and because of the physical distance between the sensor pads, we set D = 0.21 mm.

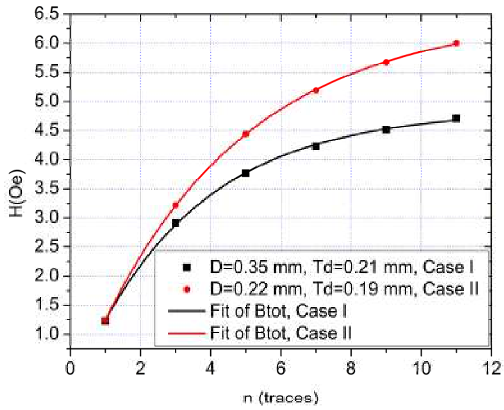

Figure 3. Total magnetic field induction in the GMR sensor area (for I = 0.5 A) dependency on the number of current traces. The asymptotic tendency of Btot for the case where D = 0.22 mm is 6.485 Oe (Case I) while for D = 0.35 mm is 4.849 Oe (Case II). In both cases, h = 0.8 mm. Note that the field multiplying effect is clearly visible. Graphs were made using data obtained with the analytical method.

We can denote that other factors also play a major role in the sensitivity of the sensors (such as biasing of the sensors, differential measurement setup, amplifying the output etc.) [10]. Thus, we can expect much better results with an optimized designed of the setup and appropriate biasing of the GMR sensors. From the results obtained with the analytical algorithm, we estimate that compared with a single biased NVE AA003-02 GMR sensor (supplied with 1 mA of current, average sensitivity S around 13.75 mV/Oe), by using multiple traces (for example, 7) on an optimized double differential design as in [10], we can expect a sensitivity S increase (for a 500mA measured current) from S = 0.0341 mV/mA (single trace) to S = 0.244 mV/mA (five traces, Case I) or S = 0.285 mV/mA (seven traces, Case II), Figure 3.

2.2. Characterization of the GMR Sensor

Commonly, GMR sensors are made from multilayered structures of the type AFM (antiferromagnetic layer)/PL(pinned magnetic layer)/NM(non-magnetic spacer layer)/FL(magnetic free layer). The free layer is the sensing layer, as the magnetization can rotate upon an applied magnetic field). The difference in the relative magnetic moments between adjacent magnetic layers produces a change in the electric resistance. When the layers are magnetized in parallel, the resistance is at a minimum value, R_p, which is the saturation resistance. When the magnetizations of the adjacent magnetic layers are antiparallel to each other, the resistance is at a maximum value, named R_{ap} (note Figure 4a). The electric resistance dependency from the angle θ, between the magnetization of adjacent magnetic layers [21]:

$$R = R_p + \frac{\Delta R_{GMR}}{2}[1 - cos\theta], \tag{8}$$

where, $\Delta R_{GMR} = R_p - R_{ap}$, is the GMR effect amplitude.

Thus, for antiparallel configuration (θ = 180°):

$$cos\theta = -1 \ \rightarrow R = R_{AP} = R_{High}, \tag{9}$$

while, for parallel configuration (θ = 0°):

$$cos\theta = 1 \ \rightarrow R = R_P = R_{Low}. \tag{10}$$

From Equations (8)–(10), we can express the rate of change in the resistance of a GMR sensor element (also called GMR ratio) by Equation (1).

The AA003-02 sensor, which will be used in the experimental setup, contains two active GMR elements, and two magnetically shielded identical sensors used to complete a Wheatstone bridge; the GMR ratio for each sensor element is between 13% to 16% [22]. Thus, in 0 field the bridge is almost balanced providing an output voltage close to 0 [22], as will be showed from experimental results. When a field is applied, the bridge becomes unbalanced and the output voltage shows a sensitivity between 3–4.2 mV/(V × Oe) [10,22].

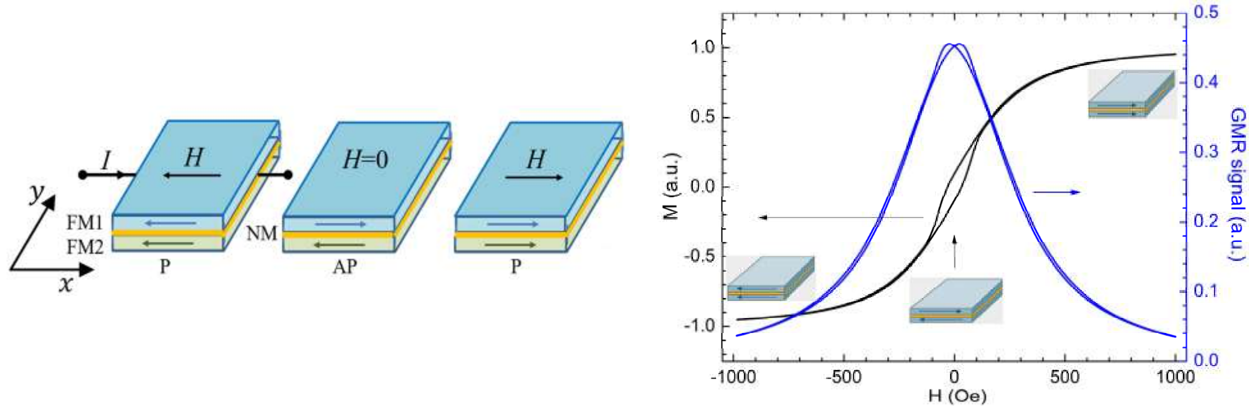

(**a**) (**b**)

Figure 4. Micromagnetic simulation of a GMR element: (**a**) Schematic illustration of a GMR structure (two ferromagnetic layers FM1, FM2 and nonmagnetic layer, NM) with three distinct states depending on the parallel (P) or antiparallel (AP) alignment of layers magnetization; (**b**) Typical field dependence of the structure magnetization along the Ox axis, M, obtained by micromagnetic simulations and the calculated GMR effect when H_{appl} is directed over Ox axis.

For a better understanding on the operation of the GMR sensor, by simulating this effect with the object oriented micromagnetic framework (OOMMF) [23], using a multi-domain approach, the layer orientation of a GMR structure in different operating points can be illustrated. The main parameters involved in configuring the simulation are: the simulated layer is $1000 \times 500 \times 10$ nm^3 and consists from Permalloy; the cell size is $5 \times 5 \times 5$ nm^3. The FL is antiferromagnetically coupled with the PL through the NM layer, the coupling field being 200 Oe, along the Ox axis. The magnetic field, H_{appl}, is applied perpendicular to the easy axis of magnetization. The saturation magnetization M_s = 710 kA/m, the exchange constant $A = 1.3 \times 10^{-11}$ J/m, and the anisotropy constant K_U = 804 J/m^3 along Ox axis, Figure 4. In [10] we described in detail the multi-domain micromagnetic approach (as well as the reasoning behind the parameters involved and how to extract simulation results) to simulate a GMR sensor structure using OOMMF.

In order to characterize the AA003-02 sensor (Figure 5), a magnetic field was applied by two round-shaped coils in a quasi-Helmholtz like configuration. From Figures 4 and 5, we can observe that the results are in good qualitative agreement with Equations (8)–(10). We can remark that the sensor presents a nonlinear response around 0 field and low sensitivity around the coercive field. We noted that when supplying the sensors with a constant current (2 mA), instead of voltage, the sensitivity of the sensors can be increased [10]. Due to practical reasons, a constant supply voltage was chosen for the sensors.

2.3. Experimental Setup and Mode of Operation

Based on the results from the analytical method, a GMR-based current measurement setup was developed. The PCB setup (named GMR Testboard) can be seen in Figure 6a. Figure 6b shows the functional block diagram of the current measurement system as well as the amplifier and data acquisition setup. Figure 7 details the individual subblock components of the entire setup. A HM8143 power supply (HAMEG, Frankfurt, Germany) is used for powering most components, while a 2635A Sourcemeter (Keithley, Solon, OH, USA) was used to generate the various measured trace currents. In terms of design rules for the current traces, a single trace in a U shaped spiral pattern (7 traces) passes through the sensors. Also, in order to amplify the useful magnetic field, the characteristics are those from Case II (note

Figure 3). Due to the thickness of the trace, the setup is able to operate with currents up to 0.5 A, however, for testing we focused on values up to 150 mA, as higher values can easily be detected. The GMR sensors, from an output point of view, operate in antiphase, in a similar differential setup as the one detailed in [10], which provides some benefits: high sensitivity, immunity to any external homogenous magnetic field affecting both sensors equally or from magnetic fields lower than 25 Oe perpendicular to the axis of sensitivity. However, for non-homogenous magnetic fields in the vicinity of the sensors, electromagnetic shielding must still be applied.

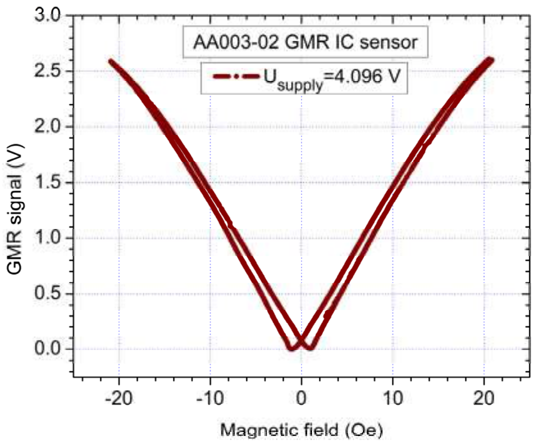

Figure 5. Typical measured magnetic field dependency for the AA003-02 GMR sensor. In this case, the sensor was supplied with 4.096 V; this voltage is generated by a very stable source which is part from the EI 1040 instrumentation amplifier.

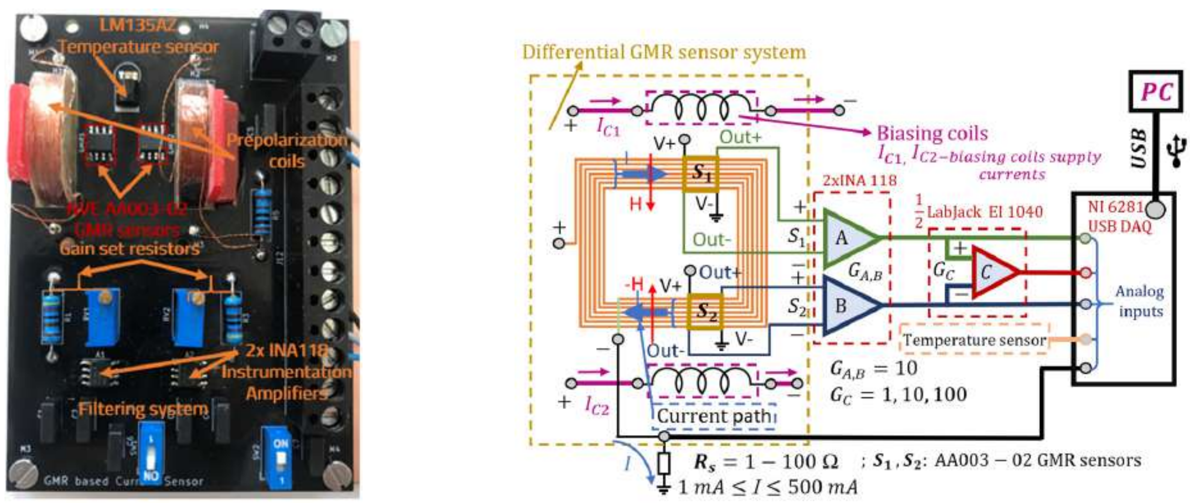

(**a**) (**b**)

Figure 6. (**a**) GMR Testboard (custom PCB) optimized for low field detection (current measurement) using GMR sensors. The PCB is based on the 7 traces, Case II from Figure 3 and integrates the sensors, biasing coils, multi-turn planar coil, filtering system (capacitors for the INA 118 amplifiers power supply to filter any high frequency components and for the output of the amplifiers when measuring an AC signal to filter any DC component). (**b**) The functional block diagram of the current measurement system as well as the amplifier and data acquisition setup; notice the "U"-shaped structure of the circuit which produces the magnetic field which is applied to the sensors is integrated through the spiral trace which constitutes the planar coil.

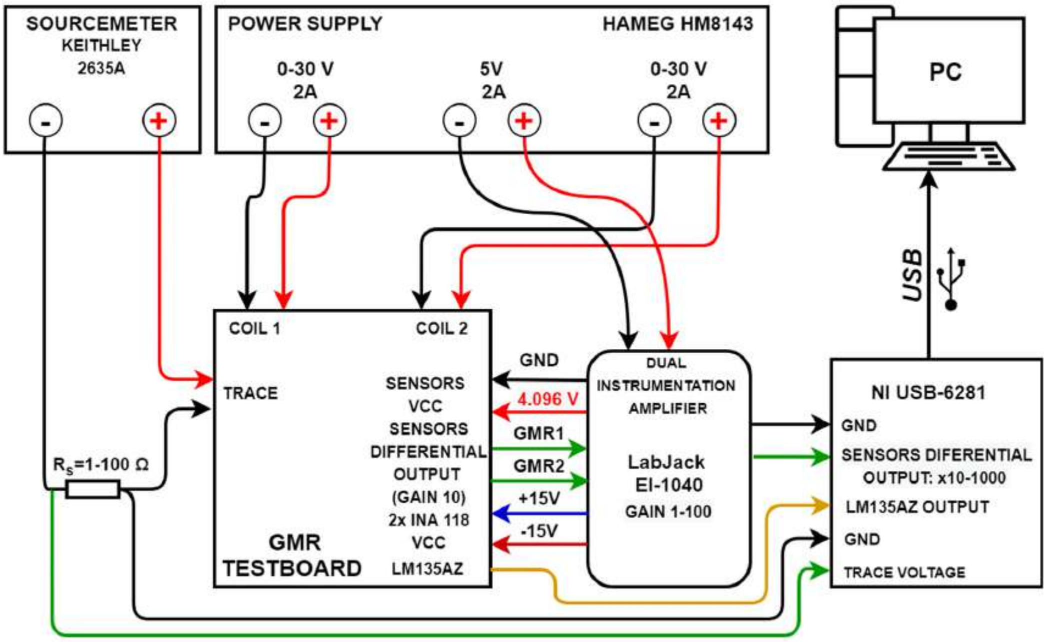

Figure 7. Subblock components of the entire setup. The GMR sensors, temperature sensor, as well as the INA118 amplifiers are supplied from the EI1040 instrumentation amplifier, which also allows a variable gain to be set as needed. On the GMR Testboard, the differential output from each sensor is amplified by a fixed gain of 10. The output voltage from the LM15AZ temperature sensor is sent directly to the DAQ board. Also note that each coil is supplied separately from the HM8143 (parallel configuration), as this allow calibration of the biasing field for each GMR sensor.

The output voltage from the sensors is amplified by two (one for each sensor) INA118 [24] instrumentation amplifiers integrated on the board. The real gain for each amplifier was set to 10 and the results were offset corrected. Furthermore, the resulting signals are further amplified by a LabJack EI1040 amplifier [25] to obtain the differential output from the two sensors which is set to a gain of 10 for low currents measurement, or 1 for higher currents measurement, resulting in a 10, 100 or 1000 total gain. The gain for the EI1040 instrumentation amplifier can be set manually or through the NI6281 USB, which represents the data acquisition board [26]. The implementation allows measurement of both AC and DC currents with the ability to bypass the included filtering system for the amplifier output. An LM135AZ temperature sensor (STMicroelectronics, Geneva, Switzerland) was also integrated in the sensor area. It should be noted that the supply lines for the GMR and temperature sensor are orientated perpendicularly compared with the current trace (any produced magnetic field lower than 20 Oe (Figure 4) is not detected by the GMR sensors) as to eliminate any additional magnetic field.

The biasing coils are placed in a simmetrical quasi Helmholtz like configuration because of the requirement for ensuring an adequate distance between each GMR sensor (such as the traces beneath each sensor to not influence the output of the other sensor). The magnetic field strength in the sensor area (H_{bias}) was precisely determined during the PCB assembly stage (before sensor placement) using a 475 DSP Gaussmeter (Lake Shore Cryotronics, Westerville, OH, USA).

More studies can be done to find out the minimum possible distance between the GMR sensors to ensure proper results. This effect could have been mitigated by using larger biasing coils but that would have contributed to the costs and power consumption of the system. As a prepolarization field is necessary for linearizing the GMR sensors output, the biasing for the sensors was set to 4–8 Oe. The relationship between the coils supply current and the bias magnetic field present in the sensor area in air is (the current I_C is expressed in mA):

$$H_{bias} = I_C \cdot 0.1391 \text{ [Oe]} \tag{11}$$

where H_{bias} is the bias magnetic field produced by the coil in the sensor area and I_C is the coil 1 and coil 2 (Figure 6b) supply current (e.g. 57.55 mA for 8 Oe bias). Note that the resistance of each biasing coil is 38 Ω.

Furthermore, like shown in [10], if we take into account the thermal influence for the sensors response, by considering that the system is thermally balanced and the same type of sensors are used, the total output voltage of the sensors from the differential system can be expressed with:

$$\Delta U = (K_{S1} + K_{S2}) \cdot H_I = (K_{S1} + K_{S2}) \cdot C \cdot I = S \cdot I \tag{12}$$

where K_{S1} and K_{S2} are the sensitivities of each sensor, S (mV/mA) is the sensitivity of the differential measurement system, $H_I = C \cdot I$ (C is a constant) is the magnetic field strength created by the current passing through the trace.

3. Results and Discussion

3.1. Experimental Results for the Current Measurement Setup

The results presented in this section are a summary and focus on demonstrating the low currents sensing capabilities of the proposed setup (Figure 6a,b). As shown in Figure 5 and in [10], bias for the sensors is needed for the output to be linearized. Note that for all results, the real sensor sensitivity is shown (without amplification). As mentioned previously, the main challenge is low currents measurements, since higher currents can be easily detected with the setup from Figure 6 for example by integrating a copper bar on the PCB backside. In Figure 8, the response obtained with the setup by measuring a variable DC current between ±150 mA is shown. The sensitivity of the measured differential output is S_{measured} = 0.2319 mV/mA which shows a good correlation between the theoretical and experimental results.

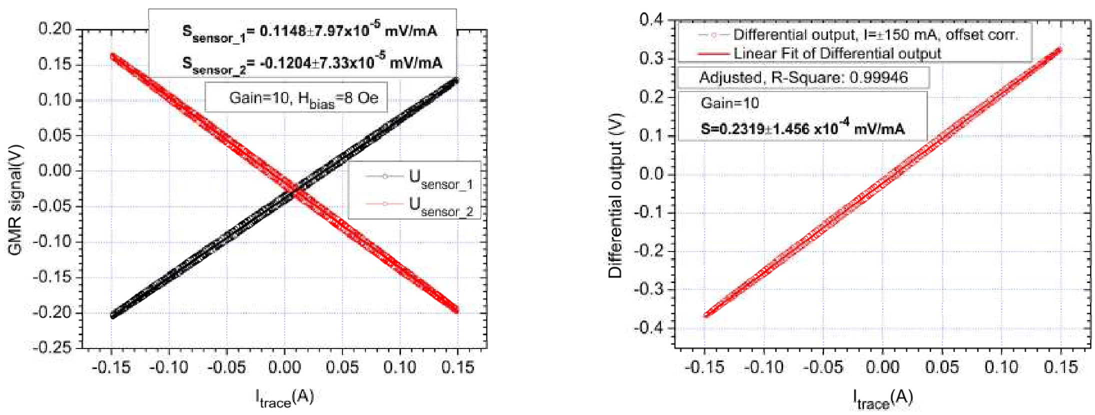

(**a**) (**b**)

Figure 8. Response of the system for a ±150 mA, DC current, H_{bias} was set to 8 Oe: (**a**) individual sensors response; (**b**) differential output.

Compared with the results presented in [10], for the NVE AG003-01E sensor evaluation kit (which utilizes the same model of sensors), measured on a single trace with a similar width 0.254 mm, the obtained sensitivity is S_{measured} = 0.0179 mV/mA while for the differential system in [10] with a trace thickness of 4 mm, for the same 150 mA test, the obtained sensitivity S_{D} = 4 mm = 0.028 mV/mA which is approximately 8.3 times lower. Thus, in this test, with the multi-trace setup an increase in sensitivity of ~13 times compared to the sensor evaluation kit was obtained and ~8.3 times compared to the already optimized differential setup from [10]. Note that for easier comparison with the results that can be obtained with the analytical method, for each testing scenario, the sensitivity of the sensors is reported (the sensitivity of the entire setup depending on amplifier configuration).

Due to the significant gains in sensor sensitivity, lower current values can be detected accurately. In Figure 9a, the differential output obtained with the setup by measuring a variable DC current between ±5 mA. Figure 9b shows the differential response obtained from the setup measuring a variable DC current between ±2 mA with different biasing fields from 4–8 Oe. The results have shown the optimal sensitivity level to be around the 8 Oe bias level. Experiments with higher bias fields were performed, but the optimal sensitivity level was confirmed to be 8 Oe. Also, for a higher bias field and current values, especially with high amplifier gains, there could be a risk in saturating the voltage bandwidth for the amplifier or DAQ board. For measuring current values around 1 mA with good accuracy, extra precautions should be taken like electromagnetic shielding of the sensor setup and extra amplifications steps. The DC detection limit is 100 μA.

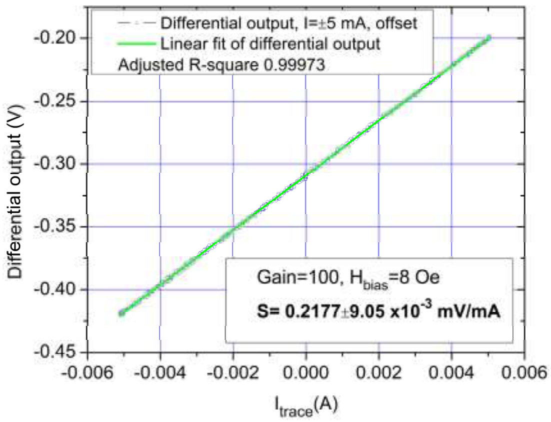

(**a**)

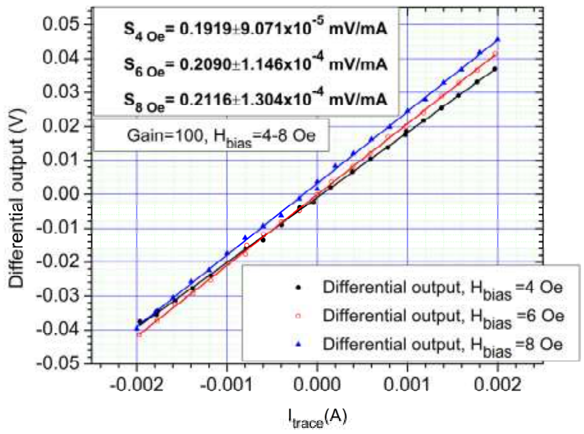

(**b**)

Figure 9. DC response of the system for low current values: (**a**) Differential output for a ±5 mA, DC current, H_{bias} was set to 8 Oe; (**b**) Differential output of sensors polarized at 4,6,8 Oe, DC, ±2 mA (in this case, the adjusted R-squared for the fit function was: adjusted $R\text{-}square_{4Oe}$ = 0.99961, adjusted $R\text{-}square_{6Oe}$ = 0.9995, adjusted $R\text{-}square_{8Oe}$ = 0.99943). Notice the linear characteristic of the output, although, for very low current values, some neliniarities can be present, but the overall linear tendency maintains.

For sensors that are perfectly matched and are subject to the same biasing field, the temperature drift of the offset can, theoretically go to zero. In [10] we measured the temperature drift of the offset to be $\Delta U_0/\Delta T \approx -7.9 \times 10^{-6}$ V/°C which means about -2.59×10^{-4} A/°C in terms of measured current, for a temperature variation of 20 °C. Also, we can note that any temperature drifts in the operating range of the bias coils lead to no significant changes to the bias magnetic field as we estimate that the temperature of these components is no larger than 37 °C during our tests. Also, all measurements were performed on the setup at thermal equilibrium state, were no significant changes to the offset were observed. Furthermore, the low current values passing through the trace caused no significant heating effects on the PCB area in the GMR sensors vicinity.

In Figure 10a,b, the response of the system when measuring a 100 Hz, 10 mA sinewave current is shown. Similar sensitivities levels can be obtained for AC/DC currents but identical biasing fields must be applied for the two sensors.

From Figure 10a,b, we can denote that the differential output maintains signal integrity (waveform of the trace current) with no distorsions. The detection limit for a 100 Hz sine wave is 100 μA (same as in DC) while for a 1 kHz sine wave is 300 μA (no significant increase in the detection limit was found at higher frequencies). We found this limitation to be due mainly to the signal processing chain and not due to the GMR sensors which have an operating frequency range from DC to 1 MHz [22].

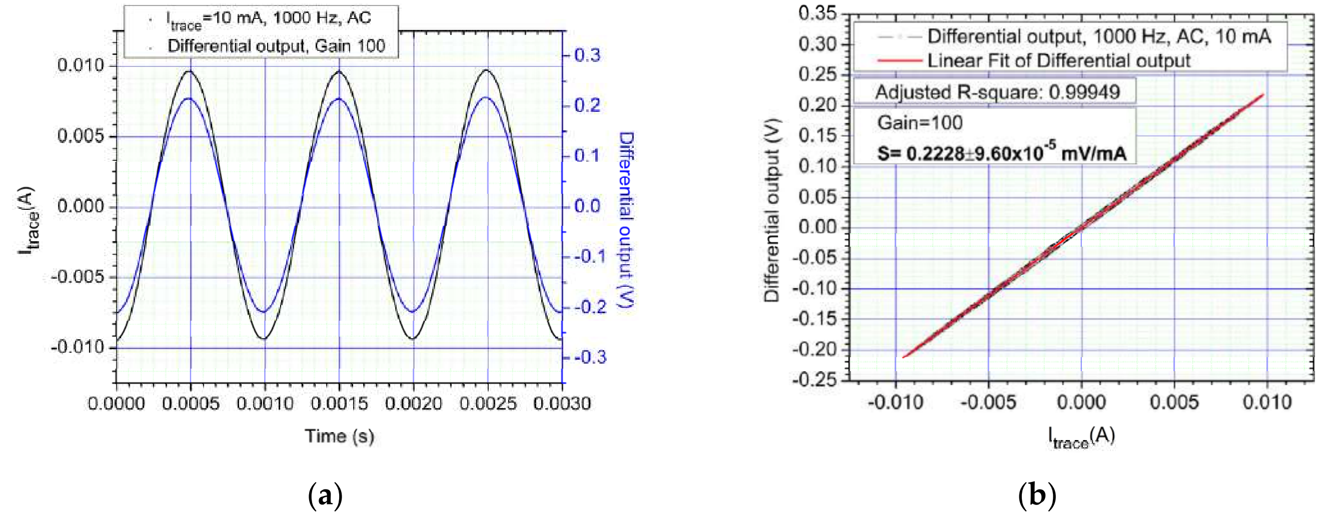

Figure 10. AC response of the system, 8 Oe biased sensors, 1000 Hz sine waveform at 10 mA: (**a**) Differential output and trace current time dependency; (**b**) Differential output of sensors. The sensitivity for the sensors in the case is S = 0.2228 mV/mA $\pm 9.6 \times 10^{-5}$. Notice the sensitivity level is similar to that of DC measurements.

The AC response to a square wave, 1 kHz, 20 mA current is detailed in Figure 11a. Multiple tests (with different biasing levels and frequencies) have determined a rise time and fall time of approximately 15 µs. Figure 11b shows the response of the system under a short 20 mA square pulse. Figure 12a,b show that even though, at lower frequencies, 8 Oe was the optimal choice in terms of biasing, at higher frequencies, 6 Oe is optimal in the present setup (from the 4–8 Oe bias fields range). From this analysis, we determined that, as expected, the rise and fall times as well as the frequency characteristics of the system this is mainly limited by the electronics (especially the instrumentation amplifiers) as the GMR sensors have a maximum frequency response limit of 1 MHz [22].

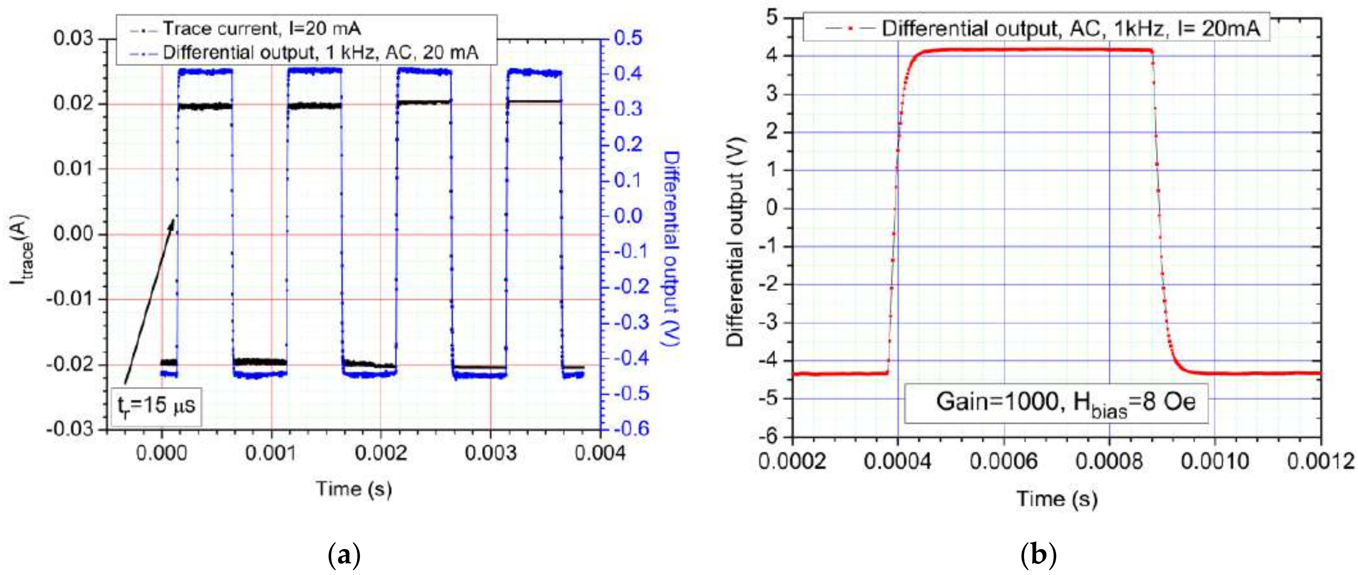

Figure 11. (**a**) AC response of the system, 8 Oe biased sensors, 1 kHz square waveform at 20 mA: a rise time and fall time of 15 µs was found in this case (measured between the 10–90% levels); The sensitivity for the sensors in this case is $S = 0.2120 \pm 7.186 \times 10^{-4}$ mV/mA; (**b**) AC response of the system, 8 Oe biased sensors, AC, 1 kHz, 20 mA pulse.

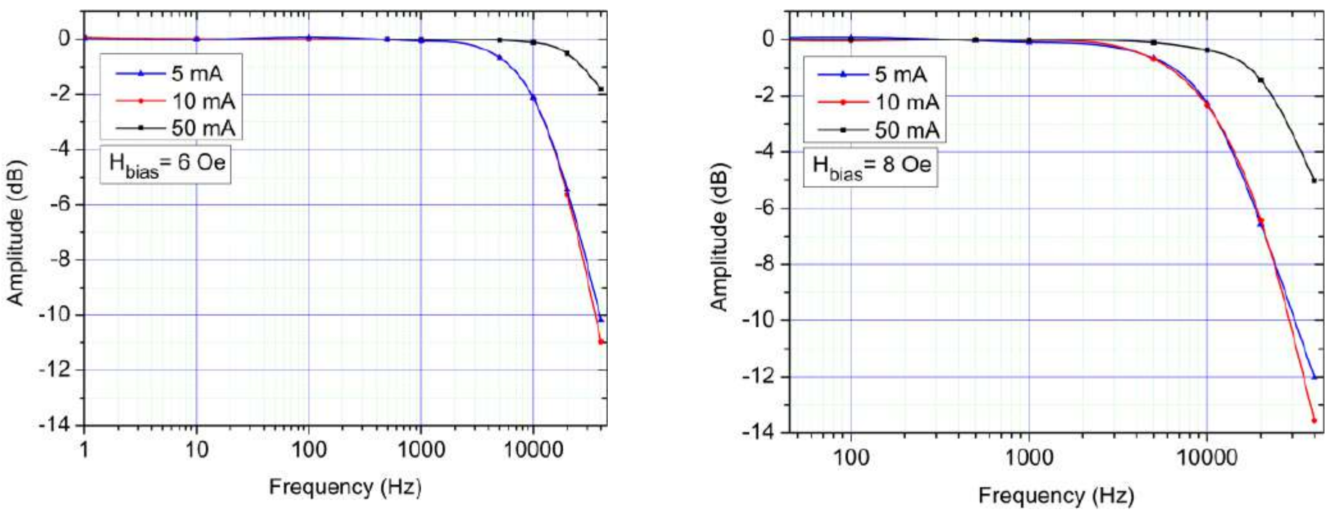

(**a**) (**b**)

Figure 12. (**a**) AC frequency response (transfer function) of the system, 6 Oe biased sensors for different measured currents; (**b**) AC frequency response (transfer function) of the system, 8 Oe biased sensors for different measured currents.

Since the planar coil has an inductive component under AC (inductance of 26.3 µH), impedance can play a role in the response of the system. The impedance-frequency (Figure 13a) characteristic can create a phase-shift between the current and voltage waveforms. The impedance of the planar coil is equal to the resistance up to around 4000 Hz ($Z = R = 2\ \Omega$).

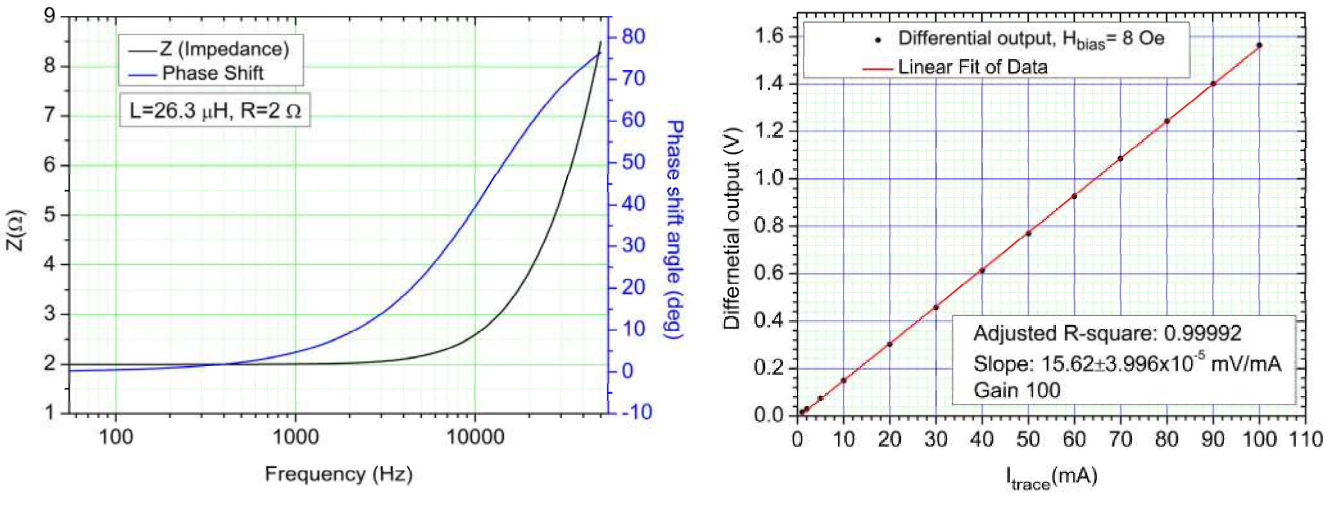

(**a**) (**b**)

Figure 13. (**a**) Impedance-frequency characteristic and current-voltage phase shift angle frequency dependency; (**b**) AC calibration curve in the 0–100 mA range for a 100 Hz sinewave. Note that the minimum trace current represented on the calibration curve is 1 mA.

Figure 13b shows the AC calibration curve for the device within the 0–100 mA range when measuring a 100 Hz sinewave. We used the adjusted R-squared term to show how well data is aligned over the fitting line. The adjusted *R-square* is 0.99992. The sensitivity of the entire setup in *S*, in the 0–100 mA range is 15.62 mV/mA. Note that there is a very good correlation between the measured current and the response of the system.

3.2. Experimental Results for the Magnetic Nanoparticles Detection Setup

Even though the developed system is not designed for magnetic nanoparticles (MNPs) detection (due to the design of the GMR sensors), it can still be used for proof-of-concept purposes. Figure 14a shows the measurement setup for the MNPs detection setup, while Figure 14b shows the waveform of the applied biasing field, H_{bias} and output signals from setup with standardized distilled water probe and MNP aqueous solution. Thus, for this purpose, on the setup (Figure 6a), two cylindrical chambers with the interior diameter of 2.5 mm and 2 mm height were attached on top of the sensors—a reference chamber on S_1, which will contain water, and in the other chamber (on S_2) an aqueous solution with PEG6000 functionalized maghemite MNPs will be pipetted (note the inset in Figure 14b). The MNPs in the aqueous solution functionalized with PEG6000 have an average magnetic diameter, d_{magn}, of 11.48 nm which has been determined in a previous study [27].

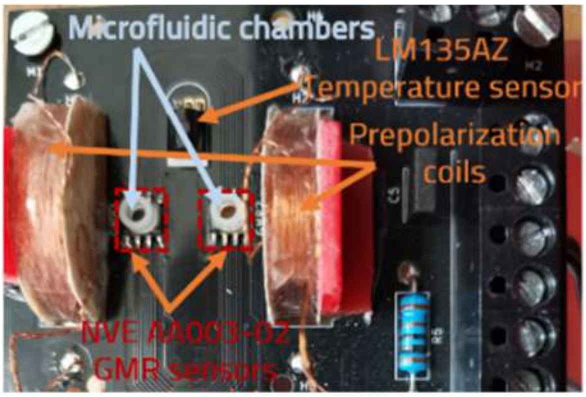

(**a**)

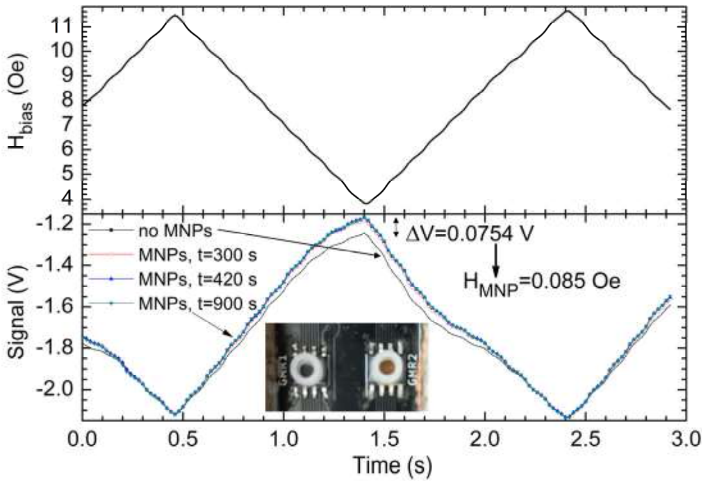

(**b**)

Figure 14. (**a**) Measurement system adapted for the detection of MNP (**b**) Waveform of the applied biasing field, H_{bias} and output signals from setup: with standardized distilled water probe and MNP aqueous solution over the sensor's surface after different elapsed times. The greatest field contribution of the MNPs was found at the H_{bias} = 4 Oe level where a ΔU = 0.0754 V signal variation was found compared with the case with no MNPs. The total gain of the signal was G = 100.

In both chambers, the same amount of liquid was pipetted: 2.5 µL distilled water on sensor 1, and the previously described aqueous MNPs solution on sensor 2. In this way, the thermal balance for the two sensors can be ensured. The system was biased at 8 Oe, then the current through the biasing coils was varied in steps at different values in the 26–84 mA interval similar to the characteristic in Figure 9b. This generated a variable magnetic field in the 3.61–11.76 Oe region, centered on 8 Oe. The graph in Figure 14b, marks different values for the biasing field. Note that this still represent a DC test, with a variable biasing level. Due to the differential measurement setup, the differential output voltage is an expression of the magnetic field generated by the magnetic nanoparticles situated on sensor 2 (Figure 14b). Given the return field lines, the effective magnetic field from sensor 2 will decrease. Figure 14b shows the detection characteristic obtained on different time intervals after pipetting the MNPs solution on sensor 2.

In this way, given the calibration process described above, the magnetic field generated by the MNPs on sensor 2 was estimated (Figure 14b). For "large" fields like 12 Oe, the contribution of the field produced by the MNP is covered by the biasing field. By analyzing Figure 14b, we can notice that the field contribution of the MNPs is greatest at a 4 Oe biasing field. Thus, for H_{bias} = 4 Oe, the MNPs generate a magnetic field of approximately H = 0.085 Oe. Using data from the magnetization curves [27] of the PEG6000 functionalized MNPs we estimated that our system determined a magnetic moment of about 0.29×10^{-4} emu for a signal variation of 0.0754 V. This magnetic moment corresponds to a mass of about 33.39 µg of powder composed from maghemite functionalised with PEG 6000. This means about 2.40 µg of pure maghemite cores. The estimation was done by comparing the magnetization curves for pure maghemite powder [28] and functionalised maghemite with PEG 6000 [27,28].

By varying the biasing field, an unequivocal detection of the presence of MNPs is obtained. The tests highlight the MNPs sedimentation process on the surface of the sensor through the amplitude of the measured signal. In [29], a detection system utilizing the same type of sensor is shown but, in that case, the MNPs solution is placed on a cylinder which rotates in the sensor vicinity (the system detects the magnetic field variations as the probe passes the sensor). Our proposed solution does not require any moving parts and allows great flexibility in the MNPs detection regime as well as possibility for autocalibration by means of the planar coil which generates a local magnetic field, similar to that generated by the MNPs.

3.3. State of the Art Comparison

Although the developed setup is for demonstration purposes and is not intended to be compared with commercial sensor solutions, a summarizing state-of-the-art performance comparison with similar magnetoresistive sensor technologies is given in Table 1.

Table 1. Summarizing state-of the art performance comparison for magnetoresistive current sensor technologies.

Parameter	This Work	[10]	[9]	MCA1101-xx-5 Series [30]	TMCS1100A Series [31]	ACS70331 Series [32]	[14]
Sensor technology	GMR	GMR	GMR	AMR	Hall	GMR	PHR (planar Hall resistance)
Sensor setup sensitivity	0.1562 to 0.2319 mV/mA	0.0272 to 0.0307 mV/mA	0.03 to 0.04 V/A [3]	35 mV/A to 350 mV/A	50 to 400 mV/A	200 to 800 mV/A	1.2 mA/LSB (12 bit)
Measurement range	DC: ±2 mA to ±300 mA [1] AC: ±2 mA to ±300 mA [1]	DC: ±75 mA to ±4 A AC: ±150 mA to ±4 A	±45 A	±5 to ±50 A	±5.75 A to ±46 A	0–2.5 A to ±5 A	±1.2 A
Detection limit	DC: 100 µA AC: 100 to 300 µA	4 mA	N/A	10 mA	N/A	5 mA	5 mA
Power consumption	Setup: ~258 mW [2] Sensors: 6.4 mW [2]	~6.4 mW	1.6 to 3.2 W	~32.5 to 35 mW	33 mW (no V_{out} load); 640 mW [4]	14.9 mW	13 mW
Calibration	Yes, biasing coil system	Yes, adjustable permanent magnet	Yes, biasing coil system	N/A	N/A	Yes, Analog-to-digital converter	Yes, Analog-to-digital converter

[1] Note that the measurement range can be easily extended by integrating a thicker copper trace or bar (e.g. on the PCB backside or above the sensor) to support higher currents. The focus of this work was to increase accuracy in the low currents range. [2] The power consumption of the setup can be reduced to ~6.4 mW by replacing the biasing system with a permanent magnet. Note that the power consumption of the biasing coils is ~251.7 mW for a 57.55 mA current (corresponding to an 8 Oe bias field) passing through the coils while the GMR sensors dissipate around 6.4 mW. [3] Not directly specified in the article but can be deducted from experimental results. [4] Maximum power dissipated when measuring a current of 16 A.

It should be mentioned that performance characteristics are dependent on the setup, electronics and configuration, and also are defined differently depending on the manufacturer. Thus, direct comparison can prove difficult and some parameters cannot be determined precisely. Table 2 shows the main advantages and disadvantages of the implemented setup. From Tables 1 and 2, we can note the performance advantage of the implemented setup, especially in terms of sensitivity, detection limit and power consumption. Also, the developed setup is much more flexible in terms of applications as the sensors can be precisely calibrated using the biasing coils and it can also be used for MNPs measurements.

Table 2. Main advantages and disadvantages of the implemented setup.

Advantages	Disadvantages
High sensor sensitivity: 0.1562 to 0.2319 mV/mA	Limited measurement range (2–300 mA) [1]
Low detection limit: DC: 100 µA AC: 100 to 300 µA	Coil biasing system consumes extra power [2]
Precision biasing with coils	Hybrid setup [3]
Precision DC/AC current sensing	Moderate components integration level
Moderately low power consumption (note Table 1)	-
Possibility for MNPs measurements	-
Low temperature drift of the offset: -2.59×10^{-4} A/°C	-

[1] The measurement range can be easily extended (note Table 1, footnote 1). [2] Biasing coils can be replaced by a permanent magnet for applications that do not require a variable biasing field. [3] The sensors setup is separate from the amplifier and data acquisition setup.

In terms of drawbacks, the biasing coils consume the majority of power in our setup, but this effect can be mitigated by replacing them with a permanent magnet in applications that do not require a variable biasing level. Also, the proposed system is a hybrid setup with moderate integration level meaning that future efforts can focus on compactness and versatility in component choice and placement. We do not consider the specified measurement range a disadvantage since can be easily extended for higher currents by integrating a thicker copper trace or bar (Table 1, footnote 1).

4. Conclusions

A very high sensitivity non-contacting current measurement setup based on a custom PCB with GMR sensors, which is optimized for low field applications was implemented. The system is designed to measure currents between 2–300 mA but the operational range can be extended, for example by integrating a copper bar on the PCB backside (Figure 6a). The setup has a sensitivity between 15.62 to 23.19 mV/mA, for biasing fields between 4 to 8 Oe with a detection limit of 100 µA in DC and 100 to 300 µA in AC from 10 Hz to 50 kHz. The reported sensor sensitivity is about 13 times higher than a single similarly biased GMR sensor and around 7 to 8.5 times increase in sensitivity compared to the optimized differential setup that we showed in [10]. A biasing field applied by two circular coils in a quasi-Helmholtz like configuration were used to linearize the system response and allow different modes of operation (different biasing fields, variable biasing fields). This approach was taken to increase the versatility of the system as a testing environment, but for a practical application, a permanent magnet has many advantages such as no extra power consumption or generated heat. The novelty of our approach consists in using a multi-trace setup that essentially constitutes a planar coil which will increase the useful magnetic field in the sensor area. An analytical method was implemented (Figure 2a, Equations (2)–(7)) to estimate this increase. Also, the sensors operate in a similar double differential setup to the one we reported in [10]. Together, this has greatly improved the operational range of the sensor for low current values. This approach was not seen in other works [9,17–19], or in commercial sensor solution based on AMR [8,30,33], Hall [31], or microfluxgate [4,6,34]. The obtained performance makes this setup suitable to be adapted and implemented in various current measurement applications for high precision electronics, smart grid applications and automotive industry.

The results were obtained without using electromagnetic shielding and for AC measurements, a basic integrated capacitor filtering system was used. It was determined that the AC frequency characteristics are mostly limited by the electronics (amplifier system). The impedance of the planar coil has a significant influence only after frequencies above

4000 Hz. The system exhibits certain qualities such as: high sensitivity (similar sensitivity levels for DC and AC currents), galvanic isolation, thermal stability (within the operating limits), preservation of signal integrity from the input current (Figures 10 and 11). The power rating of the system is very low since the sensors consume only about 6.4 mW (3.2 mW each), the biasing coil system consumes around 251.7 mW for an 8 Oe bias field, each INA118 has a quiescent current of only 350 μA and the LabJack EI1040 is very low power. The most energy consuming element in the current setup is the biasing coil system which can be easily replaced with a small permanent magnet (as shown in [10]) for each sensor in case the application does not require an AC biasing field. Consequently, the system can be described as very low power.

Furthermore, this field and sensitivity is sufficient for the detection of MNPs with the GMR sensor [35], thus, preliminary testing using the setup for an aqueous solution of PEG6000 functionalized maghemite magnetic nanoparticles was performed. With this setup, the magnetic field of the nanoparticles of about 0.085 Oe was able to be detected reliably (Figure 13b) on a standardized sample. We estimate that with a sensor design optimized for nanoparticles detection the performance can be improved even more. The current through the conductive band can be used to produce an AC excitation field for detection of the MNPs. To ensure a smaller distance between MNPs and GMR sensors, a flip-chip package type can be used in this development, as in [36]. This approach will reduce the distance between the MNPs and the sensor, which will improve sensitivity and avoid utilizing complex measurement setups like in [29], where the MNP solution is placed in a container on a rotating cylinder in the sensor's vicinity. In that case the system detects the magnetic field variations caused by the probe passing by the sensor. Our proposed solution does not require any moving parts and allows great flexibility in choosing the MNPs detection regime as well as autocalibration function through the planar coil which generates a local field similar to the one generated by the MNPs.

Finally, the theoretical (analytical method) and operational basis (practical implementation) for developing a multi-trace GMR-based high sensitivity current sensor PCB has been established. From those we can note: appropriate biasing of the sensors, adequate spacing of components to avoid parasitic magnetic fields, multi-trace and differential or double differential design, appropriate amplification, filtering and quality data acquisition. In terms of future developments, an optimized, chip sensor design that will integrate many of the advancements from the setup will developed which can increase the low field capabilities even further.

Author Contributions: Conceptualization, C.M., J.N., M.A. and M.V.; methodology, C.M, M.V, M.O.; software, M.O.; validation, M.V., E.H.; formal analysis, M.O.; investigation, C.M, M.O.; resources, M.V., J.N., M.A.; data curation, E.H.; writing—original draft preparation, C.M.; writing—review and editing, C.M., M.V., E.H.; visualization, C.M, M.V.; supervision, M.V, E.H.; project administration, M.V, M.A.; funding acquisition, M.V., J.N., M.A. All authors have read and agreed to the published version of the manuscript.

Funding: This research was funded for C.M., M.O. and J.N. by a grant of the Romanian Ministry of Research and Innovation, CCDI-UEFISCDI project number PED 315/2020 and for M.V. and M.A. by a grant of Romanian Ministry of Research and Innovation, CCDI-UEFISCDI project number 3PCCDI/2018 within PNCDI III. The APC was funded in part by Transilvania University of Brasov.

Conflicts of Interest: The authors declare no conflict of interest.

Appendix A

In this appendix section, an example calculus for the analytical method is shown. The parameters involved in the calculation are shown in Table A1 (note Figure 2a).

Table A1. Parameters for an example calculation of the analytical method.

Parameter	D [mm]	T_d [mm]	I [A]	μ_0 [H/m]	h [mm]	D_{n1} [mm]	D_{n2} [mm]
Value	0.22	0.19	0.5	$4\pi\times10^{-7}$	0.8	Equation (A1)	Equation (A2)

Parameters D_{n1} and D_{n2} are detailed in Equations (A1) and (A2).

Parameters D_{n1}, D_{n2} can be computed in function of the number of traces, n (Figure 2a), with:

$$D_{n1} = \frac{D}{2} + (n-1)D + nT_d\,, \tag{A1}$$

$$D_{n2} = \frac{D}{2} + nD + nT_d\,. \tag{A2}$$

Based on Equations (A1) and (A2), the individual D_{n1} and D_{n2} values can be calculated. Furthermore, we can substitute them in Equation (4) for calculating the magnetic field produced by each trace, whilst doubling the field value for the field produced by a similarly distanced traced from the sensor. The calculation for the individual trace components, based on the parameters in Table A1 is:

$$B_0 = \frac{\mu_0 I}{\pi D \cdot 10^{-3}} \cdot \left[arctan\left(\frac{D}{2h}\right)\right] = 1.2422 \cdot 10^{-4}\ [\text{T}], \tag{A3}$$

$$2 \cdot B_1 = \frac{\mu_0 I}{\pi D \cdot 10^{-3}} \cdot \left[arctan\left(\frac{D_{12}}{h}\right) - arctan\left(\frac{D_{11}}{h}\right)\right] = 1.9782 \cdot 10^{-4}\ [\text{T}], \tag{A4}$$

$$2 \cdot B_2 = \frac{\mu_0 I}{\pi D \cdot 10^{-3}} \cdot \left[arctan\left(\frac{D_{22}}{h}\right) - arctan\left(\frac{D_{21}}{h}\right)\right] = 1.223 \cdot 10^{-4}\ [\text{T}], \tag{A5}$$

$$2 \cdot B_3 = \frac{\mu_0 I}{\pi D \cdot 10^{-3}} \cdot \left[arctan\left(\frac{D_{32}}{h}\right) - arctan\left(\frac{D_{31}}{h}\right)\right] = 7.457 \cdot 10^{-5}\ [\text{T}], \tag{A6}$$

$$2 \cdot B_4 = \frac{\mu_0 I}{\pi D \cdot 10^{-3}} \cdot \left[arctan\left(\frac{D_{42}}{h}\right) - arctan\left(\frac{D_{41}}{h}\right)\right] = 4.81 \cdot 10^{-5}\ [\text{T}], \tag{A7}$$

$$2 \cdot B_5 = \frac{\mu_0 I}{\pi D \cdot 10^{-3}} \cdot \left[arctan\left(\frac{D_{52}}{h}\right) - arctan\left(\frac{D_{51}}{h}\right)\right] = 3.31 \cdot 10^{-5}\ [\text{T}]. \tag{A8}$$

With the results from Equations (A3)–(A8), we can compute the total field corresponding to a particular multi-trace structure (note that B_0 is the result for a single trace). The result is shown in Equations (A9)–(A13):

$$3 \text{ spires}: \ B_{total} = B_0 + 2B_1 = 3.2204 \cdot 10^{-4}\ [\text{T}] \tag{A9}$$

$$5 \text{ spires}: \ B_{total} = B_0 + 2B_1 + 2B_2 = 4.4434 \cdot 10^{-4}\ [\text{T}] \tag{A10}$$

$$7 \text{ spires}: \ B_{total} = B_0 + 2B_1 + 2B_2 + 2B_3 = 5.1891 \cdot 10^{-4}\ [\text{T}] \tag{A11}$$

$$9 \text{ spires}: \ B_{total} = B_0 + 2B_1 + 2B_2 + 2B_3 + 2B_4 = 5.6701 \cdot 10^{-4}\ [\text{T}] \tag{A12}$$

$$11 \text{ spires}: \ B_{total} = B_0 + 2B_1 + 2B_2 + 2B_3 + 2B_4 + 2B_5 = 6.0011 \cdot 10^{-4}\ [\text{T}] \tag{A13}$$

References

1. Patel, A.; Ferdowsi, M. Current Sensing for Automotive Electronics—A Survey. *IEEE Trans. Veh. Technol.* **2009**, *58*, 4108–4119. [CrossRef]
2. Soliman, E.; Hofmann, K.; Reeg, H.; Schwickert, M. Noise study of open-loop direct current-current transformer using magneto-resistance sensors. In Proceedings of the 2016 IEEE Sensors Applications Symposium (SAS), Catania, Italy, 20–22 April 2016; IEEE: Piscataway, NJ, USA, 2016; pp. 1–5. [CrossRef]
3. Ripka, P. Electric current sensors: A review. *Meas. Sci. Technol.* **2010**, *21*, 112001. [CrossRef]

4. Ripka, P.; Draxler, K.; Styblikova, R. AC/DC Current Transformer with Single Winding. *IEEE Trans. Magn.* **2014**, *50*, 1–4. [CrossRef]
5. Lenz, J.E. A review of magnetic sensors. *Proc. IEEE* **1990**, *78*, 973–989. [CrossRef]
6. Ripka, P.; Mlejnek, P.; Hejda, P.; Chirtsov, A.; Vyhnánek, J. Rectangular Array Electric Current Transducer with Integrated Fluxgate Sensors. *Sensors* **2019**, *19*, 4964. [CrossRef]
7. Yatchev, I.; Sen, M.; Balabozov, I.; Kostov, I. Modelling of a Hall Effect-Based Current Sensor with an Open Core Magnetic Concentrator. *Sensors* **2018**, *18*, 1260. [CrossRef]
8. Mlejnek, P.; Vopalensky, M.; Ripka, P. AMR current measurement device. *Sens. Actuators A* **2008**, *141*, 649–653. [CrossRef]
9. Poon, T.Y.; Tse, N.C.F.; Lau, R.W.H. Extending the GMR Current Measurement Range with a Counteracting Magnetic Field. *Sensors* **2013**, *13*, 8042–8059. [CrossRef]
10. Mușuroi, C.; Oproiu, M.; Volmer, M.; Firastrau, I. High Sensitivity Differential Giant Magnetoresistance (GMR) Based Sensor for Non-Contacting DC/AC Current Measurement. *Sensors* **2020**, *20*, 323. [CrossRef]
11. Vidal, E.G.; Muñoz, D.R.; Arias, S.I.R.; Moreno, J.S.; Cardoso, S.; Ferreira, R.; Freitas, P. Electronic Energy Meter Based on a Tunnel Magnetoresistive Effect (TMR) Current Sensor. *Materials* **2017**, *10*, 1134. [CrossRef]
12. Lee, J.; Oh, Y.; Oh, S.; Chae, H. Low Power CMOS-Based Hall Sensor with Simple Structure Using Double-Sampling Delta-Sigma ADC. *Sensors* **2020**, *20*, 5285. [CrossRef] [PubMed]
13. Weiss, R.; Mattheis, R.; Reiss, G. Advanced giant magnetoresistance technology for measurement applications. *Meas. Sci. Technol.* **2013**, *24*, 082001. [CrossRef]
14. Lee, S.; Hong, S.; Park, W.; Kim, W.; Lee, J.; Shin, K.; Kim, C.-G.; Lee, D. High Accuracy Open-Type Current Sensor with a Differential Planar Hall Resistive Sensor. *Sensors* **2018**, *18*, 2231. [CrossRef] [PubMed]
15. Jogschies, L.; Klaas, D.; Kruppe, R.; Rittinger, J.; Taptimthong, P.; Wienecke, A.; Rissing, L.; Wurz, M.C. Recent Developments of Magnetoresistive Sensors for Industrial Applications. *Sensors* **2015**, *15*, 28665–28689. [CrossRef]
16. Yang, X.; Xie, C.; Wang, Y.; Wang, Y.; Yang, W.; Dong, G. Optimization Design of a Giant Magneto Resistive Effect Based Current Sensor with a Magnetic Shielding. *IEEE Trans. Appl. Supercond.* **2014**, *24*, 1–4. [CrossRef]
17. Jedlicska, I.; Weiss, R.; Weigel, R. Linearizing the Output Characteristic of GMR Current Sensors through Hysteresis Modeling. *IEEE Trans. Ind. Electron.* **2010**, *57*, 1728–1734. [CrossRef]
18. Li, Z.; Dixon, S. A Closed-Loop Operation to Improve GMR Sensor Accuracy. *IEEE Sens. J.* **2016**, *16*, 6003–6007. [CrossRef]
19. Hudoffsky, B.; Roth-Stielow, J. New evaluation of low frequency capture for a wide bandwidth clamping current probe for ±800 A using GMR sensors. In Proceedings of the 2011 14th European Conference on Power Electronics and Applications, Birmingham, UK, 30 August–1 September 2011; pp. 1–7.
20. Ouyang, Y.; He, J.; Hu, J.; Wang, S.X. A Current Sensor Based on the Giant Magnetoresistance Effect: Design and Potential Smart Grid Applications. *Sensors* **2012**, *12*, 15520–15541. [CrossRef]
21. Rijks, T.; Coehoorn, R.; De Jong, M.; De Jonge, W. Semiclassical calculations of the anisotropic magnetoresistance of NiFe-based thin films, wires, and multilayers. *Phys. Rev. B* **1995**, *51*, 283. [CrossRef]
22. NVE Sensors Catalogue. Available online: https://www.nve.com/Downloads/catalog.pdf (accessed on 5 April 2021).
23. The Object Oriented MicroMagnetic Framework (OOMMF). Available online: https://math.nist.gov/oommf/ (accessed on 5 April 2021).
24. INA118 Instrumentation Amplifier Datasheet. Available online: https://www.ti.com/lit/ds/symlink/ina118.pdf (accessed on 5 April 2021).
25. LabJack EI1040 Datasheet. Available online: https://labjack.com/support/datasheets/accessories/ei-1040 (accessed on 5 April 2021).
26. National Instruments NI 6281 DAQ Datasheet. Available online: https://www.ni.com/pdf/manuals/375218c.pdf (accessed on 5 April 2021).
27. Volmer, M.; Avram, M. Using permalloy based planar hall effect sensors to capture and detect superparamagnetic beads for lab on a chip applications. *J. Magn. Magn. Mater.* **2015**, *381*, 481–487. [CrossRef]
28. Volmer, M.; Avram, M. Signal dependence on magnetic nanoparticles position over a planar Hall effect biosensor. *Microelectron. Eng.* **2013**, *108*, 116–120. [CrossRef]
29. Park, J. Superparamagnetic nanoparticle quantification using a giant magnetoresistive sensor and permanent magnets. *J. Magn. Magn. Mater.* **2015**, *389*, 56–60. [CrossRef]
30. Aceinna Current Sensors Catalogue. Available online: https://www.aceinna.com/current-sensors (accessed on 5 April 2021).
31. Texas Instruments TMCS1100 Hall Current Sensor Datasheet. Available online: https://www.ti.com/lit/ds/symlink/tmcs1100.pdf (accessed on 5 April 2021).
32. Allegro Microsystems ACS70331 Series GMR Current Sensor Datasheet. Available online: https://www.allegromicro.com/en/products/sense/current-sensor-ics/zero-to-fifty-amp-integrated-conductor-sensor-ics/acs70331 (accessed on 5 April 2021).
33. Sensitec Current Sensors Catalogue. Available online: https://www.sensitec.com/products-solutions/current-measurement/cfs1000 (accessed on 5 April 2021).
34. Snoeij, M.F.; Schaffer, V.; Udayashankar, S.; Ivanov, M.V. Integrated Fluxgate Magnetometer for Use in Isolated Current Sensing. *IEEE J. Solid-State Circuits* **2016**, *51*, 1684–1694. [CrossRef]

35. Volmer, M.; Avram, M. Micromagnetic Simulations on Detection of Magnetic Labelled Biomolecules Using MR Sensors. *J. Magn. Magn. Mater.* **2009**, *321*, 1683–1685. [CrossRef]
36. Xu, J.; Li, Q.; Gao, X.; Lv, F.; Guo, M.; Zhao, P.; Li, G. Shandong. Detection of the Concentration of $MnFe_2O_4$ Magnetic Microparticles Using Giant Magnetoresistance Sensors. *IEEE Trans. Magn.* **2015**, *52*. [CrossRef]

2021 International Aegean Conference on Electrical Machines and Power Electronics (ACEMP) & 2021 International Conference on Optimization of Electrical and Electronic Equipment (OPTIM) | 978-1-6654-0298-9/21/$31.00 ©2021 IEEE | DOI: 10.1109/OPTIM-ACEMP50812.2021.9590055

On Detection of Magnetic Nanoparticles Using a Commercial GMR Sensor

Marius Volmer*
Department of Electrical Engineering and Applied Phyiscs
Transilvania University of Brasov
Brasov, Romania
volmerm@unitbv.ro

Cristian Mușuroi
Electrical Engineering and Applied Physics Department
Transilvania University of Brasov
Brasov, Romania
cristian.musuroi@unitbv.ro

Mihai Oproiu
Electrical Engineering and Applied Physics Department
Transilvania University of Brasov
Brasov, Romania
petre.oproiu@unitbv.ro

Andrei Avram
Laboratory for Carbon Based Nanotechnologies and Nanostructures
National Institute for R&D in Microtechnologies - IMT Bucharest
Bucharest, Romania
andrei.thy@gmail.com

Marioara Avram
Laboratory for Micro- and Nano-Fluidics
National Institute for R&D in Microtechnologies - IMT Bucharest
Bucharest, Romania
marioara.avram@imt.ro

Elena Helerea
Electrical Engineering and Applied Physics Department
Transilvania Univeristy of Brasov
Brasov, Romania
helerea@unitbv.ro

***Abstract*—This paper describes the research for implementing a commercial giant magnetoresistive (GMR) sensor for detection of magnetic nanoparticles with potential applications in lab on a chip (LOC) device or for analysis of waste water. Micromagnetic simulations are performed to illustrate the behaviour of the detection system. The experimental setup focuses on the detection of polyethylene glycol (PEG6000) functionalized magnetic nanoparticles, commonly used in biosensors and LOC devices. Practical solutions for improving the GMR sensor measurement setup are detailed and discussed. From the experimental measurements we are able to detect a mass approximately 1.20 µg of pure maghemite cores which corresponds to a magnetic moment of approximately $9.098{\cdot}10^{-5}$ emu for a signal variation of 0.035 V. (in this case, a detection sensitivity of about 75.81 emu/g). Emphasis is placed on advantages in terms of setup sensitivity, flexibility and integration.**

Keywords—magnetic sensors, GMR effect, magnetic nanoparticles, micromagnetic simulation

I. INTRODUCTION

Magnetic nanoparticles (MNPs) and superparamagnetic beads (MBs) present a lot of interest in many fields like waste water purification, sorting, separating, purifying and detecting biomolecules in assays for rapid diagnosis applications in what is known as Lab on a Chip (LOC) device. Detection of functionalized magnetic nanoparticles, attached to biomolecules of interest, can be made by using magnetoresistive sensors (MR) based on anisotropic magnetoresistance (AMR) [1, 2], giant magnetoresistance (GMR) [2,3,4] tunnelling magnetoresistance (TMR) [5] and planar Hall effect [6,7], superconducting quantum interference devices (SQUIDs) [8]. The ability of the mentioned sensors to detect very weak magnetic field signals from MNPs, combined with their low cost, small size, and an output electric signal suitable for automated analysis, allows them to be a powerful tool for such applications.

Magnetic micro-devices have been developed in recent times for manipulation and capture of MNPs used for bio applications [9,10]. They are based on micro(electro)magnets, soft magnetic microstructures or external magnetic field generators. However, the main disadvantages of on-chip electromagnets compared with permanent magnets and external magnetic field generators are that they can increase the temperature of the chip during operation [10]. More recently, domain wall motion in nanometre thick magnetic films patterns, with special design, has been proved as an elegant method to precisely transport and capture MNPs to a target location [11,12,13] where detection takes place. These systems are quite complex, difficult to be manipulated and require specific microfabrication steps which makes them expensive.

In terms of detection, many works were made to optimize AMR, GMR and TMR sensors for MNPs detection [3, 5, 10, 14]. However, relatively low signal to noise ratio (SNR) of these sensors may often lead to erroneous detection, thus, methods to improve the SNR are of main interest.

By using MNPs in immunoassays it is possible to increase sensitivity and reduce analysis time by using external magnetic fields for magnetic separation [15]. MNPs have other advantages over traditional fluorescent and enzyme markers (such as better sensitivity [16]) which have limitation in opaque or disperse biological media. It should be noted that two different directions can be taken regarding their use: MNPs can act as a solid phase for immune complex formation or as labels for providing detection in the analysis.

GMR biosensors are low-cost alternatives to biochips [17] especially utilized in detection of DNA-DNA interactions and protein-immune sensing (with DNA or antibodies). GMR biosensors were developed as a bead array counter (BARC) system [18]. Spin-valve type GMR sensors are becoming more frequently used as biosensors due to higher accuracy and a more linear response [19]. Moreover, GMR biosensors have also been reported for genotyping [20]. The complex interaction between the magnetic layers of the spinvalve structure of a GMR sensor and MNPs are key elements in establishing the best approach for a GMR biosensor. Previous studies on [21, 22] made on spin valve structures, revealed that the output signal depends on the position of the MNPs over the sensor surface and we stressed the fact that it is more convenient to apply the magnetizing field, H_{bias}, perpendicular to the sensor surface [23]. Also, through previous studies, we emphasised the usefulness of the superparamagnetic behaviour, for biodetection processes [24].

For and actual LOC device based on GMR sensors, some considerations are necessary. Firstly, by using a non-encapsulated GMR sensor model, sensitivity can be increased, as well as the magnetic coupling between the sensor and the MNPs. Moreover, the GMR-based biosensor design should be

This work was supported for C.M., M.V, M.O., A.A. and M.A. by a grant of the Ministry of Research, Innovation and Digitization, CNCS/CCCDI – UEFISCDI, project number 3PCCDI/2018 within PNCDI III.

flexible enough to accommodate integration of other microdevices (such as microchannels, microvalves), which are an essential part of a LOC device.

In this paper, we prove the ability to detect magnetic nanoparticles using a sensor based on giant magnetoresistance (GMR) effect [25]-[27], for detection of magnetic nanoparticles, illustrating the potential use in biosensing and LOC applications. The working principle was illustrated with micromagnetic simulations and experimental measurements. Furthermore, we showed that an analysis of the derivative of the sensor output in function of the applied field can prove useful for further research (for example, when analysing the response from biofunctionalized MNPs).

The proposed method exhibits better sensitivity for the magnetic nanoparticles detection setup by using a less complex, single sensor setup and also by applying a constant magnetic field perpendicular to the sensor surface to magnetize the particles. MR sensors saturate at fields not greater than 0.01T and the detection process is highly influenced by the magnetostatic interaction between the sensor surface and MNPs. Thus, it can be noted that, in this case, the superparamagnetic behaviour of the MNPs is necessary to eliminate both the false positive detection signals and clustering processes in the liquid volume and on the surface of the sensor. Although a similar approach was demonstrated in [22, 24, 28] or, this work represents a refinement of the proposed method by utilizing offset correction and due to an increased sensitivity of about 75.81 emu/g. Furthermore, coupled with magnetorelaxometry through volume magneto immunoassay detection [29], advantages in terms of setup flexibility, size and cost can be achieved. Other MNPs sensing methods using MR sensors, although promising, show a more complex setup and often lower sensitivity [28, 30]. In terms of drawbacks, we can note hybrid setup (the sensors setup is separate from the amplifier and data acquisition setup) and low-level integration since the platform can be integrated into a microfluidic system to allow repetitive measurements with easy cleaning when utilizing biofunctionalized MNPs.

II. Materials and methods

The GMR effect can appear in multilayered magnetic structures of the type FM/NM/FM; here FM denotes magnetic layers like $Ni_{80}Fe_{20}$, Co, CoFeB with thicknesses between 1 and 10 nm whereas NM denotes a nanometer thick conductive nonmagnetic layer such as Cu or Ag which has the role to separate the FM layers that can interact by magnetostatic coupling or through exchange interaction. The physical mechanism of the GMR effect is the spin-dependent scattering at the interfaces and in ferromagnetic (FM) layers for spin-up (spin parallel to layer magnetization) and spin-down (spin antiparallel to layer magnetization) electrons [25], [27]. Consequently, in the GMR effect, the structure resistance changes according to the angle between the directions of the magnetization of adjacent layers. When the layers are magnetized in parallel direction, the resistance is at a minimum value, R_p. When the magnetizations of the adjacent magnetic layers are antiparallel to each other, the resistance is at a maximum value, named R_{ap}. In a single domain approach, the electric resistance dependency from the angle θ, between the magnetizations of adjacent magnetic layers is [25]-[27]:

$$R = R_p + \frac{\Delta R_{GMR}}{2}[1 - \cos\theta] \qquad (1)$$

where, $\Delta R_{GMR} = R_p - R_{ap}$, is the GMR effect amplitude.

Such that, for antiparallel configuration ($\theta = 180°$), $R=R_{ap}$ while for parallel configuration ($\theta = 0°$), $R=R_p$. Note that θ depends on the applied field and on physical properties of the GMR structure.

The magnitude of the GMR effect is expressed by (2), and is typically between 5-15%.

$$GMR = \frac{R_{ap} - R_p}{R_{ap}} 100 \ [\%], \qquad (2)$$

To have a workable structure, the magnetization of a ferromagnetic layer is pinned by an anti-ferromagnetic (AF) layer of FeMn or IrMn, and is named pinned layer (FM_{PL}), while the second FM layer has the magnetization free to rotate under the action of an external magnetic field and is named free layer (FM_{FL}). The AF layer has the role to “pin” the magnetization of the FM_{PL} layer through an exchange interaction at the interface between the AF and the FM_{PL} layers. This interaction manifests like a field, named *exchange biasing field, H_{ex}*, applied only to FM_{PL} Usually, H_{ex} ranges from 2 to 100 Oe. Such that, a GMR structure is of the type Substrate/Ta/FM_{FL}/NM/FM_{PL}/AF/Caping layer. The substrate consists of a single crystalline Si wafer on which a SiO_2 isolating layer is grown. The Ta layer assures the adhesion of the GMR structure which is grown above, usually, by magnetron sputtering or by atomic layer deposition techniques. The caping layer protects the GMR structure against oxidation and contamination with water molecules, etc. Also, an anisotropy field exists in such structures and is due to crystalline anisotropy and shape anisotropy. Fig.1 presents a GMR structure [25] with typical thicknesses of the involved layers.

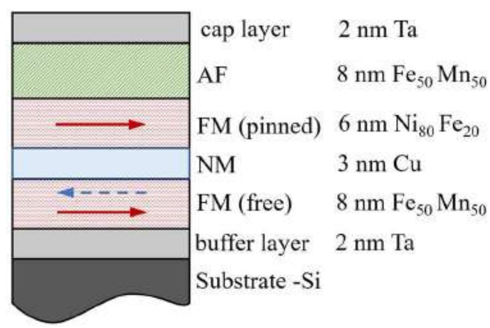

Fig. 1. A typical “exchange-biased spin-valve” GMR structure.

Based on GMR effect, high sensitivity magnetic field sensors can be patterned in microtechnology research laboratories [27] or can be found as commercial products [31, 32]. The GMR sensor used in our study, named GF708, is from Sensitec GmbH Germany, provided as flip-chip package [31]. This type of package allows a very good magnetic coupling between the sensor and the MNPs. The sensor consists of four GMR structures connected in a Wheatstone bridge configuration, Fig. 2. Two structures are placed in the gap of a magnetic flux concentrator (MC) whereas the other two GMR structures are covered by flux concentrators and are used as reference elements to complete the Wheatstone bridge. By this, the sensor has a very good thermal stability of the output voltage of about -0.35%/K and a sensitivity of 13 mV/V/Oe in the linear range between -10 to 10 Oe [31].

The chip was wire bounded and mounted on a platform which was connected to the measurement system composed from a Keithley 6221A current source and a Keithley 2182A nanovoltmeter to read the output voltage from sensor. The platform with the chip was mounted inside of a system composed from a dual Helmholtz coils setup that can provide a very uniform magnetic field. The coils were connected to a programable power supply source Kepco BOP100-10MG. All these devices, presented in Fig 3, were computer interfaced.

In terms of immunity to low, homogenous external magnetic fields both magnetic field sensors in the GF708 chip are connected in a differential setup. This is crucial when very low currents are measured because they generate a magnetic field which is comparable to the terrestrial magnetic field. Moreover, the output of the detection system, which is working in a differential regime, was set to 0 prior to making an experiment for MNPs detection in order to be confident that the output voltage is a measure of the MNPs magnetic moment.

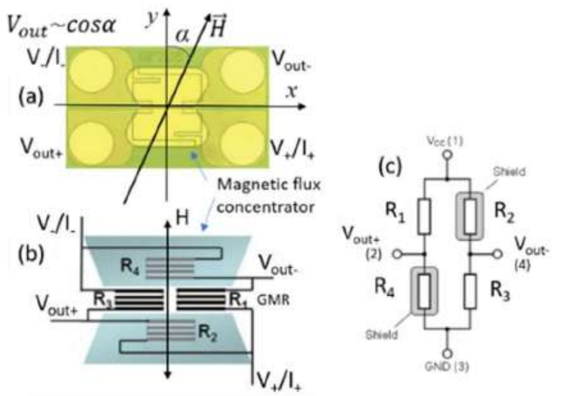

Fig. 2. (a) Overview of the GF708 sensor from the bump-side, (b) and (c) simplified schematic of the sensor with active GMR structures, $R_{1,3}$ and screened structures $R_{2,4}$; the maximum sensitivity is obtained when $\vec{H}$ is directed over y axis.

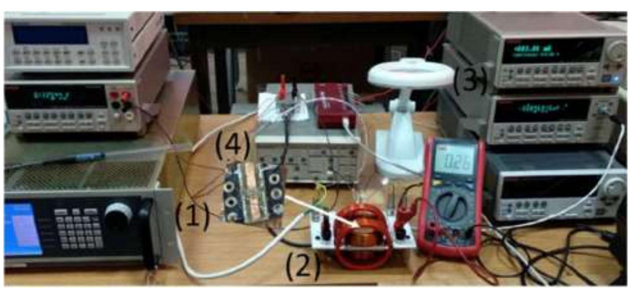

Fig. 3. The experimental setup: (1) Kepco BP 100-10MG, (2) the dual Helmholtz coil setup, (3) the Keithley 6221A current source and 2182A nanovoltmeter and (4) the platform with the GMR chip.

III. Results and Discussion

A. Micromagnetic Modelling of the Detection System

To have a qualitative understanding of the detection process, we performed micromagnetic simulations using the single domain approximation approach. A freeware micromagnetic simulator [30] was used to generate the system depicted in Fig. 4 and to simulate its behaviour. The simulation results system are presented in Fig. 5 and the underlying process is described in what follows. The simulated GMR sensor, Fig. 4 (a, b) consists of two magnetic layers of Permalloy, with a length of 1000 nm on each side. The free layer (magnetic moments marked with red arrows, Fig. 4) has a thickness of 10 nm whereas the pinned layer (violet arrows, Fig. 4) has a thickness of 5 nm. The saturation magnetization is M_S=800 emu/cc and the anisotropy field is H_K=10 Oe in both layers. The exchange bias field, used to pin the magnetization from the pinned layer is H_{ex}=100 Oe. Also note Fig.1. The Cu separation layer is 10 nm thick. The magnetic flux concentrator (MC) consists from 2 plates 1000 nm each side and 100 nm. The MC is simulated like a soft material with a relative magnetic permeability μ_r=2000.

The presence of MNPs over the sensor surface is taken into account as a thin layer of 10 nm of soft magnetic material (because they have a superparamagnetic behaviour) with M_S=450 emu/cc and μ_r=25. These are typical values for maghemite. The MNPs are placed at 100 nm above the sensor's surface. This is usually the thickness of the Si_3N_4 protective layer. Useful details on using this method of simulation and MNPs behaviour can be found in [22], [24], [33]-[36].

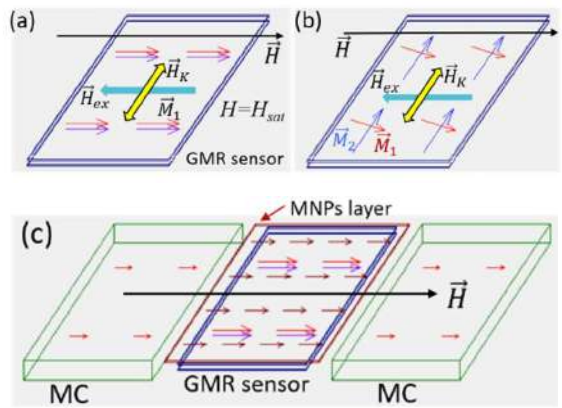

Fig. 4. The detection system showing the simulated GMR sensor (a) at saturation and (b) for $H<H_{sat}$; and (c) the full structure of the detection system consisting from GMR sensor MC and MNPs.

Fig. 7 presents the results of micromagnetic simulations for different situations in order to emphasise the role of the MC and the presence of the MNPs above the sensor surface. With a black line (a) and red line (b) the typical field dependences of the GMR sensor output without MC and with MC respectively, are plotted. The low field working region is between -100 to 100 Oe, where only the magnetization from the free layer is switching. Because of the magnetic flux concentrator, the field required to switch the magnetization from the free layer is smaller and the slope of the linear region of the GMR field characteristic is higher i.e., the sensor sensitivity is higher. When the magnetizations are antiparallel (ap-state), the structure resistance is maximum, whereas when the magnetizations are parallel (p-state), the structure resistance reaches the minimum value. At fields higher than +200 Oe, the pinned layer magnetization is also switching. That region is of no particular interest for sensing applications.

The magnetostatic coupling between MNPs and the sensor changes the field characteristic of the GMR effect as seen in Fig. 5. This is due to returning magnetic field lines from the MNPs layer which lower the effective field inside the GMR sensor. The absence of the small hysteretic behaviour in Fig. 5 is due to the single domain approach used in our simulations. The low field GMR response in the absence of MNPs is in good qualitative agreement with experimental data presented in Fig. 6a.

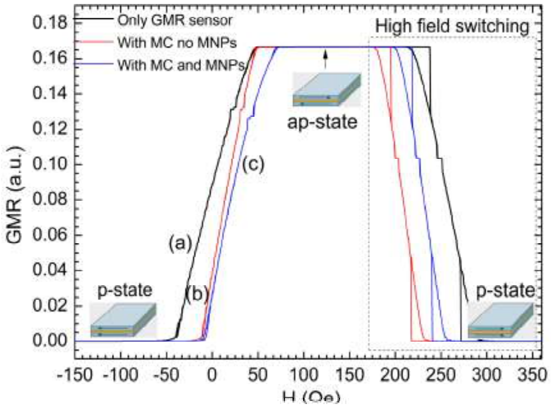

Fig. 5. Micromagnetic simulations of the GMR sensor behaviour: (a) only GMR sensor; (b) GMR sensor with magnetic flux concentrator and no MNPs and (c) GMR sensor with magnetic flux concentrator and MNPs.

B. Experimental results

The horizontal coils (Fig. 3) are used to apply a magnetic field perpendicular to the sensors surface in order to study the possible influence of this field component, H_p, on the sensor's response. Fig. 6 presents the field characteristics of the sensor without MNPs over his surface for the perpendicular field, H_p, 0 and 25 Oe.

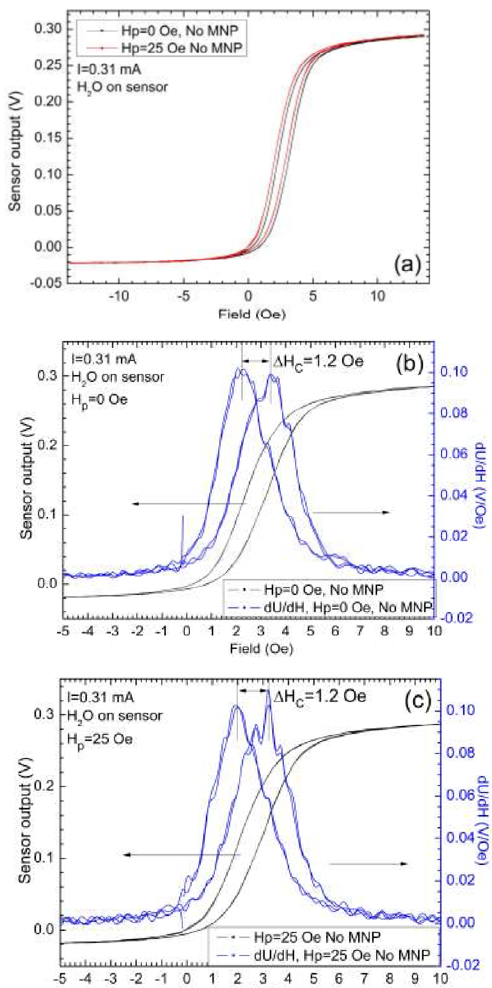

Fig. 6. The transfer curves (a) and their derivatives, (b) and (c), of the GMR sensor with magnetic field, H, for H_p=0 and 25 Oe.

A drop of 1 μl of water was placed above the chip surface to have a similar thermal equilibrium state like when the solution with MNPs is placed above the sensor. The current through sensor was established to 0.31 mA during experiments. From Fig. 6 we can observe that the sensor is insensitive to perpendicular applied fields. This behaviour is due to the fact that the demagnetizing coefficient over the direction perpendicular to the film surface is close to -1, $N_{\perp} \approx -1$, which forces the magnetization to stay in the film plane. The small displacement observed is due to a very weak in plane component of H_p. The calculated derivatives of the output signal give two peaks that correspond to the switching fields in the sensing layer (free layer) whose magnetization rotates under the applied field. As we can see from Fig. 4(b) and (c), the width of the hysteresis curve, ΔH_C=1.2 Oe, is the same both for H_p=0 and H_p=25 Oe. Only a small displacement, of about 0.3 to 0.4 Oe, is observed due to the in-plane component of H_p. However, we expect to observe a change of the switching fields when MNPs will be paced above the sensor's surface, as is depicted in Fig. 7.

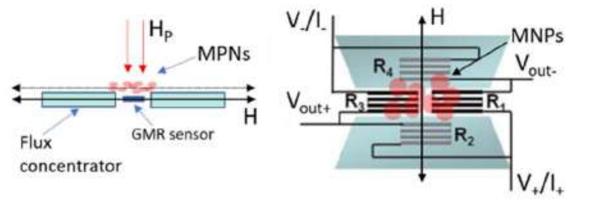

Fig. 7. Cross section and plane view schematic representation of the GMR sensor with MNPs placed on its surface.

Using the setup presented in Figs. 2 and 3 and following the measurement procedure described above, we placed different volumes of solution with MNPs over the sensor's surface. The MNPs consist from Maghemite (Fe_2O_3) nanoparticles, of 10 nm in diameter, functionalized with Polyethylene glycol 6000 (PEG 6000) which are placed in suspension in water. On these functionalized MNPs, various antibodies can be attached to be used for biodetection of specific antigens. Finally, in function of the magnetic material found above the sensor's surface, the number of specific antibody-antigens binding processes can be estimated. In this study we show the ability of the GMR based system, described above, to detect these MNPs. In order to increase the magnetic field generated by the MNPs and, hence, to increase the detection sensitivity, we applied a constant magnetic field, H_p=25 Oe, perpendicular to the sensor surface. This field will magnetize the MNPs but, as we showed in Fig. 4a, has a very small influence on the sensor behaviour. The method was previously described in [22], [24].

Fig. 8a presents the field dependences of the output voltage when a drop of 1.25 μl of solution with maghemite nanoparticles functionalized with PEG 6000 was placed above the chip surface. For comparison, the output signal when only a drop of water was placed above the chip surface is also plotted, see Fig. 8a. We can remark the deformation of the response curve toward higher fields as was predicted by the simple micromagnetic simulations. Because the MNPs deposited over the sensor surface act like shunting layer, a higher field is required to switch the magnetization in the sensing layer and to reach saturation. This behaviour can be better quantified by analysing the output signal through its derivative and representing dU/dH=f(H) like in Fig. 8b. By using this method, the switching fields can be found precisely, which can be considered as a marker of the MNPs presence above the sensor surface. We found a shift of 0.8 Oe of the response curve compared with the case without MNPs above the sensor and the width of the hysteresis curve is now ΔH_C=2.2 Oe.

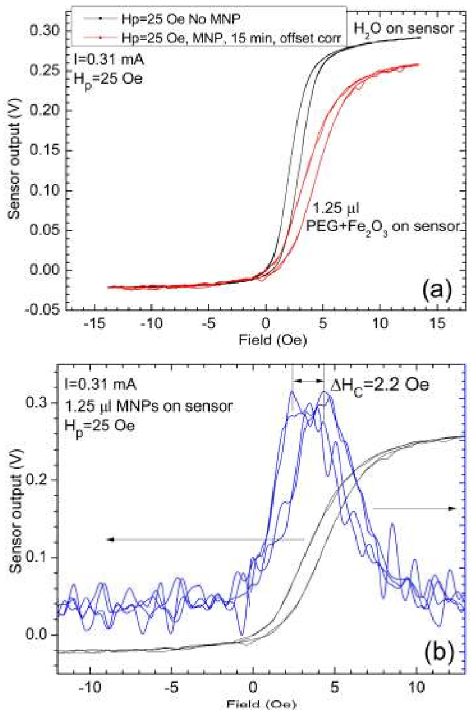

Fig. 8. (a) The field dependences of the output signal without and with MNPs over the sensor surface and (b) the calculated derivative of the output signal.

The experiments were continued by adding 0.25 µl aqueous solution of MNPs (Fe_2O_3+PEG 6000) in two stages. Again, was observed the displacement of the response curve and increases of ΔH_C. Delta U represents the difference between the signal amplitude with and without MNPs, the latter being taken as a reference signal. For example, In Fig. 8a, Delta U= -0.035 V. Fig. 9 summarizes the results of the detection experiments for 1.25, 1.50 and 1.75 µl of Fe_2O_3+PEG 6000 aqueous solution placed above the sensor surface. Fig. 10 shows the signal amplitude variation and hysteresis curve width in function of the volume of the MNPs solution obtained by applying a 0.01Hz triangle AC magnetizing field.

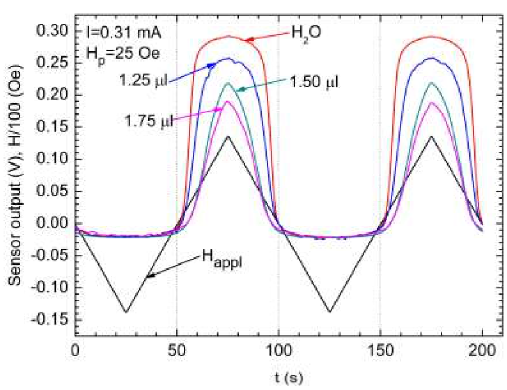

Fig. 9. GMR signal amplitude variation in function of the MNPs solution volume placed over the sensor surface. The applied magnetizing field (H_{appl}) is a 0.01 Hz triangle AC waveform.

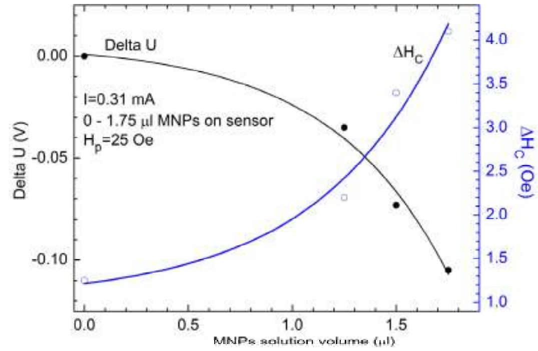

Fig. 10. Signal amplitude variation and hysteresis curve width, ΔH_C, in function of the MNPs solution volume placed over the sensor surface.

Following the method described in [24], [26], we can estimate the mass of MNPs detected in these experiments. Such that, we found that 1.25 µl of solution contains 16.7 µg of powder composed from maghemite nanoparticles, 10 nm in diameter, functionalised with PEG 6000. This means about 1.20 µg of pure maghemite cores, the remaining mass being the PEG 6000 molecules. Using data from the magnetization curves [24] of the PEG6000 functionalized MNPs we estimated that our system determined a magnetic moment of about $9.098 \cdot 10^{-5}$ emu for a signal variation of 0.035 V (in this case, a detection sensitivity of about 75.81 emu/g).

IV. Conclusions

In this paper we proposed a practical method to detect MNPs used for medical diagnosis using a commercial GMR based sensor. This method highlights, through experimental results, an improvement to the method of utilizing a perpendicularly applied magnetic field to magnetize the magnetic nanoparticles to maintain their superparamagnetic behaviour using a simpler measurement setup to the ones described in literature [28, 30] while also illustrating the usefulness of analysing the calculated derivative of the output signal. This approach shows promise for future developments using GMR biosensors for utilizing magnetorelaxometry to analyse sensor results from functionalized MNPs. Micromagnetic simulations were used to describe the detection process. We proved that even a single domain simulation method is suitable to illustrate the influence of a magnetic nanoparticle over the response of a GMR structure. This approach, can be applied as an initial step for easier and faster prototyping of a GMR sensor intended for MNPs detection. From the experimental data we show that we can easily detect a very small mass of magnetic nanoparticles, down to 1.2 µg of pure maghemite cores. Moreover, by using a flip-chip package approach, this will allow tight integration with microfluidics and simplifies the overall measurement setup as complex measurement setups like in [30], which involve the MNPs being placed in a container on a rotating cylinder in the sensor's vicinity are avoided (as such a setup reduces detection sensitivity). Further developments will consider the integration of the GMR sensor into a microfluidic channel which will allow a precise dosage of MNPs, protection against external contamination and easy washing of the sensor's surface in prior to new measurements. Thus, a more practical lab-on-a-chip implementation of a GMR biosensor is highlighted.

References

[1] M. M. Miller, G. A. Prinz, S.-F. Cheng, and S. Bounnak, "Detection of a micron-sized magnetic sphere using a ring-shaped anisotropic

magnetoresistance-based sensor: A model for a magnetoresistance-based biosensor," *Applied Physics Letters*, vol. 81, no. 12, pp. 2211–2213, 2002.

[2] M. Volmer, M. Avram, "Electrical characterization of magnetoresistive sensors based on AMR and GMR effects used for lab-on-a-chip applications", *Reviews on advanced materials science*, vol. 15, pp. 220-224, 2007.

[3] R. D. Crespo, L. Elbaile, J. Carrizo, and J. A. García, "Optimizing the sensitivity of a GMR sensor for superparamagnetic nanoparticles detection: Micromagnetic simulation," *Journal of Magnetism and Magnetic Materials*, vol. 446, pp. 37–43, 2018.

[4] G. Antarnusa, P. Elda Swastika, and E. Suharyadi, "Wheatstone bridge-giant magnetoresistance (GMR) sensors based on Co/Cu multilayers for bio-detection applications," *Journal of Physics: Conference Series*, vol. 1011, p. 012061, 2018.

[5] E. Albisetti, D. Petti, M. Cantoni, F. Damin, A. Torti, M. Chiari, and R. Bertacco, "Conditions for efficient on-chip magnetic bead detection via magnetoresistive sensors," *Biosensors and Bioelectronics*, vol. 47, pp. 213–217, 2013.

[6] Hung, T.Q., Kim, D.Y., Rao, B.P., Kim, C., Rinken, T., "Novel Planar Hall Sensor for Biomedical Diagnosing Lab-on-a-Chip" in *State of the Art in Biosensors - General Aspects.* London, United Kingdom: IntechOpen, 2013, ch. 9,. Accesed on: April, 15, 2021. [Online]. Available: https://www.intechopen.com/books/state-of-the-art-in-biosensors-general-aspects/novel-planar-hall-sensor-for-biomedical-diagnosing-lab-on-a-chip.

[7] A. D. Henriksen, B. T. Dalslet, D. H. Skieller, K. H. Lee, F. Okkels, and M. F. Hansen, "Planar Hall effect bridge magnetic field sensors," *Applied Physics Letters*, vol. 97, no. 1, p. 013507, 2010.

[8] K. Enpuku, K. Soejima, T. Nishimoto, T. Matsuda, H. Tokumitsu, T. Tanaka, K. Yoshinaga, H. Kuma, and N. Hamasaki, "Biological Immunoassays Without Bound/Free Separation Utilizing Magnetic Marker and HTS SQUID," *IEEE Transactions on Applied Superconductivity*, vol. 17, no. 2, pp. 816–819, 2007.

[9] V. Iacovacci, G. Lucarini, L. Ricotti, and A. Menciassi, "Magnetic Field-Based Technologies for Lab-on-a-Chip Applications," *Lab-on-a-Chip Fabrication and Application*, 2016. London, United Kingdom: IntechOpen, 2016, ch. 3,. Accesed on: April, 15, 2021. [Online]. Available:https://www.intechopen.com/books/lab-on-a-chip-fabrication-and-application/magnetic-field-based-technologies-for-lab-on-a-chip-applications.

[10] C. Gooneratne, R. Kodzius, F. Li, I. Foulds, and J. Kosel, "On-Chip Magnetic Bead Manipulation and Detection Using a Magnetoresistive Sensor-Based Micro-Chip: Design Considerations and Experimental Characterization," *Sensors*, vol. 16, no. 9, p. 1369, 2016.

[11] E. Rapoport, D. Montana, and G. S. Beach, "Integrated capture, transport, and magneto-mechanical resonant sensing of superparamagnetic microbeads using magnetic domain walls," *Lab on a Chip*, vol. 12, no. 21, p. 4433, 2012.

[12] A. Ehresmann, I. Koch, and D. Holzinger, "Manipulation of Superparamagnetic Beads on Patterned Exchange-Bias Layer Systems for Biosensing Applications," *Sensors*, vol. 15, no. 11, pp. 28854–28888, 2015.

[13] M. Monticelli, A. Torti, M. Cantoni, D. Petti, E. Albisetti, A. Manzin, E. Guerriero, R. Sordan, G. Gervasoni, M. Carminati, G. Ferrari, M. Sampietro, and R. Bertacco, "On-Chip Magnetic Platform for Single-Particle Manipulation with Integrated Electrical Feedback," *Small*, vol. 12, no. 7, pp. 921–929, 2015.

[14] L. T. Hien, L. K. Quynh, V. T. Huyen, B. D. Tu, N. T. Hien, D. M. Phuong, P. H. Nhung, D. T. Giang, and N. H. Duc, "DNA-magnetic bead detection using disposable cards and the anisotropic magnetoresistive sensor," *Advances in Natural Sciences: Nanoscience and Nanotechnology*, vol. 7, no. 4, p. 045006, 2016.

[15] O. Y. Galkin, O. B. Besarab, M. O. Pysmenna, Y. V. Gorshunov, and O. M. Dugan, "Modern magnetic immunoassay: Biophysical and biochemical aspects," *Regulatory Mechanisms in Biosystems*, vol. 9, no. 1, pp. 47–55, 2017.

[16] J. Schotter, P. B. Kamp, A. Becker, A. Pühler, G. Reiss, and H. Brückl, "Comparison of a prototype magnetoresistive biosensor to standard fluorescent DNA detection," *Biosensors and Bioelectronics*, vol. 19, no. 10, pp. 1149–1156, 2004.

[17] M. M. Miller, P. E. Sheehan, R. L. Edelstein, C. R. Tamanaha, L. Zhong, S. Bounnak, L. J. Whitman, and R. J. Colton, "A DNA array sensor utilizing magnetic microbeads and magnetoelectronic detection," *Journal of Magnetism and Magnetic Materials*, vol. 225, no. 1-2, pp. 138–144, 2001.

[18] D. R. Baselt, G. U. Lee, M. Natesan, S. W. Metzger, P. E. Sheehan, and R. J. Colton, "A biosensor based on magnetoresistance technology," *Biosensors and Bioelectronics*, vol. 13, no. 7-8, pp. 731–739, 1998.

[19] W. Qiu, L. Chang, Y.-C. Liang, J. Litvinov, J. Guo, Y.-T. Chen, B. Vu, K. Kourentzi, S. Xu, T. R. Lee, Y. Zu, R. C. Willson, and D. Litvinov, "Spin-Valve based magnetoresistive nanoparticle detector for applications in biosensing," *Sensors and Actuators A: Physical*, vol. 265, pp. 174–180, 2017.

[20] R. Ghosh Chaudhuri and S. Paria, "Core/Shell Nanoparticles: Classes, Properties, Synthesis Mechanisms, Characterization, and Applications," *Chemical Reviews*, vol. 112, no. 4, pp. 2373–2433, 2011.

[21] M. Volmer, M. Avram, "Detection of Magnetic-Based Bio-Molecules Using MR Sensors", *AIP Conference Proceedings*, vol. 1025, no. 1, pp. 125-130, 2008.

[22] M. Volmer and M. Avram, "Micromagnetic simulations on detection of magnetic labelled biomolecules using MR sensors," *Journal of Magnetism and Magnetic Materials*, vol. 321, no. 10, pp. 1683–1685, 2009.

[23] M. Volmer, M. Avram, "Improving the Detection Sensitivity of Magnetic Microbeads by Spin Valve Sensors,", *AIP Conference Proceedings,* vol. 1311, no. 1, pp. 261-266, 2010.

[24] M. Volmer and M. Avram, "Using permalloy based planar hall effect sensors to capture and detect superparamagnetic beads for lab on a chip applications," *Journal of Magnetism and Magnetic Materials*, vol. 381, pp. 481–487, 2015.

[25] C. Mușuroi, M. Oproiu, M. Volmer, and I. Firastrau, "High Sensitivity Differential Giant Magnetoresistance (GMR) Based Sensor for Non-Contacting DC/AC Current Measurement," *Sensors*, vol. 20, no. 1, p. 323, 2020.

[26] C. Mușuroi, M. Oproiu, M. Volmer, J. Neamtu, M. Avram, and E. Helerea, "Low Field Optimization of a Non-Contacting High-Sensitivity GMR-Based DC/AC Current Sensor," *Sensors*, vol. 21, no. 7, p. 2564, 2021

[27] R. Weiss, R. Mattheis, and G. Reiss, "Advanced giant magnetoresistance technology for measurement applications," *Measurement Science and Technology*, vol. 24, no. 8, p. 082001, 2013.

[28] L. T. Hien, L. K. Quynh, V. T. Huyen, B. D. Tu, N. T. Hien, D. M. Phuong, P. H. Nhung, D. T. Giang, and N. H. Duc, "DNA-magnetic bead detection using disposable cards and the anisotropic magnetoresistive sensor," *Advances in Natural Sciences: Nanoscience and Nanotechnology*, vol. 7, no. 4, p. 045006, 2016.

[29] B. T. Dalslet, C. D. Damsgaard, M. Donolato, M. Strømme, M. Strömberg, P. Svedlindh, and M. F. Hansen, "Bead magnetorelaxometry with an on-chip magnetoresistive sensor," *Lab Chip*, vol. 11, no. 2, pp. 296–302, 2011.

[30] J. Park, "Superparamagnetic nanoparticle quantification using a giant magnetoresistive sensor and permanent magnets," *Journal of Magnetism and Magnetic Materials*, vol. 389, pp. 56–60, 2015.

[31] Sensitec Sensors Catalogue. Accessed on: May 15, 2021. [Online]. Available: https://www.sensitec.com/service-support/download/file-category/catalog

[32] NVE Sensors Catalogue. Accessed on: May 15, 2021. [Online]. Available: https://www.nve.com/Downloads/catalog.pdf

[33] Simulmag 2.0 v2.0j beta. Accessed on: May 15, 2021. [Online]. Available: https://math.nist.gov/oommf/contrib/simulmag/

[34] M. Volmer and M. Avram, "Microbeads Detection Using Spin-Valve Planar Hall Effect Sensors," *Journal of Nanoscience and Nanotechnology*, vol. 12, no. 9, pp. 7456–7459, 2012.

[35] M. Volmer and M. Avram, "Signal dependence on magnetic nanoparticles position over a planar Hall effect biosensor," *Microelectronic Engineering*, vol. 108, pp. 116–120, 2013.

[36] T. A. Burinaru, M. Volmer, M. Avram, V. Țucureanu, A. Avram, B. Țîncu, C. Mărculescu, A. Matei, R. Marinescu, and M. Militaru, "Antibody functionalized magnetic nanoparticles for circulating tumor cells detection and capture using magnetophoresis," *IOP Conference Series: Materials Science and Engineering*, vol. 485, p. 012005, 2019.

sensors

MDPI

Article

High Sensitivity Differential Giant Magnetoresistance (GMR) Based Sensor for Non-Contacting DC/AC Current Measurement

Cristian Mușuroi, Mihai Oproiu, Marius Volmer * and Ioana Firastrau

Department of Electrical Engineering and Applied Physics, Transilvania University of Brasov, 29 Blvd. Eroilor, 500036 Brasov, Romania; cristian.musuroi@unitbv.ro (C.M.); mihai.oproiu@unitbv.ro (M.O.); firastrau@unitbv.ro (I.F.)

* Correspondence: volmerm@unitbv.ro

Received: 10 December 2019; Accepted: 3 January 2020; Published: 6 January 2020

check for updates

Abstract: This paper presents the design and implementation of a high sensitivity giant magnetoresistance (GMR) based current sensor with a broad range of applications. The novelty of our approach consists in using a double differential measurement system, based on commercial GMR sensors, with an adjustable biasing system used to linearize the field response of the system. The work aims to act as a fully-operational proof of concept application, with an emphasis on the mode of operation and methods to improve the sensitivity and linearity of the measurement system. The implemented system has a broad current measurement range from as low as 75 mA in DC and 150 mA in AC up to 4 A by using a single setup. The sensor system is also very low power, consuming only 6.4 mW. Due to the way the sensors are polarized and positioned above the U-shaped conductive band through which the current to be measured is flowing, the differential setup offers a sensitivity of about between 0.0272 to 0.0307 V/A (signal from sensors with no amplifications), a high immunity to external magnetic fields, low hysteresis effects of 40 mA, and a temperature drift of the offset of about -2.59×10^{-4} A/°C. The system provides a high flexibility in designing applications where local fields with very low amplitudes must be detected. This setup can be redesigned for a wide range of applications, thus allowing further specific optimizations, which would provide an even greater accuracy and a significantly extended operation range.

Keywords: current sensors; GMR effect; spin-valve sensor; micromagnetic simulations; Bias magnetic field

1. Introduction

Modern electronics applications often require accurate current measurements in a compact design, thus increasing the need for low power current sensing devices. Also, due to the extremely competitive market for power electronics devices, low cost for those current sensing devices is critical.

Contactless current measurement devices are based on detection of the magnetic field created by the current. When only the AC current component is measured, the most used devices are based on current transformers and Rogowski coils [1–3]. However, to measure DC/AC currents, sensors able to detect DC magnetic fields with high accuracy must be used.

The (micro)fluxgate [4,5] sensors offer high performance and stability in detection of DC/AC currents. A Fluxgate current sensor uses a high permeability magnetic core to detect magnetic fields produced by a current flow. A system of coils such as the fluxgate coil, driven by a square wave current, compensation coil, and pick-up coil are used to determine the magnetization state of the magnetic core and, hence, the current to be measured. The electronics used to drive the currents, to demodulate the signal and to manage all the sensor's functionality is quite complex and often power consuming. Now, new reported developments are ongoing, in which the fluxgate magnetometer is co-integrated along with circuitry on a die [5]. Fluxgate sensors are much more sensitive than Hall sensors and have better temperature stability, and low noise and linearity. A main disadvantage is their relatively small full range of operation, of about 2 mT. In [4] 16 integrated microfluxgate sensors TI DRV425 were used, which were placed around an Al conductor with the cross-section of 100 × 10 mm^2 able to support a current of 400 A. Using this complex system, composed from sensors, DAQ boards, and Mini-PC, a resolution of 1 mA and a temperature drift of 8 mA/°C were achieved for a maximum measured current of 400 A.

Magnetoresistive sensors (MR) made from magnetic layers and based on anisotropic magnetoresistance (AMR) [6–9], giant magnetoresistance (GMR) [10–15], and the tunneling magnetoresistance effect (TMR) [16] are now extensively studied and used for detection of DC/AC currents.

The resistance behaviour of magnetic thin films (Fe, Co, Ni, or alloys like Permalloy—$Ni_{80}Fe_{20}$) is anisotropic (AMR effect) with respect to the applied field direction [6]. The alloy's resistance depends on the angle between the magnetization and the direction of current flow. In a magnetic field, magnetization rotates toward the direction of the magnetic field and the rotation angle depends on the external field's magnitude. The resistance changes roughly as the square of the cosine of the angle between the magnetization and the direction of current flow. Based on this effect and on the planar Hall effect (PHE) which appears in such structures as a consequence of the AMR effect [6], many sensing applications have been developed. Most of these sensors are obtained using integrated circuit technology [7–9], where the resistive elements are connected in a Wheatstone bridge configuration to get high detection sensitivity around 0 field and a better thermal stability of the output signal. The resistive elements have a large aspect ratio (about 10 nm thin, a few µm wide, and tens of µm long), such that magnetization naturally aligns over the longitudinal axis (easy axis of magnetization). The Barber Pole biasing technique [6,8,9] is used to linearize the transfer function.

To achieve a uniform rotation of the magnetization in the resistive elements, the magnetic field must be applied parallel with the sensor's surface and perpendicular to the easy axis of magnetization. In [7], eight AMR sensors (model KMZ51) were placed in a circular pattern around a conductor through which the current to be measured is flowing. A linearity error of ±0.05% in the current range of ±8 A, i.e., an absolute resolution of 4 mA was reported. In [8], the AMR sensors are placed above a U-shaped current trace, the system being encapsulated in a SOIC16 package type.

Currents up to ±50 A can be measured with a zero offset current up to 120 mA. For a current range of ±5 A, the zero offset current can reach a maximum value of 60 mA; the sensitivity is 350 mV/A (with signal conditioning) with a non-linearity error up to 0.5% F.S. (full scale). In [9], the AMR chip with a Wheatstone bridge was placed above the U-shaped conductor. As a common factor, these sensors contain, in their structure, a compensation conductor located above the MR elements [8,9]. Through this conductor a feedback current is driven to compensate the external magnetic field so that the sensor always works around a single point.

This feedback current is a measure of the detected current. Also, as the internal magnetization has no preferred direction along the longitudinal axis, a flipping of 180° can occur due to overcurrent spikes or due to exposure to certain external magnetic fields. This flipping of the magnetization results in a different sensitivity of the system. To overcome this problem, an internal coil (KMZ51) or external controlled magnetic field should be used to reset the magnetization to the initial orientation. Care should be taken to avoid a current passing directly underneath the device itself as the magnetic field generated by that current will be parallel to the printed circuit board (PCB) surface and will affect the functionality of the AMR sensors.

In 1988, the giant magnetoresistance (GMR) effect was discovered in a $[Fe/Cr]_n$ magnetic multilayer. It was found that a change of relative magnetic moment orientation between adjacent magnetic layers results in a significant change of resistance. When the layers are magnetized in parallel, the resistance is at a minimum value, R_{p}. When the magnetizations of the adjacent magnetic layers are antiparallel to each other, the resistance is at a maximum value, named R_{ap}. The physical mechanism of the GMR effect is the spin dependent electric transport in ferromagnetic transition metals. Thus, a new and dynamic field in science, named spintronics, has emerged from this discovery. In 2007, the importance of this discovery was awarded with a Nobel Prize in Physics. Many different applications have been developed subsequently, including low field sensors, position sensors, velocity sensors, Magnetic Random-Access Memory (MRAM) [12], and hard disks read heads. GMR sensors offer high sensitivity, wide frequency range, small size, low power consumption, and they are compatible with many other state-of-the-art technologies [13]. GMR sensors also have a number of drawbacks, from which we can note nonlinearity, hysteresis, offset, and a temperature dependent output that can reduce measurement accuracy [14]. In addition, the output of some of GMR sensors is unipolar, which limits its application in AC measurements [2].

In terms of theoretical considerations, several methods have been proven effective in improving the GMR sensor response. Using a bias field parallel to the sensitive axis can shift the operating point of the sensor to the linear region, thus reducing the hysteresis behavior and creating a bipolar signal. This field can be created either by using a permanent magnet or a coil system with DC, AC, or short pulse currents which can have either open or closed-loop control [14]. Optimization in terms of signal measurement (such as using a differential measurement method) and acquisition can also be performed.

Regarding the application of GMR sensors as current sensors, a multitude of studies have been performed to improve their characteristics. In [14], a closed-loop operation was used to improve the linearity of the GMR sensor. Hysteresis modelling compensation is used in [11] to reduce hysteresis and temperature dependency. In [15], low frequency capture is used to extend the sensor response up to ±800 A. Compared with AMR sensors, GMR sensors, offer a higher sensitivity and, in most cases, are more stable to overcurrent or magnetic field spikes.

2. Materials and Methods

2.1. Principle of Operation

The proposed current measurement method is an indirect one (the GMR sensor acts as a magnetometer by measuring the magnetic field produced by the current trace on which it is installed). Thus, if a current, I, passes through a wire, the magnetic field B will produce a change of the output voltage on the GMR sensor. Figure 1 illustrates the non-contacting current measurement demonstrator setup.

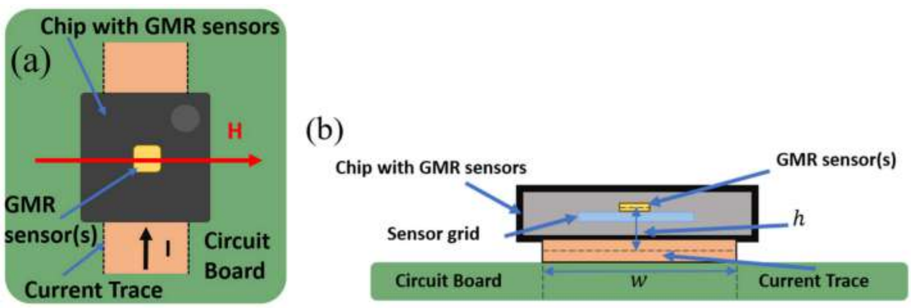

Figure 1. Non-contacting current measurement basic setup using a conducting trace and a giant magnetoresistance (GMR) based sensor chip: (**a**) plane view; (**b**) cross section (adapted from [17]).

The current, I, from the conductive trace (denoted as "Current trace") generates a magnetic field, whose component, B_x, will be detected by the GMR sensor. To estimate B_x, we derived an analytical method, which assumes that the sensor is centered above the trace at distance h, Figure 2.

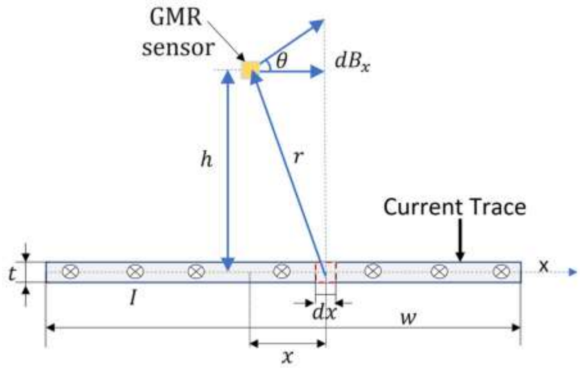

Figure 2. Cross section representing the parameters of the analytical model implemented for field calculations.

Assuming a long conductive trace, the elementary field produced by the current dI is expressed, using the Biot-Savart law, by:

$$dB = \mu_0 \frac{dI}{2\pi r}, dI = \frac{I}{w}dx \tag{1}$$

and

$$dB_x = dB \cdot cos\theta = \mu_0 \frac{h}{2\pi} \cdot \frac{I}{w} \cdot \frac{dx}{h^2 + x^2} \tag{2}$$

where $\mu_0 = 4\pi \times 10^{-7}$ H/m is vacuum magnetic permeability; w is the trace width, and h is the distance from the trace to sensor.

Usually, the trace thickness is between 0.018 to 0.036 mm and h is about 0.4–0.8 mm for low-profile surface mount packages chips. So, we can assume, in Equation (1), a linear current density I/w to calculate the field.

By integrating Equation (2) and doing some basic calculations we obtain (where I is in A and w, h are in m):

$$B_x = \left[\frac{I}{w} \cdot \arctan\left(\frac{w}{2h}\right)\right] \cdot 4 \cdot 10^{-7} [\mathrm{T}]. \tag{3}$$

The results from Equation (3) can be expressed in [G] by:

$$B_x = \left[\frac{I}{w} \cdot \arctan\left(\frac{w}{2h}\right)\right] \cdot 4 \cdot 10^{-3} [\mathrm{G}]. \tag{4}$$

If h = 0.8 mm (for sensor AA003-02 produced by Nonvolatile Electronics (NVE) [13], w = 2 mm and I = 4 A, $B_x = 7.16 \times 10^{-4}$ T.

In the linear region of the sensor's response we can express the output voltage as:

$$\Delta U_a = S_{eff} \cdot B \tag{5}$$

where S_{eff} is the effective sensitivity which depends on the sensor type and supply voltage.

For an AA003-02 GMR based sensor, S = 2.6 mV/(V × Oe). At a supply voltage V_S = 5 V one obtains S_{eff} = 13 mV/Oe and an estimated output voltage ΔU_a = 93.18 mV if I = 4 A. The results obtained with this analytical method have proven to be consistent and more accurate than those that can be obtained by utilizing the web application from [17]. When the current in trace is smaller than 1 A, the magnetic field to be detected by a sensor becomes comparable with the earth's magnetic field which implies some practical issues regarding low currents measurement.

2.2. Characterization of the GMR Sensor

The rate of change in the resistance of a GMR element is expressed by:

$$GMR = \frac{R_{ap} - R_p}{R_{ap}} 100[\%]. \tag{6}$$

Usually, the multilayered structures, from which the GMR sensors are patterned, are of the type AFM/PL/NM/FL, Figure 3a, where AFM denotes an antiferromagnetic layer of IrMn, PL (named pinned layer or fixed layer) is a ferromagnetic layer of $Ni_{80}Fe_{20}$ (named Permalloy) or NiFeCo and NM is a very thin nonmagnetic layer of Cu (0.1–2 nm). The free layer, FL, also known as the sensing layer, as the magnetization can rotate upon an applied magnetic field, is usually deposited from $Ni_{80}Fe_{20}$ or NiFeCo. The GMR ratio for such structures is about 5%–15% [13,14]. The AA003-02 sensor, which contains two active GMR elements connected in a Wheatstone bridge, has a GMR ratio between 13%–16% [18].

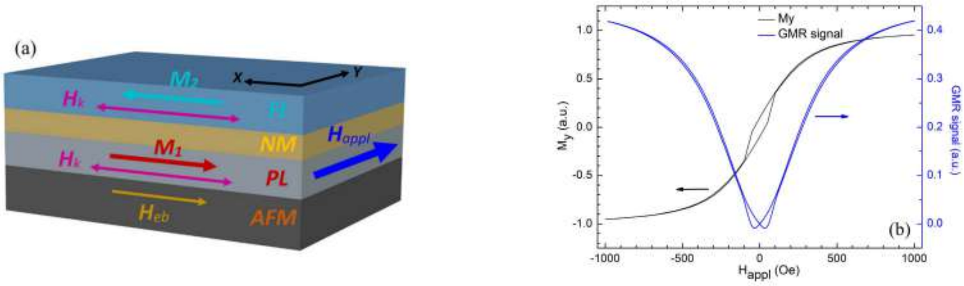

Figure 3. (**a**) Typical structure of a GMR sensor; (AFM—antiferromagnetic pinning layer; PL—pinned magnetic layer; NM—nonmagnetic spacer layer; FL—free magnetic layer (**b**) The simulated field dependence of the magnetization along the Oy axis (My) and the calculated GMR effect when H_{appl} is directed over the Oy axis.

Thus, a simple approach to simulate the field dependence of a GMR sensor signal is to calculate the behavior of the magnetization from the free layer (because the magnetization in the pinned layer can be assumed to be fixed for low applied fields.). For this purpose, we used the OOMMF (Object Oriented MicroMagnetic Framework) micromagnetic simulator [19]. The simulated layer is 1000 × 500 × 10 nm^3 and consists from Permalloy; the cell size is 5 × 5 × 5 nm^3. The FL is antiferromagnetically coupled with the PL through the NM layer, the coupling field being 200 Oe, along the Ox axis. The field, H_{appl}, is applied perpendicular to the easy axis of magnetization (Ox), Figure 3a.

For simulations, we assumed M_s = 710 kA/m (saturation magnetization), A = 1.3 × 10^{-11} J/m (exchange constant), and an anisotropy constant, K_U = 804 J/m^3 along Ox axis. These are typical material parameters used in micromagnetic simulations [19–23]. The cell size is determined by the exchange length, l_{ex}, which for Permalloy is 5 nm [20]. To get reliable results, the side of the cell should not exceed l_{ex}. However, sometimes, a larger cell size can be used if the simulation results converge to those obtained for 5 nm (or lower) and are in good agreement with experimental results. Also, care should be taken when reversal processes are studied, as we did in this paper, to show the hysteretic behavior of the magnetization along Oy axis and the GMR effect.

The saturation magnetization, Ms, can take values between 700 kA/m to 860 kA/m [19–23]. We found by VSM (vibrating sample magnetometer) measurements, on magnetic thin films with Permalloy (10 nm), that M_S = 710 kA/m, which is in agreement with [22], which shows a decrease of the saturation magnetization for very thin films. For the exchange constant, A, values between 10 pJ/m [20] to 13 pJ/m are reported [19,21,23]. We used A = 13 pJ/m. By using a larger value for K_U (instead of the default value of 500 J/m^3) [19,23], we stressed the importance of the uniaxial anisotropy, typical for strips used to microfabricate GMR sensors, to keep the magnetization along the Ox axis when H_{appl} = 0.

The simulated GMR response may be expressed as a function of relative magnetization angle, θ, between the free and pinned layer [23] with a relation of the type $a + b(1 - cos\theta)$; a is a term which describes the structure resistance at saturation whereas b represents the magnitude of the GMR effect. For real structures, a and b depend on the stack structure. Figure 3b, presents the simulated field dependence of the magnetization along the Oy axis (My) and, based on this result, the calculated GMR response. The magnetic domain structure of the simulated layer is responsible for the small hysteretic behavior seen for the field dependence of My and GMR, even if the field is applied over the hard axis. In a single domain approach, there is no hysteresis for both My and GMR field dependencies, whereas in a multi domain approach, a hysteresis effect is present.

To sum up, the results presented in Figure 3b for the GMR effect are in good qualitative agreement with the data from Figure 4 which shows the typical measured field dependencies of the output voltage made on the AA003-02 sensor for different driving currents. One can observe that: (i) the sensitivity can be increased by supplying the sensors with a higher current (for example, I = 2 mA) and (ii) the sensor presents a nonlinear response around 0 field and low sensitivity around the coercive field. These observations motivate the necessity of a biasing field applied along the Oy axis. The driving current through the sensor was supplied by a Keithley 6221 source and the voltage was measured by using a Keithley 2812A nanovoltmeter. The magnetic field was generated by two rectangular-shaped coils in a quasi Helmholtz-like configuration which were supplied by a Kepco BOP100–10MG power supply.

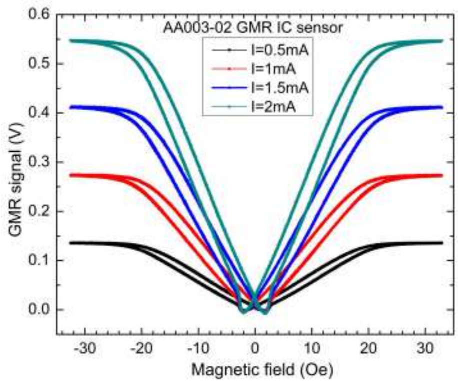

Figure 4. Typical measured field dependencies of the output signal for AA003-02 GMR sensor for different driving currents.

2.3. GMR based Non-Contacting Current Sensing

Before implementing our differential measurement setup, initial tests were done using an evaluation kit, NVE AG003-01E, for current measurement [24] with AA003-02E GMR sensors. The AA003-02E sensor is a differential system on its own as can be seen in Figure 5a,b. The sensor operates as a Wheatstone bridge with four GMR elements, from which, two are magnetically shielded and two are active sensors. The structure is well balanced, such that it delivers an output voltage $U \sim 0$ when $H = 0$, as shown in Figure 4.

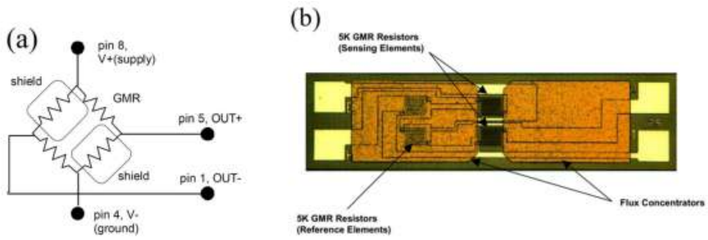

Figure 5. (**a**) NVE AA003-02E GMR sensor functional block diagram; (**b**) photomicrograph of an NVE sensor element [18].

A support holds the current sensor evaluation kit, Figure 6a, inside the coils, Figure 6b, which will be used to bias the GMR sensor in a linear region of its field-dependence characteristic, Figure 4.

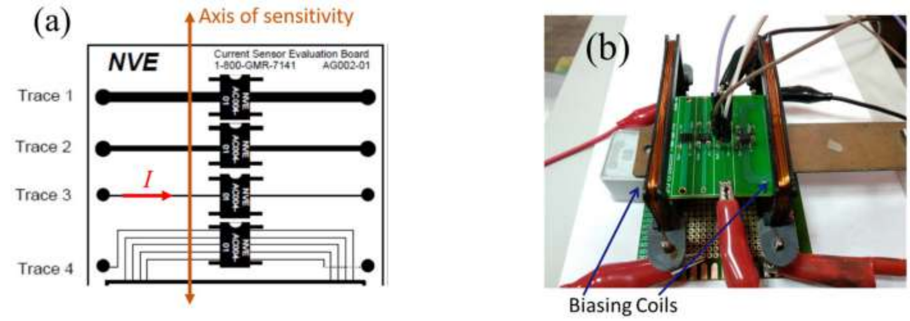

Figure 6. (**a**) Schematic of the evaluation board. The current trace 3 (w = 0.254 mm) was used for tests; (**b**) image of the experimental setup used for GMR current sensing.

The detection system was characterized by applying a very low frequency 0.16 AC current in the conductive trace (Figures 7–9). For these tests, the sensors were supplied with a constant current of 1 mA. The tests were made with unbiased (Figure 7), and biased sensors (Figures 8 and 9). Figure 7 presents the output characteristics obtained when the sensor is unbiased. We must remark on the nonlinear response of the sensor and the hysteretic effect of the output signal, Figure 7a,b.

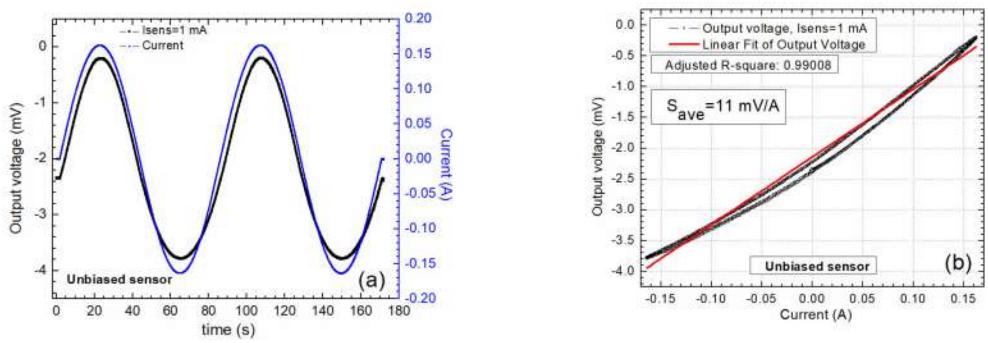

Figure 7. Output characteristics when the sensor AA003-02 is unbiased: (**a**) Comparison between the input current and the output voltage wave forms; (**b**) the output voltage as a function of the applied current through the current trace.

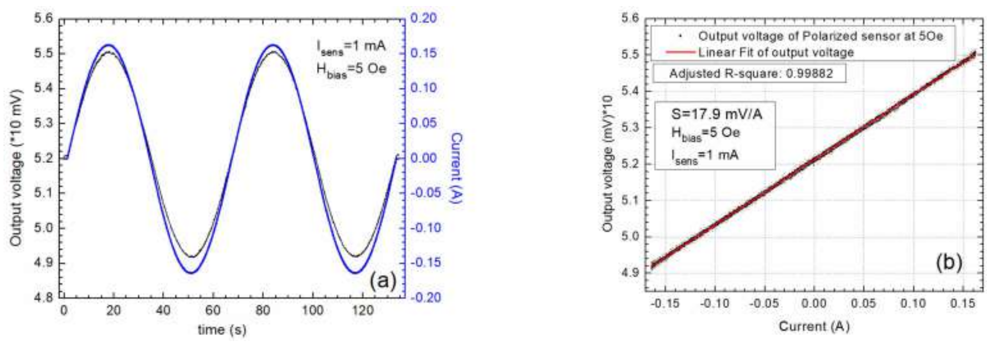

Figure 8. Output characteristics when the sensor AA003-02 is biased at 5 Oe: (**a**) Comparison between the input current and the output voltage wave forms; (**b**) the output voltage as a function of the applied current through the current trace; the sensitivity is 17.9 mV/A.

When the sensor is biased at H_{bias} = 5 Oe or H_{bias} = –5 Oe, the output signals follow accurately the waveform of the applied current (Figures 8a and 9a), and the sensor's output is linearized with no hysteretic effects (Figures 8b and 9b). Also, from Figures 8 and 9, the importance of the biasing field polarity in relation with the polarity of the applied field (generated by the current I) is emphasized. That would allow an output signal in phase or out of phase with π with the applied current. These findings are used for designing the differential measurement setup in order to increase the sensitivity and to immunize the system from unwanted external magnetic fields and temperature fluctuations.

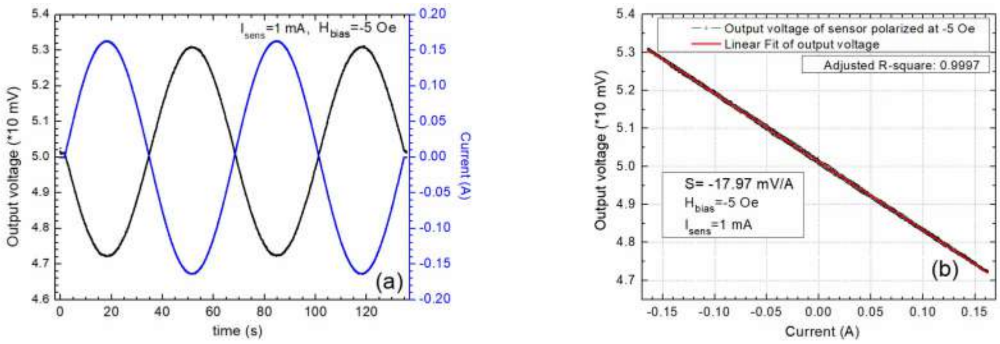

Figure 9. Output characteristics when the sensor AA003-02 is biased at −5 Oe: (**a**) Comparison between the input current and the output voltage wave forms; (**b**) the output voltage as a function of the applied current through the current trace; the sensitivity is −17.9 mV/A.

2.4. Differential Sensor Setup and Mode of Operation

A differential measurement system using two AA003-02E GMR sensors was developed. The PCB of the custom current measurement system can be seen in Figure 10. The GMR sensors are placed to operate in a differential configuration, i.e., for one sensor the output voltage increases while, for the second sensor the output voltage decreases when a current, I, is flowing through the U-shaped conductive band, Figure 10a. The width of the conductive band w, is 2 mm. In the same time, external magnetic fields, from unwanted sources are canceled using this setup. The high/low current path represent the same trace, the difference being the connected fuses used to protect the load during the tests. The 100 nF capacitor is used to filter the sensors supply voltage. Due to this mode of operation, it can be noted that the sensor is not affected by overcurrent because there is galvanic isolation between the sensors and the current trace. Even if the current produces a quite large magnetic field, this will not affect the sensor's functionality, i.e., the magnetization of the pinned layer is not affected and the magnetization of the free layer will return to its initial orientation; this is because of the manufacturing technology [18] where an AF (antiferromagnetic) layer or a synthetic AF layer is used to bias the pinned layer. This means, there is no need of an external magnetic field to reset the sensors like is done in the case of many AMR sensors [7,25].

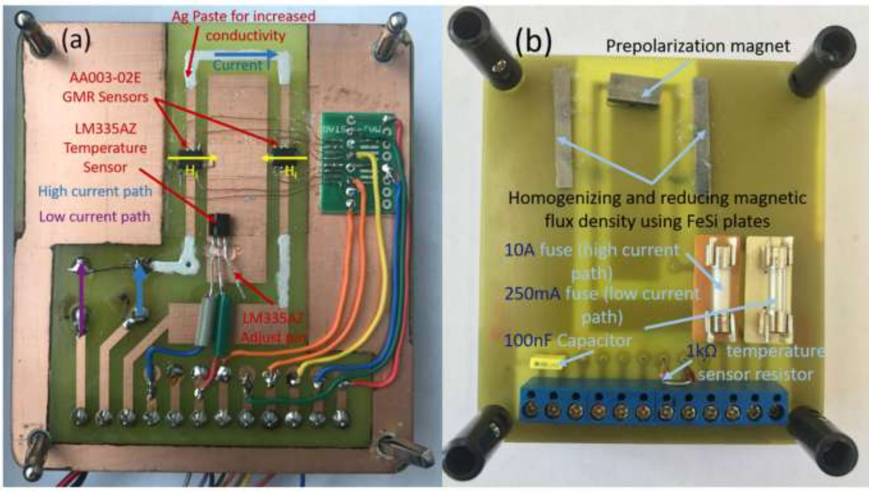

Figure 10. Custom PCB for current measurement using GMR sensors: (**a**) backside; (**b**) frontside. Note that the Ag paste is used to increase the cross section (and consequently, electrical conductivity) in the contacting areas, thus reducing the overall electrical resistance of the "U" shaped current trace.

On the other hand, if we refer to overcurrent protection of the load, at this stage we did not implement the electronics used to trigger the protection when the corresponding signal from sensors surpasses a reference value.

Figure 10b shows the adjustable biasing system formed by a movable permanent magnet and two FeSi plates to homogenize (and also reduce) the effective magnetic flux density. In terms of design choices, the biasing field was set to 8 Oe. The system operates as follows: The permanent magnet generates a magnetic field in the direction of the sensitive axis of the GMR sensors (this shifts the GMR sensor response to a linear operation regime. Regarding the configuration of the permanent magnet, the magnetic field lines between the two Fe-Si plates are almost parallel, thus leading to a more homogeneous magnetic field at the location of the GMR sensors. This is done because the used magnet produces a much stronger magnetic field than is necessary for linearizing the sensors output, and can easily saturate the GMR sensor response for this kind of operation. The permanent magnet is precisely placed such that the polarization field for each sensor is almost the same. In order to increase/reduce this field, this magnet can be rotated or shifted up/down slightly when at the same time monitoring the sensors output to ensure similar polarizing fields.

The functional block diagram of the experimental setup can be seen in Figure 11 and it consists of the custom PCB, LabJack EI1040 Dual Instrumentation amplifier [26], and a Labjack U12-DAQ card [27] connected to a PC via USB.

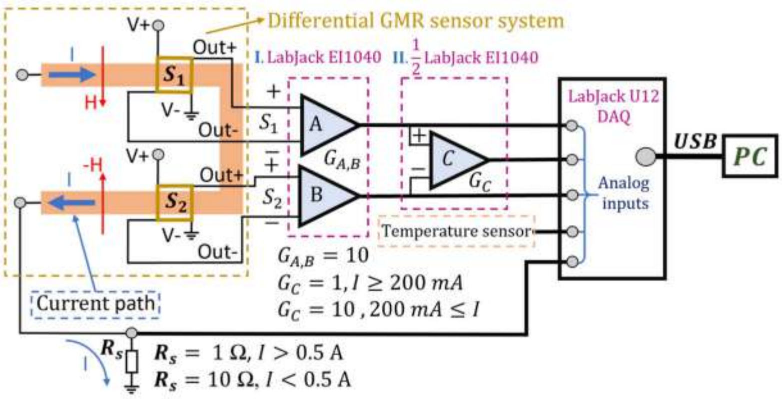

Figure 11. Current measurement differential system using GMR sensors: functional block diagram.

In Figure 11, the amplifier setup for current measurement is also depicted. In this, case, a LabJack EI1040 Dual Instrumentation amplifier [26] is used to amplify the output signals from sensors; each channel was set to a gain of 10. The resulting signal is further amplified by another LabJack EI1040 amplifier which is set to a gain of 10 for low currents measurement, or 1 for high currents measurement. The resulting signals are sent to differential analog inputs on the LabJack U12 DAQ. Thus, for currents below 200 mA, the total resulting gain is 100. The gain for each instrumentation amplifier can be set manually or through the LabJack U12 digital input/output interface [27]. An image of the experimental setup can be seen in Figure 12a. For the purpose of this article, and practical implementation reasons, the AA003-02 GMR sensors were supplied with a 4.096 V constant voltage, generated by a thermally compensated source, from the EI 1040 Dual Instrumentation amplifier. For this voltage, the current through each sensor was about 0.8 mA (the internal resistance for each sensor is 5 kΩ as can be seen in Figure 5b). In order to avoid any possible contact with the current trace, the sensors were wired-bonded directly to the external circuit instead of mounting them on the PCB.

Since two almost identical AA003-02E sensors were used, the result is a double differential measurement system where the benefits and precision compared with a single differential measurement setup were further amplified. Figure 12b presents how the differential current measurement system operates: The sensors were both biased with a field of 8 Oe. From Figure 10a, one can note that since the sensors were placed in such a way that they operate in antiphase, the differential output from the sensors will subtract the influence of other external magnetic fields. In essence, any external homogenous magnetic field (not directly from the current trace) affecting both sensors equally will be subtracted from the differential output as one can see from Equation (7).

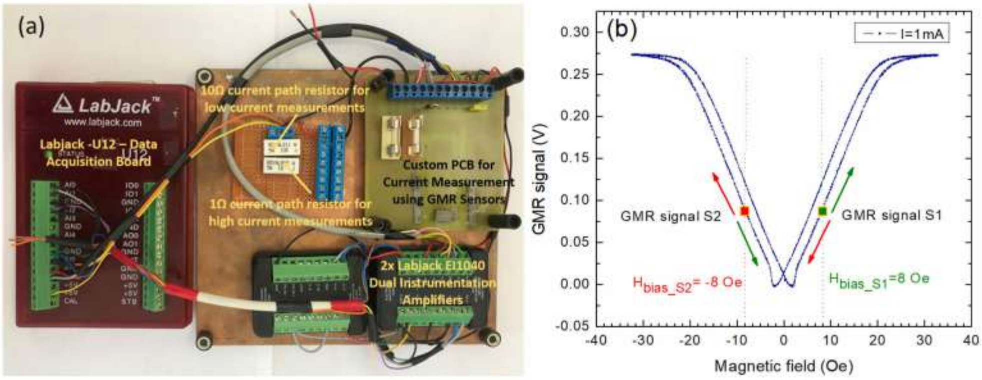

Figure 12. Differential measurement system: (**a**) experimental setup; (**b**) mode of operation illustration for H_{bias} = 8 Oe: when a current I is applied through the U-shaped band, the voltage on sensor 1 increases (green arrow) whereas the voltage on sensor 2 decreases (orange arrow). For H_{bias} = −8 Oe, the voltage on sensor 1 decreases whereas the voltage on sensor 2 increases when the same current I is applied (see Figures 8 and 9).

Although we agree that is impossible to have a measurement system totally immune to external magnetic fields, some specific properties of our differential system can be exploited to minimize these perturbations. As the sensors are made from very thin (nm) magnetic/nonmagnetic layers, they are not sensitive to perpendicular applied magnetic fields, lower than a few hundred Oe, due to the large shape anisotropy which keeps the magnetization in the film plane. Also, if the external magnetic fields are applied in the film plane but over a direction perpendicular to the axis of sensitivity, Figure 6a, the sensor's response can be neglected for fields lower than 25 Oe (Figure 4).

Thus, we can note that the influence of the external currents can be minimized by a proper design of the measurement system using the following observations: The external current lines (if they exist in the sensor's vicinity) must be directed parallel with the axis of sensitivity (i.e., the magnetic field they create is perpendicular to the axis of sensitivity). The differential configuration can be affected by non-homogeneous external magnetic fields but to meet such a situation, the system has to be in the vicinity of magnetic field sources like coils and ferromagnetic components that can induce distortions of the magnetic field lines. In such a situation, electromagnetic shielding must be applied to the detection system, Figure 10. Also, the effect of these perturbations can be minimized by digital signal processing.

Furthermore, resulting from the operation of the differential measurement system, the following general equation can be derived for an input parameter x and a temperature variation ΔT:

$$y = (K_{S1}x + S_1\Delta T) - [K_{S2}(-x) + S_2\Delta T)] \tag{7}$$

where y represents the differential output, K_{S1} and K_{S2} are the sensitivities of each sensor for the useful input signal, and $S_{1,2}\Delta T$ is the signal change caused by thermal fluctuations.

By taking into account that each sensor is thermally balanced, one can assume that $S_1\Delta T \rightarrow 0$ and $S_2\Delta T \rightarrow 0$. As the current through the trace creates a magnetic field $H_I = C{\cdot}I$ (where C is a constant) we can express the output voltage of the differential system as:

$$\Delta U = (K_{S1}{\cdot}H_I + S_1\Delta T + K_{S1}{\cdot}H_{ext}) - [K_{S2}(-H_I) + S_2\Delta T + K_{S1}{\cdot}H_{ext}] \tag{8}$$

By rearranging the terms, Equation (8) becomes:

$$\Delta U = (K_{S1} + K_{S2}){\cdot}H_I + (S_1 - S_2){\cdot}\Delta T + (K_{S1} - K_{S2}){\cdot}H_{ext}. \tag{9}$$

By considering that $S_1 \approx S_2$ (for the same type of sensors), i.e., the system is thermally balanced, and the differences between the sensors output variation created by external fields are negligible, Equation (9) becomes:

$$\Delta U = (K_{S1} + K_{S2}) \cdot H_I = (K_{S1} + K_{S2}) \cdot C \cdot I = S \cdot I \tag{10}$$

where S (V/A) is the sensitivity of the differential measurement system.

3. Results and Discussion

The results presented in this section are a summary of many tests done for different input currents both in DC and AC. From Figure 13a we can denoted that the sensors response is nonlinear in the −1.5 A to 1.5 A current region, which would not allow low currents measurement without biasing. Figure 13b presents the output characteristic of the differential system obtained for unbiased sensors for a DC current between −3 A to 3 A. The response from each sensor is slightly different and presents a hysteretic behavior. The differential output is chaotic, and thus unusable.

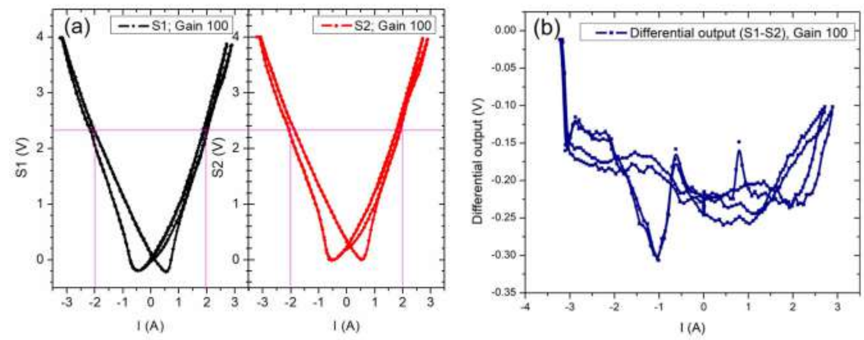

Figure 13. Measured signals on unbiased sensors for: (**a**) individual sensors; (**b**) differential setup. For these tests, the signal was amplified by 100 times.

In what follows, the results obtained with sensors biased at 8 Oe and using the setup from Figures 10 and 11 will be presented. Figure 14 presents the system response when measuring a variable DC current between −2 A to 2 A. The sensitivity for the differential output is S = 0.0307 V/A. Due to inherent hysteresis effects (note Figures 12b and 13a), a hysteresis effect of 0.04 A was observed in the range of ±2 A.

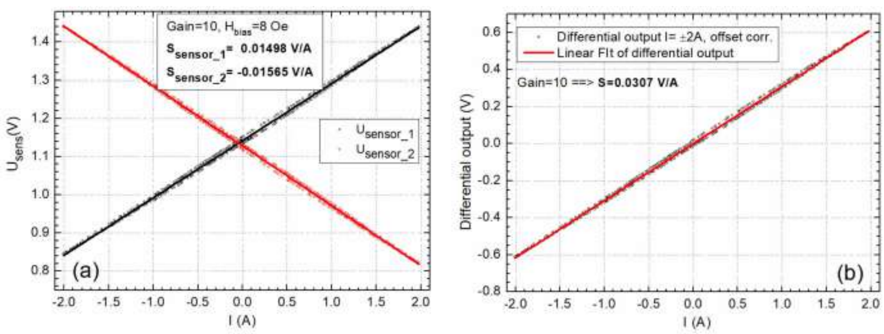

Figure 14. Differential output of sensors polarized at 8 Oe, DC ±2 A: (**a**) individual sensors response; (**b**) differential output.

In Figure 15a, the system’s output when measuring a variable DC current from −4 A to 4 A is presented, while Figure 15b presents the signals variation over time. As expected, the sensitivity is almost the same but the hysteretic effects are lower. Above 4 A, the thermal stability of the setup is negatively impacted as heating occurs.

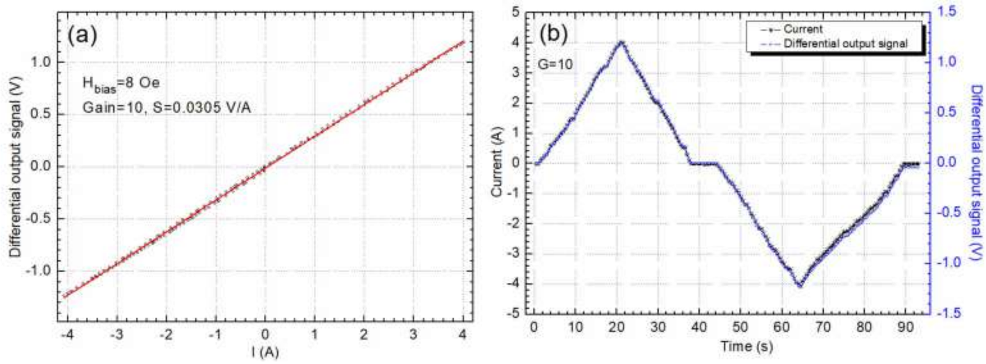

Figure 15. The response of the differential system when the current varies between −4 to 4 A following an arbitrary wave form: (**a**) differential output characteristic, (**b**) the signals variation over time.

For the differential measurement system, the temperature drift of the offset can, theoretically, go to zero for sensors that perfectly matched and are subjected to the same biasing field. The temperature drift of the offset was measured with the sensors biased in order to place them in a linear operation regime and to have the same (almost) output voltage when no current is applied in the conductive band, Figure 12b. The measured temperature drift of the offset is $\Delta U_0/\Delta T \approx -7.9 \times 10^{-6}$ V/°C which means about -2.59×10^{-4} A/°C in terms of measured current, for a temperature variation of 20 °C. Thus, it can be noted that the temperature drift of the offset is affected mainly by the temperature dependence of the GMR effect. Also, we can note that any temperature drifts in the operating range of the bias magnet and FeSi plates lead to no significant changes to the bias magnetic field as we estimate that the temperature of these components is no larger than 37 °C during our tests. Moreover, we used a ferrite magnet from NVE to bias the sensors (which has a Curie temperature up to 300 °C).

The thermal drift of the sensor is defined by the TCoutput change with temperature using a constant current source) and TCOV (output change with temperature using a constant voltage source). According to the catalogue [18], for a single sensor, TCIO is +0.03 %/°C, while TCOV is −0.1 %/°C. Since the sensors are supplied with 4.096 V constant voltage, TCOV is relevant in this case. An LM335AZ temperature sensor was mounted on the PCB for measuring temperature (Figure 10a). Figure 16a shows the time dependence of the temperature of the PCB in the sensors vicinity for I = 1 A, 2 A, and 3 A respectively. One can observe that for a current of 3A passing through the conductive band, the temperature reaches a plateau at about 36 °C after 2000 s. Figure 16b shows the thermal drift of the differential output for I = 1 A, 2 A, and 3 A. The obtained values are: $TCOV_{1A}$ = 0.07 %/°C, $TCOV_{2A}$ = −0.0134 %/°C, and $TCOV_{3A}$ = −0.12 %/°C.

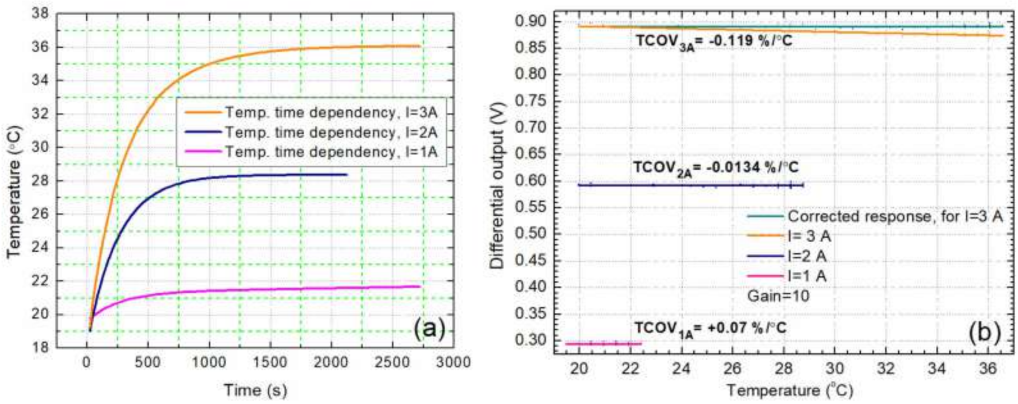

Figure 16. (**a**) The time dependency of the sensors temperature for I = 1 A, 2 A, and 3 A; (**b**) the thermal drift of the differential output. The temperature variation is caused by the Joule heating of the conductive band.

We can identify two possible effects responsible for the measured thermal drifts: (i) variation of the resistance of the metallic layers with temperature and (ii) temperature dependence of the GMR effect. The influence of the first effect is almost canceled by the Wheatstone bridge connection of the sensors inside the chip, Figure 5a, and by the differential measurement setup, Figure 11. This can be seen from data presented in Figure 16b, when very low magnetic field is applied to sensors for I = 1 A and 2 A respectively. On the other hand, the effect of spin fluctuations is shown to play an important role in the temperature-dependency of the GMR amplitude. As a consequence, the GMR effect shows an almost linear decrease when temperature is raised [28,29].

From Figure 16b we found a linear decrease of the output voltage, which is more important for I = 3 A where a larger amount of heat can be transferred to sensors and, hence, we expect a larger temperature variation of the GMR effect. This has an effect on the setup we used, but this can be compensated by applying a correction factor proportional with the measured temperature variation and using the calculated TCOV. Figure 16b presents the compensated response for I = 3 A through the conductive band.

Thus, we can note that the system is thermally stable and can provide reliable data within a temperature interval between 20 to 37 °C.

In terms of low currents sensing capabilities, the limitation is due to some factors like: the sensor's field sensitivity, electric noise of the detection setup, and the width of the current path. We found that the implemented differential system is effective with currents as low as 75 mA, Figure 17a. For lower currents, the signal from the sensors is very weak and more precautions should be taken into account regarding electrical shielding, the noise of the signal amplifier, and the DAQ system. As we can see from Equation (3) and Figures 8 and 9, a current line with a smaller width favours the measurement of low currents. However, a larger width of the conducting band is needed for measuring larger currents without excessive heating. For example, when I = 75 mA and w = 0.254 mm, H = 0.186 Oe, whereas H = 0.1344 Oe for I = 75 mA and w = 2 mm respectively.

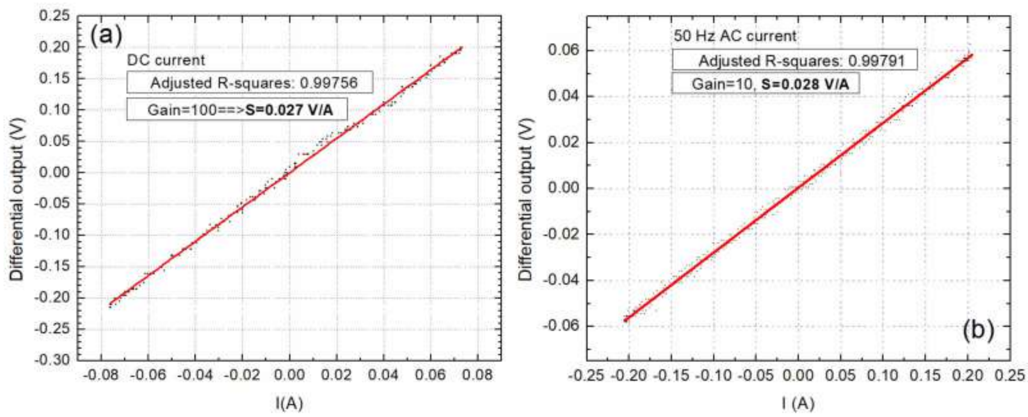

Figure 17. Differential output of sensors polarized at 8 Oe: (**a**) DC, 75 mA, (**b**) AC, 200 mA.

In Figure 17b, the response of the system when measuring a 200 mA, 50 Hz, alternative current is shown. In this case, a current of 150 mA is required in order for the output to be sufficiently linear. Below these thresholds, the nonlinearities in the sensor's response provide an inaccurate differential output. That is due to the fact that at low currents, the sensors output no longer accurately follows the waveform of the magnetic field generated by said current. Thus, the output signal appears distorted and does not represent the actual sine waveform. This is also true when measuring DC currents, as the differential output can be scattered creating some nonlinearities in the response (Figure 17a).

In Figure 18a, the AC response of the system when measuring a 50 Hz sine waveform at 3 A is shown. The harmonic analysis for this measurement is shown in Figure 18b. A THD (total harmonic distortion) of 0.176% was obtained in this case. We can notice that the signal integrity is very good with little to no distortion (the fundamental frequency is the major amplitude, while the effect of the

3rd, 5th, and 7th harmonics is negligible). Note that the frequency limits of the response in AC are mostly limited by the DAQ system, as the sensors have a theoretical maximum frequency response of 1 MHz [18]. Further studies can be done to find the actual AC frequency limitations of the system.

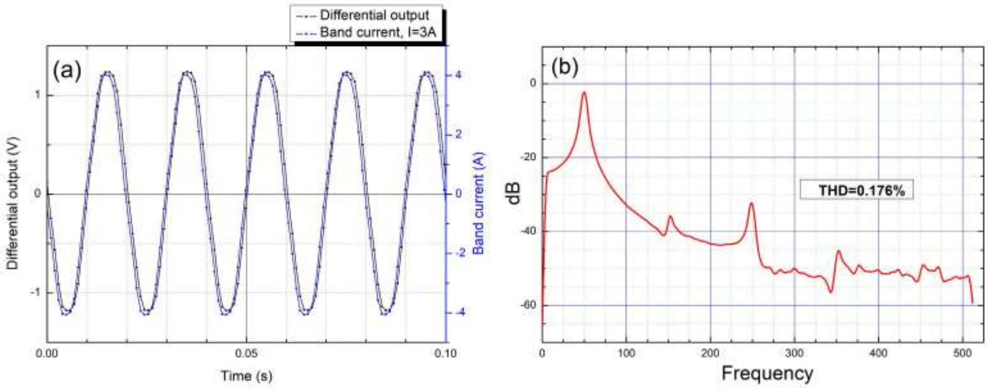

Figure 18. Biased sensors, AC 3A: (**a**) differential response and band current; (**b**) harmonic analysis.

Figure 19 shows the AC calibration curve for the device within the 0–3 A range. We used the adjusted R-squared term to show how well data is aligned over the fitting line. The adjusted. R-square is 0.99943. The calculated full-scale error is 0.66%. Note that there is a very good correlation between the measured current and the response of the system.

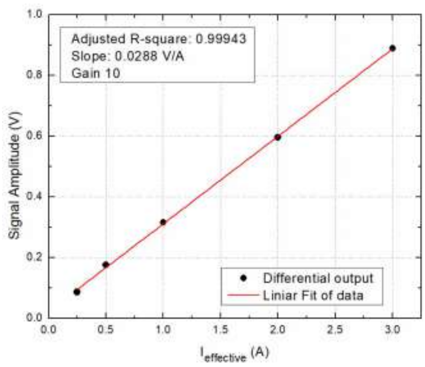

Figure 19. 8 Oe biased sensors: AC calibration curve within the 0–3 A range.

What is noteworthy for the implemented system's output is that all the signal acquisition is done without implementing any filtering system. In this way, the system's viability to measure both DC and AC currents was demonstrated. Thus, it can be noted that for a specific application (in DC or AC), further signal improvements can be made.

4. Conclusions

A high sensitivity non-contacting current measurement experimental setup based on giant magnetoresistance (GMR) sensors was implemented. The sensitivity of this detection setup is between 0.0272 to 0.0307 V/A with low (40 mA) hysteretic effects. A biasing magnetic field was used to linearize the field dependences of the sensors. Moreover, the implemented differential GMR system is very versatile, being able to measure both DC and AC currents. The current measurement system (Figure 12a) was proven to be able to measure accurately and for extended periods of time in DC from 75 mA up to around 4 A, and in AC from 150 mA up to 4 A. This system has the following advantages: high sensitivity, galvanic isolation, thermal stability (when operating at specified parameters), immunity to low external magnetic fields, and preservation of signal integrity for the input current, as can be seen in Figures 15 and 18. These results were obtained without EMF shielding or filtering systems. The custom PCB for the system was designed to measure currents up to 10 A (by taking into account the copper trace width [17]), however, in practice, it was observed that significant heating occurs when measuring currents larger than 4 A for an extended period of time (Figure 16).

Moreover, in terms of performance comparison of the implemented sensor setup with other solutions on the market, we can note the following: The novelty of our approach consists in using a double differential measurement system, Figure 11, based on commercial GMR sensors, with an adjustable biasing system used to linearize the field response of the system. This approach was not seen in other works [14,30–32] or was implemented in commercial sensors like microfluxgate [4,5] or based on AMR effect [7–9]. As we are using a movable permanent magnet to bias the sensors and there is no compensation coil, the power consumption of our detection system (DAQ card and PC is not included) is very small, of about 6.4 mW (as each sensor has a power consumption of 3.2 mW, as noted in [18]).

To improve the measurement accuracy of a magnetometer using the same type of sensor like we used in this study, a closed-loop GMR–compensation coil is used in [14,30], the system operating similarly as in [8,9]. With this method, a sensitivity of about 0.03 V/A to 0.04 V/A (with signal conditioning) is reported in [30] which is quite similar to our result obtained without a feedback coil. The power consumption was reported to be 1.6 W at low currents through the conductive band to 3.2 W for currents up to 45 A.

In [9], for the MCA1101-xx-5 series current sensors, a sensitivity between 35 mV/A up to 350 mV/A for current sensors in the 5–50A range which is typical for AMR effect sensors, but lower than GMR based sensors. In [31], a temperature coefficient TCOV of −0.17 %/°C of the sensor's output voltage is obtained while for our system a TCOV between −0.0134 %/°C to −0.117 %/°C has been measured. Also, in [8], typical CMS2000 series AMR sensors, have a typical offset voltage at room temperature of ±20 mV compared with our setup of -7.9×10^{-6} V/°C. This result emphasizes the benefit of our double differential measurement system to lower the thermal drift of the output signal.

Furthermore, the present setup aims to serve as a novel proof concept of concept application, and with future development, the operation range and utility of the system can be improved greatly. The current implementation is a compromise between low current and high current measurement. For example, by taking into account, Equation (4), we can note that low currents sensing capabilities can be improved by using a narrower trace. Also, for high currents measurement, a setup utilizing a much thicker trace and thicker PCB can be used. Thus, by redesigning of the setup, a significant increase in the operation range can be achieved. Further improvements can also include a size reduction (by integrating the amplifiers on the same PCB), EMF shielding and implementing a filtering system.

Finally, the differential sensing method presented in this article can be used for other specific applications requiring a high degree of sensitivity. As measuring low currents implies accurate detection of magnetic fields smaller than 0.5 G, some of the results presented in this paper will be used to develop a high sensitivity detection setup of magnetic nanoparticles (MNPs) used to label biomolecules in lab-on-a-chip (LOC) applications [33–37]. As we showed by micromagnetic simulations [35,36] and experiments [34], to achieve a large signal from MNPs, they must be polarized in quite a large magnetic field that can saturate the spintronic sensors. To avoid this, we proposed a specific polarization setup for MNPs, where the field is applied perpendicular to the sensor's surface [35–37]. The MNPs will be localized on the surface of one GMR sensor whereas the second one will be used as reference sensor. The in-plane components of the magnetic fields locally generated by MNPs will be detected by GMR sensors using the differential setup described in Figure 11. The current through the conductive band will be used to produce an AC excitation field for detection of the MNPs. To ensure a smaller distance between MNPs and GMR sensors, a package flip-chip package type will be used in this development, as in [34].

Author Contributions: C.M. and M.V. conceived and designed the experimental setup and algorithms; M.O. performed the experiments, I.F. performed micromagnetic simulations and contributed to the design. All authors contributed to discussion and analysis of the research and to the writing of the paper. All authors have read and agreed to the published version of the manuscript.

Funding: This work was supported by a grant of the Romanian Ministry of Research and Innovation, CCDI-UEFISCDI project number 3PCCDI/2018, within PNCDI III.

Acknowledgments: Transilvania University of Brasov provided administrative and material support.

Conflicts of Interest: The authors declare no conflicts of interest.

References

1. Wang, J.; Si, D.; Tian, T.; Ren, R. Design and Experimental Study of a Current Transformer with a Stacked PCB Based on B-Dot. *Sensors* **2017**, *17*, 820. [CrossRef] [PubMed]
2. McNeill, N.; Gupta, N.K.; Burrow, S.G.; Holliday, D.; Mellor, P.H. Application of reset voltage feedback for droop minimization in the unidirectional current pulse transformer. *IEEE Trans. Power Electron.* **2008**, *23*, 591–599. [CrossRef]
3. www.vishay.com. Available online: http://www.vishay.com/docs/30304/currentmeasurement.pdf (accessed on 31 December 2019).
4. Ripka, P.; Mlejnek, P.; Hejda, P.; Chirtsov, A.; Vyhnánek, J. Rectangular Array Electric Current Transducer with Integrated Fluxgate Sensors. *Sensors* **2019**, *19*, 4964. [CrossRef] [PubMed]
5. Snoeij, M.F.; Schaffer, V.; Udayashankar, S.; Ivanov, M.V. Integrated Fluxgate Magnetometer for Use in Isolated Current Sensing. *IEEE J. Solid-State Circuits* **2016**, *51*, 1684–1694. [CrossRef]
6. Volmer, M.; Neamtu, J. Micromagnetic analysis and development of high sensitivity spin-valve magnetic sensors. *J. Hysics Conf. Ser.* **2011**, *268*, 012032. [CrossRef]
7. Mlejnek, P.; Vopalensky, M.; Ripka, P. AMR current measurement device. *Sens. Actuators A* **2008**, *141*, 649–653. [CrossRef]
8. Available online: https://www.aceinna.com/current-sensors (accessed on 31 December 2019).
9. Available online: https://www.sensitec.com/products-solutions/current-measurement (accessed on 31 December 2019).
10. Yang, X.; Xie, C.; Wang, Y.; Wang, Y.; Yang, W.; Dong, G. Optimization Design of a Giant Magneto Resistive Effect Based Current Sensor With a Magnetic Shielding. *IEEE Trans. Appl. Supercond.* **2014**, *24*, 1–4. [CrossRef]
11. Jedlicska, I.; Weiss, R.; Weigel, R. Linearizing the Output Characteristic of GMR Current Sensors through Hysteresis Modeling. *IEEE Trans. Ind. Electron.* **2010**, *57*, 1728–1734. [CrossRef]
12. Daughton, J.M.; Chen, Y.J. GMR materials for low field applications. *IEEE Trans. Magnet.* **1993**, *29*, 2705–2710. [CrossRef]
13. Elmatboly, O.; Homaifar, A.; Zolghadri, M. Giant magneto resistive sensing of critical power system parameters. In Proceedings of the 31st Annual Conference of IEEE Industrial Electronics Society, 2005 (IECON 2005), Raleigh, CA, USA, 6–10 November 2005; p. 6.
14. Li, Z.; Dixon, S. A Closed-Loop Operation to Improve GMR Sensor Accuracy. *IEEE Sens. J.* **2016**, *16*, 6003–6007. [CrossRef]
15. Hudoffsky, B.; Roth-Stielow, J. New evaluation of low frequency capture for a wide bandwidth clamping current probe for ±800 A using GMR sensors. In Proceedings of the 2011 14th European Conference on Power Electronics and Applications, Birmingham, UK, 30 August–1 September 2011; pp. 1–7.
16. Vidal, E.G.; Muñoz, D.R.; Arias, S.I.R.; Moreno, J.S.; Cardoso, S.; Ferreira, R.; Freitas, P. Electronic Energy Meter Based on a Tunnel Magnetoresistive Effect (TMR) Current Sensor. *Materials* **2017**, *10*, 1134. [CrossRef] [PubMed]
17. www.nve.com. Available online: https://www.nve.com/spec/calculators.php#tabs-Current-Sensing (accessed on 31 December 2019).
18. www.nve.com. Available online: https://www.nve.com/Downloads/catalog.pdf (accessed on 31 December 2019).
19. National Institute of Standards and Technology. *OOMMF User's Guide, Version 1.0*; Donahue, M.J., Porter, D.G., Eds.; Interagency Report NISTIR 6376; National Institute of Standards and Technology: Gaithersburg, MD, USA, 1999. Available online: http://math.nist.gov/oommf/ (accessed on 31 December 2019).

20. Jamet, S.; Rougemaille, N.; Toussaint, J.C.; Fruchart, O. 25—Head-to-head domain walls in one-dimensional nanostructures: An extended phase diagram ranging from strips to cylindrical wires. In *Woodhead Publishing Series in Electronic and Optical Materials, Magnetic Nano- and Microwires*; Vázquez, M., Ed.; Woodhead Publishing: Sawston, UK, 2015; pp. 783–811. ISBN 9780081001646. [CrossRef]
21. Rapoport, E.; Montana, D.; Beach, G.S.D. Integrated capture, transport, and magneto-mechanical resonant sensing of superparamagnetic microbeads using magnetic domain walls. *Lab Chip* **2012**, *212*, 4433–4440. [CrossRef] [PubMed]
22. Ounadjela, K.; Lefakis, H.; Speriosu, V.S.; Hwang, C.; Alexopoulos, P.S. Thickness Dependence of Magnetization and Magnetostriction of NiFe and NiFeRh Films. *J. Phys. Colloq.* **1988**, *49*, C8-1709–C8-1710. [CrossRef]
23. Feng, Y.; Liu, J.; Klein, T.; Wu, K.; Wang, J. Localized detection of reversal nucleation generated by high moment magnetic nanoparticles using a large-area magnetic sensor. *J. Appl. Phys.* **2017**, *122*, 123901. [CrossRef]
24. www.nve.com. Available online: https://www.nve.com/Downloads/AG003_01E_KIT.pdf (accessed on 31 December 2019).
25. He, D. AMR Sensor and its Application on Nondestructive Evaluation. In *Magnetic Sensors—Development Trends and Applications*; Asfour, A., Ed.; IntechOpen: London, UK, 2017. [CrossRef]
26. Labjack.com. Available online: https://labjack.com/support/datasheets/accessories/ei-1040 (accessed on 31 December 2019).
27. Labjack.com. Available online: https://labjack.com/support/datasheets/u12/installation/software-installation (accessed on 31 December 2019).
28. Hasegawa, H. Theory of the temperature-dependent giant magnetoresistance in magnetic multilayers. *Phys. Rev. B* **1993**, *47*, 15080. [CrossRef]
29. Stobiecki, F.; Stobiecki, T.; Ocker, B.; Maass, W.; Powroznik, W.; Paja, A.; Loch, C.; Röll, K. Temperature Dependence of Magnetisation Reversal and GMR in Spin Valve Structures. *Acta Physica Polonica A* **2000**, *97*, 523–526. [CrossRef]
30. Poon, T.Y.; Tse, N.C.F.; Lau, R.W.H. Extending the GMR Current Measurement Range with a Counteracting Magnetic Field. *Sensors* **2013**, *13*, 8042–8059. [CrossRef]
31. Weiss, R.; Mattheis, R.; Reiss, G. Advanced giant magnetoresistance technology for measurement applications. *Meas. Sci. Technol.* **2013**, *24*, 082001. [CrossRef]
32. Zhu, K.; Philip, W.T. Performance Study on Commercial Magnetic Sensors for Measuring Current of Unmanned Aerial Vehicles. *IEEE Trans. Instrum. Meas.* **2018**, *10*. [CrossRef]
33. Eickenberg, B.; Meyer, J.; Helmich, L.; Kappe, D.; Auge, A.; Weddemann, A.; Wittbracht, F.; Hütten, A. Lab-on-a-Chip Magneto-Immunoassays: How to Ensure Contact between Superparamagnetic Beads and the Sensor Surface. *Biosensors* **2013**, *3*, 327–340. [CrossRef]
34. Xu, J.; Li, Q.; Gao, X.; Lv, F.; Guo, M.; Zhao, P.; Li, G. Shandong Detection of the Concentration of $MnFe_2O_4$ Magnetic Microparticles Using Giant Magnetoresistance Sensors. *IEEE Trans. Magn.* **2015**, *52*. [CrossRef]
35. Volmer, M.; Avram, M. Micromagnetic Simulations on Detection of Magnetic Labelled Biomolecules Using MR Sensors. *J. Magn. Magn. Mater.* **2009**, *321*, 1683–1685. [CrossRef]
36. Volmer, M.; Avram, M. *Improving the Detection Sensitivity of Magnetic Micro Beads by Spin Valve Sensors*; The AIP (American Institute of Physics) Conference Proceedings: One Physics Ellipse College Park, MD, USA, 2010; Volume 1311, pp. 261–266. ISBN 978-0-7354-0866-1.
37. Volmer, M.; Avram, M. Using Permalloy Based Planar Hall Effect Sensors to Capture and Detect Superparamagnetic Beads for Lab on a Chip Applications. *J. Magn. Magn. Mater.* **2015**, *381*, 481–487. [CrossRef]

Journal of Magnetism and Magnetic Materials 381 (2015) 481–487

Contents lists available at ScienceDirect

Journal of Magnetism and Magnetic Materials

journal homepage: www.elsevier.com/locate/jmmm

Using permalloy based planar hall effect sensors to capture and detect superparamagnetic beads for lab on a chip applications

Marius Volmer [a,*], Marioara Avram [b]

[a] Transilvania University of Brasov, Electrical Engineering and Applied Physics Department. Eroilor 29, Brasov 500036, Romania
[b] National Institute for Research and Development in Microtechnologies, Str. Erou Iancu Nicolae 32B, 72996 Bucharest, Romania

ARTICLE INFO

Article history:
Received 18 August 2014
Received in revised form
16 October 2014
Accepted 27 October 2014
Available online 6 November 2014

Keywords:
Magnetic sensor
Planar Hall effect
Anisotropic magnetoresistance
Lab-on-a-Chip

ABSTRACT

Experimental studies have been carried out on planar Hall effect (PHE) sensors used to detect magnetic nanoparticles employed as labels for biodetection applications. Disk shaped sensors, 1 mm diameter, were structured on Permalloy film, 20 nm thick. To control the sensor magnetisation state and thus the field sensitivity and linearity, a DC biasing field has been applied parallel to the driving current. Maghemite nanoparticles (10 nm) functionalised with Polyethylene glycol (PEG) 6000 were immobilised over the sensor surface using particular magnetisation state and applied magnetic fields. In order to obtain a higher response from the magnetic nanoparticles, it was used a detection setup which allows the application of magnetic fields larger than 100 Oe but avoiding saturation of the PHE signal. Based on this setup, two field scanning methods are presented in this paper. During our experiments, low magnetic moments, of about 1.87×10^{-5} emu, have been easily detected. This value corresponds to a mass of 9.35 μg of maghemite nanoparticles functionalised with PEG 6000. The results suggest that this type of structure is feasible for building low cost micrometer sized PHE sensors to be used for high-resolution bio sensing applications.

1. Introduction

Superparamagnetic (SPM) micro- and nanobeads are versatile tools in lab-on-a-chip (LOC) applications. Because of their magnetic properties and small dimensions, they offer possibilities to label, actuate, and detect with high sensitivity chemical and biological species. The magnetite or maghemite beads, which are among the most used for LOC applications, show superparamagnetic behavior above the blocking temperature, T_B, i.e., the measured magnetic moment in the absence of an external magnetic field is zero. An external magnetic field can magnetize the nanobeads, like a paramagnet but their magnetic susceptibility is much larger than the one of paramagnets and the saturation effect appears for large applied fields. This SPM behavior is useful in LOC applications because can be avoided unwanted capture of the beads over the sensors surface and can be minimised false detection signals when magnetic sensors are used. From ZFC-FC magnetisation measurements made on maghemite nanoparticles, 10 nm in diameter, we have obtained $T_B = 252$ K.

Magnetic sensors, based on giant magnetoresistance (GMR), tunneling magnetoresistance (TMR) [1,2] or planar Hall effect (PHE) [3–5], can be integrated in biochip platforms for measuring the fringe fields created by SPM beads used as labels for different biomolecular targets. In fact, the presence of beads at the sensor surface forms the basis for most SPM bead sensing platforms. It should be noted that for this detection setup it has been observed, both by experiments and micromagnetic simulations, a signal dependence on the spatial location of magnetic nanoparticles over the sensor surface [6–8]. This issue becomes very important when a small number of biomolecules must be detected using the surface immobilisation method because the signal output of the sensor may experience large variations depending on the position of the beads.

Finally, we should mention that the strong localized stray field from domain walls (DWs) in sub micrometer ferromagnetic tracks can trap individual SPM beads with forces up to hundreds of pN and manipulate them [9]. So, a strong magnetostatic interaction between the magnetic beads and the sensor surface can appear and be responsible not only for the actuation and capturing of magnetic beads over the sensor surface but, also, for complex changing of the magnetic moments orientation in the sensing layer due to the stray field produced by the beads.

Based on these findings we investigate the behavior of Permalloy based PHE sensor disks under different applied fields in order to find the conditions for which the magnetostatic interaction between the SPM beads and the sensor surface become large

* Corresponding author. Fax: +40 268 41 57 12.
E-mail address: volmerm@unitbv.ro (M. Volmer).

http://dx.doi.org/10.1016/j.jmmm.2014.10.172
0304-8853/

enough to capture the beads inside of the sensor surface and, then, to detect their presence. We show that very simple and low cost structures can offer high detection sensitivity, which can be lower than 10^{-5} emu, and the possibility to capture SPM nanobeads over the sensor surface.

In a previous study, [7], the chip with PHE sensors was mounted on a soft magnetic grid. A constant biasing field was applied in the film plane, parallel with the driving current through the sensor, and then removed before making measurements. The signal dependence on beads position over the sensor surface has been studied. Now, the chip with the same design of the PHE sensors is placed on a non magnetic grid. By this, the magnetization state of the PHE sensors can be precisely controlled using both in plane and perpendicular applied fields allowing flexibility in setting up various detection methods as we will show in this paper. In addition, we expect an increasing of sensor's output dynamic compared to the case when the chip was mounted on a magnetic grid. This behavior was evidenced by our micromagnetic simulations presented in the previous study i.e., a larger difference between the PHE signals with and without nanobeads over the sensor surface.

2. Experiments

A Permalloy film, 20 nm thick, has been deposited on to oxidised Si substrate. No magnetic anisotropy axis has been defined during the deposition. Disk-shaped PHE sensors, 1 mm diameter, were structured on the Permalloy film by using photolithography technique. Also, have been patterned Au pads, 250 μm length, that are in contact with the Permalloy disks to define the PHE structures, Fig. 1(a), [7]. The sensors were passivated by sputtering a 200 nm thick TiO_2 layer to protect them against the fluid used during the experiments. In Fig. 1(a) are illustrated the electrical connections setup, the directions of the applied, H_{appl} and biasing, H_{bias}, fields respectively. This is typical setup used for field sensing. Two detection sites have been defined on the chip by using pairs of measurement and reference sensors. The chip was mounted on a custom designed non magnetic grid, made from glass-reinforced epoxy printed circuit board. The chip with PHE sensors was placed in a home-made system composed of Helmholtz coils which are able to generate well defined and uniform magnetic fields over three orthogonal directions; two of these fields are generated in the film plane. The measurement system, used to study the field dependences of the AMR and PHE effects, consists in Keithley 6221 programmable current source, Keithley 2182 A nanovoltmeter, and three programmable high current sources. The DC driving current through the sensors, I_{sens}=5 mA, was chosen to maximize the output signal but without affecting the thermal stability of the structure. The resistance between the current or the voltage contacts is about 120 Ω. A DC detection setup was used to read out the sensor because the frequency of the sweeping magnetic field was 0.01 Hz. The integration time, i.e. the period of time the input signal is measured, was 20 ms. In addition, a digital filter has been used. For each displayed reading, five measurements were averaged. This offers the best compromise between noise performance and speed. For this setting, the noise level was about 35 nV.

The magnetization curves for functionalised maghemite nanoparticles with Polyethylene glycol (PEG) 6000 were measured at room temperature with 7 T Mini Cryogen Free Measurement System from Cryogenic.

3. Results and discussion

The PHE is due to the anisotropic magnetoresistance (AMR) effect found in magnetic materials. A study presented in [10] clearly illustrates the field dependence of the AMR effect using a typical Hall effect measurement setup which is, from electrical point of view, similar to a Wheatstone bridge. In such experiments the field is applied in the film plane. It was found a quadratic dependence of the PHE signal on the magnetization, M, in Ni, Co, Fe, and Ni_xFe_{1-x} films. The output signal also shows an angular dependence such that a general equation, of the type [7] $U_{PHE} \sim I_{sens} M^2 \sin 2\theta$, can be used to describe the PHE signal; θ is the angle between the magnetization vector and the driving current through the sensor, I_{sens}. In turn, M depends on the applied field and the signal can be used as a probe of the structure magnetisation.

In a previous study [7] we presented the AMR curves measured for the sensors, S1 and S2, placed on the chip and connected like in Fig. 1(a). The applied field, H_{appl}, makes the angles 45° (for S1) and 135° (for S2) with the driving current and H_{bias}=0; in this case $\sin 2\theta = \pm 1$. The AMR effect saturates for fields higher than 50 Oe which means that the sensors cannot be used for detection of in plane applied fields higher than 25–50 Oe. The magnetization curve [7] of the four sensors, placed on the chip, shows a very small hysteresis effect. We used a simple method to find with precision the coercive field by applying the biasing field parallel to the driving current through the sensor S1, like in Fig. 1(a), and to sweep this field between ±150 Oe; H_{appl}=0. In this way, the film magnetisation will be parallel or antiparallel with the sensor

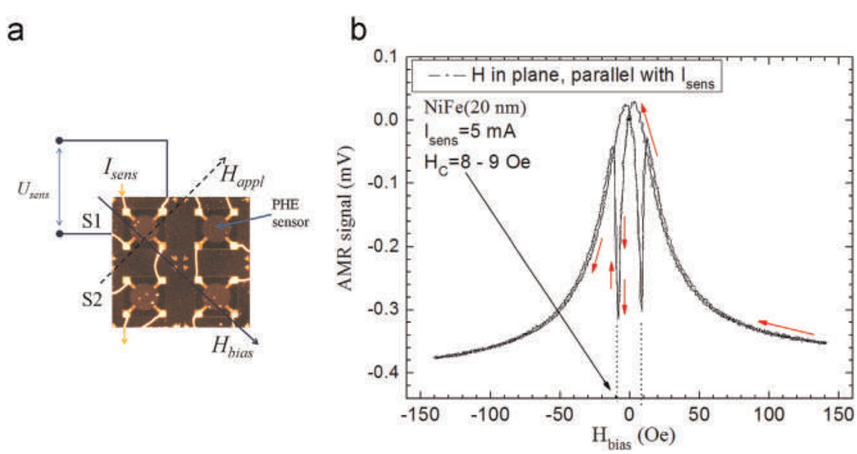

Fig. 1. (a) Enlarged top view of the chip with 4 PHE sensors (adapted with permission from M. Volmer and M. Avram, Signal dependence on magnetic nanoparticles position over a planar Hall effect biosensor, Microelectron. Eng. 108 (2013) 116–120, Elsevier). The biasing field, H_{bias}, and the applied field, H_{appl}, directions are illustrated. Also, the electrical connections are indicated; (b) The AMR signal measured when the biasing field is swept between ±150 Oe. The arrows are guides for the eyes.

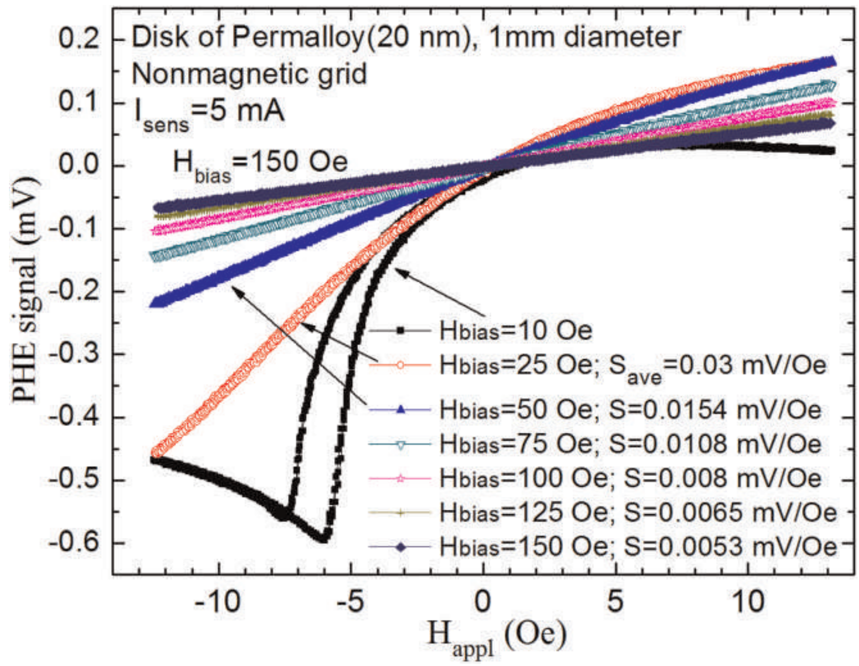

Fig. 2. The low field dependences of the PHE signal, without SPM nanobeads of maghemite over the sensor surface for different biasing fields; H_{appl} is directed like in Fig. 1(a). Voltage offsets have been subtracted.

current, I_{sens}. The coercive states will generate two sharp peaks in the sensor's signal, Fig. 1(b), for $H_{bias} = \pm 9$ Oe. Two complete hysteresis cycles were used to acquire data. It is to note the large field sensitivity around the coercive field which is, in modulus, about 0.072 mv/Oe in the linear region.

Because there are no anisotropy and exchange biasing fields typical for multilayered structures, we used a biasing field, H_{bias}, which can tune the magnetization state in the sensing layer. The low field dependences of the PHE signal, measured for the sensor S1, are presented in Fig. 2. The applied field is in the film plane, perpendicular to the driving current, I_{sens}, as is illustrated in Fig. 1(a).

For biasing fields smaller than 25 Oe the field dependences $U_{PHE}(H_{appl})$ show a nonlinear behavior and hysteretic effects. The magnetisation processes are more complex, presenting magnetic moments rotation and domain walls movement which generates nonlinearity and hysteretic effects. The very good linearity of the measured signal for H_{bias} higher than 25 Oe suggests that the main mechanism of the magnetization reversal processes that take place in the sensing layer is based on the magnetic moments rotation. The output voltage will be mainly proportional with sin 2θ which presents linear field dependence for small values of H_{appl}. However, higher torque is needed to rotate the magnetic moments and the field sensitivity decreases as is illustrated in Fig. 2. So, depending on the desired application and the measurement range, the adequate biasing field can be chosen.

Now, it is worth to mention that many works have been devoted to find optimal structures for PHE sensors. Structures like NiFe(5 nm)/IrMn(20 nm)/NiFe(20 nm) [11] or exchange biased spin valves like NiFe(16 nm)/Cu(1.2 nm)/NiFe(2 nm)/IrMn(15 nm) [4,12] are among the most used to deposit cross-shaped PHE sensors (NiFe-Permalloy). Sensitivities between 3 μV/Oe and 7 μV/Oe for a driving current of 1 mA trough the sensor are reported for applied fields in the range of ± 15 Oe [3–5,11,12]. It should be noted that other geometries like ring-shape [13] or elliptical-shape structures have been considered in last time to increase, by a geometrical factor, the PHE signal. However, by this study, we demonstrate that very good results can be obtained, also, by using simple Permalloy PHE sensors. Sensitivities up to 6 μV/(Oe · mA) are reported in Fig. 2.

As we proved both by experiments and micromagnetic simulations [7,8], for nanobeads detection the setup presented in Fig. 1(a) is not efficient because: (i) for fields lower than 50 Oe the SPM nanobeads present a very small magnetic moment and (ii) for higher applied fields, required to magnetise the beads and to have a signal from them, the sensor output will be saturated. To illustrate these aspects, we present, in Fig. 3, the magnetisation curves for maghemite nanoparticles (10 nm) functionalised with PEG 6000.

Fig. 3(a) shows the magnetisation curve obtained by VSM at room temperature for 30 μl of aqueous solution containing maghemite nanoparticles functionalised with PEG 6000. The field dependence of maghemite magnetisation is strongly affected at higher fields by the diamagnetic behavior due to water and PEG molecules. Fig. 3(b) presents the magnetisation curves, as measured and with diamagnetic correction, for 1.27 mg powder of functionalised maghemite nanoparticles. The high field magnetization curve, shown in the inset, allows us to estimate the diamagnetic contribution of the PEG 6000 molecules. To obtain 1.27 mg of powder, we used 107.7 mg of aqueous solution which was dried at 56 °C. We used this approach in order to lower the diamagnetic contribution and to obtain the „magnetic diameter" of the functionalised maghemite nanoparticles. After applying the diamagnetic correction and fitting the magnetisation data from Fig. 3(b) with the Langevin function [1], we obtained $d_{magn} = 11.48$ nm. From measurements made on not functionalised maghemite powder [7] we found $d_{magn} = 9.88$ nm which was consistent with the XRD measurements made on the same type of powder.

From Fig. 3 it comes that the nanobeads have to be magnetised in fields higher than 100 Oe to reach a large enough magnetisation state, close to saturation, that can be detected by the PHE sensor. Thus, in order to avoid the sensor saturation, we chose to apply the magnetising field perpendicular to the sensor surface. Because the sensor is less sensitive to perpendicular fields no higher than hundreds of Oe, only the in plane components of the field generated by the beads will produce changes of the magnetisation in the

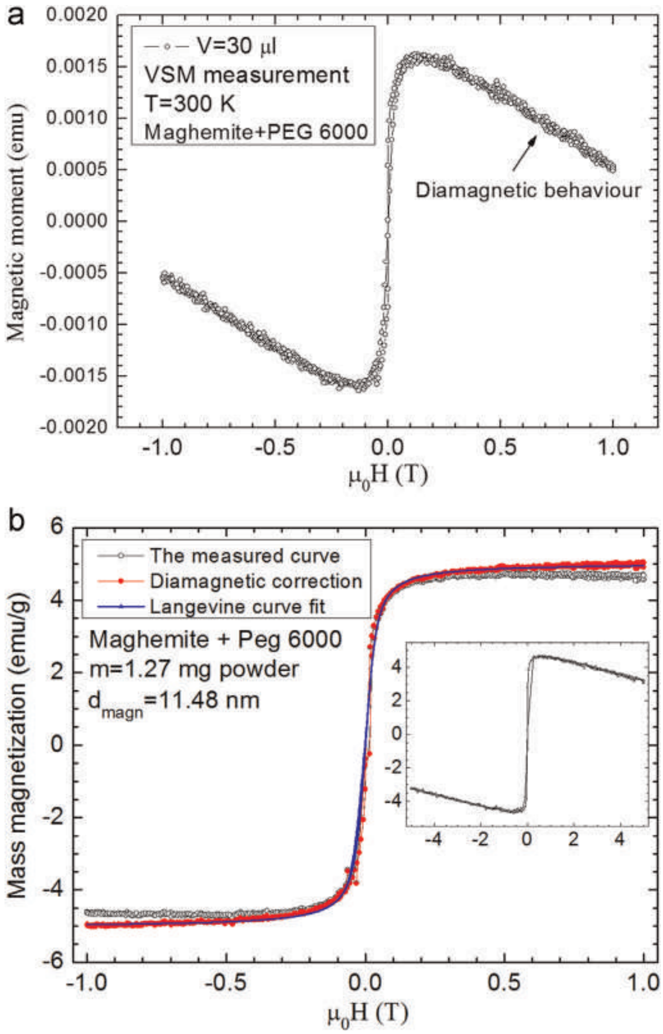

Fig. 3. Magnetization curves obtained by VSM for maghemite nanoparticles functionalised with PEG 6000 (a) in aqueous solution and (b) as powder; the inset shows the high field magnetization curve.

sensing layer. Also, small in-plane components can be found due to any misorientation of the applied magnetic field lines. Values of H_{appl} higher than 50 Oe can be used to magnetise the nanobeads without the risk to saturate the sensor.

In what follows H_{bias} will be directed along the driving current, I_{sens}, and the applied field will be perpendicular to the sensor surface (sensor S1). Two field scanning methods will be used: (i) H_{bias} will be swept between ± 30 Oe for constant values of H_{appl} and (ii) H_{appl} varies between ± 130 Oe for constant values of the biasing field. The measurements have been made without and with PEG 6000 functionalized SPM maghemite beads placed over the sensor surface.

One drop of 0.7 µl of aqueous solution with functionalised maghemite nanoparticles was placed on the sensor surface. Evaporation of water was carried out in a magnetic field (H_{appl} $=130$ Oe) applied perpendicular to the sensor surface previously polarized to the coercive state. The current through the sensor was, $I_{sens}=5$ mA. In these conditions the magnetic nanobeads have been retained inside of the sensor surface because of the complex domain structure, typical for a coercive state, which generates stray fields perpendicular to the surface. It has to mention that in a uniform magnetized state of the sensor layer, the SPM nanoparticles will accumulate mostly near edges with nonzero normal magnetization values [14]. This effect can be minimized by using structures with magnetic compensation layer [15].

Fig. 4 presents the field dependences of the sensor signal when H_{bias} is swept between ± 30 Oe for $H_{appl}=0$, ± 45 Oe and ± 90 Oe respectively. These dependences are measured without and with functionalised maghemite beads above the sensor surface.

The magnetostatic coupling between the SPM beads and the sensor surface is responsible for the change of the signal amplitude in the coercive state where the structure is more sensitive to any field perturbations. The beads are magnetised not only by the applied field but also by the biasing field and by the field due to the driving current, I_{sens}, through the sensor. The variation of the sensor signal, ΔU_S, due to the SPM beads, increases with H_{appl} because their magnetic moments increase, like was illustrated in Fig. 3. So, for these measurements, the highest amplitude of ΔU_S, is observed for $H_{appl}=\pm 90$ Oe. The direction of coercive field shift depends on the polarity of the applied field because of the small in plane components of H_{appl} and because of the magnetostatic coupling between the beads, polarised by this field, and the sensor surface. Using data presented in Fig. 3(a) and Fig. 3(b), we can estimate the value of the detected magnetic moment and the corresponding mass of the maghemite powder over the sensor surface. From Fig. 3(a), the measured magnetic moment at 90 Oe (0.009 T in air) is $m=8\times 10^{-4}$ emu for 30 µl. Because the volume of the liquid drop placed on the sensor's surface is 0.7 µl, we can estimate a value of 1.87×10^{-5} emu of the magnetic moment produced by this drop for an applied field of 90 Oe. After water evaporation, this magnetic moment produces a variation of -0.08 mV of the output signal, Fig. 4(c). It should be noted that for this value of the applied field the diamagnetic contribution can be neglected. Using data from Fig. 3(b) we get a value of 9.35 µg powder composed from maghemite functionalised with PEG 6000. This means about 6.83×10^{-7} g of pure maghemite cores. The estimation was obtained by comparing the magnetization curves for pure maghemite powder [7] and functionalised maghemite with PEG 6000, Fig. 3(b).

The results of the second field scanning method are presented in Fig. 5 where H_{appl} is swept between ± 150 Oe for $H_{bias}=0$ and ± 16 Oe respectively. Two cycles have been scanned for each measurement to see data repeatability. These dependences have the same shape like the field dependences of the PHE signal, for low biasing fields, plotted in Fig. 2. The sign of the slopes depends on the polarity of the sensor magnetisation through the biasing field.

The presence of the SPM beads over the sensor surface will generate in-plane components of the magnetic field. These fields will produce changes of the magnetic moments orientation in the film plane which will generate a PHE signal. For $H_{bias}=0$, the sensor is in a remnant state which depends on the initial magnetisation. This is clearly illustrated in Fig. 5(a) where are plotted the field dependences of the PHE signal for remnant states that originate from $H_{bias}=40$ Oe and -40 Oe respectively. The large variation of the PHE signal and the hysteretic effects are in good agreement with the data presented in Fig. 2 for low biasing fields. As the biasing field increases, the signal linearity increases but, also, the field sensitivity decreases, like in Fig. 2. In Fig. 5(b) are presented the field dependences of the PHE signal when H_{bias} $=\pm 16$ Oe. The amplitude of the signal variation, ΔU_S ≈ -0.06 mV, is smaller than in the previous case, Fig. 5(a), but the signal has a very good linearity and stability. The remnant steady state can be easy affected by small electromagnetic perturbations because Permalloy is a soft magnetic material. By this, the sensor signal will change. If the biasing field is decreasing from ± 16 Oe to ± 8 Oe the amplitude of the signal variation is $\Delta U_S\approx -0.09$ mV field but the signal nonlinearity increases. The shape of the field dependences represents a transition between the characteristics presented in Fig. 5(a) and (b).

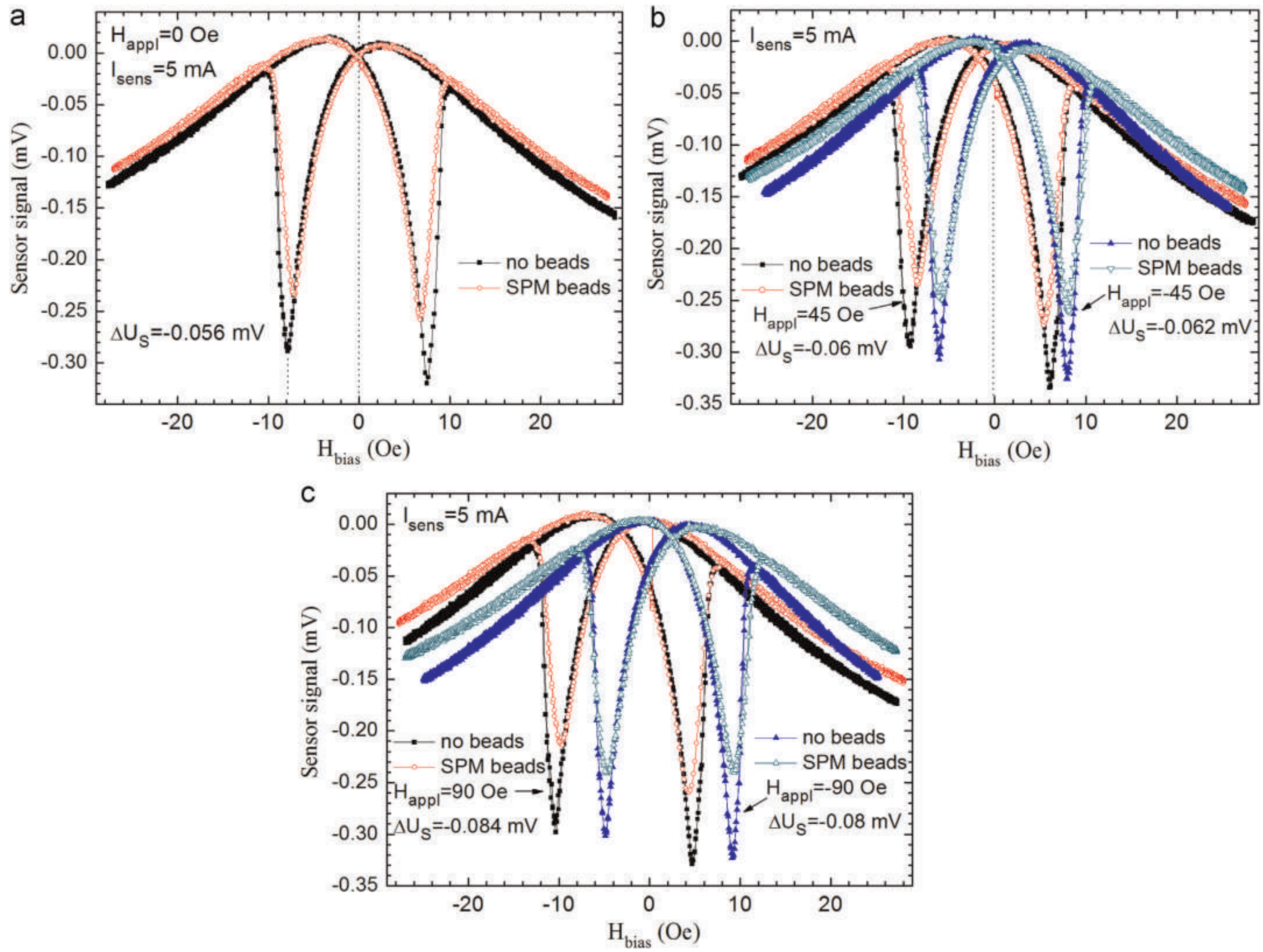

Fig. 4. The field dependences of the sensor signal when H_{bias} is swept between ± 30 Oe for (a) $H_{appl}=0$ Oe, (b) $H_{appl}=\pm 45$ Oe and (c) $H_{appl}=\pm 90$ Oe respectively. Two cycles have been scanned for each measurement to see data repeatability.

In our previous study [7], the highest signal variation was $\Delta U_S \approx -0.03$ mV for a magnetic moment of 7.14×10^{-6} emu, which means about -0.238×10^{-3} emu/mV. The sensor was in the remnant state and chip placed on a soft magnetic grid. Now, with the sensor in the remnant state, we obtained an average signal variation $\Delta U_S \approx -0.161$ mV, Fig. 5(a), for a magnetic moment of 1.87×10^{-5} emu which means about -0.116×10^{-3} emu/mV. This increasing of sensor's output dynamic, compared to the case when the chip was mounted on a soft magnetic grid, was anticipated by our micromagnetic simulations [7] and observed in the present measurements. So, from these data, we estimate that magnetic moments of about 10^{-6} emu can be easily detected with this sensor for a signal variation of 0.01 mV. Also, it has to mention that, by functionalizing the maghemite nanoparticles with PEG molecules, increases the distance between the magnetic cores and the sensor surface. The same is happening in the biodetection experiments where different biomolecules are used to functionalize the magnetic cores.

At this stage of the study it is an open question in choosing the best field scanning method. The first scanning method allows the using of a small permanent magnet to generate the constant applied field whereas the biasing field can be obtained through an integrated system on the chip. By applying AC biasing fields, sharp voltage pulses can be obtained and then processed. The constant applied field has to be removed during the washing process of the sensor surface. On the other hand, maintaining a constant biasing field and varying the applied field perpendicular to the sensor surface can generate a more stable and ordered magnetic structure in the sensing layer which rotates under the action of the in-plane components of the magnetic fields. Further experiments performed on micrometer sized sensors and using combinations of DC/AC fields will offer additional information regarding the best field scanning method in order to obtain higher detection sensitivity with low noise and good signal stability.

Finally, we present, in Fig. 6, the field dependences of the sensor signal when H_{appl} is swept between ± 150 Oe for $H_{bias}=4$ Oe. This state is obtained by coming from $H_{bias}=-40$ Oe, so it is between the remnant and the coercive states.

The magnetisation state for this biasing field will suffer irreversible changes by sweeping the perpendicular applied field. This is reflected by the field dependence of the sensor signal. We see how the starting and the ending points, for two complete cycles, are in different positions. Such values of the biasing fields, close to the coercive field, can generate large signal variation but as a

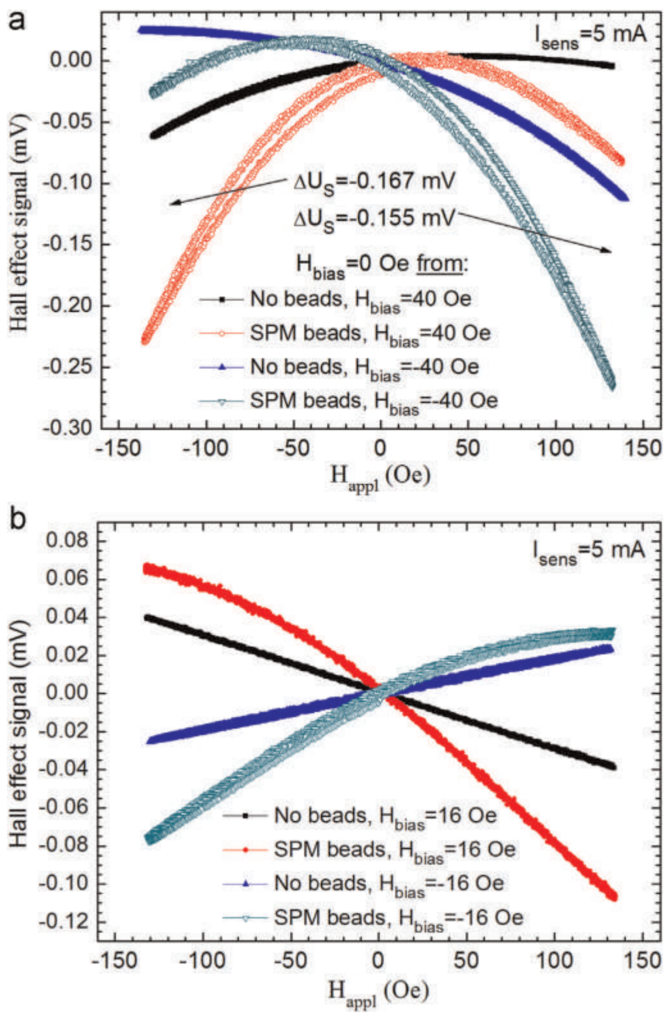

Fig. 5. The field dependences of the sensor signal when H_{appl} is swept between ± 150 Oe for (a) $H_{bias}=0$ and (b) $H_{bias}= \pm 16$ Oe respectively; H_{appl} is perpendicular over the sensor surface.

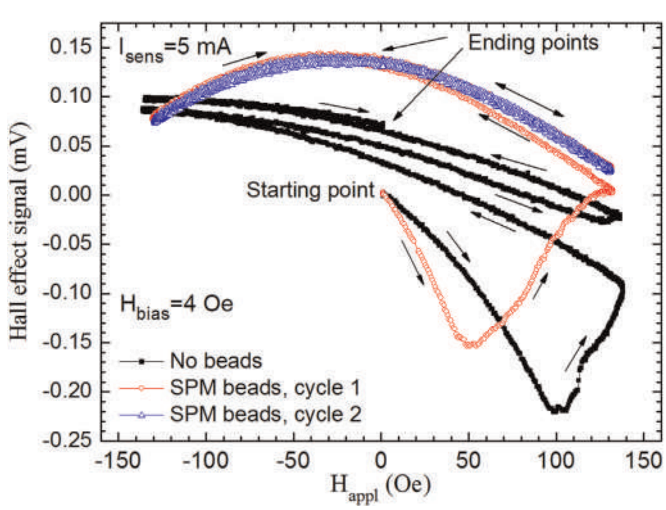

Fig. 6. The field dependences of the sensor signal when H_{appl} is swept between ± 150 Oe for $H_{bias}=4$ Oe; initially the sensor was polarised at $H_{bias}=-40$ Oe. The arrows are guides for the eyes.

singular pulse which is not repeating in amplitude for the next field cycles. The structure has to be re-magnetised for $H_{bias} = -40$ Oe and then placed in a biasing field like was described above to obtain again this pulse. It has to mention that a symmetrical behavior has been obtained for $H_{bias} = -4$ Oe after the structure has been placed in a field of 40 Oe.

4. Conclusions

A Permalloy based PHE sensor, 1 mm in diameter and 20 nm thick, used to capture and detect SPM nanobeads has been studied. For this purpose, a home-made characterisation system, composed from Helmholtz coils, has been developed in order to control with precision the sensor magnetization state.

Two field scanning methods were used and we found that high detection sensitivities, up to 0.116×10^{-3} emu/mV, can be obtained for different magnetization states in the sensing layer. So, magnetic moments of the order of 10^{-6} emu can be detected with this sensor for a signal variation of 0.01 mV. We observed large signal variations of the sensor output when the magnetic layer is polarized closed to the coercive state. So, particular magnetization states, like remnant or coercive, can provide convenient methods for the capture and detection of SPM nanobeads.

Further experiments which employ the using of special combinations of DC and AC magnetic fields will be made. The main limitation of our system, in what concerns the lowest magnetic moment that can be detected, comes from the relatively large dimension of the PHE sensors. However, we are confident that this type of structure is feasible for building low cost Permalloy based micrometer sized PHE sensors, with tunable properties, to be used for high-resolution detection applications. Spintronic structures will also be considered to develop such type of microsensors. In order to have a better control of the amount of fluid located above sensor, the chip will be integrated in a microfluidic system. We estimate that by lowering the sensor's dimension to micrometer scale and integrating the biasing system in the same chip, a better control of the magnetization state of the sensitive layer will be possible and higher sensitivities will be obtained.

Acknowledgments

The authors are grateful for the financial support from the project PN2 CELLIMUNOCHIP No. 2/2012 in the frame of the National Partnership Program.

References

[1] G. Li, S. Sun, R.J. Wilson, R.L. White, N. Pourmandc, S.X. Wang, Spin valve sensors for ultrasensitive detection of superparamagnetic nanoparticles for biological applications, Sens. Actuators A 126 (2006) 98–106.
[2] J. Germano, V.C. Martins, F.A. Cardoso, T.M. Almeida, L. Sousa, P.P. Freitas, M. S. Piedade, Spin valve sensors for ultrasensitive detection of superparamagnetic nanoparticles for biological applications, Sensors 9 (6) (2009) 4119–4137.
[3] K.M. Chui, A.O. Adeyeye, Li Mo-Huang, Detection of a single magnetic dot using a Planar Hall sensor, J. Magn. Magn. Mater. 310 (2007) e992–e993.
[4] B.D. Tu, L.V. Cuong, T.Q. Hung, D.T. Huong Giang, T.M. Danh, N.H. Duc, C. Kim, Optimization of spin-valve structure NiFe/Cu/NiFe/IrMn for planar hall effect based biochips, IEEE Trans. Magn. 45 (6) (2009) 2378–2382.
[5] C.D. Damsgaard, S.C. Freitas, P.P. Freitas, M.F. Hansen, Exchange- biased planar hall effect sensor optimized for biosensor applications, J. Appl. Phys. 103 (2008) 07A302.
[6] G. Li, S. Sun, S.X. Wang, Spin valve biosensors: signal dependence on nanoparticle position, J. Appl. Phys. 99 (2006) 08P107.
[7] M. Volmer, M. Avram, Signal dependence on magnetic nanoparticles position over a planar Hall effect biosensor, Microelectron. Eng. 108 (2013) 116–120.
[8] M. Volmer, M. Avram, Microbeads detection using spin-valve PHE sensors, J. Nanosci. Nanotechnol. 12 (2012) 7456–7459.
[9] E. Rapoport, D. Montana, G.S.D. Beach, Integrated capture, transport, and magneto-mechanical resonant sensing of superparamagnetic microbeads using magnetic domain walls, Lab Chip 12 (2012) 4433–4440.

[10] C. Prados, D. Garcia, F. Lesmes, J.J. Freijo, A. Hernando, Extraordinary anisotropic magnetoresistance effect under 35 Oe field at room temperature in Co/Ni multilayers, Appl. Phys. Lett. 67 (5) (1995) 718–720.
[11] L. Ejsing, M.F. Hansen, A.K. Menon, H.A. Ferreira, D.L. Graham, P.P. Freitas, Planar hall effect sensor for magnetic micro- and nanobead detection, J. Magn. Magn. Mater. 293 (2005) 677–684.
[12] Tran Quang Hung, Sunjong Oh, Jong-Ryul Jeong, CheolGi Kim, Spin-valve planar Hall sensor for single bead detection, Sens. Actuators A 157 (1) (2010) 42–46.
[13] B. Sinha, S. Oh, T.S. Ramulu, J. Lim, D.Y. Kim, C. Kim, Planar hall effect ring sensors for high field-sensitivity, Adv. Mater. Res. 317-319 (2011) 1136–1140.
[14] F.W. Østerberg, B.T. Dalslet, C.D. Damsgaard, S.C. Freitas, P. Freitas, M.F. Hansen, Bead capture on magnetic sensors in a microfluidic system, IEEE Sensors J 9 (2009) 682–688.
[15] B.T. Dalslet, M. Donolato, M.F. Hansen, Planar hall effect sensor with magnetostatic compensation layer, Sensors Actuators A 174 (2012) 1–8.

Microelectronic Engineering 108 (2013) 116–120

Contents lists available at SciVerse ScienceDirect

Microelectronic Engineering

journal homepage: www.elsevier.com/locate/mee

Signal dependence on magnetic nanoparticles position over a planar Hall effect biosensor

Marius Volmer [a,b,*], Marioara Avram [b]

[a] Transilvania University of Brasov, Eroilor, 29, Brasov 500036, Romania
[b] National Institute for Research and Development in Microtechnologies, Str. Erou Iancu Nicolae 32B, 72996 Bucharest, Romania

ARTICLE INFO

Article history:
Available online 26 February 2013

Keywords:
Magnetic sensor
Planar Hall effect
Micromagnetic simulation
Lab-on-a-chip

ABSTRACT

Experimental and micromagnetic studies have been carried out on the planar Hall effect (PHE) sensor signal dependence on the spatial locations of magnetic nanoparticles used as labels in biodetection applications. Disk-shaped structures, made from Permalloy, 1 mm diameter and 20 nm thick, were deposited on to oxidised Si substrate. To have a better control of the sensor sensitivity and linearity, a DC biasing field has been applied parallel to the driving current. The magnetic nanoparticles of maghemite were placed on different positions over the sensor surface using small water droplets and well defined magnetic field gradients. In our experiments the magnetic field was applied perpendicular to the sensors surface in order to avoid the saturation of the PHE signal. The results of our experiments are explained by means of micromagnetic simulations where magnetostatic interactions between magnetic nanobeads and sensor are clearly highlighted. With such simple and low cost sensors, magnetic moments lower than 7×10^{-6} emu can been detected which means a total mass of maghemite nanobeads lower than 2×10^{-7} g.

1. Introduction

The recent development of lab-on-a-chip (LOC) applications using magnetic micro/nano bead-based biochemical detection is a promising approach in reducing biological or chemical laboratories to a microscale system [1,2]. In these systems the magnetic beads are used to label the biological structures of interest. Depending on their size, we can talk about micro beads (diameters of about 1–3 μm) and nanobeads which can have diameters between 10 and 200 nm. The beads are made, usually, from magnetite or maghemite and do not show a net magnetic moment in the absence of an external magnetic field. This superparamagnetic behaviour is very important for LOC applications in order to minimise false biodetection signals. When a magnetic field is applied these particles acquire a net magnetic moment and behave like very small magnetic field sources. The fields produced by these beads are usually detected using giant magnetoresistance (GMR), tunneling magnetoresistance (TMR) [1,3] or planar Hall effect (PHE) spin-valve sensors [4,5]. The PHE sensors are based on the anisotropic magnetoresistance (AMR) effect and because of the measurement setup, which is very similar to a Wheatstone bridge [6], have become very attractive due to their thermal stability and a higher signal-to-noise ratio (S/N) when compared to spin valve GMR sensors [4,5]. Therefore, the PHE sensor has advantages for more accurate detection of the small stray fields of the magnetic beads [5]. The output voltage is of the type $U_{PHE} \sim I_{sens} \cdot M^2 \cdot \sin 2\theta$, where θ is the angle between the magnetization vector, M, and the sensor driving current, I_{sens}. A very good linearity and sensitivities between 3 μV/Oe [4] and 7 μV/Oe [5] for a driving current of 1 mA trough the sensor are reported for applied fields in the range of ±15 Oe. However, the sensitivity of the PHE sensors is not so high compared to GMR or TMR sensors. In the last few years multilayer structures, like $IrMn/Ni_{80}Fe_{20}$ [4], trilayers of type Co(10 nm)/Cu(2 nm)/NiFe(10 nm) [7] or exchange bias spin valves like Ta(/NiFe(16 nm)/Cu(1.2 nm)/NiFe(2 nm)/IrMn(15 nm)/Ta(5 nm) [5,8] have been studied to increase the sensor sensitivity (NiFe denotes Permalloy). Usually, cross-shaped structures are considered to deposit PHE sensors. In these structures, the exchange biasing field due to antiferromagnetic layer, like FeMn or IrMn, is strong enough to pin the magnetization of the adjacent ferromagnetic layer (named pinned layer). In turn, this pinned layer will induce an ordered magnetization state in the free layer. When a magnetic field is applied in the film plane, perpendicular to biasing field and driving current, the magnetization of the ferromagnetic free layer will rotate coherently and a signal, U_{PHE}, will be obtained. It should be mentioned two effects that can lower the sensor field sensitivity: (i) the shunting effect due to nonmagnetic and pinned ferromagnetic layers (i.e., the effective current which is flowing through the sensing layer is smaller than I_{sens}) and (ii) the sensor sensitivity dependence with the anisotropy field, H_K, and

* Corresponding author at: Transilvania University of Brasov, Eroilor, 29, Brasov 500036, Romania. Tel./fax: +40 268 41 57 12.
E-mail addresses: mariusvolmer@yahoo.com, volmerm@unitbv.ro (M. Volmer).

0167-9317/$ - see front matter © 2013 Elsevier B.V. All rights reserved.
http://dx.doi.org/10.1016/j.mee.2013.02.055

the exchange field, H_{ex} of the type $S \sim 1/(H_K + H_{ex})$, [8]. Higher values for H_K and H_{ex} means a more ordered magnetic state but implies a higher torque to rotate the magnetization of the sensing layer. By reducing these fields and considering other geometries like ring-shape, disk-shape or elliptical-shape structures, the PHE signal can be increased sometimes more than 100 times [9]. It is to mention that micrometer sized AMR rings provide the ideal geometry for single microsphere detection [1]. The strong magnetostatic interaction between the magnetic beads and the sensor's magnetic layer is responsible for two effects: (i) the actuation and capturing of magnetic beads [10,11] and (ii) magnetic domains rotation in the sensing layer due to the fringe field produced by the beads [10–14]. So, for the sensitive detection, however, not only the sensor sensitivity is important but also the equivalence between the sensor size and the diameter of magnetic bead must be optimized. The evidence of a single 2.8 μm diameter micro-bead detection using a PHE sensor, based on a spin-valve structure with 3 μm × 3 μm the active surface, was presented in [5]. In this paper we report results regarding detection of superparamagnetic (sppm) nanobeads of maghemite using disk-shaped Permalloy based PHE sensors. Our measurements show that the sensor signal depends on the spatial locations of magnetic nanoparticles over the sensor surface. The experimental results are explained by means of micromagnetic simulations where the magnetostatic interactions between the magnetic nanobeads and sensor are highlighted [12,13].

2. Experiments

Permalloy based PHE sensors, disk-shaped of 1 mm diameter and 20 nm thick, were deposited on oxidised Si substrate. No magnetic anisotropy axis has been induced during the deposition process. On each chip four sensors were defined using photolithographic technique and connected like in Fig. 1(a) where, also, are illustrated the directions of the external applied field, H_{appl} and biasing field, H_{bias} in order to obtain the PHE signal. The sensors S1 and S2 are connected in series. The same is with the other two sensors which are on the chip. Because of this geometry the biasing field, when is applied, makes the angles 90° and 0° with the current direction in S1 and S2, respectively. Fig. 1(b) details the PHE measurement setup for S2 in what concerns the applied fields, the driving current trough the sensor, I_{sens}, and the angle, θ, between M and I_{sens}. The magnetization curve of the four sensors, measured with 7T Mini Cryogen Free Measurement System from Cryogenic, is presented in Fig. 1(c) and shows a very small hysteresis effect. The chip was mounted on a grid which is made from soft magnetic material; the remnant magnetic induction of the grid is about 2 G. The chip thickness, 0.5 mm, gives the distance between the grid and the surface of the sensors and assures a small magnetostatic coupling between them. The AMR effect was measured [6] for sensors S1 and S2, Fig. 1(d), taking the advantage of the setup presented in the inset. The measurement system consists in Keithley 6221 programmable current source, Keithley 2182A nanovoltmeter and a programmable magnetic field source. There was no applied biasing field before the measurement. The AMR effect saturates for fields lower than 50 Oe. The sense of signal variation for S1 and S2 can be explained by considering the angles between the applied field and the driving current, I_{sens}.

In our experiments, described in what follows, the field was applied parallel to the sensor surface, like in Fig. 1(a), and perpendicular to the sensor surface. The results are explained by using a freeware micromagnetic simulator, SimulMag [14], with which we were able to design the generic sensor structure, the polarising system, the sppm nanobeads and to analyse the behaviour of this complex system [13] in applied magnetic fields.

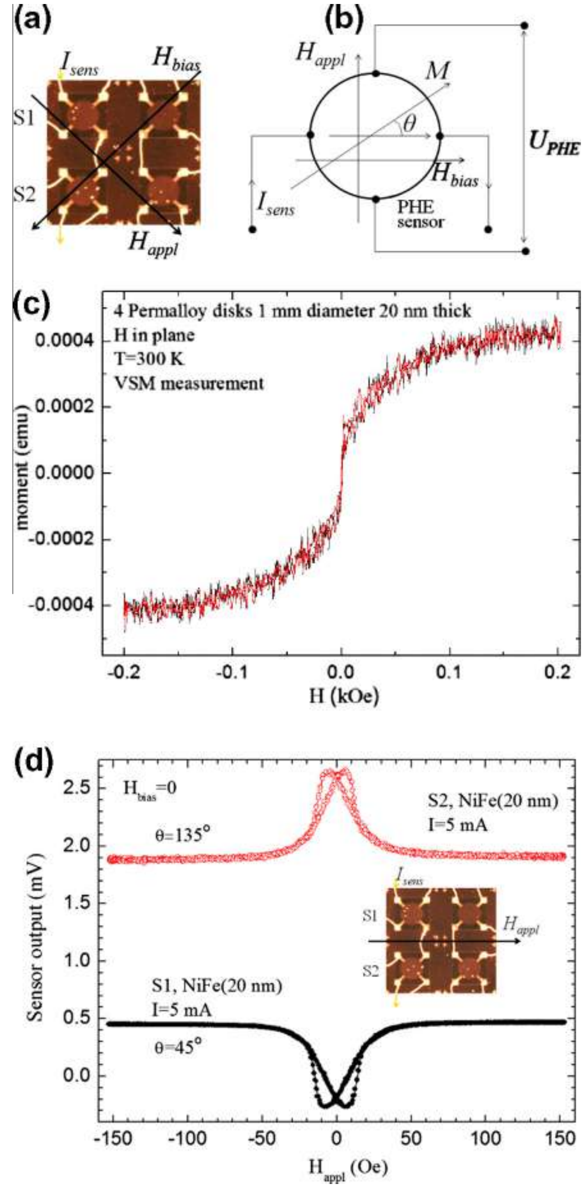

Fig. 1. (a) The chip with PHE sensors, (b) the schematic used to explain the PHE setup, (c) the magnetization curve of the Permalloy based PHE sensors and (d) the measured AMR signal when the field is directed like is shown in inset.

3. Results and discussion

To overcome the absence of the anisotropy and exchange fields, we used a biasing field, H_{bias}, which creates a uniform magnetization state in the sensing layer [13]. We found that after biasing the structures at 500 Oe and then turning off H_{bias}, the PHE sensors will keep a relatively well ordered magnetic state because of the magnetic grid on which the chip is mounted. Fig. 2(a) presents the low field dependences of the PHE signal measured on the sensor S2, in the above biasing conditions, without and with sppm maghemite nanobeads (10–12 nm in diameter) placed on the sensor surface, like we see in the inset. The field, H_{appl}, is directed in the film plane, perpendicular to the driving current and the direction of H_{bias} which has been previously applied. The very good linearity and high sensitivity of the measured signal suggests that the main mechanism of the magnetization reversal processes that take place in the sensing layer is based on the magnetic moments rotation. We observed, in our experiments, that for applied fields higher than 20 Oe the initial magnetization state will be destroyed and the reversal processes will be mainly due to domain walls movement which generates nonlinearity and hysteretic effects.

The field dependences are almost identical in both cases and only a small drift can be observed, Fig. 2(a). This result, for the linear region of the PHE signal, is comparable with data shown in [5] which reveals, basically, a shift of the field dependence of the output signal when the beads are on the sensor surface. For nanobeads detection this behaviour is not useful because cannot offer a net and unambiguous signal. Moreover, at small applied fields the sppm nanobeads present a weak magnetic moment, Fig. 2(b), and their contribution to the total field inside of the sensor is negligible. The nanobeads have to be magnetised in fields higher than 100 Oe, but for these values the sensor saturates and no signal can be obtained. For this reason, we choose to apply the field perpendicular to the sensor surface. Because the sensor is less sensitive to perpendicular low fields, only the in plane components of the field generated by the beads will produce a rotation of the sensing layer magnetization. Values of H_{appl} higher than 10 Oe can be used to magnetise the nanobeads without the risk to saturate the sensor. In a previous study [13] we obtained, by micromagnetic simulations, a signal dependence on magnetic nanoparticles position over the planar Hall effect biosensor. In our experiments the beads were placed on the sensor surface using a sharp tip made from wood which has been immersed in aqueous solution that contains the maghemite nanobeads. Because of the surface tension the same quantity of liquid droplets will remain on the tip for each immersion. We had this confirmation in previous experiments used to measure the diameters and the mass of the spots; one drop of aqueous solution was found to be about 20 μg and forms a spot of about 0.5 mm in diameter. The water evaporation has been done in magnetic field applied perpendicular to the sensor surface (150 Oe) and an applied current trough the sensor, I_{sens} = 5 mA. In these conditions the magnetic nanobeads have been retained in desired places, inside of the sensor surface. The mass of nanobeads that remain after the water evaporation was much smaller than 10 μg and cannot be weighed. The estimation will be done from magnetic data. The magnetic field, H_{appl}, was swept between ±150 Oe, perpendicular to the sensor surface. Two cycles have been scanned for each measurement to see data repeatability. It is to mention that before each new measurement the surface was washed in order to remove the sppm nanobeads and a short magnetic pulse, of 500 Oe, was applied like was described previously in order to re-set a uniform magnetic state in the sensing layer. Then, H_{appl} was swept for two cycles in order to stabilize the magnetic structure inside the sensor. Because beneath the sensors is a magnetic grid, the field and magnetic moments distributions inside the sensor will be affected by the presence of this material. The typical "S" shape field dependence of the Hall voltage will not be observed. Fig. 3 presents the measured signal in the absence and the presence of sppm nanobeads placed on the sensor surface in two positions denoted with "SE" and "N", respectively; in the figure inset are explained these coordinates. As is expected, when the nanobeads are placed near the "E" position, i.e. on the sensor driving current direction, the response amplitude is lower than in the "N" position where the torque exerted on the sensor magnetization is higher.

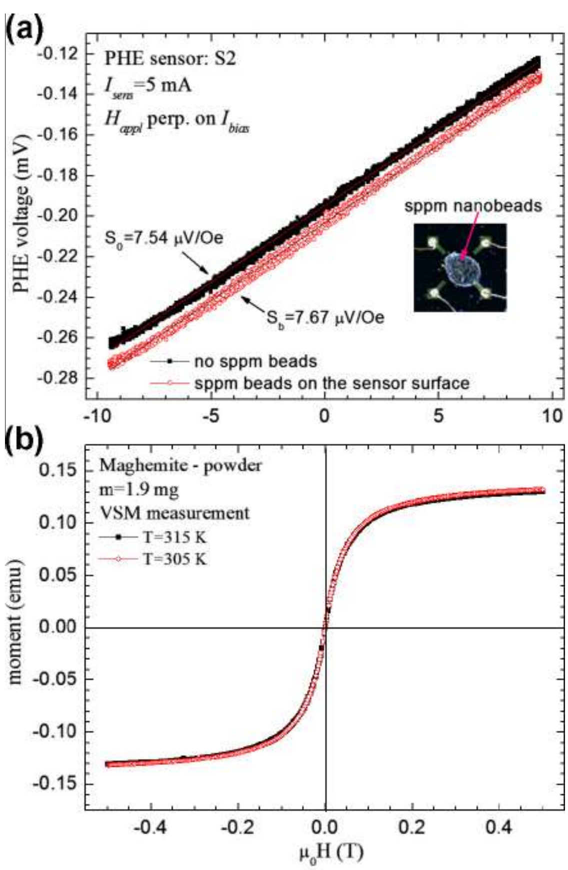

Fig. 2. (a) The field dependences of the PHE signal, without and with sppm nanobeads of maghemite placed over the sensor surface, when H_{appl} is directed in the film plane and (b) the magnetization curve of the maghemite nanobeads used in this study.

Comparing the shapes of the field characteristics presented in Fig. 1(d) for S2 and Fig. 3, we have the confirmation that the signals represent typical AMR curves. This is due to the magnetic grid which facilitates the appearance of the in plane magnetic fields components. Magnetic moments that are parallel or perpendicular to the driving current will not give a signal because $\sin 2\theta \approx 0$. The other components that are close to 45° or 135° give an important signal which corresponds to the AMR effect. The micromagnetic simulations were performed in order to give a better understanding of the experimental data. Fig. 4(a) presents the image of the structure used to simulate this behaviour; H_{appl} is directed perpendicular to the sensor plane. The current, I_{bias}; which is flowing through the flat band, generates the biasing field. Details regarding the PHE structure design, biasing system and field behaviour simulation for this complex system have been presented in [12,13]. The micromagnetic simulations presented in Fig. 4(b) give a good qualitative agreement with data from Fig. 3(a) and show, also, the field behaviour of the AMR effect when the grid is nonmagnetic and no beads are above the sensor. As expected, an almost flat

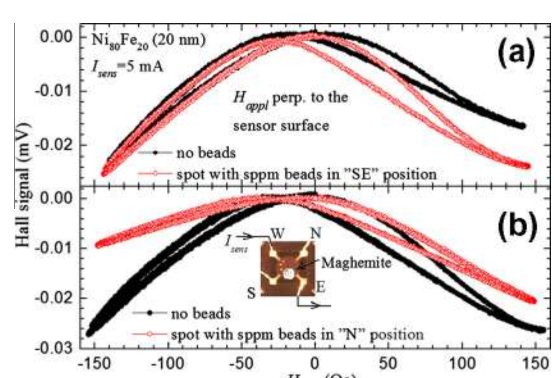

Fig. 3. The output of the PHE sensor measured with sppm nanobeads placed in two positions.

characteristic is obtained because the sensor is less sensitive for perpendicular applied magnetic fields. Also, a very small signal was obtained by micromagnetic simulations when the nanoparticles are located above the sensor centre and the chip is mounted on a nonmagnetic grid. This result is in good agreement with [15].

Because in our experiments the spot was localised in a region between the "SE" position and the centre of the sensor, we present, in Fig. 4(b), the results of the micromagnetic simulations for two positions.

To estimate the magnetic moment detected in these experiments we placed 14 spots, 0.5 mm in diameter, of water with maghemite suspension on a plastic foil. After the water evaporation the foil was folded and introduced in VSM where the $M(H)$ characteristic was measured, Fig. 5.

From this measurement, taking the magnetization value at 150 Oe, results the magnetic moment at this field for one maghemite spot deposited over the sensor surface: 7.14×10^{-6} emu. The mass magnetization at this applied field can be calculated, using data from Fig. 2(b) and then, the maghemite mass contained in one spot was estimated to about 2.14×10^{-7} g.

We observed, by some experiments and micromagnetic simulations that the magnetic nanoparticles can be trapped in some regions, inside of the sensor's surface by using magnetic fields with well defined gradients produced by the sensor himself and by the driving current which is flowing through the sensor. This is in good agreement with [11] where nanotrack-guided domain walls can propel individual trapped beads through an aqueous medium at speeds approaching 1000 μm/s. So, an integrated platform for the capture, transport, and detection of individual superparamagnetic microbeads can be defined [10]. Because the planar Hall effect is based on magnetisation rotation in the sensing layer, which gives the ability to measure magnetic fields with frequencies up to MHz, the sensor is capable to measure distribution of nanoparticles in short periods of time, the limitation being imposed by the fluid viscosity.

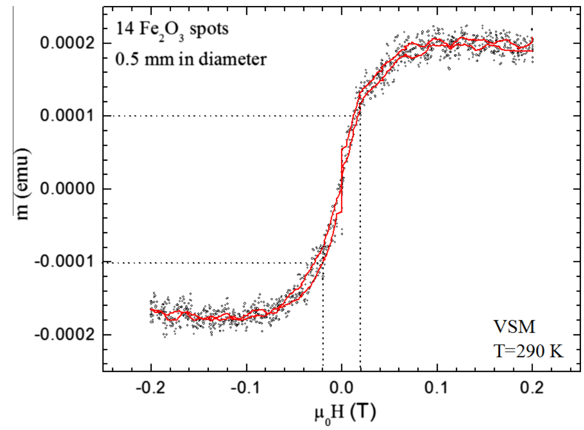

Fig. 5. VSM measured magnetization curve for 14 maghemite spots, 0.5 mm in diameter.

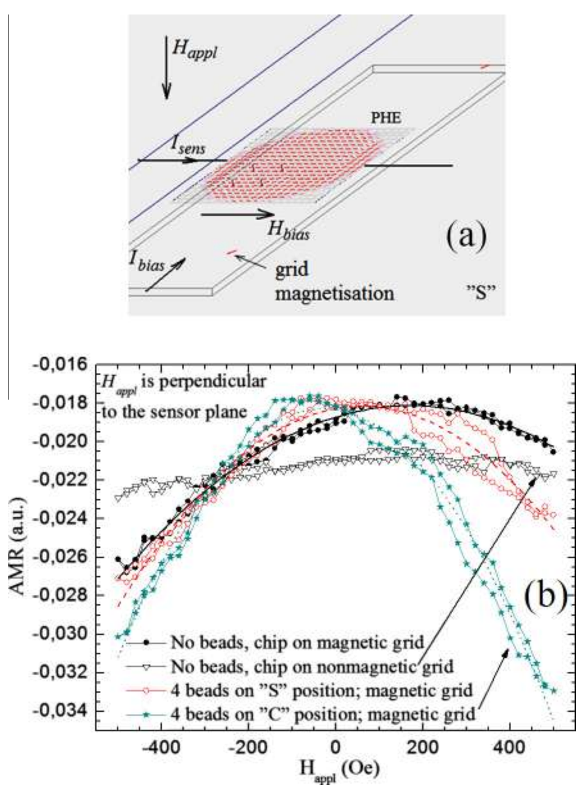

Fig. 4. (a) Details regarding the structure used for micromagnetic simulations and (b) results of the micromagnetic simulations for different positions of the sppm nanobeads above the sensor surface; "C" means that the nanobeads are located above the centre.

4. Conclusions

In this paper we have presented aspects regarding maghemite nanobeads detection using a PHE sensor made from a single layer of Permalloy, 1 mm in diameter and 20 nm thick. We obtained good detection sensitivity. The output signal depends both in amplitude and shape on the nanoparticles position over the sensor surface. The experimental data was interpreted by means of micromagnetic simulations and highlights the influence of the magnetic grid on the sensor behaviour. The superparamagnetic behaviour of the nanobeads and the magnetostatic interaction between the sensor and nanobeads has been considered for these simulations. The needs to apply, prior to make the measurement, a biasing field will be eliminated in the next experiments. For this reason and to improve the detection limit, micrometer sized spintronic PHE sensors will be used. Obtaining a well defined magnetic state in the sensing layer in structures with low values for H_K and H_E is a challenging task as well as the decreasing of the shunting effects due to nonmagnetic and pinned layers. Based on these studies the layout of the spintronic sensors has been designed and future experiments will be carried out.

Acknowledgements

The research presented in this paper is supported by the Sectoral Operational Programme Human Resources Development (SOP HRD), financed from the European Social Fund and by the Romanian Government under the contract number POSDRU/89/1.5/S/63700.

References

[1] Daniel L. Graham, Hugo A. Ferreira, Paulo P. Freitas, Trends Biotechnol. 22 (9) (2004) 455–462.
[2] Guanxiong Li, Shouheng Sun, Robert J. Wilson, Robert L. White, Nader Pourmandc, Shan X. Wang, Sens. Actuators A 125 (2006) 98–106.
[3] J. Germano, V.C. Martins, F.A. Cardoso, T.M. Almeida, L. Sousa, P.P. Freitas, M.S. Piedade, Sensors 9 (6) (2009) 4119–4137.
[4] L. Ejsing, M.F. Hansen, A.K. Menon, H.A. Ferreira, D.L. Graham, P.P. Freitas, Appl. Phys. Lett. 84 (2004) 4729–4731.
[5] Tran Quang Hung, Sunjong Oh, Jong-Ryul Jeong, CheolGi Kim, Sens. Actuators A 157 (1) (2010) 42–46.
[6] C. Prados, D. Garcia, F. Lesmes, J.J. Freijo, A. Hernando, Appl. Phys. Lett. 67 (5) (1995) 718–720.
[7] K.M. Chui, A.O. Adeyeye, J. Magn. Magn. Mater. 310 (2007) 992–993.

[8] B.D. Tu, L.V. Cuong, T.Q. Hung, D.T. Huong Giang, T.M. Danh, N.H. Duc, C. Kim, IEEE Trans. Magn. 45 (6) (2009) 2378–2382.
[9] B. Sinha, S. Oh, T.S. Ramulu, J. Lim, D.Y. Kim, C. Kim, Adv. Mater. Res. 317–319 (2011) 1136–1140.
[10] E. Rapoport, D. Montana, G.S.D. Beach, Lab Chip 12 (2012) 4433–4440.
[11] E. Rapoport, G.S.D. Beach, Appl. Phys. Lett. 100 (2012) 082401–082404.
[12] M. Volmer, M. Avram, AIP Conf. Proc. 1311 (2010) 261–266.
[13] M. Volmer, M. Avram, J. Nanosci. Nanotechnol. 12 (9) (2012) 7456–7459.
[14] <http://math.nist.gov/oommf/contrib/simulmag/>.
[15] G. Li, S. Sun, S.X. Wang, J. Appl. Phys. 99 (2006) 08P107.

Optimisation of Spin-Valve Planar Hall Effect Sensors for Low Field Measurements

Marius Volmer[1] and Jenica Neamtu[2]

[1]Electrical Engineering and Applied Physics Department, Transilvania University of Brasov, Brasov, 500036 Romania
[2]National Institute for Research and Development in Electrical Engineering "ICPE-CA," Bucharest, 030138 Romania

In this paper are presented results of galvanomagnetic measurements and micromagnetic simulations performed on low-field magnetic sensors based on the planar Hall effect (PHE). Disc-shaped structures of the type Co/Cu/$Ni_{80}Fe_{20}$, 4 mm diameter, deposited by magnetron sputtering onto Si substrate, were used to build magnetic sensors. At this stage of study, no uniaxial anisotropy axes were defined during the samples deposition. Two types of applications have been considered: (i) magnetic field measurements and (ii) rotation sensing. In order to obtain a coherent rotation of the magnetization inside the PHE sensor under the action of an applied magnetic field, H_{appl}, DC or AC magnetic biasing fields were used. By these means the magnetic sensitivity and the hysteresis width of the PHE signal can be tuned. Sensitivities between 0.07 and 0.17 μV·A^{-1}·m have been obtained for a driving current of 10 mA. Micromagnetic simulations were used to explain some field angular behavior of these sensors.

***Index Terms*—Anisotropic magnetoresistance, magnetic sensors, micromagnetic simulations, planar Hall effect, spin valves.**

I. Introduction

THE MAGNETORESISTANCE (MR) behavior of ferromagnetic thin films originates from the spin-orbit coupling between electrons and magnetic moments of the lattice atoms and is quantum mechanical in origin. Extraordinary effects are created by the microscopic part of the flux density $(\mu_0 M)$ whereas the ordinary effects are created by the macroscopic part $(\mu_0 H)$. Anisotropic magnetoresistance (AMR) effect also arise from the spin-orbit coupling, but it is anisotropic with respect to magnetization direction. AMR depends on the crystal structure of the material and the spin of the atoms situated in the crystal. It depends on the domain structure of the ferromagnet. In general the resistivity is larger if the current is applied parallel or antiparallel to the magnetization (longitudinal effect) than if the current is applied perpendicularly to the magnetization (transversal effect). This difference between the two states of magnetization is measured as the AMR effect. The applied magnetic field rotates the magnetization (if it is not pinned by the shape anisotropy or by the exchange interaction with an antiferromagnetic layer) of the film thus influencing the magnetoresistance of the film.

To develop practical applications, such as contactless potentiometer or magnetic field sensors, it requires a low thermal drift of the MR signal. For this purpose it is convenient to operate the device in a Wheatstone bridge configuration. Each arm corresponds to one MR element [1]. Such a demand can be easily achieved by exploiting the planar Hall effect (PHE). Because of the AMR effect will appear an electric field perpendicular to the applied current, in a Hall effect geometry, when the magnetic field is in the film plane [1]–[3]. Using this setup we get direct access to the anisotropic part of the resistance with the advantage of a reduced thermal drift of the output signal. In a single domain approximation, the PHE voltage, U_{PHE}, is expressed by

$$U_{\mathrm{PHE}} = CM^2 j \sin 2\theta \tag{1}$$

where C is a constant determined by the structure properties, j is the current density, M is the saturation magnetization and θ is the angle between the current and the magnetization vector that, in turn, is determined by the value and direction of the external magnetic field, Fig. 1.

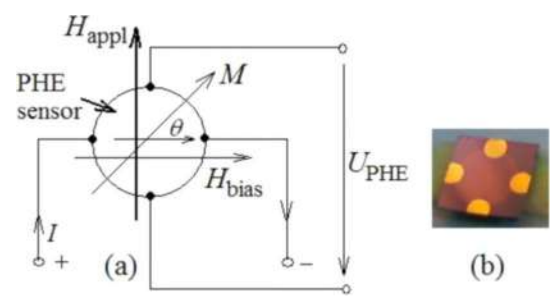

Fig. 1. (a) Setup used for biasing the PHE sensor. (b) Image of the deposited sensor.

Although the signal derived from the PHE is small, there is a higher signal-to-noise ratio (S/N) and a better thermal stability when compared to GMR spin valve (SV) sensors, hence it has the potential of detecting very small fields produced by various sources like single micro- or nanoparticles [4]–[7]. If the magnetization is initially oriented along the driving current inside the sensor, a rotation with angle θ produces a variation of the PHE voltage proportional with sin2 θ. This property can be used to build magnetic sensors. In order to obtain a coherent rotation of the magnetization inside the PHE sensor under the action of an applied magnetic field, a magnetic biasing can be used, as can be seen in the schematics presented in Fig. 1.

The micromagnetic simulations were made using a method that minimises the free energy of the system in magnetic field based on the Stoner-Wohlfarth model [8], [9].

Manuscript received August 16, 2011; accepted October 14, 2011. Date of current version March 23, 2012. Corresponding author: M. Volmer (e-mail: volmerm@unitbv.ro).

Color versions of one or more of the figures in this paper are available online at http://ieeexplore.ieee.org.

Digital Object Identifier 10.1109/TMAG.2011.2173671

II. Experimental Procedure

Disc-shaped spin valve structures of the type Si/Ta(3 nm)/Co(30 nm)/Cu(7 nm)/Ni_{80} Fe_{20}(70 nm)/Ta(3 nm) and Si/Ta(3 nm)/$Fe_{50}Mn_{50}$(11 nm)/Co(5 nm)/Cu(3 nm)/$Ni_{80}Fe_{20}$(10 nm)/Ta(3 nm) have been used to build PHE sensors like in Fig. 1(b). The films were patterned as discs with a diameter of about 4 mm. The four-lead setup consists of four Cu strips (200 nm thickness) forming a square of 3 mm each side, disposed as is shown in Fig. 1(b). In what follows, Py denotes $Ni_{80}Fe_{20}$ (Permalloy). The structures were deposited using a UHV magnetron sputtering machine, ATC2200 AJA, with the base pressure of $0.5 \cdot 10^{-4}$ mTorr. During sputtering of the multilayered structures, a magnetic field of 16 kA/m was applied in the film plane. For MR and PHE characterization the measurement system consists of a programmable current source Keithley 6221 and a nanovoltmeter 2182 A. To generate and control the magnetic field we used a bipolar 4 quadrants BOP 10–100 MG power source that drives an electromagnet. The field is measured using a Lake Shore 475 DSP gaussmeter. A coil is inserted in the gap of this electromagnet. The field generated by the electromagnet is perpendicular on the field generated by this coil. The electromagnet was used to supply the polarizing field, $H_{\rm bias}$, whereas the coil was used to generate small magnetic fields, $H_{\rm appl}$, in order to measure the PHE signal. The sample was introduced inside of this coil and the driving current was parallel with $H_{\rm bias}$. All the measurements were made using a driving current of 10 mA through the PHE sensors.

III. Results and Discussion

Many other samples, of the type presented above, have been characterized for MR and PHE but the best results in what concern the field sensitivity were obtained with these two SV structures. Therefore we present results regarding field and angular dependences of the PHE signal for these two samples.

A. Si/Ta(3 nm)/Co(30 nm)/Cu(7 nm)/$Ni_{80}Fe_{20}$(70 nm)/Ta(3 nm)

When a DC biasing setup is used, Fig. 1(a), the magnetization keeps, in principle, the same value, but rotates under the action of the applied field. If the rotation angle is small, the variation of the PHE is proportional with 2 θ. Fig. 2 presents the field dependencies of the PHE voltage for different values of the biasing field, $H_{\rm bias}$, measured for the Co(30 nm)/Cu(7 nm)/$Ni_{80}Fe_{20}$(70 nm) structure.

The hysteresis effects that appear for low biasing fields can be lowered for a higher biasing field, but the sensitivity decreases to 0.03–0.056 μV·A^{-1}·m. So, a balance between sensitivity and hysteretic effects can be done in function of the desired application. For lower biasing fields, the magnetization do not saturates and the film will not behave like a single domain structure which rotates when $H_{\rm appl}$ is applied. So, when $H_{\rm bias}$ increases, the magnetization increases until reaches the saturation value. This reduces the hysteresis effects but the increase of $H_{\rm bias}$ has opposite effects in what concern the sensor's sensitivity as we can see from Fig. 2. In the case of ML structure, the coupling effects between the magnetic layers trough the nonmagnetic layer (Cu) and the higher anisotropy of the Co layer will play important roles on the field behaviour of the PHE signal. When the biasing field is higher, the Co layer tends to maintain the orientation of the NiFe layer magnetization because of the positive magnetostatic coupling between them. When the biasing field is low, there are hysteretic effects because of the reversal mechanism of magnetisation which is mainly due to domain wall movement.

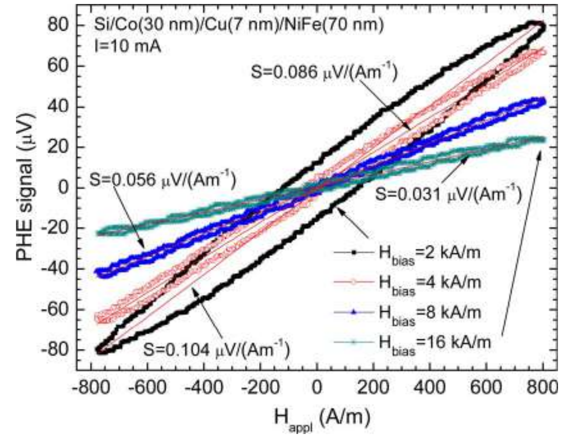

Fig. 2. Field dependencies of the PHE for Co(30 nm)/Cu(7 nm)/$Ni_{80}Fe_{20}$(70 nm) structure for different biasing fields, $H_{\rm bias}$.

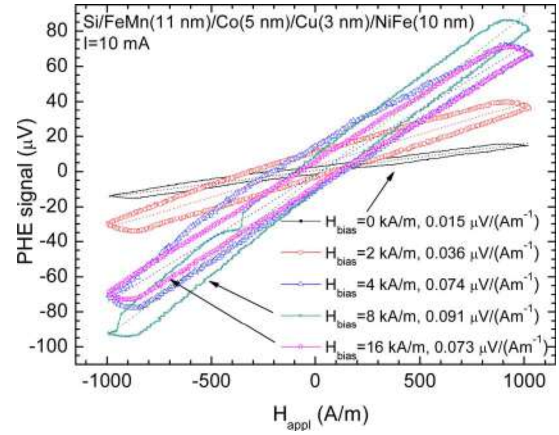

Fig. 3. Field dependencies of the PHE for Si/Ta(3 nm)/$Fe_{50}Mn_{50}$(11 nm)/Co(5 nm)/Cu(3 nm)/$Ni_{80}Fe_{20}$(10 nm)/Ta(3 nm) ML structure for different biasing fields, $H_{\rm bias}$.

The influence of the biasing field on the PHE signal and the role played by the Co layer were also confirmed by micromagnetic simulations. To perform these simulations we have considered a biasing setup like in Fig. 1(a), with a disc-shaped structure divided in a mesh with magnetic single domains [9], [10].

B. Si/Ta(3 nm)/$Fe_{50}Mn_{50}$(11 nm)/Co(5 nm)/Cu(3 nm)/$Ni_{80}Fe_{20}$(10 nm)/Ta(3 nm)

Fig. 3 presents the field dependencies of the PHE voltage for different values of the DC biasing field, $H_{\rm bias}$, measured in accordance with the setup presented in Fig. 1(a). Before making these measurements, the sensor was saturated in a field of 800 kA/m applied like $H_{\rm bias}$, Fig. 1(a).

These field dependencies emphasise, by comparison with the data presented in Fig. 2, the importance of the thickness of the Co pinned layer. The thinner Co layer is not able to induce in the free layer of Permalloy a magnetization state close to the single domain one in the absence of the biasing field. For

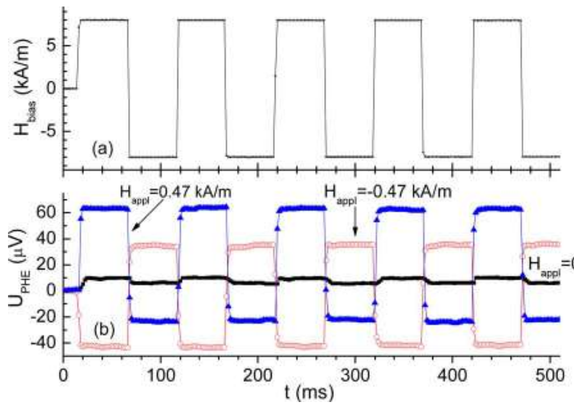

Fig. 4. Waveforms of the biasing field and PHE signals for $H_{appl} = 0, -0.47$ and 0.47 kA/m.

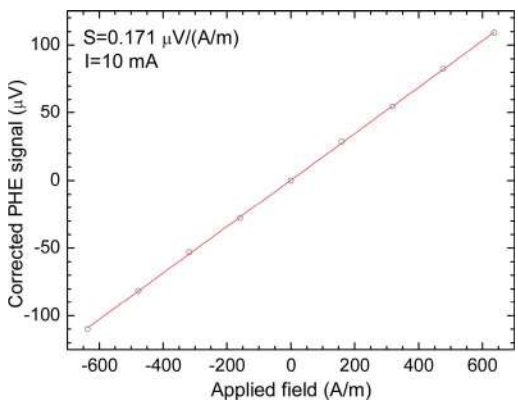

Fig. 5. Calibration curve of the AC square wave biased sensor.

$H_{bias} = 0$, the field sensitivity of the PHE voltage is very small, 0.015 μV·A^{-1}·m, because the film magnetization, M, has a low value. When H_{bias} increases, the field sensitivity increases which means that the magnetization of the free layer reaches the saturation state. A sensitivity of 0.091 μV·A^{-1}·m is obtained for a biasing field strength of 8 kA/m (about 100 Oe). A further increase of the biasing field lowers the field sensitivity of the PHE voltage. A higher biasing field tends to maintain, together with the Co layer, the orientation of the NiFe free layer magnetization. To obtain the same signal like in the case when $H_{bias} = 8$ kA/m, a higher torque is needed to rotate the magnetization of the free layer, i.e., a higher applied field is needed. When $H_{bias} = 16$ kA/m the field sensitivity becomes 0.073 μV·A^{-1}·m which is the same sensitivity when $H_{bias} = 4$ kA/m.

To improve the sensor linearity and to cancel the hysteretic effects, we used AC square wave biasing field with the peak amplitude equal to 8 kA/m. To apply this setup, we used a coil, instead of the electromagnet, to produce the pulsing biasing field. Using the coil it was possible to accurately control the amplitude and the waveform of the pulsing biasing field, avoiding the effects of the high inductance and hysteretic behavior which are typical for an electromagnet. The applied field is produced by pair of Helmholtz coils. The peak to peak amplitude of the PHE signal is dependent on the applied field strength. The phase difference between the AC PHE signal and the AC biasing field depends on the applied field polarity. By this means the polarity of the applied field can be established (synchronous rectifying process). Fig. 4 presents the waveforms of the AC square wave biasing field and the waveforms of the measured PHE signals for $H_{appl} = 0. -0.47$ and 0.47 kA/m. The frequency of the biasing field was 10 Hz for these experiments.

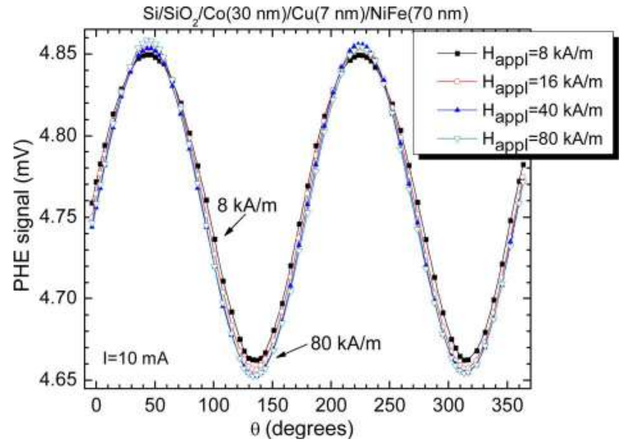

Fig. 6. Angular dependence of the PHE voltage measured for different values of the applied field.

From Fig. 4 we can see the phase difference (180°) between the waveforms for both polarities of the applied field. The asymmetries of these three wave forms arise from the misalignment between the injected driving current, I, and the direction of the applied field. Subtracting from the AC signal measured at different applied fields the signal for $H_{appl} = 0$, the peak to peak amplitude of the corrected signal is a function of H_{appl}. The calibration curve that results is presented in Fig. 5.

The field sensitivity, in this case, is about twice the field sensitivity when a DC biasing field of 8 kA/m is used. Also, it is to note the linearity and symmetry of the corrected signal.

C. Angular Dependence of the PHE

The equation that describes the PHE predicts a periodic dependence of the signal on the angle, θ, between the current direction and the film magnetization. This dependence, in $\sin 2\theta$, suggests applications of the PHE such as contactless potentiometer, magnetic compass, etc. We present, in Fig. 6, the angular dependencies of the PHE voltage measured for the ML Si/Co(30 nm)/Cu(7 nm)/$Ni_{80}Fe_{20}$(70 nm) for different values of the applied field; there is no biasing field. At this stage of our research we did not made measurements for weak magnetic fields, useful for compass applications. The applied magnetic field rotates with respect to the current direction, Fig. 1. The amplitude of the PHE signal depends on the field strength when $H_{appl} < 40$ kA/m as can be seen in Fig. 6. This is because the magnetization needs a field higher than 16 kA/m to saturate and to follow the orientation of H_{appl}. If $H_{appl} > 40$ kA/m the curves that describe the angular dependence of the PHE will have the same amplitude. For the linear regions of the angular dependence, the sensitivity is about 2.9 μV/degree and is almost independent on the field amplitude if $H_{appl} > 16$ kA/m. These aspects are important for designing practical applications because the signal becomes field independent when H_{appl} is higher than a critical value.

IV. Conclusion

PHE measurements for various DC and AC pulsing biasing fields have been made. The sensitivity and linearity of the field dependence of the PHE signal can be tuned through the biasing field. By using AC square wave biasing fields the linearity and symmetry of the PHE signal can be improved and the zero error can be automatically corrected. Sensitivities up to 0.171 μV$\cdot$A$^{-1}\cdot$m can be achieved. The field behavior of the PHE signal depends on the spin valve structure.

The same structure can be used to build rotation sensors. For this reason we used disc-shaped SV structures.

Further improvements will be made regarding the deposition on the same substrate of the field generator stripe and the PHE sensor using the IC technology. A better alignment between the biasing field, H_{bias}, and the injected current, I, will be achieved in this way.

Acknowledgment

This work was supported by the Romanian National Authority for Scientific Research under Grants PCCE-ID_76/2010 and PN2 72-165/2008.

References

[1] C. Prados, D. Garcia, F. Lesmes, J. J. Freijo, and A. Hernando, "Extraordinary anisotropic magnetoresistance effect under 35 Oe field at room temperature in Co/Ni multilayers," *Appl. Phys. Lett.*, vol. 67, pp. 718–720, 1995.

[2] Montaigne, A. Schuhl, F. N. Van Dau, and A. Encinas, "Development of magnetoresistive sensors based on planar Hall effect for applications to microcompass," *Sens. Actuator A*, vol. 81, pp. 324–327, 2000.

[3] E. M. Epshtein, A. I. Krikunov, and Y. F. Ogrin, "Planar Hall effect in thin-film magnetic structures. Cobalt films on silicon substrates," *J. Magn. Magn. Mater.*, vol. 258–259, pp. 80–83, 2003.

[4] K. M. Chui, A. O. Adeyeye, and L. Mo-Huang, "Detection of a single magnetic dot using a planar Hall sensor," *J. Magn. Magn. Mater.*, vol. 310, pp. e992–e993, 2007.

[5] A. Schuhl, F. N. Van Dau, and J. R. Childress, "Low-field magnetic sensors based on the planar Hall effect," *Appl. Phys. Lett.*, vol. 66, pp. 2751–2753, 1995.

[6] F. N. Van Dau, A. Schuhl, J. R. Childress, and M. Sussiau, "Magnetic sensors for nanotesla detection using planar Hall effect," *Sens. Actuator A*, vol. 53, pp. 256–260, 1995.

[7] B. D. Tu *et al.*, "Optimization of spin-valve structure NiFe/Cu/NiFe/IrMn for planar Hall effect based biochips," *IEEE Trans. Magn.*, vol. 45, no. 6, pp. 2378–2382, Jun. 2009.

[8] J. O. Oti, SimulMag Version 2.0j, Micromagnetic Simulation Software, User's Manual. Boulder, CO, Electromagnetic Technology Division, National Institute of Standards and Technology, 80303 [Online]. Available: http://math.nist.gov/oommf/contrib/simulmag/

[9] M. Volmer and J. Neamtu, "Simulated and measured hysteresis curves for thin films," *Phys. B: Condensed Matter*, vol. 372, pp. 198–201, 2006.

[10] M. Volmer and J. Neamtu, "Electrical and micromagnetic characterization of rotation sensors made from Permalloy multilayered thin films," *J. Magn. Magn. Mater.*, vol. 322, pp. 1631–1634, 2010.

Journal of Magnetism and Magnetic Materials 322 (2010) 1631–1634

Contents lists available at ScienceDirect

Journal of Magnetism and Magnetic Materials

journal homepage: www.elsevier.com/locate/jmmm

Electrical and micromagnetic characterization of rotation sensors made from permalloy multilayered thin films

Marius Volmer [a,*], Jenica Neamtu [b]

[a] Transilvania University of Brasov, Eroilor 29, Brasov 500036, Romania
[b] Advanced Research Institute for Electrical Engineering, Splaiul Unirii 313, Bucharest 030138, Romania

ARTICLE INFO

Available online 7 July 2009

Keywords:
Magnetic sensor
Anisotropic magnetoresistance
Planar Hall effect
Stoner–Wolfarth
Micromagnetic simulation
Magnetic film

ABSTRACT

Planar Hall effect (PHE) measurements were performed on permalloy (Py)-based thin films and multilayered structures like FeMn/Py/Cu/Py. FeMn is used for pinning the magnetization of the adjacent Py layer by exchange biasing effect. Here, we present some results of our measurements made on square- and ring-shaped thin-film structures used as rotation sensors. At low magnetic fields, i.e., less than 200 Oe, we observed hysteretic effects and distortions from the expected sinusoidal shape of the angular dependence of the PHE voltage. This is due to hysteretic behaviour of the magnetic material and some coupling effects in the multilayered structure. In order to have a better understanding of this behaviour, micromagnetic simulations were performed to obtain the angular dependence of the sample magnetization for different intensities of the rotating magnetic field. To get better results, the film plane was divided into a number of single domains which interact between them and with the applied magnetic field.

1. Introduction

The sensors made from magnetic films are of particular interest because their electrical response is strongly related to their magnetic state. Thin films made from permalloy ($Ni_{80}Fe_{20}$) and multilayered structures based on this ferromagnetic material are intensively used for building magnetic sensors, write–read heads for high-density data storage or magnetic memories. Because of the anisotropic magnetoresistance effect (AMR) which is found in such structures, an electrical field perpendicular to the applied current will be generated even when the magnetic field is in the film plane. This is the planar Hall effect (PHE). Therefore, using a Hall effect setup we get direct access to the anisotropic part of the film resistance with the advantage of a good thermal stability of the output signal. The PHE voltage can be expressed by a simple phenomenological expression [1]

$$U = CM^2 j \sin 2\theta \quad (1)$$

where C is a constant determined by the film geometry and material properties, j the current density, M the saturation magnetization and θ the angle between the current and the magnetization vector that, in turn, is determined by the value and direction of the external magnetic field. The PHE can be used to obtain information regarding the magnetic properties of the material by means of electrical measurements. Also, from relation (1) it comes that this effect can be used to build high-sensitivity magnetic sensors for field measurements, detection of magnetic-labelled biomolecules, rotation sensors or contactless potentiometer applications.

Two types of films were used: (i) $Ni_{80}Fe_{20}$(10 nm) thin film, and (ii) a FeMn (3 nm)/$Ni_{80}Fe_{20}$(10 nm)/Cu(4 nm)/$Ni_{80}Fe_{20}$(10 nm) multilayer (ML) structure. The samples were grown on oxidised Si substrates by thermal deposition.

2. Results and discussion

The results presented in this paper are for square- and ring-shaped structures used for PHE measurements. The square-shaped samples have the side of 5 mm and the contacts were placed on the corners using silver paste and Cu wires. For ring-shaped structures, the four stripes for electrical contacts were defined during the film deposition and placed over two orthogonal diagonals. The ring has an external diameter of 6 mm and an interior diameter of 2 mm. The four lead setup used to investigate the PHE is presented in Fig. 1(a) [2,3]; θ defines the angle between the electrical current, I_1, and the applied field H. However it is difficult to define such an angle for the ring-shaped structure. So we will define, by convention, the same angle, θ, taking the angle between line which passes through the contacts by which is injected the current I_1 and the direction of the field H. This measurement setup gets the maximum response from the AMR

* Corresponding author. Tel.: +40 268 412921; fax: +40 268 414690.
E-mail address: volmerm@unitbv.ro (M. Volmer).

0304-8853/$ - see front matter
doi:10.1016/j.jmmm.2009.06.085

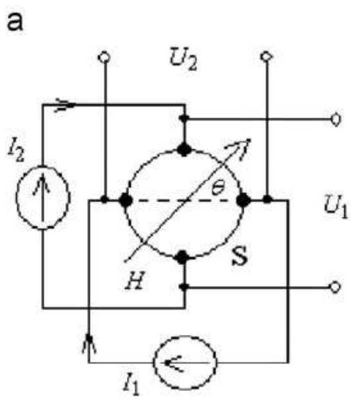

Fig. 1. (a) The four lead setup used for PHE measurements and (b) the equivalent Wheatstone bridge model to account the electrical behaviour of the sample. The magnetic field, H, is applied in the film plane.

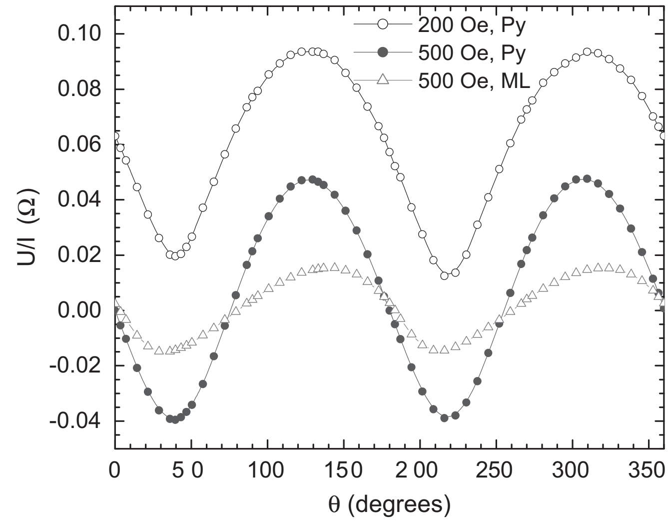

Fig. 2. Angular dependence of the PHE, for different values of the applied field, measured for $Ni_{80}Fe_{20}$(10 nm) thin film, denoted as Py, and for FeMn (3 nm)/$Ni_{80}Fe_{20}$(10 nm)/Cu(4 nm)/$Ni_{80}Fe_{20}$(10 nm) ML structure. Different offset values were introduced in order to make these dependencies more visible. The current through the samples was $I=1.77$ mA.

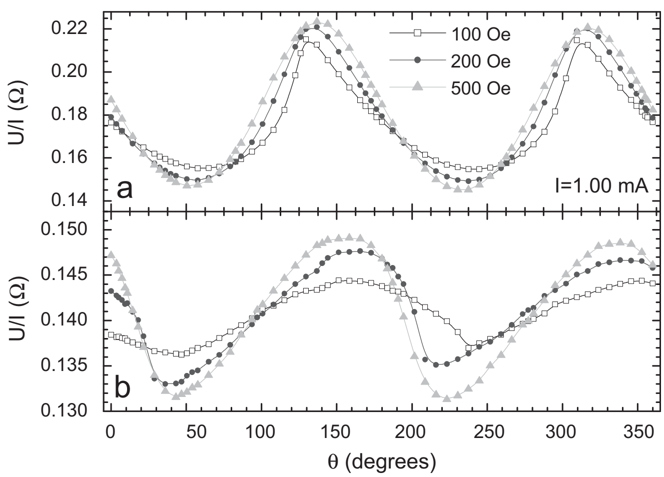

Fig. 3. Angular dependence of the PHE effect, for different values of the applied field, measured for (a) $Ni_{80}Fe_{20}$(10 nm) film and (b) for FeMn(3 nm)/$Ni_{80}Fe_{20}$(10 nm)/Cu(4 nm)/$Ni_{80}Fe_{20}$(10 nm) ML ring-shaped structures. The current through the samples was $I=1.00$ mA.

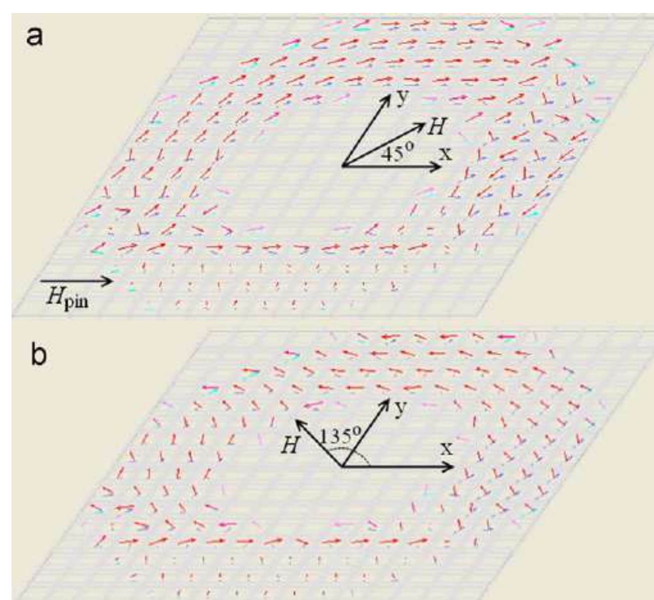

Fig. 4. The orientations of the magnetic moments in the ring-shaped ML structure for two directions (a) 45° and (b) 135° of the applied magnetic field; $H=100$ Oe. The dark arrows are from the free layer and the grey arrows are from the pinned layer.

effect with the advantage of a lower thermal drift. The equivalent resistor arrangement model [4] is presented in Fig. 1(b) and helps us to understand the angular behaviour of the PHE voltage.

The DC current sources I_1 and I_2 drive the same current, I, through the sample, S, and are computer controlled. When the source I_1 is ON, the source I_2 is OFF and the measured PHE voltage is U_1. When the source I_2 is ON, the source I_1 is OFF and the measured PHE voltage is U_2. In this way, for a given angle, θ, between the magnetic field, H, and the direction of the current driven by I_1, we made two measurements for the PHE. Because for an ideal experimental setup $U_1=U_2$ we will take as reference for angle measurements the direction of the current I_1 for both measurements. The PHE voltage was detected using a Keithley digital multimeter model 2700 equipped with a scan card in order to switch between channels I_1, U_1 and I_2, U_2. The angular dependence was achieved by using a stepper-motor allowing rotation with a precision of 0.1°. Classical measurements, i.e. angular dependence of the voltage U_1, show a distortion of the symmetry with respect to the abscissa axis. The results are far from the behaviour predicted by Eq. (1). These results were observed both for square- and ring-shaped structures and are due to contacts misalignment and hysteretic behaviour of the magnetic films, especially at low fields [2,3]. We explained this by micromagnetic simulations and we showed that the film magnetization cannot follow accurately the direction of the magnetic field when $H<200$ Oe [2,3]. Due to the coupling effects between the magnetic layers through the Cu layer and pinning effects in the ML structure, the hysteretic behaviour is increased. To compensate the errors due to contacts misalignment and to increase the sensor sensitivity, we made two measurements of the PHE voltage for each angle over two orthogonal directions using the setup presented in Fig. 1(a). Making the PHE measurements for permalloy and ML structures over these two orthogonal directions we obtained, by summating the voltages U_1 and U_2, a response $U=(U_1+U_2)/2$ with a sinusoidal behaviour with two periods for a complete rotation [2]. For square-shaped samples the results are presented in Fig. 2.

As we have shown previously [2,3], for disk-shaped $Ni_{80}Fe_{20}$(10 nm) thin film, the PHE angular dependence has almost the same amplitude for applied fields higher than 200 Oe because the structure saturates easily. This was also proved by micromagnetic simulations regarding magnetization behaviour in rotating field. The same was obtained for the square-shaped sensor made from $Ni_{80}Fe_{20}$(10 nm) thin film. On the other hand, the coupling effects between the magnetic layers in the ML structure alter the PHE angular dependence and introduce hysteretic effects. The film starts to saturate for fields higher than 500 Oe. Because when the total magnetic moment decreases it is expected to have a lower amplitude of the PHE voltage as we can see in Fig. 2.

In what follows, we report on PHE measurements made on ring-shaped structures of Py- and Py-based ML. The results are presented in Fig. 3.

Because of the shape of these structures, the magnetization cannot follow accurately the field direction and, for low amplitudes of H, the PHE angular dependence is strongly distorted. This situation can be illustrated by the results of micromagnetic simulations performed on a ring-shaped ML structure. In Fig. 4 are presented the orientations of the magnetic moments in the ML structure for two directions of the applied field; $H=100$ Oe.

Because of the tendency to have closure domains in this ring-shaped structure and the interaction between the magnetic layers, there is a region in which the magnetic moments change their orientation rotating in a direction perpendicular to the film plane in order to minimise the free energy of the system. We see that the magnetic moments from the free layer follow roughly the orientation of the applied field. We run micromagnetic simulations to see the angular dependence of magnetization for $Ni_{80}Fe_{20}$(10 nm) film and for FeMn(3 nm)/$Ni_{80}Fe_{20}$(10 nm)/Cu(4 nm)/$Ni_{80}Fe_{20}$(10 nm) ML ring-shaped structures. The results are presented in Fig. 5.

We observe from these results a lower value of magnetization for the ML structure and strong hysteretic effects for $H<200$ Oe for both the structures. These results can be correlated with the magnetic moment's configurations presented in Fig. 4, and show why the PHE signal for $H=100$ Oe is so small and distorted. To perform these simulations we used a special design which consists of a collection of single domains of permalloy, with a side length of 90 nm and a thickness of 10 nm, which interact between them and with the applied magnetic field [3,5,6]. Also, the interaction between the magnetic layers through the nonmagnetic layer was taken into account and the coupling constant was calculated considering the Néel model for positive magnetostatic interlayer coupling [5,7]. Using data obtained from micromagnetic simulations, Fig. 5, we can calculate the field dependence of the PHE signal. The results are presented in Fig. 6.

These data are relatively in good agreement with experimental data presented in Fig. 3. There is a 180° phase difference between the measured and calculated data and is due to the experimental setup. From Figs. 3(a) and 6(a) we see that for $H>200$ Oe the PHE signal becomes field insensitive which is very important regarding the sensor stability for small field variations. The smaller values of the PHE signal and the angular behaviour seen in Fig. 3(b), for the ML structure, is well described by the results of micromagnetic simulations presented in Figs. 5(b) and 6(b). To obtain a PHE signal stable at field variations a value of H greater than 500 Oe is required.

Because for $\theta=135°$ the PHE signal has a maxima we can expect to have, for this angle, the best response in what concern the field dependence of the PHE signal. We present, in Fig. 7, the

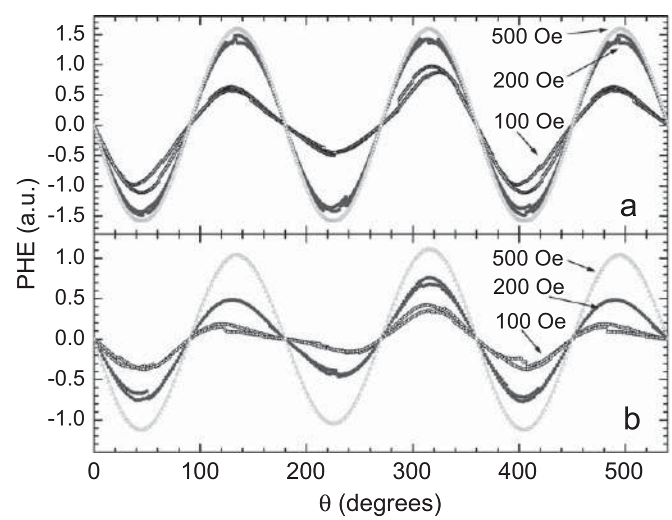

Fig. 6. The calculated PHE angular dependence for different values of the applied magnetic fields for (a) $Ni_{80}Fe_{20}$(10 nm) film and (b) for FeMn(3 nm)/$Ni_{80}Fe_{20}$(10 nm)/Cu(4 nm)/$Ni_{80}Fe_{20}$(10 nm) ML ring-shaped structures.

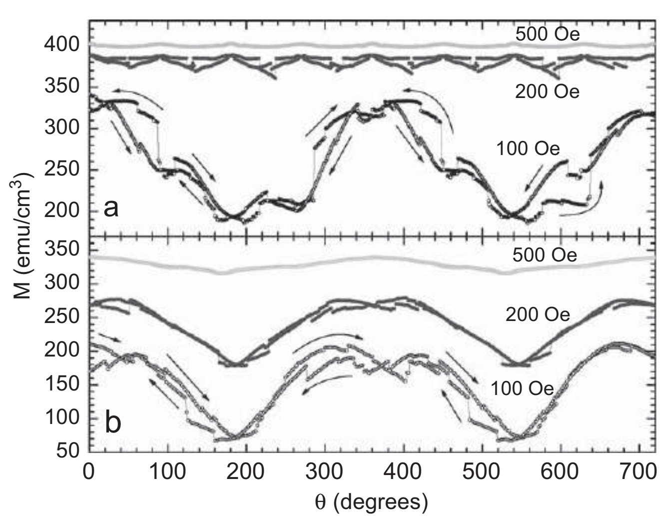

Fig. 5. Micromagnetic simulations of the angular dependence of the magnetization for (a) $Ni_{80}Fe_{20}$(10 nm) film and (b) for FeMn(3 nm)/$Ni_{80}Fe_{20}$(10 nm)/Cu(4 nm)/$Ni_{80}Fe_{20}$(10 nm) ML ring-shaped structures. The arrows are guide for the eyes.

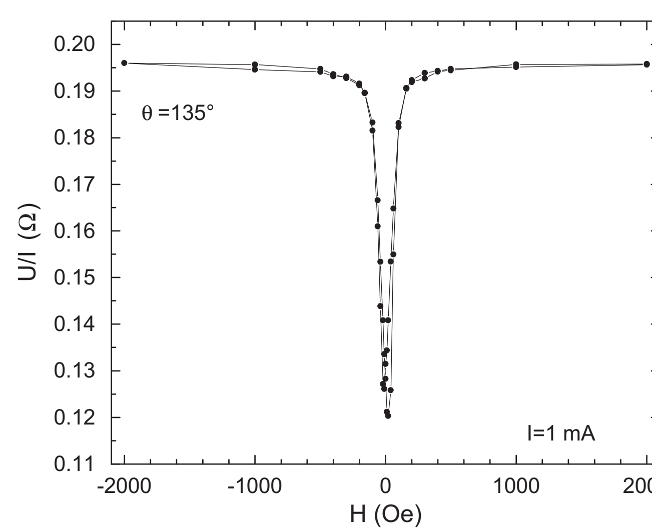

Fig. 7. Field dependence of the PHE signal for a ring-shaped $Ni_{80}Fe_{20}$(10 nm) thin film; H is applied in the film at an angle $\theta=135°$ according to Fig. 1(a).

field dependence of the PHE for a ring-shaped magnetic sensor made from $Ni_{80}Fe_{20}$(10 nm) thin film.

The structure presents a very sharp variation of the PHE signal for small magnetic fields and almost without hysteretic effects because of the shape of the sensor.

3. Conclusions

We studied the angular response of the PHE for $Ni_{80}Fe_{20}$(10 nm) and FeMn(3 nm)/$Ni_{80}Fe_{20}$(10 nm)/Cu(4 nm)/$Ni_{80}Fe_{20}$(10 nm) ML square- and ring-shaped structures. By micromagnetic simulations, we have shown the origin of the distortions which can be seen for low magnetic fields. By making PHE measurements over two orthogonal directions for each angle, we were able to compensate the errors that appear due to contact misalignments, hysteretic effects and homogeneities defects. The optimum value of the magnetic field strength is between 200 and 500 Oe for $Ni_{80}Fe_{20}$(10 nm) structures higher than 500 Oe for the ML structures. Despite of their simplicity, the $Ni_{80}Fe_{20}$(10 nm) structures are very convenient to be used to build low-cost rotation sensors and magnetic field sensors based on the PHE. We believe that a careful tuning of the interlayer coupling in the ML structures can increase the angular and field dependence of the PHE signal because of the GMR effect.

Acknowledgment

This work was supported by the Grant PN2 71-127/2007 SPINVALVE.

References

[1] E.M. Epshtein, A.I. Krikunov, Yu.F. Ogrin, J. Magn. Magn. Mater. 258–259 (2003) 80.
[2] M. Volmer, J. Neamtu, J. Magn. Magn. Mater. 316 (2007) e265–e268.
[3] M. Volmer, J. Neamtu, Physica B 403 (2008) 350–353.
[4] C. Prados, D. Garcia, et al., Appl. Phys. Lett. 67 (1995) 718.
[5] M. Volmer, J. Neamtu, Physica B 372 (2006) 198.
[6] John O. Oti in: SimulMag Version 1.0, Micromagnetic Simulation Software, User's Manual, Electromagnetic Technology Division, National Institute of Standards and Technology Boulder, Colorado 80303, December 1997.
[7] J.C.S. Kools, et al., IEEE Trans. Magn. 31 (1995) 3918.